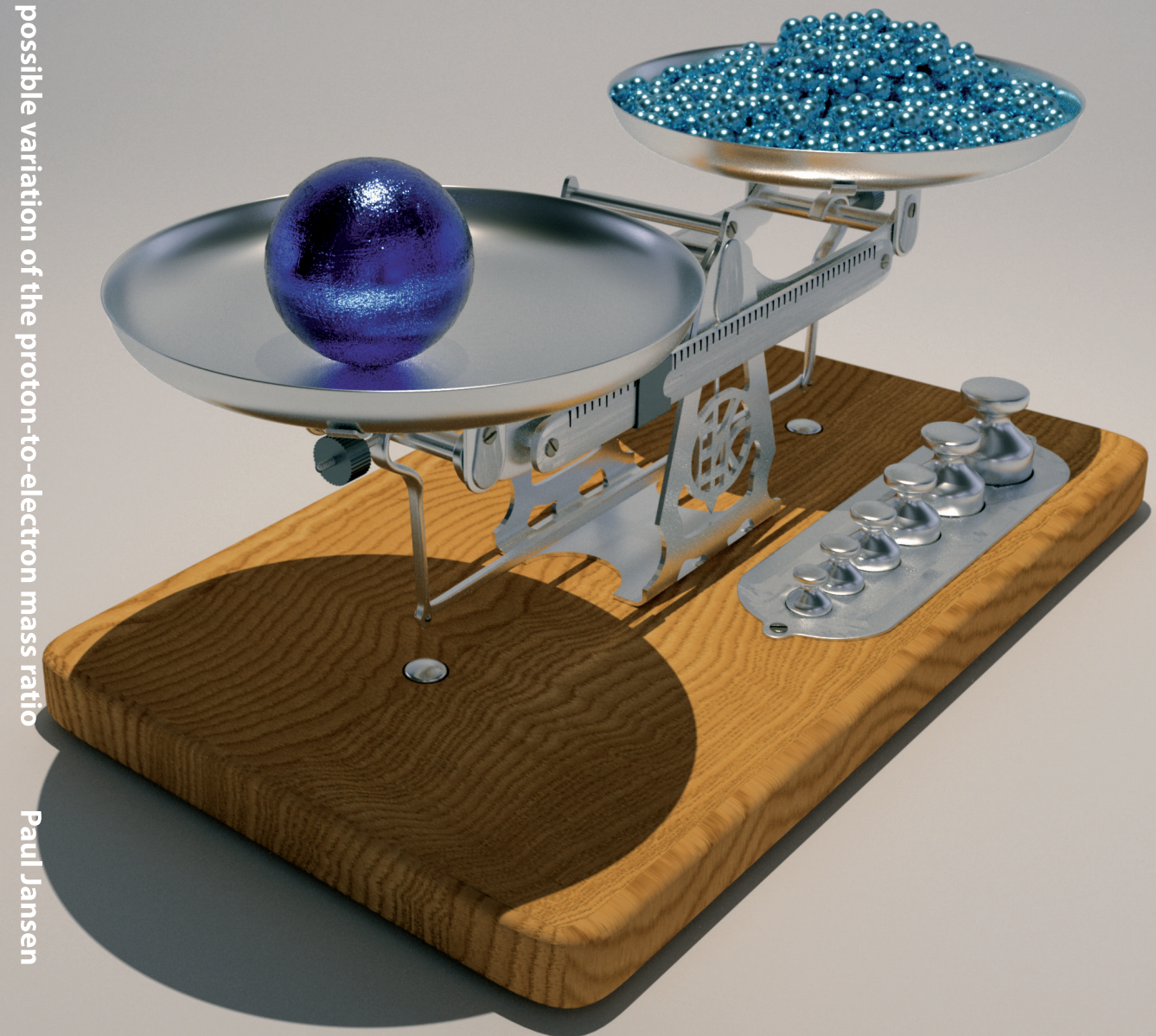


Polyatomic molecules for probing a possible variation of the proton-to-electron mass ratio

Paul Jansen



Polyatomic molecules for probing a possible variation of the proton-to-electron mass ratio

Paul Jansen

**Polyatomic molecules for probing a possible variation of
the proton-to-electron mass ratio**

VRIJE UNIVERSITEIT

**Polyatomic molecules for probing a possible variation of
the proton-to-electron mass ratio**

ACADEMISCH PROEFSCHRIFT

ter verkrijging van de graad Doctor aan
de Vrije Universiteit Amsterdam,
op gezag van de rector magnificus
prof. dr. B. Oudega,
in het openbaar te verdedigen
ten overstaan van de promotiecommissie
van de Faculteit der Exacte Wetenschappen
op maandag 1 juli 2013 om 15.45 uur
in de aula van de universiteit,
De Boelelaan 1105

door

Paul Jansen

geboren te Velsen

promotor: prof. dr. W. M. G. Ubachs
copromotor: dr. H. L. Bethlem

*We were led by a star.
– Led by a bottle, more like.*

Scene from Monty Python's Life of Brian

This thesis was approved by the members of the reviewing committee:

Prof. Dr. H. Bakker (AMOLF, Amsterdam and University of Amsterdam)
Prof. Dr. W. J. Buma (University of Amsterdam)
Dr. I. Kleiner (LISA, CNRS UMR 7583, UPEC and UPD, Paris)
Prof. Dr. G. J. M. Meijer (FHI, Berlin and Radboud University Nijmegen)
Prof. Dr. S. Stolte (Vrije Universiteit Amsterdam, and Jilin University, China)



The work described in this thesis was carried out in the Institute for Lasers, Life and Biophotonics of the VU University Amsterdam and was supported by the Netherlands Organization for Scientific Research (NWO) via a VEDI grant and by the European Research Council (ERC) by a Starting grant.

The cover depicts an artist impression by the author of determining the proton-to-electron mass ratio; the weight of the proton is almost balanced by the 1836 electrons.

ISBN: 978-90-6464-674-4

Printed by: GVO drukkers & vormgevers B.V. | Ponsen & Looijen

CONTENTS

CHAPTER 1: INTRODUCTION AND SUMMARY	1
1.1 High-resolution spectroscopy	4
1.1.1 Rabi's molecular-beam resonance method	4
1.1.2 Ramsey's method of separated oscillatory fields	6
1.1.3 A Zacharias fountain	8
1.2 Stark deceleration of neutral molecules	9
1.3 Energy level structure and Stark shift in ammonia	12
1.3.1 The inversion splitting in ammonia	12
1.3.2 Rotational structure of ammonia	15
1.3.3 Stark shift in ammonia	17
1.3.4 Sensitivity of the inversion frequency to a variation of μ	19
1.4 Intermezzo: the escape of an alpha particle	22
1.5 Radioastronomical observations of MeOH	25
1.6 Outline of this thesis	28
CHAPTER 2: TOWARDS A MOLECULAR FOUNTAIN	29
2.1 Introduction	29
2.2 The ammonia molecule	31
2.3 Experimental setup	32
2.4 Experimental results and numerical simulations	36
2.4.1 Operation of the Stark decelerator	36
2.4.2 Focusing and bunching of slow molecules	39
2.5 Conclusions and outlook	44
CHAPTER 3: VELOCITY MAP IMAGING OF A SLOW BEAM OF AMMONIA MOLECULES INSIDE A QUADRUPOLE GUIDE	47
3.1 Introduction	47
3.2 Experimental setup	48
3.3 Characterizing the ion optics	50
3.4 Experimental results	52
3.5 Conclusions	56
CHAPTER 4: DECELERATING AND TRAPPING OF AMMONIA MOLECULES IN A RING-TYPE DECELERATOR	57
4.1 Introduction	57
4.2 Ring decelerator concept	58
4.2.1 Electric potential	58
4.2.2 Waveform considerations	61
4.2.3 Calculation of forces and trajectories	62

4.3	Experimental setup	65
4.4	Results	66
4.4.1	Guiding, deceleration and trapping of ammonia	66
4.4.2	Phase-space matching	69
4.4.3	Phase jumps	71
4.4.4	Parametric resonances	73
4.5	Conclusions	75
CHAPTER 5: METHANOL AS A SENSITIVE PROBE FOR SPATIAL AND TEMPORAL VARIATIONS OF THE PROTON-TO-ELECTRON MASS RATIO		77
5.1	Introduction	77
5.2	Molecular structure of methanol	78
5.3	Sensitivity coefficients	79
5.4	Numerical results	81
5.5	Conclusions	83
CHAPTER 6: SENSITIVITY OF TRANSITIONS IN INTERNAL ROTOR MOLECULES TO A POSSIBLE VARIATION OF THE PROTON-TO-ELECTRON MASS RATIO		85
6.1	Introduction	85
6.2	Hindered internal rotation	87
6.2.1	Hamiltonian	87
6.2.2	Eigenfunctions and eigenvalues	90
6.2.3	Level schemes and selection rules	93
6.3	Scaling and sensitivity coefficients	94
6.4	“Toy” model	98
6.5	Conclusion and outlook	104
CHAPTER 7: SENSITIVITY TO A POSSIBLE VARIATION OF THE PROTON-TO-ELECTRON MASS RATIO OF TORSION-WAGGING-ROTATION TRANSITIONS IN METHYLAMINE (CH₃NH₂)		107
7.1	Introduction	107
7.2	Hamiltonian and energy level structure	109
7.3	Scaling relations of the molecular parameters	111
7.3.1	Pure rotational constants	113
7.3.2	CH ₃ torsion and the h_{3v} parameter	113
7.3.3	Inversion and the h_{2v} parameter	115
7.3.4	q_2 and r_2 parameters	116
7.3.5	Higher order terms	116
7.4	Sensitivity of selected transitions	116
7.5	Conclusion	122
SAMENVATTING		125
APPENDIX A: SCALING OF MOLECULAR CONSTANTS		131

APPENDIX B: SENSITIVITY COEFFICIENTS OF SELECTED TRANSITIONS IN METHANOL	135
BIBLIOGRAPHY	145
DANKWOORD	155
PUBLICATIONS	157

INTRODUCTION AND SUMMARY

The structure of our Universe is determined by the laws of physics. These laws have two characteristics: they are written in terms of mathematical equations and they contain empirical parameters, the so-called constants of nature. This can be illustrated with the simple example of the gravitational force at the surface of the Earth. The well-known expression for this force is

$$F_g = mg. \quad (1.1)$$

Mathematically this equation tells us that if we drop a body, whether it be a sphere of lead¹ or a molecule under vacuum conditions, from a certain height, the attractive gravitational force, F_g , experienced by the body is linearly proportional to its mass, m , while the value of the “coupling” constant g tells us that the body falls with an acceleration of about 10 m/s^2 . In this expression, g is treated as a constant, but a careful analysis of experimental data reveals that g varies across the surface of the earth and that its assumed constancy is only a first estimate.

The fact that g does not represent a *fundamental* constant should not come as a surprise, since Eq. (1.1) is an approximation of Newton’s law of universal gravitation

$$F_g = G \frac{mM}{r^2}, \quad (1.2)$$

¹This famous experiment of two falling bodies is frequently attributed to Galileo Galilei but was actually first reported by the Flemish scientist and engineer Simon Stevin in his book *De beghinselen der weeghconst* published in 1586:

“Let us take (as the very learned Mr Jan Cornets de Groot, most industrious investigator of the secrets of nature and myself have done) two spheres of lead, the one ten times larger and heavier than the other, and drop them together from a height of 30 feet onto a board or something on which they will give a perceptible sound. Then it will be found that the lighter will not be ten times longer on its way than the heavier but that they will fall together onto the board so simultaneously that their two sounds seem to be one and the same rap.” (translated from old Dutch [1])

where G is the gravitational constant, m and M are the masses of the bodies involved and r is the distance between the centers of mass of the two bodies. At the earth's surface, Eq. (1.2) reduces to Eq. (1.1). Hence, we arrive at the fascinating result that Newton's law of universal gravitation is able to explain the value of the constant g in terms of three variables and a more fundamental constant G . It is natural to ask whether it is possible to account for the value of this new constant G also at a more fundamental level, as we did for g . So far, it turns out that the answer to this question is negative and that G – at least at this moment – represents a true fundamental constant of nature, that is, the strength or coupling constant of the gravitational force, and its value cannot be explained by any theory. In fact, one of the first scientists to question the constancy of G was P.A.M. Dirac in connection with his *Large Number Hypothesis* [2]. In order to explain peculiar coincidences that exist between the ratios of size scales in the Universe to that of force scales, Dirac hypothesized a cosmology in which the value of G is inversely proportional to the age of the Universe. Although later measurements proved that Dirac's theory was wrong [3, 4], these observations constituted the first search for a variation of a fundamental constant.

This simple example of the gravitational force touches upon one of the fundamental aims of science, that is, to discern the order that exists between and amongst experimental observations at the most basic level. The flagship of fundamental science is arguably the Standard Model of particle physics which explains how all matter in our Universe is built up from 12 fundamental particles and held together by 3 fundamental forces. The Standard Model distinguishes two basic groups of matter particles, quarks and leptons, that are paired in three generations. The interaction between the particles is governed by the electromagnetic force, the strong nuclear force, and the weak nuclear force. Gravity, the fourth fundamental force of nature, it is not (yet) included in the Standard Model. Each of the forces in the Standard Model have an associated coupling constant that is a measure of the strength of the interaction. The values of these coupling constants are not predicted by the Standard Model nor by any other theory and can only be obtained through experiments. In fact, the Standard Model does not require these constant to be constant, and statements about their constancy over space and time are based on experimental observations and on a strong believe in Einstein's equivalence principle. Nonetheless, a small change in any of these constants has a dramatic impact on the appearance of our Universe. The fine structure constant $\alpha = 1/137.035999074(44)$ [5], for example, determines the overall strength of the electromagnetic interaction, and is crucial for the existence of atoms and their binding into molecules and it determines largely why complex molecules can exist at all.

Another dimensionless constant is the proton-to-electron mass ratio $\mu = m_p/m_e = 1836.15267245(75)$ [5]. Unlike the electron, which belongs to the family of leptons, the proton is not a fundamental particle but a composition of three quarks. The combined rest mass of the three valence quarks ($\sim 10 \text{ MeV}/c^2$ [6, 7]), however, only accounts for about 1% of the proton's mass ($938 \text{ MeV}/c^2$). Most of the mass is determined by the nuclear binding energy that holds these quarks together. As a consequence, the value of μ provides a measure of the fundamental interaction strength of the strong nuclear force, α_s . The interplay between the values of α and α_s gives rise to the so-called Hoyle resonance that facilitates the triple-alpha process required for the production

of carbon-12 atoms [8, 9]. A variation in α or α_s on the order of a few percent reduces the stellar production of carbon or oxygen up to three orders of magnitude [10]. From these examples, it appears as if the values of the fundamental constants in our Universe are fine-tuned to allow for the existence of life in it².

Physical theories extending the Standard Model have presented scenarios that allow for, or even predict, spatial-temporal variations of the constants of nature. A possible spatial or temporal variation of the fine structure constant, α , or the proton-to-electron mass ratio, μ , can be detected by comparing transitions in atoms and molecules as a function of time and/or position [11]. As these transitions have, in general, a different dependence on α and μ , a possible variation will manifest itself as a shift of the transition frequencies. The research described in this thesis is concentrated on a possible variation of μ . Theories, based on the assumption of Grand Unification, have predicted that $\Delta\mu/\mu$ is much larger than $\Delta\alpha/\alpha$, making the proton-to-electron mass ratio a preferred test ground for probing drifts in fundamental constants [12]. Experiments searching for signatures of a variation of fundamental constants can be roughly divided into two main classes: astronomical searches and laboratory searches. In astrophysical searches, the frequencies of two or more atomic and molecular absorptions from distant objects are compared with the frequencies as measured in the laboratory. This allows one to determine the apparent redshift – and hence distance to the object – and a possible variation. The main advantage of this approach is the long accumulation time that is probed for systems at high redshift, however, this comes at the cost of limited control over the experimental parameters and a significant complication of the data analysis [13]. Laboratory searches, on the other hand, offer great control over the experimental parameters, but have the disadvantage that only a short period of time can be probed, thus requiring measurements with an extremely high resolution.

The sensitivity of any experiment searching for a frequency shift $\Delta\nu$ due to the variation of μ depends both on the size of the shift, i.e., the inherent sensitivity of the molecular transition, and on the ability to measure this shift. For sake of comparison, we assume that a possible variation of μ can be described adequately by a linear model. Hence, the ability to detect a temporal variation of μ is given by

$$\left(\frac{\partial\mu}{\partial t}\right)/\mu = \left(\frac{\partial\nu}{\nu}\right)/(K_\mu\Delta t), \quad (1.3)$$

with $(\partial\mu/\mu)/\partial t$ the fractional rate of change of μ , $\partial\nu/\nu$ the fractional frequency precision of the measurement, K_μ the inherent sensitivity of a transition to a variation of μ , and Δt the time interval that is probed in the experiment. For a sensitive test, one needs molecular transitions that are observed with a good signal to noise and narrow linewidth, and that exhibit high K_μ . In addition, one needs to compare at least two transitions, preferably in the same molecule, that possess a different sensitivity in order to detect a possible variation of μ . The three terms on the right-hand side of Eq. (1.3) are important for any experiment that aims to probe temporal variation of μ

²Hoyle's reasoning that the resonant state of carbon had to exist since carbon-based life exists, is an example of the application of the anthropic principle. This principle states that observations of the physical Universe must be compatible with the conscious life that observes it.

and determine the ability to detect such a variation. In order to increase the sensitivity of the experiment one has to find a suitable combination of (i) the resolution of the experiment, (ii) the range in sensitivities of the transitions that are being probed, and (iii) the time interval between successive measurements. In this thesis, these different terms form a starting point for approaching possible variation of μ .

The remainder of this chapter is structured as follows. In Sec. 1.1, high-resolution spectroscopy, such as the molecular-beam resonance method and the separated oscillatory fields method, are introduced. The ideas presented in this section provide the framework for the molecular fountain experiment that is discussed in Chapter 2. This fountain experiment is based on the technique of Stark deceleration that will be described in Sec. 1.2.

In Sec. 1.3, the ammonia molecule, which is used in the experiments described in this thesis, is treated in detail. The sensitivity coefficients for the inversion frequency of the ammonia molecule are derived in this section as well. Sec. 1.4 is a short intermezzo containing a discussion on the calculation of K_μ coefficients of alpha emitters.

In Sec. 1.5 the results of an observation campaign at the 100 m Effelsberg radio telescope are presented. In this survey four methanol lines are used to constrain μ variation on a cosmological time scale.

1.1 High-resolution spectroscopy

1.1.1 Rabi's molecular-beam resonance method

The energy or frequency resolution of any spectroscopic experiment is limited by the interaction time of the investigated species with the radiation field that drives the transitions. The interaction time depends on both the size of the interaction region and on the velocity of the examined particles flying through the field. Precision measurements of nuclear, molecular, and atomic properties began in 1938 when Isidor Rabi introduced the molecular-beam resonance method [14, 15]. A schematic representation of a typical molecular-beam-resonance setup is shown in Fig. 1.1a. After the molecules emerge from the source, they pass through two regions of inhomogeneous magnetic or electric fields. Neutral molecules that possess a magnetic or electric dipole moment will be deflected from the molecular beam axis by such inhomogeneous fields and will not reach the detector. In the absence of the second field, these molecules would be lost, however, if the field gradient of the second field is directed oppositely to that of the first field, it can refocus the deflected beam onto the detector [16]. The refocusing depends upon the magnitude and orientation of the magnetic or electric dipole moment and thus on the quantum state of the molecule. If an oscillatory field of length L , that is placed between the two deflection fields, drives transitions to another quantum state, the signal intensity will be reduced.

A detailed derivation of the line shape of a such a Rabi resonance can be found in Ref. [16], here we only will summarize the main results. Consider a closed two level system with eigenstates $|1\rangle$ and $|2\rangle$ of energy E_1 and E_2 , respectively, that are the solutions of the time-independent Schrödinger equation $H\psi_n = E_n\psi_n$. At time $t_0 = 0$, this

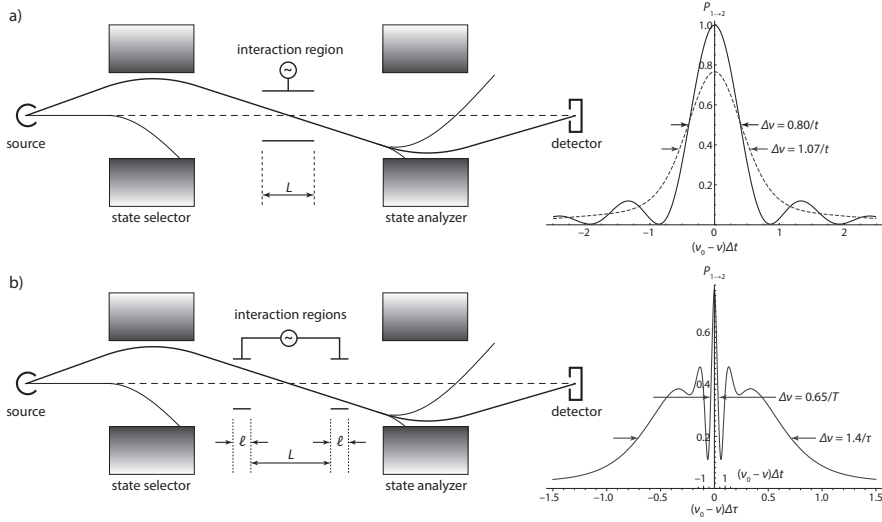


FIGURE 1.1: (a) Schematic diagram of a molecular-beam resonance apparatus (left-hand side) and corresponding line shapes (right-hand side). The solid curve is the ideal line shape for a mono-energetic molecular beam, whereas the dashed curve is the line shape averaged over all velocities in the beam. For both curves the magnitude of the perturbation, b , and measuring time, t , were chosen such as to produce the smallest line width. (b) Schematic diagram of a separated oscillatory field apparatus (left-hand side) and corresponding line shape (right-hand side). Note that the central part of the curve is calculated near resonance, while the outer parts are calculated off resonance.

system enters a region where it is subjected to an oscillatory perturbation that induces transitions between the states $|1\rangle$ and $|2\rangle$. The oscillating field with frequency $\omega/2\pi$ causes a perturbation V that is of such a form that the elements of the perturbation matrix are

$$V_{ij}(t) = -\frac{q_e \mathcal{E}_{z0}}{2} (e^{i\omega t} + e^{-i\omega t}) \mu_{ij}, \quad \text{with } \mu_{ij} = -q_e \langle i|z|j\rangle, \quad (1.4)$$

where q_e is the magnitude of the electron charge, \mathcal{E}_{z0} is the amplitude of the light wave that is chosen to be polarized along the z direction, and μ_{ij} is the dipole matrix element. From parity selection rules it follows that $\mu_{11} = \mu_{22} = 0$ and from the fact that the dipole element represents a measurable quantity and H is Hermitian we find $\mu_{21} = \mu_{12}$. For notational convenience, we define $b = \mu_{12} \mathcal{E}_{z0} / (2\hbar)^3$.

Assuming that at time $t_0 = 0$ only the lowest level is populated, the probability $P_{1 \rightarrow 2}$

³Note that in this notation $2b = \Omega_R$, where Ω_R is the Rabi frequency for the transition between states $|1\rangle$ and $|2\rangle$.

of a transition from state $|1\rangle$ to state $|2\rangle$ is given by

$$P_{1 \rightarrow 2} = \frac{(2b)^2}{(\omega_0 - \omega)^2 + (2b)^2} \sin^2 \left\{ \frac{1}{2} \sqrt{(\omega_0 - \omega)^2 + (2b)^2} t \right\},$$

with $\omega_0 = (E_2 - E_1)/\hbar$. (1.5)

It can be seen that this probability reaches a maximum when $\omega = \omega_0$ and that the full half-width of this line shape depends on b and t . If the interaction time t is fixed while b is varied at resonance, $P_{1 \rightarrow 2}$ reaches a maximum when $t = \pi/2b$. The line shape of Eq. (1.5) for these parameter values is shown as the solid curve on the right-hand side of Fig. 1.1a. Under these conditions, the full half-width of $P_{1 \rightarrow 2}$ is given by $\Delta\omega = 3.19b$, or, in units of Hz $\Delta\nu = 0.80/t$.

In practice, the conditions for the ideal line shape of Eq. (1.5) to be valid are rarely met exactly. In many cases, for instance, the interaction time is not fixed due to the velocity distribution of the particles in the beam and Eq. (1.5) has to be averaged over the range of velocities. The average of $P_{1 \rightarrow 2}$ is then

$$\langle P_{1 \rightarrow 2} \rangle = \frac{(2b)^2}{(\omega_0 - \omega)^2 + (2b)^2} \left[\frac{1}{2} - I \left(\sqrt{(\omega_0 - \omega)^2 + (2b)^2} t \right) \right],$$

with $I(x) = \int_0^\infty e^{-y^2} y^3 \cos(x/y) dy$. (1.6)

The integral function $I(x)$ has to be evaluated numerically. The maximum transition probability at resonance is reached when the measuring time and the magnitude of the perturbation are related by $2bt = 1.200\pi$ [16] and has a value of $\langle P_{1 \rightarrow 2} \rangle = 0.75$. The shape of the resulting resonance curve predicted by Eq. (1.6) is shown as the dashed curve on the right-hand side of Fig. 1.1a. The full half-width is $\Delta\omega = 3.574b$, or

$$\Delta\nu = 1.072/t, \quad (1.7)$$

in units of Hz. Compared to the line width of a mono-energetic beam, the effect of the velocity spread is to broaden the resonance by roughly 25%. Moreover, as can be seen on the right-hand side of Fig. 1.1a, the periodic features of the Eq. (1.5) are washed out and the linewidth becomes Gaussian.

1.1.2 Ramsey's method of separated oscillatory fields

Eq. (1.7) suggests that an unrestricted increase in the resolution of spectral lines could be realized by increasing the length of the oscillatory field region. In practice, however, this unlimited increase in precision cannot be achieved. The main problem that is associated with increasing the length of the field region is the requirement to maintain a completely uniform field over this length. As a consequence, the resonance frequencies are not constant during the measurement resulting in a line width that is much broader than predicted by Eq. (1.7) and often increases with increasing length, rather than decreases [16]. These difficulties were overcome when Norman Ramsey introduced the

method of separated oscillatory field in 1949 [17, 18]. As the name suggests, this method involves the sequential application of the oscillatory field that drives the transition with a field-free region in between. This technique exploits interference of quantum superposition states and bears great resemblance with Young's double slit experiment in optics.

The left-hand side of Fig 1.1b shows a schematic configuration of a typical setup consisting of two oscillatory field regions of length ℓ , separated by a distance L . The traversal time of a single field region is denoted by τ , whereas the traversal time between the two field regions is denoted by T . The transition probability for a mono-energetic two-level system is given by [16]

$$P_{1 \rightarrow 2} = 4 \frac{(2b)^2}{a^2} \sin^2\left(\frac{1}{2}a\tau\right) \times \left[\cos\left(\frac{1}{2}\delta\omega T\right) \cos\left(\frac{1}{2}a\tau\right) - \left(\frac{\omega_0 - \omega}{a}\right) \sin\left(\frac{1}{2}\delta\omega T\right) \sin\left(\frac{1}{2}a\tau\right) \right]^2, \quad (1.8)$$

with $a = [(\omega_0 - \omega)^2 + (2b)^2]^{1/2}$, and $\delta\omega = \bar{\omega}_0 - \omega$, where $\hbar\bar{\omega}_0$ is the average energy separation between the two states over the distance L .

The first term in the above expression is just 4 times the probability of a Rabi transition defined in Eq. (1.5), whereas the second term gives rise to an interference pattern that depends on the relative phase difference, $\delta\omega T$, between the system and the oscillatory field. This process can be visualized on a Bloch sphere where the south and north pole correspond to state $|1\rangle$ and $|2\rangle$, respectively, as shown in Fig. 1.2. In order to maximize the interference between the two oscillating fields, the first field creates an equal superposition of states $|1\rangle$ and $|2\rangle$, that is, $P_{1 \rightarrow 2} = \frac{1}{2}$. This probability is achieved when $a\tau = \pi/2$, and such a pulse is referred to as a “ $\pi/2$ pulse”. Consider a beam of molecules in state $|1\rangle$ that enters the first field region which is near resonant with the $|1\rangle \rightarrow |2\rangle$ transition and creates an equal superposition of states $|1\rangle$ and $|2\rangle$ (Fig. 1.2a). The time evolution of the coefficients in the superposition corresponds to a rotation of the state vector around the vertical axis of the Bloch sphere. This rotation can be separated into two counter-rotating components in the horizontal plane; the angular frequency of the driving field ω , and the eigenfrequency of the system ω_0 . It is therefore convenient to define a coordinate frame that co-rotates with the frequency of the driving field [19]. In this new coordinate system, the relative phase of $|1\rangle$ and $|2\rangle$ evolves at a frequency of $\delta\omega$. If, at the time that the second pulse is applied, the relative phase has completed an integer number of cycles (Fig. 1.2b), the pulse will transfer all population to the upper state. However, if the phase has completed a half-integer number of cycles, the pulse will return the system to its ground state (Fig. 1.2c). By scanning the frequency of the driving field one obtains a pattern of so-called Ramsey fringes.

The line shape predicted by Eq. (1.8) is only valid for a mono-energetic beam of particles. In order to obtain an expression for a realistic beam, the transition probability of Eq. (1.8) should be averaged over the velocities in the beam, as was done in the previous section. Ramsey [16] derives two convenient expressions by averaging in two

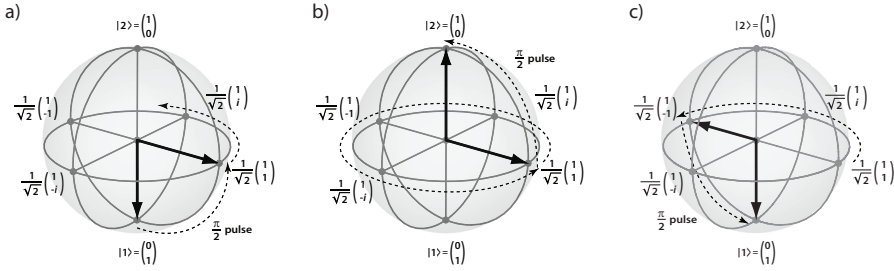


FIGURE 1.2: Bloch sphere visualization of the separated oscillatory fields method. a) The initial $\pi/2$ pulse creates an equal superposition of states $|1\rangle$ and $|2\rangle$, which starts rotating about the vertical axis at a frequency $\delta\omega$. b) After an integer number of rotations, the second pulse projects all population onto state $|2\rangle$, hence completing the transition. c) After a half-integer number of rotations the second pulse rotates the state vector back to the initial state $|1\rangle$.

limiting cases, that is, near resonance and off resonance, resulting in

$$\langle P_{1 \rightarrow 2} \rangle = \frac{1}{4} - \frac{1}{4} I(\delta\omega T + 4b\tau) - \frac{1}{4} I(\delta\omega T - 4b\tau) + \frac{1}{2} I(\delta\omega T) - \frac{1}{2} I(4b\tau), \quad (1.9)$$

and

$$\langle P_{1 \rightarrow 2} \rangle = \frac{(2b)^2}{a^2} \left(1 - \frac{3}{4} \frac{(2b)^2}{a^2} \right) - 2 \frac{(2b)^2 (\omega_0 - \omega)^2}{a^4} I(a\tau) - \frac{1}{2} \frac{(2b)^4}{a^4} I\left(\frac{1}{2}a\tau\right), \quad (1.10)$$

respectively. The maximum transition probability at resonance is found when $2b\tau = 0.600\pi$. For this value of b , an indication of the general line shape over the entire resonance region is plotted on the right-hand side of Fig. 1.1b where the transition probabilities from Eqs. (1.9) and (1.10) are plotted on the same curve. The full width at half maximum of the central fringe is given by $\Delta\nu = 0.65/T$, which is almost a factor of two smaller than the resonance width of a Rabi transition. Furthermore, in the separated oscillatory field method the driving field needs have a constant phase over the short distance ℓ , whereas in the Rabi method the driving field needs to be uniform over the entire length L . As a consequence, the resonance width of a Ramsey transition can be reduced to an arbitrary value by increasing the length of the field-free region.

1.1.3 A Zacharias fountain

The method of separated oscillatory fields provides a line width of the resonance peaks that is 40 percent narrower than the corresponding width for a single oscillatory field measurement. In addition, the sharpness of the resonance is not reduced by instantaneous temporal or spatial fluctuations in a field that is applied between the two coils, as only the space-averaged value of the energy appears in Eqs. (1.9) and (1.10). By the end of 1952, Jerrold Zacharias realized that a further improvement in resolution is feasible by adjusting the design of the separated oscillatory field molecular-beam

apparatus shown in Fig. 1.1b [16, 20]. Instead of using an apparatus with a molecular-beam axis that is oriented horizontally, Zacharias proposed to construct a vertical setup that would exploit the slow tail of an atomic cesium beam⁴. Atoms with an upward velocity of 10 m/s would fly up some 5 m before falling back under gravity and hit a detector alongside the source. An oscillatory field placed about a meter below the top of the apparatus would then act as both the first and second field region to perform the Ramsey spectroscopy. The total interrogation time, that is, the time between the first and second traversals through the oscillating field, in such a “fountain” experiment would be in the order of a second and would result in Ramsey fringes with a 1 Hz resolution. Eventually, Zacharias’ fountain experiment failed due to the unexpected deficiency of the required ultraslow cesium atoms, which were scattered out of the beam before they could emerge from the oven [22], and the experiment was abandoned in 1957 [21].

It was not until the mid eighties, when the great progress in laser cooling and trapping techniques for atoms, stimulated renewed interest in Zacharias’ idea [23, 24]. The first atomic fountain was demonstrated by Kasevich *et al.* in 1989 using laser-cooled sodium atoms [25]. An atomic fountain based on laser-cooled cesium atoms was realized in Paris by Clairon *et al.* in 1991 [26]. Nowadays, state-of-the-art laser-cooled cesium atomic fountain clocks realize the International System of Units’ (SI) definition of the second with a relative accuracy of 3×10^{-16} [27]. The advances in laser cooling and trapping of atoms provided the source of slow particles that was lacking in Zacharias’ initial attempts. It is therefore expected that a similar control over the motion of molecules is of crucial importance for a successful demonstration of a molecular fountain. We will employ Stark deceleration to obtain a relatively dense packet of molecules at a low velocity. Stark deceleration is a technique that uses time-varying inhomogeneous electric fields to decelerate part of a molecular beam to a computer-controlled velocity and can therefore be used to create a source of slow molecules required for a molecular fountain experiment.

1.2 Stark deceleration of neutral molecules

Since the first implementations of atomic and molecular beams, scientists have tried to manipulate the trajectories of the particles in the beam by applying magnetic or electric field gradients. Probably the most famous of these attempts is the Stern-Gerlach experiment that was aimed at probing space quantization via measuring the deflection of a beam of atoms with a magnetic moment when moving through an inhomogeneous magnetic field [28]. A more elaborate manipulation scheme was conceived by Rabi, who introduced the molecular beam magnetic resonance method that consists of two successive magnets with oppositely directed inhomogeneous field gradients [14, 15]. The invention of electrostatic lenses [29], which are capable of focusing neutral particles in selected quantum states, has been of utmost importance for establishing population inversion in a beam of ammonia molecules and resulted in the invention of the

⁴Knowledge of J. R. Zacharias’ work has been passed down in the oral tradition. In Ref. [21] an account of the fountain experiment is given based on interviews with Zacharias’ coworkers.

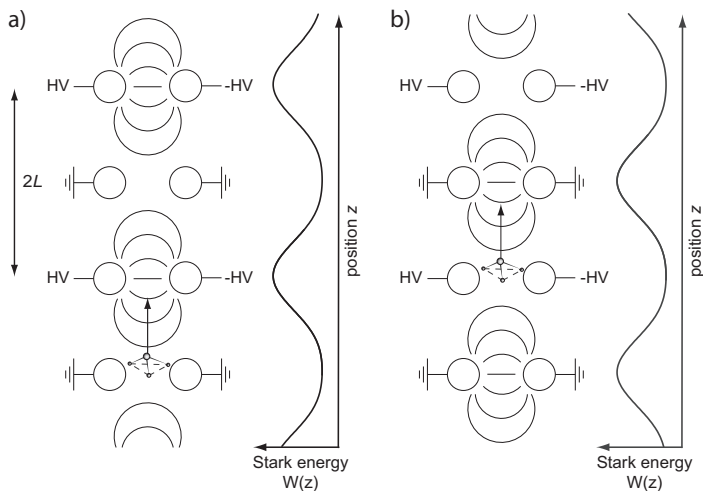


FIGURE 1.3: The operation principle of a Stark decelerator; molecules lose kinetic energy upon repeated switching between two high-voltage configurations shown in panel (a) and (b).

maser [30]. The manipulation of atomic and molecular beams with external fields in the past exclusively involved the transverse motion of the molecules [31]. In this section we describe how the longitudinal velocity of molecules in a beam can be manipulated using time-varying electric fields⁵.

In a Stark decelerator, the longitudinal velocity of a beam of polar molecules is manipulated using an array of inhomogeneous electric fields, as shown in Fig. 1.3. The principle of a Stark decelerator is equivalent to that of a charged-particle accelerator, the difference being that in a Stark decelerator the force experienced by a polar molecule depends on its electric dipole moment and on the field gradient, whereas in a charged-particle accelerator the force depends on the particle's charge and on the electric field strength. As a consequence, the force exerted on molecules in a Stark decelerator is quantum-state specific and typically eight orders of magnitude smaller than the forces that are typically obtained in charged-particle accelerators [33]. Since the first demonstration of Stark deceleration using metastable CO molecules [34], the technique has routinely been applied to many other molecules [35, Table 1].

As the name suggests, a Stark decelerator, exploits the Stark effect that originates from the interaction of a polar molecule with an electric field. The Stark effect can either be positive or negative, that is, the energy shift increases or decreases with increasing electric field strength, respectively. The force, F_{Stark} , that acts upon a molecule in a

⁵It is interesting to note that deceleration of molecules was first attempted by John King in Zacharias' lab at MIT in 1958. King and Zacharias intended to produce a slow ammonia beam to obtain a maser with an extremely narrow linewidth [32].

specific quantum state in an electric field follows from

$$F_{\text{Stark}} = -\frac{dW_{\text{Stark}}}{dr} = \mu_{\text{eff}} \frac{\partial |\vec{E}|}{\partial r} \quad \text{with } \mu_{\text{eff}} = -\frac{\partial W_{\text{Stark}}}{\partial |\vec{E}|}, \quad (1.11)$$

with W_{Stark} the Stark shift and $|\vec{E}|$ the electric field magnitude.

As a consequence, molecules that possess a negative Stark shift experience a force toward a region of higher electric field and are referred to as high-field seekers, while molecules with a positive Stark shift experience a force toward a region of lower electric field and are referred to as low-field seekers. The ground state of any molecule is always high-field seeking.

When a polar molecule in a low-field-seeking state – for example, an ammonia molecule in the $|J, MK\rangle = |1, 1\rangle$ state – approaches a region of high electric field that is produced by a pair of electrodes as indicated in Fig. 1.3, part of the initial kinetic energy of the molecule is transformed into (potential) Stark energy and the molecule slows down. However, the molecule will regain its initial kinetic energy as it leaves the region of high electric field again. This latter acceleration can be avoided if the electric field is abruptly switched off before the molecule has regained its initial velocity.

The electric-field strength that can be obtained experimentally is typically limited to about 200 kV/cm. The kinetic energy that is lost in such an electric field is about two orders of magnitude smaller than the kinetic energy of the molecular beam. Nevertheless, full control over the longitudinal motion of the molecules in the beam can be achieved by repeating the deceleration process many times. In a Stark decelerator this is accomplished by using an array of equidistant field stages, separated by a distance L , as shown in Fig. 1.3. Each stage consists of two cylindrical metal rods with radius r that are placed $2r + d$ apart and each rod is connected to either a positive or negative switchable power supply. The rods that form every other electric-field stage are connected to each other. In addition to the deceleration force, molecules in a low-field-seeking state experience a force toward the beam axis, as the electric field is higher near the electrodes than on the axis. However, this focusing only occurs in the direction perpendicular to the electrodes while there acts virtually no force in the direction parallel to the electrodes. In order to achieve a net focusing force in both transverse directions throughout the decelerator, subsequent electric field stages are oriented orthogonally. Note that for clarity all electrodes in Fig. 1.3 are depicted with the same orientation.

At a given time, the even-numbered stages are switched to high voltage and the odd-numbered stages are grounded, or vice versa. The Stark energy of a molecule in a low-field-seeking state as a function of the longitudinal position z for the two situations is sketched in Fig. 1.3. It is convenient to define the so-called “synchronous molecule”, i.e., the molecule to which the switching of the electric fields is synchronized. When the synchronous molecule reaches a position that is close to the top of the Stark potential, the stages that were at high voltage are switched to ground and the stages that were grounded are switched to high voltage. As a consequence, the molecule finds itself in front of a new potential hill and again loses kinetic energy as it climbs up this hill. When the molecule is close to the maximum of the potential hill, the voltages are switched

back to the initial configuration. By repeating this process, the velocity of the molecule is reduced in a semi-continuous fashion [31, 33].

The amount of energy that is lost per stage depends on the position of the synchronous molecule at the moment that the fields are being switched. In analogy with concepts used in charged-particle accelerators, this position is expressed in terms of a phase angle ϕ_0 that has a periodicity of $2L$. A phase angle of $\phi_0 = 90^\circ$ corresponds to a maximum loss of kinetic energy, while a phase angle of $\phi_0 = -90^\circ$ corresponds to a maximum gain of kinetic energy. An important property of the Stark decelerator is that the deceleration process does work not only for the synchronous molecule, but for all molecules that at the entrance of the decelerator occupy a phase-space volume that is close to the phase-space coordinate of the synchronous molecule.

1.3 Energy level structure and Stark shift in ammonia

All experiments that are described in this thesis are based on ammonia molecules for a number of reasons. (i) The ammonia molecule is studied in great detail in the past and spectroscopic information for many of its molecular states can be found in the literature. (ii) Ammonia exhibits a classically forbidden large amplitude motion, associated with the inversion of the molecule, that results in an enhanced sensitivity to a variation of μ . (iii) The relatively low mass and large dipole moment of the ammonia molecule make that ammonia can be decelerated effectively with a Stark decelerator. In this section some features of the ammonia molecule are discussed that are relevant for the work described in this thesis.

1.3.1 The inversion splitting in ammonia

In the electronic ground state, the ammonia molecule has the form of a regular pyramid, whose apex is formed by the nitrogen atom, while the base consists of an equilateral triangle formed by the three hydrogen atoms. In the electronic ground state, there exists a particular vibrational motion which is associated with the inversion of the molecule. The angle between the line connecting the centroid of the base with the apex and one of the NH bonds is referred to as the umbrella angle ρ , as the vibrational motion of the molecule resembles the movement of an umbrella which is being opened and closed, and during which ρ oscillates at a fairly rapid rate around its equilibrium value [36, 37]. After a large number of such vibrations, the nitrogen atom may penetrate the hydrogen plane, and begin oscillations on the other side. Note that this tunneling would normally destroy a conventional umbrella. The potential energy $V(\rho)$ of this system, neglecting all other degrees of freedom, is shown in Fig. 1.4 as a function of ρ . Note that in the Born-Oppenheimer approximation this potential curve is identical for all isotopologues of ammonia. The two minima of $V(\rho)$ correspond to symmetrical configurations of the molecule such that the nitrogen atom is located on either side of the plane formed by the three hydrogen atoms at the equilibrium angles $\rho_0 = 68^\circ$ and 112° . The molecule can vibrate around ρ_0 in either of the two potential wells with an angular frequency of $\tilde{\nu}_0 = 950 \text{ cm}^{-1}$ [36, 37]. As seen from Fig. 1.4, the potential forms

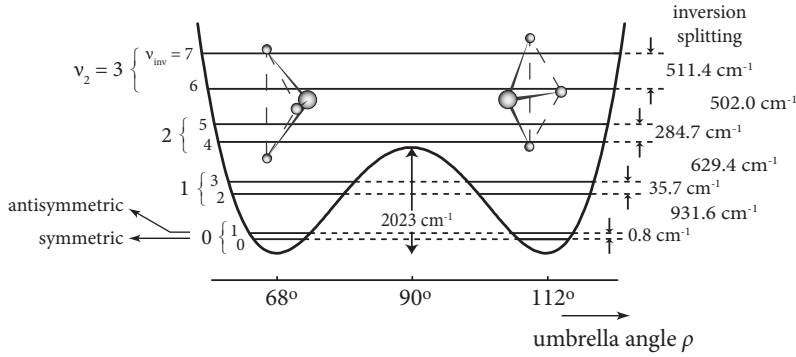


FIGURE 1.4: Potential energy curve for the electronic ground state of NH_3 as a function of the umbrella angle ρ . Due to tunneling through the potential barrier each vibrational level is split in a symmetric and antisymmetric component.

a barrier at $\rho = 90^\circ$, i.e., when the nitrogen atom is in the plane of the hydrogen atoms. The one-dimensional Schrödinger equation for the motion along the symmetry axis of the molecule is given by

$$-\frac{\hbar^2}{2\mu_{\text{red}}} \frac{d^2\psi(z)}{dz^2} + V(z)\psi(z) = E\psi(z), \quad (1.12)$$

with μ_{red} the reduced mass⁶ and $z = d_{\text{NH}} \sin \rho$, where d_{NH} the NH bond distance. If the barrier between the two potential wells were of infinite height, the two wells would be totally disconnected and each energy eigenvalue of the system would be doubly degenerate. The eigenfunctions associated with a given energy would be linear combinations of the ‘left’ and ‘right’ wave functions $\hat{\psi}_L$ and $\hat{\psi}_R$ which have zero amplitude for $z \geq 0$ and $z \leq 0$, respectively [37]. These wave functions are sketched in Fig. 1.5(a) for the lowest vibrational state ($v = 0$). However, as the barrier is finite, quantum-mechanical tunneling of the nitrogen atom through the plane of the hydrogen atoms couples the two wells. This tunneling motion lifts the degeneracy, and the energy levels are split into doublets. Moreover, due to the tunneling the wave functions $\hat{\psi}_L$ and $\hat{\psi}_R$ do not vanish for $z \geq 0$ and $z \leq 0$, respectively. The wave functions for a barrier of finite height, ψ_L and ψ_R , are sketched in Fig. 1.5(b). Due to the coupling between the two wells, these functions do not correspond to eigenfunctions of Eq. (1.12), as the true eigenfunctions must be either symmetric or antisymmetric with respect to the inversion operator $z \rightarrow -z$ [37]. The energy eigenfunctions are shown in Fig. 1.5(c) and are given by

$$\psi_1 = \frac{1}{\sqrt{2}}(\psi_L + \psi_R), \text{ and } \psi_2 = \frac{1}{\sqrt{2}}(\psi_L - \psi_R), \quad (1.13)$$

⁶As a simple approximation we assume that the distance between the hydrogen atoms remains constant during the motion in which case $\mu_{\text{red}} = 3m_{\text{H}}m_{\text{N}}/(3m_{\text{H}} + m_{\text{N}})$, with m_{H} and m_{N} the mass of the hydrogen and nitrogen atom, respectively.

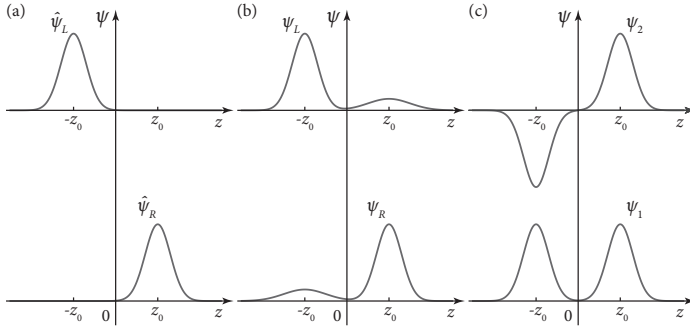


FIGURE 1.5: Schematic wave functions for the ammonia molecule; (a) In case of an infinite barrier, the two wells are totally disconnected and each energy eigenvalue of the system is doubly degenerate. The eigenfunctions associated with a given energy are linear combinations of the ‘left’ and ‘right’ wave functions $\hat{\psi}_L$ and $\hat{\psi}_R$. (b) In case of a finite barrier, coupling between the two wells causes a leakage of amplitude to the other side of the barrier. The corresponding wave functions ψ_L and ψ_R are not eigenfunctions to the Hamiltonian nor are they orthogonal to each other. (c) The true eigenfunctions ψ_1 and ψ_2 are the symmetric and antisymmetric combination of $\hat{\psi}_L$ and $\hat{\psi}_R$.

where we have assumed that ψ_L and ψ_R are normalized to unity. The symmetrical wave function ψ_1 corresponds to the lowest energy of the doublet, whereas the antisymmetrical wave function ψ_2 corresponds to the higher energy. The vibronic ground state is designated as $X(0)$ for the symmetric component and $X(1)$ for the antisymmetric component. The tunneling through the barrier with a height of 2023 cm^{-1} is responsible for an energy splitting of 0.8 cm^{-1} and 36 cm^{-1} in the ground vibrational and first excited vibrational states, respectively. These energies are much smaller than the energy corresponding to the normal vibrational motion ($\tilde{\nu}_0 = 950 \text{ cm}^{-1}$), since the inversion of the molecule is severely hindered by the presence of the potential barrier.

The inversion frequency for ammonia has been calculated by Dennison and Uhlenbeck [38], who used the Wentzel-Kramers-Brillouin (WKB) approximation to obtain

$$\nu_{\text{inv}} = \frac{\nu_0}{\pi A^2}, \text{ with } A = \exp \left\{ \frac{2\pi}{h} \int_0^{z_0} [2\mu_{\text{red}} (V(z) - W)]^{\frac{1}{2}} dz \right\}, \quad (1.14)$$

with ν_0 the frequency of vibration in one of the potential minima and W the total vibrational energy. Due to the appearance of μ_{red} in the exponent of Eq. (1.14), the inversion splitting depends exponentially on the mass of the proton. In the ground state of NH_3 , $A^2 = \nu_0 / (\pi \nu_{\text{inv}}) \approx e^6$ and if the reduced mass is increased by a factor of two, such as would be roughly done by changing from NH_3 to ND_3 , the inversion splitting decreases by a factor of $\exp(6[\sqrt{2} - 1]) \approx 12$, as was already pointed out by Townes and Schawlow [36]. A more detailed discussion of the mass dependence of the inversion splitting will be presented in Sec. 1.3.4.

1.3.2 Rotational structure of ammonia

Although the NH_3 molecule is a floppy molecule, the rotational energy levels can be described to a good approximation with the Hamiltonian of a rigid oblate symmetric top [36]

$$\hat{H}_v^{\text{rot}} = B_v \cdot \vec{J}^2 + (C_v - B_v) \cdot J_z^2, \quad (1.15)$$

with \vec{J} the total angular momentum, J_z the projection of \vec{J} onto the molecular symmetry axis and B_v and C_v the effective rotational constants for a vibrational state v . Including centrifugal distortion terms in the simple Hamiltonian of Eq. (1.15) results in electronic ground state energies given by [39]

$$E_v(J, K) = T_v + B_v J(J+1) + (C_v - B_v) K^2 - D_{JJ,v} [J(J+1)]^2 - D_{JK,v} J(J+1) K^2 - D_{KK,v} K^4. \quad (1.16)$$

The rotational constants B_v and C_v and the centrifugal distortion constants $D_{JJ,v}$, $D_{JK,v}$, and $D_{KK,v}$ for NH_3 in the $X(0)$ and $X(1)$ state can be found in Ref. [40]. The inversion splitting between the $X(0)$ and $X(1)$ doublets in the rovibrational ground state is given by $v_{\text{inv}} = T_1 - T_0$.

The symmetric top eigenfunctions are given by [41]

$$|JKM\rangle = (-1)^{M-K} \left(\frac{2J+1}{8\pi^2} \right)^{\frac{1}{2}} D_{-M-K}^J(\phi, \theta, \chi) = \left(\frac{2J+1}{8\pi^2} \right)^{\frac{1}{2}} D_{MK}^{J*}(\phi, \theta, \chi), \quad (1.17)$$

where $D_{MK}^J(\phi, \theta, \chi)$ are the Wigner rotation matrices and ϕ, θ , and χ are the Euler angles. The rotational eigenstates are hence given by

$$|JKM; \varepsilon\rangle = \frac{1}{\sqrt{1 + \delta_{K,0}}} [|JKM\rangle + \varepsilon |J-KM\rangle], \quad (1.18)$$

where ε is the parity index in ρ -space and given by $\varepsilon = \mp(-1)^J$, the $-$ refers to the symmetric inversion level and the $+$ to the antisymmetric inversion level⁷. The rotational energy level diagram of the ground state of NH_3 is given in Fig. 1.6. The dashed lines indicate levels that are Pauli forbidden as the overall wave function, including nuclear spin, is not antisymmetric. Fig. 1.6 also shows the rotational energy level diagram of the $B(v_2 = 3)$ Rydberg state of ammonia. In the experiments that are described in Chapters 2 to 4, the ammonia molecules are ionized using a (2+1) REMPI scheme via the $B(v_2 = 3)$ state. As the B state possesses a flat geometry, there is no tunneling barrier and inversion splitting is absent. The vibronic wave function has either E'' or E' symmetry for even or odd v_2 , respectively, and is twofold degenerate. As a consequence, Coriolis coupling effects and vibrational l -type doubling give a considerable

⁷Note that the overall parity of the molecular wave function, p , under the inversion operation, E^* , is given by $p = \varepsilon (-1)^{J-K+1}$ [40].

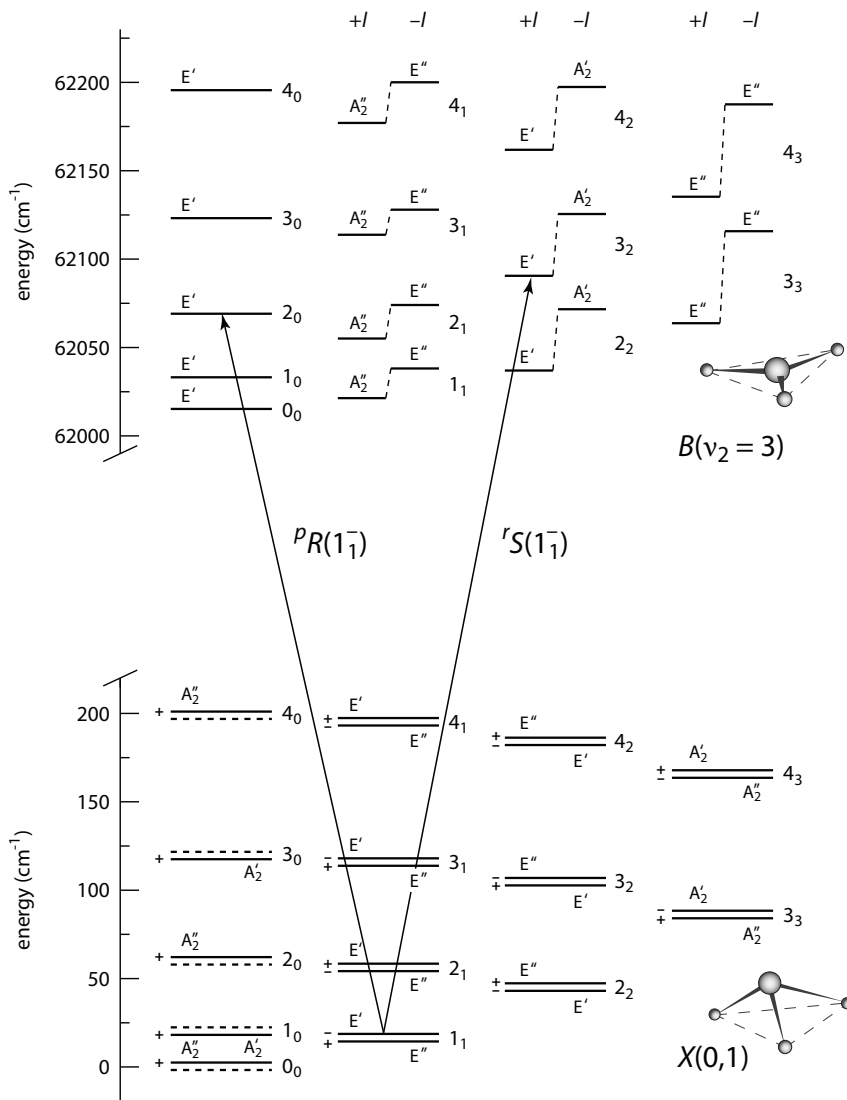


FIGURE 1.6: Rotational energy level diagram for the X and B electronic states of NH_3 . Each level is characterized by the rotational quantum numbers J_K and the symmetry label of the rovibronic wave function. In the electronic ground state, the parity index ε is given, while in the B state the vibrational angular momentum l is given. Solid arrows indicate $B \leftarrow X$ transitions. The structure of the ammonia molecule changes from pyramidal in the electronic ground state to planar in the B state. The inversion doubling has been exaggerated for clarity. Energies were calculated using PGOPHER [42] and the constants from Refs. [40, 43].

contribution to the molecular Hamiltonian and cause additional shifts and splittings of the rigid rotor energy levels [44]. In addition, upper levels of the electronic ground state inversion doublets can only be probed via a $B(v_2 = \text{odd})$ band, whereas the lower inversion doublets can only be probed via a $B(v_2 = \text{even})$ band, as the vibrational wave functions for the ground state and first excited vibrational state are of A'_1 and A''_2 symmetry, respectively.

1.3.3 Stark shift in ammonia

In the absence of an electric field the energy levels do not depend on the spatial orientation of the angular momentum vector and hence each J_K state is $(2J+1)$ fold degenerate. However, in an external electric field this degeneracy is lifted and each state splits in $(J+1)$ states of which all but $M = 0$ are doubly degenerate. The effect of a static electric field on the energy level structure of ammonia can be calculated by perturbation theory provided the external electric field is much smaller than the internal electric field of the electron-nuclei interactions, as is usually the case. Assuming the electric field is uniform over a region of atomic dimensions, the perturbation term takes the form

$$\hat{H}' = -\mu_{\text{el}}|\vec{E}|\cos\theta, \quad (1.19)$$

where μ_{el} is the permanent electric dipole moment and \vec{E} the electric field vector. According to first-order perturbation theory

$$\begin{aligned} \langle JKM|\hat{H}'|JKM\rangle &= -\mu_{\text{el}}|\vec{E}|\langle JKM|\cos\theta|JKM\rangle, \\ &= -\mu_{\text{el}}|\vec{E}|(-1)^{M-K}(2J+1)\begin{pmatrix} J & J & 1 \\ M & -M & 0 \end{pmatrix}\begin{pmatrix} J & J & 1 \\ K & -K & 0 \end{pmatrix}, \\ &= -\mu_{\text{el}}|\vec{E}|\frac{MK}{J(J+1)}, \end{aligned} \quad (1.20)$$

where we have used $\cos\theta = D_{00}^1$ and Eq. (3.118) of Zare [41] and the analytical expressions for the $3j$ symbols [41]. The second order correction to the energy is given by

$$\begin{aligned} \langle JKM|\hat{H}'|J'K'M'\rangle &= -\mu_{\text{el}}|\vec{E}|\langle JKM|\cos\theta|J'K'M'\rangle, \\ &= -\mu_{\text{el}}|\vec{E}|(-1)^{M'-K'}\sqrt{(2J+1)(2J'+1)} \\ &\quad \times \begin{pmatrix} J & J' & 1 \\ M & -M' & 0 \end{pmatrix}\begin{pmatrix} J & J' & 1 \\ K & -K' & 0 \end{pmatrix}, \end{aligned} \quad (1.21)$$

for which the $3j$ symbols are only nonzero if $M = M'$, $K = K'$, and $J' = J \pm 1$. Thus, the second-order energy is affected only by the two neighboring states. To account for the second-order perturbation, we need to evaluate a 6×6 energy matrix of the form

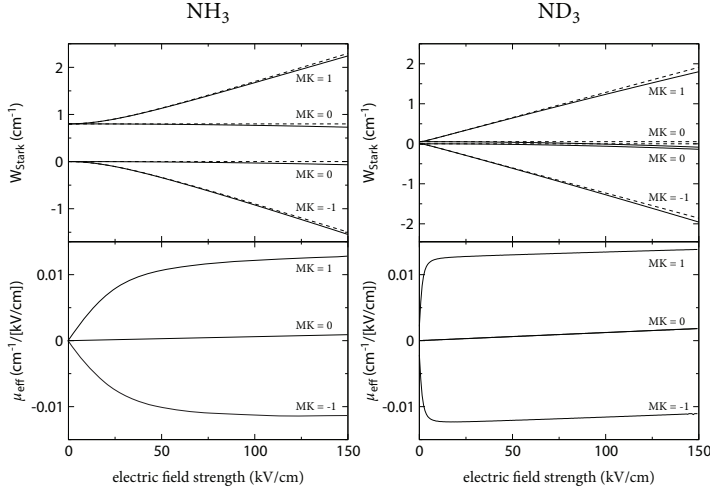


FIGURE 1.7: Stark energy level diagrams and effective dipole moments for the $|J, K\rangle = |1, 1\rangle$ state of NH_3 (left-hand side) and ND_3 (right-hand side).

$$\begin{bmatrix} E_1(J+1, K) & a_{J+1} & 0 & b_{J+1} & 0 & 0 \\ a_{J+1} & E_0(J+1, K) & b_{J+1} & 0 & 0 & 0 \\ 0 & b_{J+1} & E_1(J, K) & a_J & 0 & b_J \\ b_{J+1} & 0 & a_J & E_0(J, K) & b_J & 0 \\ 0 & 0 & 0 & b_J & E_1(J-1, K) & a_{J-1} \\ 0 & 0 & b_J & 0 & a_{J-1} & E_0(J-1, K) \end{bmatrix}, \quad (1.22)$$

where the diagonal terms $E_{v=0,1}(J, K)$ and off-diagonal terms a_J are given by Eqs. (1.16) and (1.20), respectively. The expression for b_J follows from Eq. (1.21)

$$\begin{aligned} b_J &= -\mu_{\text{el}} |\vec{E}| \langle JKM | \cos \theta | J-1KM \rangle, \\ &= -\mu_{\text{el}} |\vec{E}| \sqrt{\frac{(J^2 - K^2)(J^2 - M^2)}{J^2(2J-1)(2J+1)}}. \end{aligned} \quad (1.23)$$

For low electric fields, the second order Stark correction and the interaction between different J levels, i.e. the b_J terms, can be neglected and the Stark energy takes the approximate form

$$W_{\text{Stark}} = -\varepsilon \sqrt{\left(\frac{W_{\text{inv}}}{2}\right)^2 + \left(\mu_{\text{el}} |\vec{E}| \frac{MK}{J(J+1)}\right)^2} + \varepsilon \frac{W_{\text{inv}}}{2}, \quad (1.24)$$

where ε is the parity index that was introduced in Sec. 1.3.2.

The Stark energies and effective dipole moments for the $|J, K\rangle = |1, 1\rangle$ state of NH_3 and ND_3 were calculated from Eq. (1.22) and are shown on the left and right-hand side of Fig. 1.7, respectively. The dashed lines also shown in the figure are obtained by using the two two-level approximation of Eq. (1.24). It is seen that for fields up to 50 kV/cm,

the interaction with neighboring levels can be neglected and Eq. (1.24) is used to obtain the Stark shift of ammonia in Chapters 2 and 4.

1.3.4 Sensitivity of the inversion frequency to a variation of μ

In Section 1.3.1 the inversion splitting of the ammonia molecule was discussed. Since this splitting is due to the tunneling of the nitrogen atom through the plane formed by the hydrogen atoms, its frequency is very sensitive to the effective mass that tunnels. This can be seen from the factor of $\sqrt{\mu_{\text{red}}}$ appearing in the exponent of Eq. (1.14). An additional factor of $\mu_{\text{red}}^{-1/2}$ is expected which is due to the mass dependence of the harmonic oscillator. It was first pointed out by Van Veldhoven *et al.* [45], and later by Flambaum and Kozlov [46], that the strong dependence of the inversion splitting on the reduced mass of the ammonia molecule can be exploited to probe variation of μ . If the reduced mass – or rather the proton-to-electron mass ratio – shifts over space and/or time, so does the inversion frequency. Theoretically, the μ_{red} dependence of the inversion frequency is expected to follow the formula [47]

$$\nu_{\text{inv}} = \frac{a_0}{\sqrt{\mu_{\text{red}}}} e^{-a_1 \sqrt{\mu_{\text{red}}}}, \quad (1.25)$$

where a_0 and a_1 are fitting constants. In Fig. 1.8 the frequencies of the different ammonia isotopologues are plotted as a function of their reduced mass [45, 47–50]. The solid line in Fig. 1.8 shows a fit according to Eq. (1.25) with $a_0 = 68 \text{ THz} \times \text{amu}^{1/2}$ and $a_1 = 4.7 \text{ amu}^{-1/2}$. If we assume that no effects depending on quark structure persist, that is, if the proton and neutron masses scale in a similar manner, the sensitivity coefficient follows from

$$K_{\mu}^{\text{inv}} = \frac{\mu}{\nu} \left(\frac{\partial \nu}{\partial \mu} \right) = -\frac{1}{2} a_1 \sqrt{\mu_{\text{red}}} - \frac{1}{2}. \quad (1.26)$$

For $^{14}\text{NH}_3$, this results in a sensitivity coefficient $K_{\mu}^{\text{inv}} = -4.2$. This is almost an order of magnitude more sensitive to a variation of the proton-to-electron mass ratio than pure vibrational transitions that have a sensitivity coefficient of $K_{\mu}^{\text{vib}} = -\frac{1}{2}$. By comparing the inversion frequency of ammonia with a suitable frequency standard over an extended period of time, an upper limit on a temporal variation of μ or a positive effect can be obtained [46, 51].

In Chapter 5, the methanol molecule is discussed that – just like ammonia – possesses a classically-forbidden large-amplitude motion. In addition to normal rotation along the three principle axis of the center-of-mass frame, methanol exhibits internal rotation along the CO bond. This rotation is not free, but hindered by the interaction between the hydrogens of the methyl group and hydroxyl group, similar to the inversion motion of ammonia. The sensitivity of a pure torsional transition in methanol has a sensitivity coefficient of $K_{\mu} = -2.5$. However, in Chapter 5 we will see that some transitions in methanol with $|\Delta K| = 1$ have sensitivity coefficients that can be more than an order of magnitude larger than this. The enhancement of these sensitivity

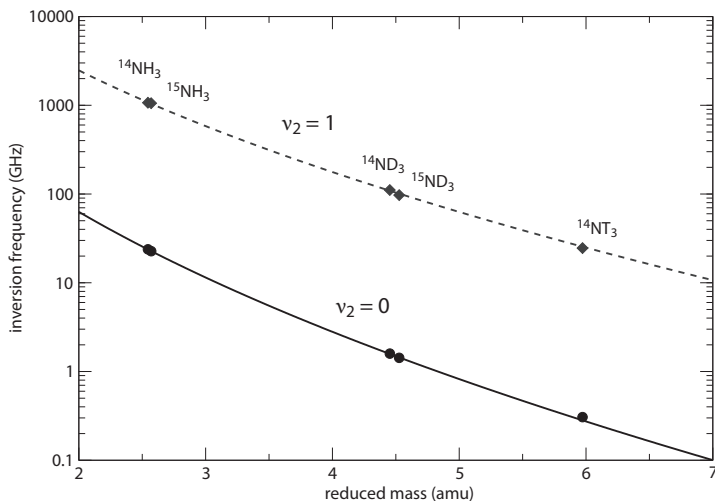


FIGURE 1.8: Inversion frequency for various isotopologues of ammonia in the ground ($\nu_2 = 0$) and first excited ($\nu_2 = 1$) vibrational state with $J = 1$ and $K = 1$, as a function of the reduced mass of the ν_2 vibration. The solid and dashed lines are a fit according to Eq. (1.25), with $a_0 = 68$ and $88 \text{ THz} \times \text{amu}^{1/2}$ and $a_1 = 4.7$ and $3.9 \text{ amu}^{-1/2}$, for the ground state and first excited vibrational state of ammonia, respectively.

coefficients is caused by an accidental near degeneracy between two levels that have a different dependence on μ .

Such degeneracies do not occur in the vibrational ground state of ammonia, but may happen in the first vibrational excited $\nu_2 = 1$ state that experiences a much lower effective inversion barrier than the $\nu_2 = 0$ state. Molecular constants for the $\nu_2 = 1$ state of $^{14}\text{NH}_3$ can for instance be found in Ref. [52] and from these the energy of each inversion-rotational state can be approximated with Eq. (1.16). In Fig. 1.9, a rotational energy diagram of ammonia in the $\nu_2 = 1$ state is shown. Similar to the ground state of ammonia, half of the energy levels with $K = 0$ do not exist as a consequence of the Pauli principle. Two interesting transitions have been indicated in the figure; the inversion-rotation transition at 140 GHz between the antisymmetric component of the $J_K = 1_1$ doublet and symmetric component of the 2_1 doublet, and the $\Delta K = \pm 3$ forbidden transition at 2.9 GHz between the symmetric component of the $J_K = 3_0$ doublet and antisymmetric component of the 3_3 doublet. Transitions with $\Delta K = \pm 3$ are allowed through perturbative mixing of the symmetric and antisymmetric $J_K = 3_0$ and 3_3 wave functions and gain amplitude due to the accidental degeneracy between these two levels [53]. However, this mixing only allows symmetric to symmetric and antisymmetric to antisymmetric transitions to occur. Thus, to probe the 2.9 GHz transition directly, a two-photon transition is required.

In order to estimate the sensitivities of rotation-inversion transitions it suffices to account for the μ dependence of the dominant rotational parameters B_v , C_v , and the inversion splitting. The rotational parameters have a sensitivity coefficient of $K_\mu^{\text{rot}} = -1$

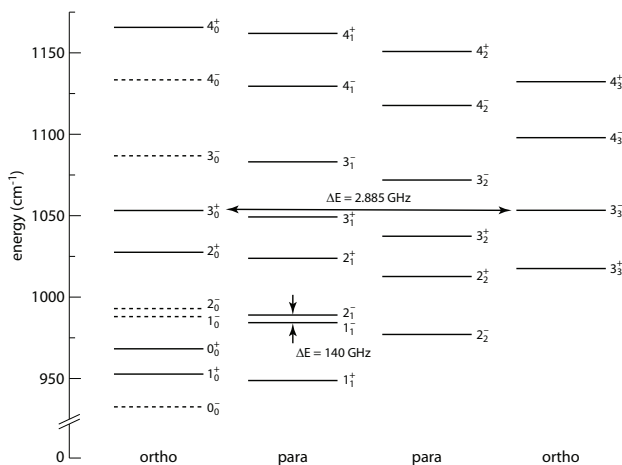


FIGURE 1.9: Rotation-inversion levels of $^{14}\text{NH}_3$ in the $\nu_2 = 1$ state. Two transitions are indicated in the figure. The lower inversion component of the $J_K = 3_0$ doublet is very close (2.885 GHz) to the upper inversion component of the $J_K = 3_3$ level and causes mixing of the wave functions. A two-photon transition between these states has a sensitivity coefficient $K_\mu = -938$ (note that single-photon transitions between these states are not allowed). The rotation-inversion transition between the upper component of the $J_K = 1_1$ doublet and lower component of the $J_K = 2_1$ doublet at 140 GHz has a sensitivity coefficient $K_\mu = +18.8$.

as they are inversely proportional to the reduced mass of the molecule. The sensitivity of the inversion splitting can be obtained by fitting Eq. (1.25) to the inversion frequencies for the $\nu_2 = 1$ state of the various ammonia isotopologues. This fit is shown in Fig. 1.8 with $a_0 = 88 \text{ THz} \times \text{amu}^{1/2}$ and $a_1 = 3.9 \text{ amu}^{-1/2}$. From Eq. (1.26) we deduce a sensitivity coefficient $K_\mu^{\text{inv}} = -3.6$ for the normal isotopologue of ammonia⁸. If coupling between inversion and rotation energy can be neglected, the sensitivity coefficient for inversion-rotation transitions within the $\nu_2 = 1$ state simplifies to

$$K_\mu = \frac{K_\mu^{\text{rot}} \Delta E_{\text{rot}} + K_\mu^{\text{inv}} \Delta E_{\text{inv}}}{h\nu}, \quad \text{with } h\nu = \Delta E_{\text{rot}} + \Delta E_{\text{inv}}. \quad (1.27)$$

The torsional splittings of ammonia in the first excited vibrational state, as well as the frequencies of the transitions indicated in Fig. 1.9, are well-known from experiments [54]. Using these tabulated frequencies Eq. (1.27) predicts sensitivities of $K_\mu = -938$ and $+18.8$ for the 2.9 and 140 GHz transitions, respectively. It should be noted, however, that it is not trivial to measure these transitions to a high accuracy in a molecular beam experiment, as it requires active pumping of ammonia from the $\nu_2 = 0$ to the $\nu_2 = 1$ state at a wavelength around $10.5 \mu\text{m}$. The transition around 2.8 GHz is even more complicated as it involves an additional two-photon transition in the microwave domain once the molecules are prepared in the $\nu_2 = 1$ state. Note that either higher

⁸The same sensitivity coefficient can be obtained by using Eq. (13) of Ref. [46] and the values of the inversion splitting and the vibrational frequency in the $\nu_2 = 1$ mode from Fig. 1.4

excited vibrational states in ammonia or the $v_2 = 1$ state in other isotopologues of ammonia, may have sensitive transitions that are more accessible experimentally.

1.4 Intermezzo: the escape of an alpha particle

In Sec. 1.3.1, the inversion of the ammonia molecule was treated and the energy splitting as predicted from the WKB approximation was given (Eq. 1.14). Historically, the first successful application of the WKB approximation involved the process in which heavy nuclei emit alpha particles. The half-lives of these nuclides span a range over 20 orders of magnitude [55], from about $t_{1/2} = 0.3 \mu\text{s}$ in Po^{212} to $t_{1/2} = 13.9 \text{ Gyr}$ in Th^{232} .

The decay of an unstable parent nucleus into an alpha particle and a daughter nucleus, is a process encountered commonly in nuclei with an atomic number $Z > 82$ [56]. The number of parent nuclei at a certain time, $N(t)$ is described by exponential decay

$$N(t) = N_0 e^{-\lambda t}, \quad (1.28)$$

with N_0 the initial number of parent nuclei and $\lambda = \ln 2/t_{1/2}$ the decay constant. The emittance of an alpha particle happens spontaneously, and part of the energy that is released is available as kinetic energy for the emitted alpha particle, Q_α . Geiger and Nuttall discovered a linear relationship between the logarithm of the decay constant and the logarithm of kinetic energy of the emitted alpha particle for nuclides belonging to a certain natural decay chain [57]. This relation, which is known as the Geiger-Nuttall law, can be expressed as [58]

$$\ln \lambda' = a_0 - a_1 \frac{Z}{\sqrt{Q_\alpha}}, \quad (1.29)$$

where we have introduced a primed version of λ to distinguish between the decay rate λ in Hz and the dimensionless number of decay events in one second λ' , Z is the atomic number of the parent nuclide and a_0 and a_1 are empirical constants. In Fig. 1.10a the logarithms of the experimental values for λ' of the four natural radioactive decay series are plotted as a function of $Z/\sqrt{Q_\alpha}$. The solid line is a fit according to the Geiger-Nuttall law with $a_0 = 96.6$ and $a_1 = 3.0 (\text{MeV})^{1/2}$. The remarkable dependence upon kinetic energy was explained independently by quantum mechanical tunneling by Gamow [59] and by Gurney and Condon [60].

From scattering experiments in which nuclei of heavy atoms were bombarded with alpha particles it was known that the potential energy between the nucleus and the alpha particle follows Coulomb's law for the range that could be probed with the kinetic energy of the alpha particles used, while these heavy nuclei emitted α particles with less kinetic energy than expected from such a potential. In addition, scattering of alpha particles from nuclei of light atoms revealed that the potential departs from this $1/r$ dependence when $r < r_1$ where it drops very rapidly [56]. It was reasoned [59, 60] that the shape of the potential energy can be described qualitatively by the curve that is shown in Fig. 1.10b and that the alpha particle exists inside the nucleus where it is bound by the strong nuclear force. The Coulomb energy between the alpha particle and the daughter nucleus follows from

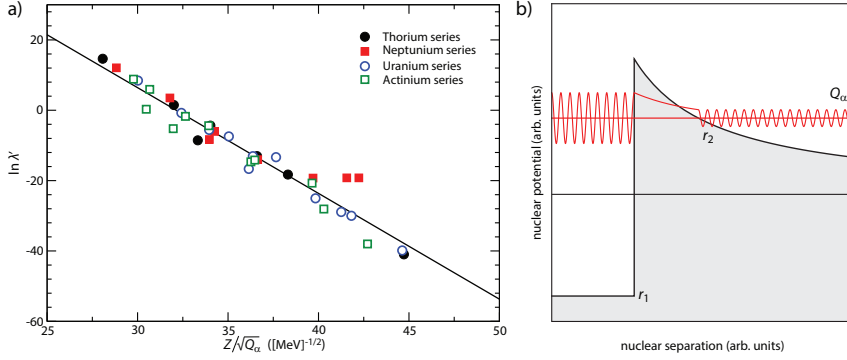


FIGURE 1.10: (a) A plot of the experimental λ' values of the four natural radioactive decay series as a function of $Z/\sqrt{Q_\alpha}$. The solid line is a fit according to the Geiger-Nuttall law with $a_0 = 96.6$ and $a_1 = 3.0 \text{ (MeV)}^{1/2}$. (b) Schematic diagram of the potential energy between an alpha particle and daughter nucleus. For $r < r_1$ the Coulomb potential is dominated by the strong nuclear force.

$$V(r) = \frac{Z_\alpha Z_d e^2}{4\pi\epsilon_0 r}, \quad \text{with } r > r_1, \quad (1.30)$$

where Z_α and Z_d refer to the atomic number of the alpha particle and daughter nucleus, respectively, e is the elementary charge, and ϵ_0 is the electric permittivity of free space. The alpha decay constant can be expressed by the equation [61]

$$\lambda = \omega T, \quad (1.31)$$

where ω is the frequency at which the alpha particle hits the barrier (or the α particle formation rate) and T is the probability of transmission through the barrier. Similar to the inversion of the ammonia molecule, the application of the WKB approximation results in

$$T = e^{-2G}, \quad (1.32)$$

where the Gamow factor, G , is given by

$$G = \frac{1}{\hbar} \int_{r_1}^{r_2} \sqrt{2\mu_{\text{red}} [V(r) - Q_\alpha]} dr \quad \text{and} \quad \mu_{\text{red}} = \frac{M_\alpha M_d}{M_\alpha + M_d}, \quad (1.33)$$

with M_α and M_d the mass of the alpha particle and daughter nucleus, respectively. From Fig 1.10 and Eq. (1.30) it is easily seen that

$$Q_\alpha = \frac{Z_\alpha Z_d e^2}{4\pi\epsilon_0 r_2}. \quad (1.34)$$

Eq. (1.33) can now be written as

$$G = \frac{2}{\hbar} \frac{\sqrt{2\mu_{\text{red}} Q_\alpha}}{r_2} \int_{x_0}^{x_1} \sqrt{1 - x^2} dx, \quad \text{with } x = \sqrt{r/r_2}. \quad (1.35)$$

TABLE 1.1: Comparison between the logarithm of the observed [55] and calculated decay constants of selected isotopes. Sensitivity coefficient are listed in the last column. The calculated values of the decay constant can differ up to several orders of magnitude from the experimental ones, although the general trend is reproduced qualitatively.

Isotope	$\ln \lambda'_{\text{obs}}$	$\ln \lambda'_{\text{calc}}$	K_{μ}	Isotope	$\ln \lambda'_{\text{obs}}$	$\ln \lambda'_{\text{calc}}$	K_{μ}
^{210}Bi	-13.3	-6.2	-26.4	^{222}Rn	-13.1	-13.4	-30.0
^{211}Bi	-5.2	1.0	-22.8	^{221}Fr	-6.0	-6.8	-26.7
^{212}Bi	-8.6	-3.9	-25.3	^{223}Ra	-14.2	-11.1	-28.9
^{213}Bi	-8.3	-7.2	-27.0	^{224}Ra	-13.0	-13.2	-30.0
^{214}Bi	-7.5	-10.0	-28.3	^{226}Ra	-25.0	-25.3	-36.0
^{210}Po	-16.7	-13.8	-30.2	^{225}Ac	-14.0	-12.6	-29.7
^{211}Po	0.3	6.6	-20.0	^{227}Ac	-20.7	-24.0	-35.3
^{212}Po	14.7	15.1	-15.8	^{227}Th	-14.7	-11.3	-29.0
^{213}Po	12.1	12.8	-17.0	^{228}Th	-18.3	-18.6	-32.7
^{214}Po	8.3	8.7	-19.0	^{229}Th	-26.5	-23.3	-35.0
^{215}Po	6.0	6.3	-20.2	^{230}Th	-28.9	-29.3	-38.0
^{216}Po	1.6	1.6	-22.6	^{232}Th	-41.0	-41.6	-44.2
^{218}Po	-5.6	-5.6	-26.1	^{231}Pa	-28.0	-24.7	-35.7
^{215}At	8.8	9.8	-18.4	^{233}U	-29.6	-29.5	-38.1
^{217}At	3.1	1.4	-22.7	^{234}U	-30.0	-30.3	-38.5
^{218}At	-0.8	0.4	-23.2	^{235}U	-38.0	-33.0	-39.9
^{219}At	-4.4	-5.0	-25.9	^{238}U	-39.9	-40.5	-43.6
^{220}Rn	-4.4	-4.8	-25.7	^{237}Np	-32.2	-29.8	-38.3

By substituting $x = \cos \theta$, the integral can be solved analytically, and after integrating from r_1 to r_2 we obtain [61]

$$G = \frac{r_2}{\hbar} \sqrt{2\mu_{\text{red}} Q_{\alpha}} \left[\arccos \sqrt{\frac{r_1}{r_2}} - \sqrt{\frac{r_1}{r_2} \left(1 - \frac{r_1}{r_2} \right)} \right], \quad (1.36)$$

The distance r_1 can be estimated by assuming that the influence of the strong nuclear force stops abruptly when the alpha particle and daughter nucleus are just touching each other, thus r_1 is the sum of their radii

$$r_1 = r_0 \left(A_{\alpha}^{1/3} + A_d^{1/3} \right), \quad \text{with } r_0 = 1.2249 \text{ fm}. \quad (1.37)$$

The relation between the number of emitted alpha particles in one second, λ' , and the energy Q_{α} (MeV) can be expressed by the following equation, where we have used $\omega = 1.94 \times 10^{20}$ Hz [61]

$$\ln \lambda' = 46.7121 - 1.2599 \times (Z - 2) \sqrt{\frac{\mu_{\text{red}}}{Q_{\alpha}}} \left[\arccos \sqrt{X} - \sqrt{X(1 - X)} \right], \quad (1.38)$$

with

$$X = 0.3472 \times \frac{r_1 Q_{\alpha}}{Z - 2}. \quad (1.39)$$

The decay constants for the various alpha emitters that follow from this equation are listed in Table 1.1, together with the experimental values from Ref. [55]. As can be seen from the table, the calculated values can be several orders of magnitude off from the

observed ones. This should not come as a surprise since the Gamow theory of alpha decay is a rather crude model that assumes spherical nuclei and ignores effects due to nuclear angular momentum. Nevertheless, it is able to describe the observed features qualitatively and explains the dependencies of the Geiger-Nuttall law.

For thick barriers $r_1/r_2 \ll 1$ and the part of Eq. (1.36) between the square brackets can be replaced by the first terms of its Taylor series, i.e., $\pi/2 - 2\sqrt{r_1/r_2}$. After taking the logarithm and rearranging terms, the functional form of the Geiger-Nuttall law is retrieved.

The range of nuclear half-lives spans more than twenty orders of magnitude while the reduced mass of the alpha particle and daughter nucleus varies only slightly. This drastic dependence suggest naively that the half-lives of alpha emitters are extremely sensitive to a possible variation of μ . It is therefore interesting to derive a sensitivity coefficient for the process of alpha decay. In principle, the reduced mass and nuclear potential both depend on the strong nuclear force α_s and, as a consequence, so do the half-lives of the nucleides. As a rough approximation, we assume that if α_s changes, the effect due to the change in the reduced mass is much larger than the effect due to the change in the nuclear potential. In this case, the sensitivity coefficient K_μ is defined via

$$\frac{\Delta\lambda}{\lambda} = K_\mu \frac{\Delta\mu}{\mu}, \quad (1.40)$$

which results in the following expression for K_μ

$$K_\mu = -0.6299 \times (Z - 2) \sqrt{\frac{\mu_{\text{red}}}{Q_\alpha}} \left[\arccos \sqrt{X} - \sqrt{X(1 - X)} \right]. \quad (1.41)$$

Calculated sensitivity coefficients for several isotopes are listed in Table 1.1. These values should be treated with caution, but in general cover a range from $K_\mu = -15$ to -45 . Although these numbers are quite large, any shift due to a variation of μ , will be hidden by the uncertainties in the measurement of the nuclear half-lives that are typically determined with relative accuracies of $10^{-5} - 10^{-1}$ [62].

1.5 Radioastronomical observations of MeOH

The discussion in the previous section was focused mainly on high-precision laboratory experiments to probe a possible variation of μ . However, a search for a drift of μ on a cosmological time scale has also been made operational by comparing observations of spectral lines of the hydrogen molecule in distant galaxies with accurate laboratory measurements [65]. Although such observations do not provide the well-controlled environment of the laboratory, a long accumulation time is achieved. Unfortunately, the sensitivity coefficients of the molecular hydrogen lines [66] are more than an order of magnitude smaller than pure rotational lines. This has stimulated interest in astrophysical observations of inversion transitions of ammonia at high redshift, which led to stringent constraints on μ variation [67, 68] at a redshift $z < 1$.

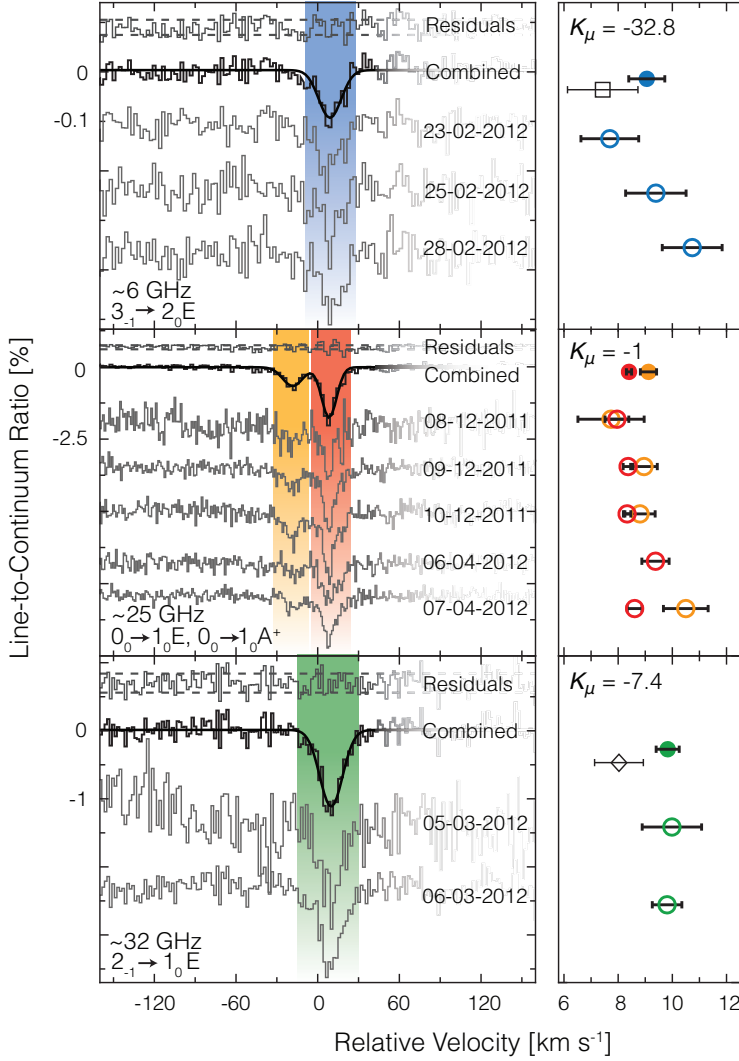


FIGURE 1.11: Methanol absorption lines on a Local Standard of Rest velocity scale relative to $z=0.88582$, observed towards PKS1830-211. The transitions and their approximate observed frequencies and sensitivity coefficients are indicated in each panel. For each spectrum the position of a fitted Gaussian is shown in the graph at the right. Residuals are shown at the top of each combined spectrum with dashed lines indicating $\pm 1\sigma$ offsets. The black square (upper right panel) and the black diamond (lower right panel) represent the single line observations from Ellingsen *et al.* [63] and Muller *et al.* [64], respectively.

In Chapter 5, we present calculated sensitivity coefficients for transitions in methanol. Some of these transitions turn out to be an order of magnitude more sensitive than the inversion lines of ammonia. This is not only important for laboratory searches of μ variation, but also for astrophysical searches, since methanol is abundantly present in the Universe and more than a 1000 lines have been recorded in our local Galaxy [69]. So far, searches for methanol absorption in far-distant galaxies have yielded detection in the gravitational lens system PKS1830-211 [64] only. We have used the 100 m Effelsberg radio telescope to observe four methanol lines in this system. The redshift of the main molecular absorptions from the galaxy is $z = 0.88582$ [64, 70] corresponding to a look-back time of 7.0 billion years, or about half the age of the Universe. A complete analysis of the observed lines is beyond the scope of this thesis and here the main results are summarized only.

The recorded spectra are shown in Fig. 1.11. For a single transition, the spectra taken on various days were averaged together, weighting the individual scans by their integration time. The lines were calibrated by the total continuum so that their strength is expressed as line-to-continuum flux density ratio. The profiles, devoid from underlying structure, were fitted as a single Gaussian.

The velocities between different transitions relative to $z = 0.88582$ are interrelated via

$$\frac{V}{c} = -K_\mu \frac{\Delta\mu}{\mu}, \quad (1.42)$$

where c is the speed of light and $\Delta\mu/\mu$ represents the deviation from the current laboratory value of μ , defined so that a positive sign indicates a larger μ in the high-redshift absorbing galaxy (i.e. $\Delta\mu = \mu_z - \mu_{\text{lab}}$). Therefore, to determine the fractional change in μ , the peak positions of the four transitions are plotted in Fig. 1.12 (in V/c) versus K_μ , and a (dashed) line is fitted to the data. However, as we will see in Chapter 5, the four lines belong to two different symmetry species of methanol (A and E), which can be treated as two separate species. Therefore, the data were analyzed in two different ways: first, only the three transitions from E levels were fitted, while in the second stage also the A transition was added to the sample. The analysis of the E transitions results in $\Delta\mu/\mu = (-0.1 \pm 7.6) \times 10^{-8}$, which is consistent with a non-varying μ at the level of 1.5×10^{-7} (95 % confidence level). The reduced chi-squared, χ^2_ν , which is a measure of the quality of the fit, is ~ 2.0 . The fit on all four transitions has a much larger χ^2_ν of 6.4, which might be attributed to segregation issues, and it delivers $\Delta\mu/\mu = (11.0 \pm 6.8) \times 10^{-8}$.

We have investigated the variability of the source as a possible systematic effect and have derived a conservative systematic uncertainty of $\Delta\mu/\mu$ of 7.0×10^{-8} . Thus, we obtain a limit on varying μ to be $\Delta\mu/\mu = (\check{0}.1 \pm 7.6_{\text{stat}} \pm 7.0_{\text{sys}}) \times 10^{-8}$ or, if the statistical and systematic uncertainties are added in quadrature, a limit of $\Delta\mu/\mu = (0.0 \pm 1.0) \times 10^{-7}$. The $\Delta\mu/\mu$ constraint provided here is an improvement over previous tests in the radio-domain [63, 64, 67, 68, 71].

While the present study yields an upper limit to $\Delta\mu/\mu$, which is statistically more constraining than previous studies, the methanol method is ground-breaking for its robustness against systematic effects. In particular, the methanol method is much

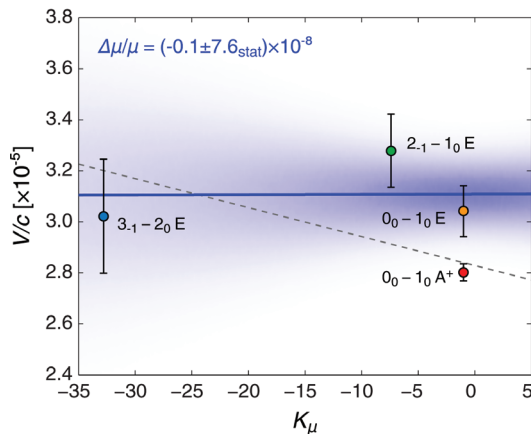


FIGURE 1.12: The positions of the four observed methanol lines versus their sensitivity coefficients. The bold straight line represents the fiducial result of a fit to the E type lines, while the dashed line represents a fit to all four lines. The shaded surface is a density plot of simulated data points from the bold fitted line and reflects the confidence bands of the fit.

less sensitive to the assumption that all absorbing species reside in the same physical location and hence are at the same redshift.

1.6 Outline of this thesis

The contents of this thesis can roughly be divided into two parts; the first part consists of Chapters 2 to 4, while the second part consists of Chapters 5 to 7. In Chapter 2, the initial design of a molecular fountain based on a Stark-decelerated molecular beam is presented. Unfortunately, our first attempt to detect molecules that fall back under gravity failed and possible explanations for this are given in Chapter. 2 as well. In Chapters 3 and 4 we describe two changes that we have made to the setup, which hopefully will result in the detection of molecules falling back under gravity.

In this chapter, the methanol molecule was already mentioned a few times. A detailed discussion of methanol and the calculation of sensitivity coefficients to a variation of μ for selected transitions is presented in Chapter 5. Methanol is a representative of a class of molecules that undergo hindered internal rotation, a large-amplitude motion that is classically forbidden and shows great similarity with the inversion motion of the ammonia molecule. The concepts introduced in Chapter 5 will be generalized in Chapter 6 and applied to other molecules that exhibit hindered internal rotation. A simple model is derived that provides insight in the physics involved and aides in the identification of other internal-rotor molecules that possibly possess large K_μ coefficients. Methylamine (CH_3NH_2) represents a more complex class of molecules and will be discussed in Chapter 7.

TOWARDS A MOLECULAR FOUNTAIN

The first part of this chapter is based on Bethlem *et al.* [51] and describes the design of a molecular fountain using a Stark-decelerated molecular beam. In this setup, ammonia molecules are decelerated to a few meter per second, cooled to sub microKelvin temperatures using a lens system consisting of two linear and one cylindrical quadrupoles and subsequently launched. The molecules fly upwards some 30 cm before falling back under gravity, thereby passing a microwave cavity twice. The effective interrogation time in such a Ramsey type measurement scheme includes the entire flight time between the two traversals through the driving field (see also Chapter 1), which is on the order of half a second. We present numerical simulations of the trajectories through the decelerator and estimate the expected count rate. In the second part of the chapter, we show measurements and simulations of slow molecules behind the decelerator and focusing lenses that characterize the setup. Unfortunately, with this system we were unable to observe molecules falling back under gravity. We give possible explanations for this and propose two changes to the setup that will hopefully bring a successful operation of the fountain within reach.

2.1 Introduction

The demonstration of cooling and manipulation techniques for molecules offer new possibilities for precision measurements in polyatomic species. The accuracy and reproducibility of any experiment depends on how well experimental conditions are controlled. Control over the motion of atoms and atomic ions using laser cooling and trapping techniques has dramatically increased the precision of atomic frequency standards. An accuracy exceeding 10^{-15} is now routinely obtained in atomic fountains based on laser-cooled atoms [72, 73], in atoms trapped in optical lattices [74], and in single ions trapped in an rf quadrupole field [75]. A demonstration of the latter technique using Al^+ ions resulted in an unprecedented accuracy at the low 10^{-17} level [76].

It is expected that the emerging techniques to cool and manipulate molecules [31, 33, 77] will have a similar impact on the precision of frequency measurements in molecules [51].

It was argued in Chapter 1 that a dense source of slow particles was crucial for the realization of the first atomic fountain experiment. For our fountain experiment we have chosen to employ the well-established technique of Stark deceleration to provide a source of slow and controlled molecules. Stark deceleration exploits the fact that a polar molecule experiences a force in an inhomogeneous electric field [31, 33] which originates in the interaction of a body-fixed dipole moment with an externally applied electric field. Although this interaction is many orders of magnitude weaker than the interaction between a charged particle and an electric field, the resulting force is nonetheless sufficient to achieve complete control over the molecules. As a proof-of-principle, high-resolution microwave spectra of ND_3 [45] and OH [78] have been recorded on Stark-decelerated beams.

It is unlikely that the precision obtained in any molecular fountain will be able to compete with that obtained in their atomic counterparts. However, rather than providing a frequency standard, the advantages of a molecular fountain lie in the possibility it offers for precision tests of fundamental physics theories [51]. The sensitivity of any experiment searching for a frequency shift due to a certain physical phenomenon depends both on the magnitude of the shift, that is, the inherent sensitivity of the system to a certain effect, and on the ability to measure this shift. The structure (and symmetry) of molecules makes them inherently more sensitive for a number of tests. For instance, in certain molecules like YbF and ThO , time-reversal symmetry violating interactions leading to a permanent electric dipole moment are three orders of magnitude stronger than in atoms [79, 80]. Molecules are also used in the study of weak interactions leading to an anapole moment of the nucleus [81], in the search for a difference in transition frequency between chiral molecules that are each others mirror-image [82], and for constraining a possible variation of the proton-to-electron mass ratio [83, 84]. The demonstration of a fountain will be relevant for all these experiments.

In principle, a molecular fountain may be used to study transitions in many polar molecules. For this experiment, however, we plan to use a specific isotopologue of ammonia, $^{15}\text{NH}_3$, for a number of reasons: (i) The microwave spectrum of ammonia is very well studied. In fact, it was used in the first demonstration of an *atomic* clock by Condon and Lyons in 1948 [21] and the first demonstration of the maser by Townes¹, Gordon and Zeiger in 1955 [30]. The energies of the hyperfine levels of the four most common symmetric isotopologues ($^{14}\text{NH}_3$, $^{15}\text{NH}_3$, $^{14}\text{ND}_3$, and $^{15}\text{ND}_3$) have been determined with an accuracy of better than 100 Hz [45, 48–50]. We choose NH_3 over ND_3 because the inversion frequency is higher and because NH_3 has a more convenient Stark shift. We choose $^{15}\text{NH}_3$ over $^{14}\text{NH}_3$ because it has a less complicated hyperfine structure. (ii) Ammonia has a strong Stark shift, a relatively small mass and a high vapour pressure. Together, these properties make ammonia very suitable for Stark

¹A highly personal account of some of the leading events in 20th-century physics that led to the discovery of the maser can be found in the interesting book *How the Laser Happened* written by Charles Townes.

deceleration [85]. (iii) The ammonia molecule is a sensitive probe for variations of the proton-electron mass ratio. The inversion frequency in ammonia is determined by the tunneling rate of the nitrogen atom through the barrier between the two equivalent configurations of the molecule and is exponentially dependent on the reduced mass of the system [45, 46, and Chapter 1]. By monitoring the inversion frequency over a period of a few years, a possible variation of the proton-to-electron mass ratio can be constrained or measured.

2.2 The ammonia molecule

The ammonia molecule has been described in Chapter 1. In the electronic ground state of ammonia, the three hydrogen atoms are located in a plane below or above the nitrogen atom, thus forming a regular pyramid. As the barrier between the two configurations is not infinite, the nitrogen atom can tunnel through the plane formed by the hydrogens to inverse the orientation of the molecule. This tunnel motion gives rise to a splitting between the two inversion levels. Quantum mechanical tunneling depends strongly on the effective mass that tunnels, reflected by the variation in inversion splittings among the various isotopologues of the ammonia molecule. In the lightest isotopologue, $^{14}\text{NH}_3$, the splitting is 23.7 GHz [49, 50], whereas in the heavier isotopologue, $^{15}\text{ND}_3$, it is 1.43 GHz [45]. This remarkable sensitivity of the inversion frequency to the reduced mass of the molecule and hence to the proton-to-electron mass ratio μ in combination with the ability to decelerate ammonia molecules [85], makes ammonia very suitable for constraining possible variation of μ .

The various ammonia isotopologues have different possible symmetries of the nuclear spin wave functions of the identical protons/deuterons. The overall wave function of ammonia is a product of the electronic, vibrational, rotational and nuclear wave functions and should be either symmetric or antisymmetric under interchange of any two identical particles, in accordance with the symmetrization postulate of quantum mechanics. In the ground state of ammonia the electronic wave function is always symmetric while the vibrational wave function is symmetric for the lower component of the inversion doublet and antisymmetric for the upper component of the doublet [86]. Hence, each ro-vibrational level of the ammonia molecule combines with a nuclear spin wave function of one specific symmetry. The nuclear wave functions of molecules in levels where the quantum number K is a multiple of 3 have A symmetry (ortho) and the levels where K is not a multiple of 3 have E symmetry (para). In a molecular beam, the molecules are adiabatically cooled and only the lowest rotational levels in the vibrational and electronic ground state are populated. The ortho and para symmetry species of ammonia cannot be interconverted easily and may therefore be considered as two independent molecular species and the symmetry of the nuclear wave functions is preserved during the expansion. Hence, the ratio of the populations in the ortho and para levels is identical to that in the original sample. For NH_3 this implies that 60% of the molecules reside in the $|J, K\rangle = |1, 1\rangle$ level which is the ground state of para ammonia [51]. The remainder of the molecules is distributed over the $|J, K\rangle = |0, 0\rangle$

and $|1, 0\rangle$ levels of ortho ammonia. It is interesting to note that the existence of the two distinct symmetry species allows for the deceleration of ammonia. The $|J, K\rangle = |1, 1\rangle$ level is the only populated state with a significant Stark effect and would otherwise be populated to a much lesser extent.

2.3 Experimental setup

The Stark shift is the potential energy of a molecule in an electric field. Therefore, in an inhomogeneous electric field, a polar molecule experiences a mechanical force. If we define $\mu_{\text{eff}} = -(\partial W_{\text{Stark}}/\partial |\vec{E}|)$, this force becomes

$$\vec{F}(\vec{r}) = \mu_{\text{eff}} \nabla |\vec{E}| \quad (2.1)$$

We will use this force to decelerate and manipulate the molecules. Fig. 2.1 shows a schematic view of the molecular fountain. The setup consists of three differentially pumped vacuum chambers. In the first chamber, a pulsed ($\sim 100 \mu\text{s}$) ammonia beam is released into vacuum from a solenoid valve (General Valve series 99) at a 10 Hz repetition rate. By cooling the valve housing to -50°C and seeding the ammonia molecules in xenon (typically 5%), the average velocity of the beam is lowered to 300 m/s. The translational temperature of the beam is below 1 K and the rotational temperature is below 5 K. The most intense part of the beam passes through a 1 mm skimmer into the second chamber where the molecules are decelerated using a Stark decelerator consisting of an array of 101 equidistant ($L = 5.5 \text{ mm}$) electric field stages. Each stage is formed by two parallel 3 mm diameter cylindrical metal rods, spaced 2 mm apart. The two opposite rods are switched to +10 and -10 kV by four independent HV switches (Behlke HTS 150-03-GSM) that are triggered by a programmable delay generator. The velocity of the molecular beam is controlled completely by a computer-generated burst sequence.

A molecule in a state with a positive Stark shift ($\epsilon = -1$) will experience an increase in potential energy when entering a region of increasing electric field, conform Eqs. 1.11 and eq:deltaWstark. The gain in potential energy will be compensated by a decrease in kinetic energy and the molecule slows down. If the electric field is switched off before the molecule has left the field, the molecule will not regain the lost kinetic energy and will remain its lower velocity. The amount of kinetic energy that is converted into potential energy depends on the magnitude of the Stark shift in the applied electric field. Applying a voltage difference of 20 kV over 2 mm creates an electric field of about 100 kV/cm and results in a Stark shift of approximately 1.0 cm^{-1} . Using 100 pulsed electric field stages, the molecules are decelerated from 300 m/s to about 5 m/s. At the exit of the decelerator the decelerated packet of molecules has a volume of approximately 1 mm^3 and a temperature of about 30 mK [51, 85].

During the deceleration process, the phase space density, i.e. the product of position and velocity spread, remains constant. Electrostatic lenses can either decrease the position spread at the cost of the velocity spread (position focus) or decrease the velocity spread at the cost of the position spread (velocity focus). The former process is known as adiabatic cooling and the latter is known as adiabatic compression or

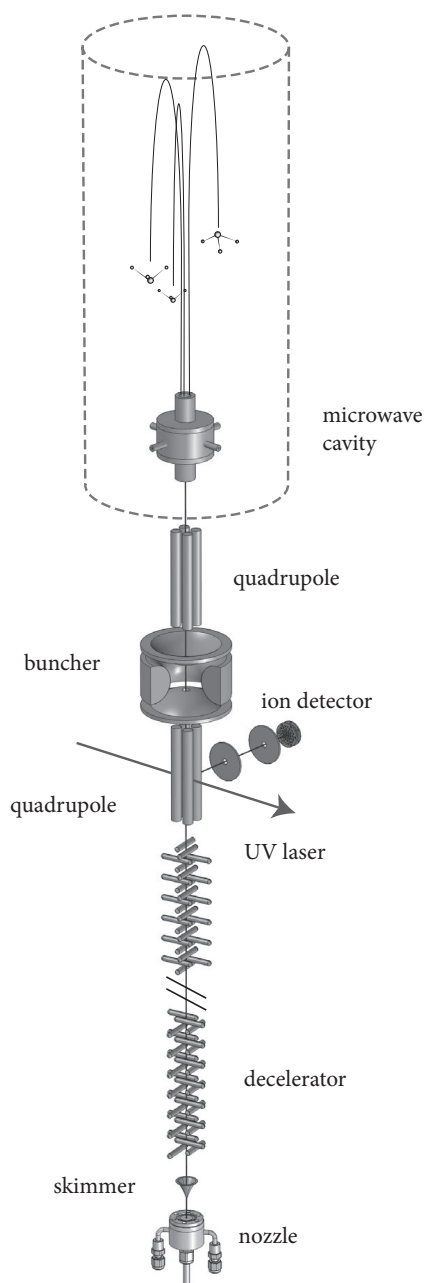


FIGURE 2.1: Schematic view of the molecular fountain setup. Note that for characterizing the setup the microwave cavity is replaced by a third linear quadrupole and a second detection zone.

bunching [87]. In the fountain setup both schemes are used to control the trajectories of the decelerated molecules. To this end, a combination of two linear quadrupoles and a cylindrical quadrupole is used. The linear quadrupoles are composed of four 20 mm diameter rods which are placed symmetrically on the outside of a circle with a diameter of 20 mm. By applying a voltage difference between adjacent electrodes an electric field is created. The voltage applied to the rods is pulsed to allow for a controllable focusing strength and effective lens position and to minimize fringe effects from the edges of the electrodes. The quadrupole field is zero at the center and increases linearly away from the center [29]

$$E(r) = \frac{V_0}{R_0^2} r, \quad (2.2)$$

where V_0 is the electric potential that is applied between two adjacent rods and R_0 the inner radius of the quadrupole. Thus, molecules in a low-field-seeking state ($\epsilon = -1$) will experience a force towards the beam axis. If the Stark energy is much smaller than the inversion splitting, inserting Eqs. (1.24) and (2.2) in Eq. (2.1) results in a perfect harmonic force with an angular frequency given by

$$\omega = \sqrt{\frac{k}{m}}, \quad \text{with} \quad k = \frac{2}{W_{\text{inv}}} \left[\frac{\mu_{\text{el}} MK V_0}{J(J+1) R_0^2} \right]^2, \quad (2.3)$$

where m is the mass of the molecule. For the parameters of our setup and for a voltage difference between the quadrupole rods of 10 kV, this results in an angular frequency of about $\omega/2\pi = 500$ Hz for molecules in the upper state of the inversion doublet. Assuming that the velocity v_s of the synchronous molecule along the beam axis is constant, i.e. ignoring gravity, the equations of motion can be solved to obtain the focusing distance of the lens

$$L_3 = \frac{L_1 + \frac{1}{\kappa} \tan \kappa L_2}{\kappa L_1 \tan \kappa L_2 - 1} \quad \text{with} \quad \kappa = \frac{\omega}{v_s}, \quad (2.4)$$

with L_1 and L_3 the object and focal distance, respectively, and L_2 the effective length of the lens. Note that this result for a quadrupole lens is identical to the expression given by Stolte *et al.* for a hexapole lens [88]. Hence, for a given geometry, a spatial focus can be obtained by using an effective length of

$$L_2^{\text{sf}} = \frac{L_1 + L_3}{\kappa^2 L_1 L_3 - 1}, \quad (2.5)$$

where we have used the paraxial approximation, i.e. $\tan \theta \approx \theta$. Likewise, a velocity focus ($L_3 \rightarrow \infty$) is achieved when

$$L_2^{\text{vf}} = \frac{1}{\kappa^2 L_1}. \quad (2.6)$$

Equations (2.5) and (2.6) are identical to those given by Heiner *et al.* [89].

The two linear quadrupoles are used to expand and cool the beam in the transverse direction. The cylindrical quadrupole, or buncher, is used to do the same in the vertical

direction. The geometry of this cylindrical lens is identical to that of a Paul trap for charged particles [90]. The lens consists of two endcaps and a ring electrode. The inner radius R_1 of the ring electrode is 30mm and the endcaps are spaced $\sqrt{2}R_1$ apart. In the endcaps, 2 mm diameter holes allow the molecular beam to pass through. The electric field in the buncher has a quadrupole symmetry and is given by

$$E(r, z) = \frac{V_0}{R_1^2} \sqrt{r^2 + 4z^2}, \quad (2.7)$$

where r and z are the cylindrical coordinates with respect to the center of the buncher and V_0 is the voltage difference applied between the endcaps and ring electrode. The force experienced by an ammonia molecule inside the lens is again harmonic with an angular frequency of about $\omega/2\pi = 110$ Hz in the longitudinal direction if $V_0 = 10$ kV. Note that the angular frequency in the longitudinal direction is twice as large as in the radial direction.

The quadrupole lenses are used to maximize the overlap of the packet of ammonia molecules with the focus of a tunable UV laser. The laser is tuned to state-selectively ionize ammonia using a (2+1) REMPI scheme via the $B(v_2 = 3)$ state. The nascent ions are mass-selectively detected using the quadrupole electrodes as an extraction field in a Wiley-McLaren type mass spectrometer setup [91]. Eventually, the inversion transition in ammonia will be excited using Ramsey's method of separated oscillatory fields [18], resulting in an expected resolution of $\Delta\nu \sim 1$ Hz [51].

In Fig. 2.2 simulated trajectories of some ammonia molecules through the quadrupole focusing lenses are plotted. The exit of the Stark decelerator is taken as the origin, and the grey shaded areas indicate the position of the quadrupoles and microwave cavity. On the right-hand side of the figure, the envelope of the beam is plotted in phase space at three positions in the fountain: (i) at the exit of the decelerator, (ii) at the center of the lower linear quadrupole where the molecules are detected, and (iii) at the apogee of the ballistic trajectories. In the phase space plots, only molecules that make it through the fountain without hitting the aperture of the cavity or quadrupoles are plotted. Therefore, the area bounded by the bold lines represents the transverse acceptance of the fountain. As the trajectories are fully symmetric around the apogee, the phase-space distributions for the beam going up and falling down are identical. With the settings used in the simulation, a 4:1 image is created from the exit of the decelerator to the detection region and a 1:100 image from the detection region to the apogee of the fountain [51]. As a consequence of the applied quadrupole pulses, the beam has a low temperature (230 nK) and low density in the interaction region (velocity focus) and a relatively high temperature (1 mK) and density in the detection region (spatial focus). Using the cylindrical quadrupole a similar imaging is performed along the z axis. From simulations taking into account nonlinear contributions to the force, the phase-space acceptance for molecules that make it through the fountain was found to be $0.005 \text{ mm}^3 (\text{m/s})^3$ [51]. The phase-space volume occupied by a packet of molecules exiting the Stark decelerator is approximately 1 mm^3 by $5 (\text{m/s})^3$, resulting in an efficiency of about 40 ppm. As a single decelerated bunch contains approximately 10^6 ammonia molecules, about 40 molecules are expected to be focused back onto

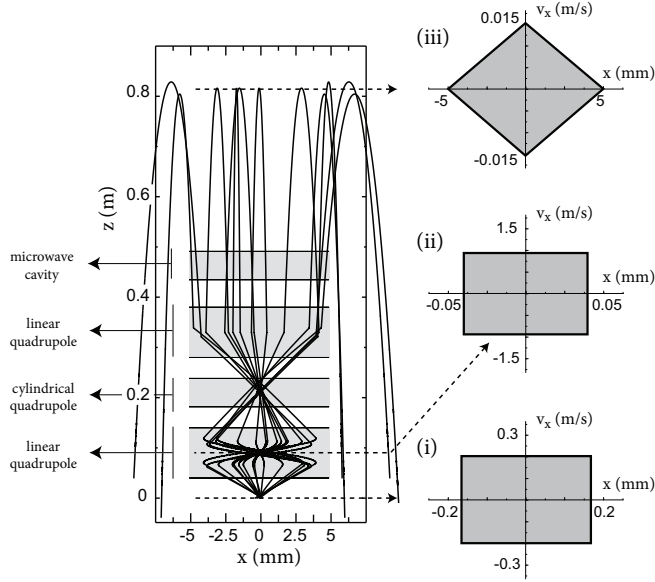


FIGURE 2.2: Simulated trajectories of some ammonia molecules through the quadrupole lens system. On the right-hand side of the figure phase-space distributions of the beam are shown at three different positions in the fountain: (i) at the exit of the decelerator, (ii) at the detection zone, and (iii) at the apogee of the fountain. Note the different scales of the three graphs.

the detection region per fountain cycle where they are detected with near-unity efficiency [51].

In order to characterize the apparatus, the initial setup is slightly different than the design depicted in Fig. 2.1. Instead of the microwave cavity a third linear quadrupole with a length of 500 mm is mounted on top of the second linear quadrupole to be able to guide the molecules during the full trajectory. Moreover, a second detection zone is placed 420 mm behind the exit of the decelerator.

2.4 Experimental results and numerical simulations

2.4.1 Operation of the Stark decelerator

In Fig. 2.3, time-of-flight profiles of NH_3 are shown as obtained using the setup described above. Traces (a) and (c) show time-of-flight profiles obtained with the decelerator off at the lower and upper detection zone, respectively. The mean arrival time at the lower and upper detection zone is 2.2 and 3.3 ms, respectively, corresponding to an average velocity of 300 m/s. The FWHM of the velocity distribution is around 80 m/s, corresponding to a translational temperature of about 2.8 K in the moving frame of the molecular beam. Traces (b) and (d) show again time-of-flight profiles obtained at the lower and upper detection zone, respectively. However, the fields on

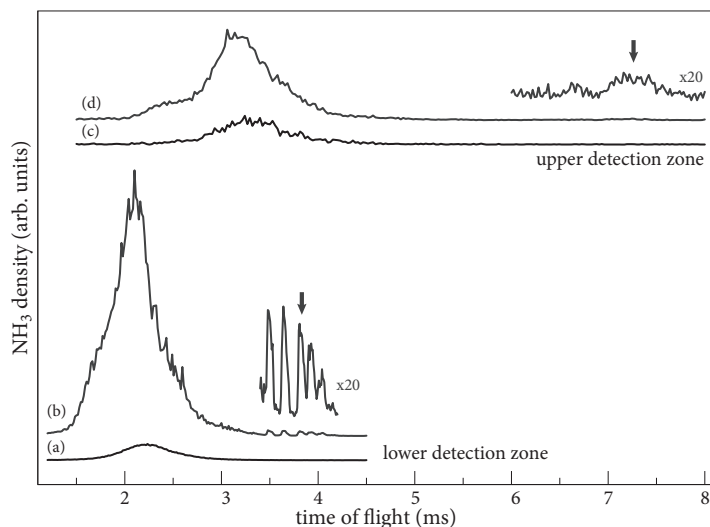


FIGURE 2.3: Observed time-of-flight distributions of ammonia. Trace (a) and (c) show the undecelerated beam at the lower and upper detection zone, respectively. The traces (b) and (d) give time-of-flight profiles for which the electric field sequence is switched such as to decelerate molecules from 300 to 100 m/s ($\phi_0 = 56^\circ$) at the lower and upper detection zone, respectively. Also shown are magnifications of the decelerated packets, the decrease in NH_3 density is attributed to the longer flight distance. Different traces have been given an offset for clarity.

the decelerator stages are switched such as to decelerate the central part of the original beam from 300 m/s to 100 m/s, corresponding to a constant phase angle of $\phi_0 = 56^\circ$. The signal of the undecelerated molecules is increased by approximately a factor of 15, as molecules that are not in sync with the switching of the fields experience an effective transverse focusing force. At later time intervals, five peaks are seen that correspond to decelerated molecules. The molecules that arrive around 3.8 ms are those that were at the right position near the entrance of the decelerator at the start of the time sequence and that passed through all 101 deceleration stages in sync with the deceleration fields. These molecules entered the decelerator with a velocity of 300 m/s and exit the decelerator with a velocity of 100 m/s. The earlier peaks originate from molecules that were either one or two periods further inside the decelerator at the start of the time sequence. These molecules also entered the decelerator with a velocity of 300 m/s, but since they missed the last two or four deceleration stages they exit the decelerator with a velocity of 108 or 115 m/s, respectively. The peak that appears at a later time in the time-of-flight distribution originates from molecules entering the decelerator with a lower initial velocity, catching up with the time sequence one period later. Throughout the decelerator, it trails the synchronous packet by 11 mm, exiting the decelerator with the same final velocity of 100 m/s. The signal of the decelerated molecules at the first detection zone is about half that of the molecular beam when the decelerator is off. This intensity is relatively low due to the velocity spread of the

decelerated molecules that results in a broadening of the packet during its time of flight. The spreading is even more apparent at the upper detection zone where the packet is diffused almost entirely.

2.4.1.1 Asymmetry issues of the decelerator potentials

It was found that the intensity of the decelerated molecules increased significantly when asymmetric voltages were applied to the decelerator rods. This is illustrated in Fig. 2.4, in which the asymmetry is defined as

$$\mathcal{S} = \frac{V_+ - |V_-|}{V_+ + |V_-|}, \quad (2.8)$$

with V_+ and V_- the positive and negative potentials applied to the rods of the decelerator, respectively. It can be seen that the signal intensity is three times larger if an asymmetry close to -0.08 is applied to the decelerator when compared to the symmetric situation. As the individual decelerator rods are conditioned to withstand AC potentials up to 10 kV, the asymmetry translates to voltage values of $V_+ = +8.5$ kV and $V_- = -10$ kV. On further inspection it was found that the asymmetry could be traced to a single decelerator rod and it is therefore assumed that this mounting rod is slightly bend. Note that these settings result in an effective phase angle that is slightly lower than in the symmetric case.

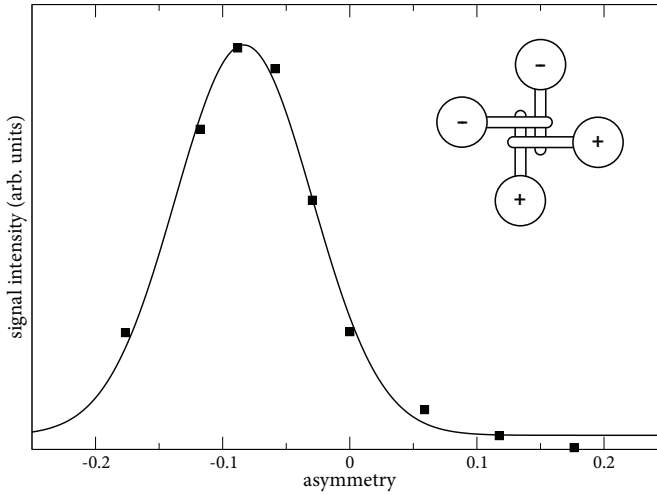


FIGURE 2.4: Intensity of decelerated molecules ($v_s = 100$ m/s) as a function of the asymmetry applied to the decelerator, conform Eq. (2.8). The inset shows a top view of the four decelerator combs. The measurements were performed with a total potential difference of 17 kV between the electrodes.

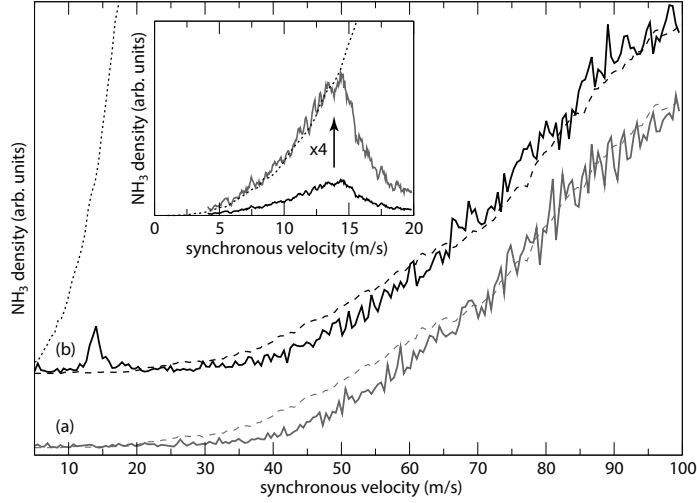


FIGURE 2.5: Density of NH_3 molecules at the lower detection zone as a function of the final synchronous velocity with $\phi_0 = 56^\circ$. In the measurement of trace (a) no electric field pulses were applied to the quadrupole and the signal scales roughly as v^3 . In the measurement of trace (b) the lower quadrupole was set to focus molecules with a velocity of 14 m/s at the detection zone. Dashed lines represent the normalized density of ammonia molecules at the detector and are obtained from a 3D simulation assuming a uniform acceptance of the decelerator. Dotted lines indicate the normalized molecular density at the detector for a packet of molecules that is perfectly imaged by the quadrupole. The inset shows a measurement where the effective quadrupole length was adjusted according to Eq. (2.5). Although the shape of the curve is well reproduced by the simulations, the measured signal intensity is about a factor of 4 smaller than predicted.

2.4.2 Focusing and bunching of slow molecules

2.4.2.1 Radial focusing of decelerated molecules

In Fig. 2.5, the signal of decelerated molecules at the lower detection zone is plotted as a function of the final synchronous velocity for a constant phase angle. Trace (a) shows the signal intensity at the lower detection zone when no voltage is applied to the quadrupole lens. In the measurement of trace (b) the lower quadrupole was set to transversally focus molecules with a vertical velocity of 14 m/s at the position of the laser focus. As a result, a sharp peak at this velocity is observed. Note that for a given voltage the quadrupole will focus molecules within a small velocity interval only, conform Eq. (2.5). In order to understand the observed decrease in signal one should realize that the spreading of the decelerated packet of molecules in each direction is described by $\Delta q = \sqrt{\Delta q_0^2 + (\Delta v_q L / v_s)^2}$, with $q = \{x, y, z\}$, L the distance from the end of the decelerator to the detection zone, and v_s the final synchronous velocity (along z). The velocity spread of the decelerated packet of molecules, for a given phase angle, does not depend on the final velocity and, consequently, the density at the detector scales

roughly as $\Delta q^{-3} \sim v_z^3$. By applying an appropriate voltage to the quadrupole lens, the velocity spread in the radial direction is compensated for and the density of molecules is expected to scale as $\Delta z^{-1} \sim v_z$. The inset of Fig. 2.5 shows a measurement in which the effective quadrupole length is adjusted according to Eq. (2.5) to account for the different final velocities emitted by the decelerator.

The dashed lines in Fig. 2.5 represent the normalized density of ammonia molecules at the detector and are obtained from a 3D simulation assuming a constant density of molecules at the end of the decelerator. It can be seen that for velocities up to 60 m/s the simulation fits quite well with the experimental data. For lower velocities, however, the measured density is lower than expected from simulation. Dotted lines indicate the normalized molecular density at the detector for a packet of molecules that is perfectly imaged by the quadrupole. From this curve it follows that the measured density of ammonia molecules is a factor of 4 smaller than in the simulation.

In order to understand this decrease in signal, the density of molecules at the end of the decelerator was simulated as a function of the final synchronous velocity for a constant phase angle $\phi_0 = 60^\circ$. The result of this simulation is shown in Fig. 2.6. It is observed that the number of molecules in the packet as well at its phase-space density drops at low velocities. This decrease is a direct consequence of the fact that

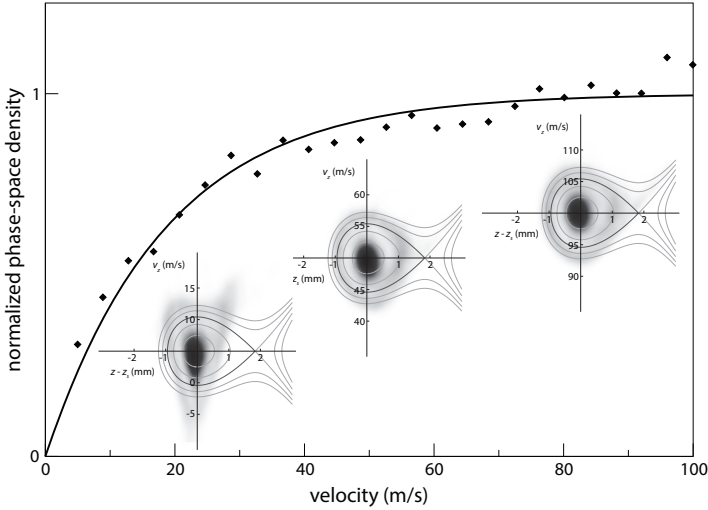


FIGURE 2.6: Simulated three-dimensional phase-space density at the end of the decelerator as a function of the final velocity with a constant phase angle $\phi_0 = 60^\circ$. Diamonds represent the normalized number of molecules within a phase-space volume of $1 \text{ mm}^3 (\text{m/s})^3$ around the synchronous molecule. It should be noted that the phase-space density was found to depend upon the bin size. The solid line is intended to guide the eye. A similar decrease in phase-space density was observed by Sawyer [92, Fig. 5.5]. Also shown are phase-space diagrams for $v_z = 100$, $v_z = 50$, and $v_z = 5$ m/s. The gray-shaded areas represent the density of molecules at a certain position in phase space and were obtained from 3D-numerical simulations. The solid curves are particle trajectories obtained from a simple 1D-model.

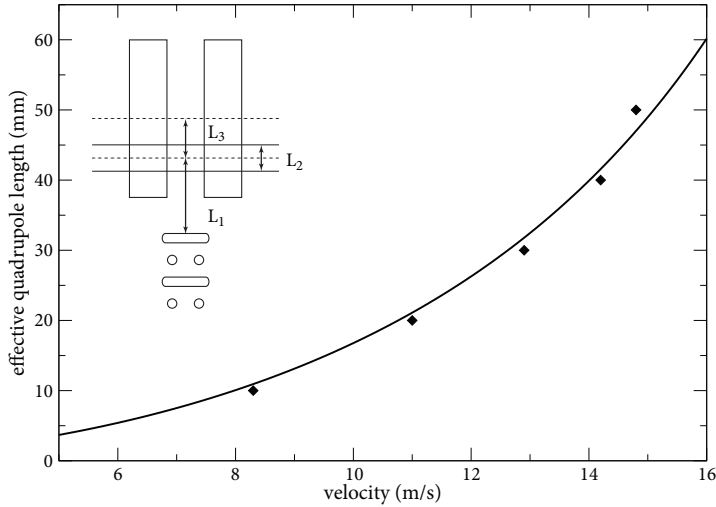


FIGURE 2.7: Effective quadrupole length around $\frac{1}{4}$ th of the total length of the lower quadrupole at a voltage difference of 11 kV as a function of the final velocity. The solid line is a fit according to Eq. (2.5) and yields an angular frequency of $\omega/2\pi = 592$ Hz at $V_0 = 11$ kV, in good agreement with Eq. (2.3). The inset shows a schematic representation of the lens system and indicates the important parameters.

the approximations used to derive the phase stability are valid at high velocity only, and break down at low velocities, where the characteristic wavelength of the longitudinal and transverse motion of the molecules becomes comparable to the periodicity of the decelerator. This can also be observed from the phase-space portraits for different final velocities that are shown as the insets in Fig. 2.6. Although it is difficult to obtain a good indication of the absolute number of molecules in these plots, it can be seen that the concept of phase stability breaks down at low velocities.

The angular frequency of the quadrupole can be obtained by taking velocity scans while either varying the effective length or the voltage difference applied to the rods. The diamonds in Fig. 2.7 represent focused velocities for different effective lengths of the lower quadrupole with $V_0 = 11$ kV, varied around $\frac{1}{4}$ th of the total length. The solid line is a fit according to Eq. (2.5) and yields an angular frequency of $\omega/2\pi = 592$ Hz at $V_0 = 11$ kV, in good agreement with Eq. (2.3).

By switching the quadrupole at the appropriate voltage and time, a packet of decelerated molecules with a mean velocity of 5 m/s can be focused at the laser focus. The resulting time-of-flight profile is plotted in Fig. 2.8. The inset shows a schematic drawing of the lowest quadrupole and the effective pulses that were used to focus the molecules as well as some simulated trajectories. Note that we have used two pulses in order to maximize both the opening angle of the quadrupole and the tightness of the focus. The large opening angle is accomplished by pulsing the quadrupole just after the molecules have entered the lens. This reduces the clipping by the quadrupole rods and increases the acceptance of the lens system. The length of the pulse has been chosen

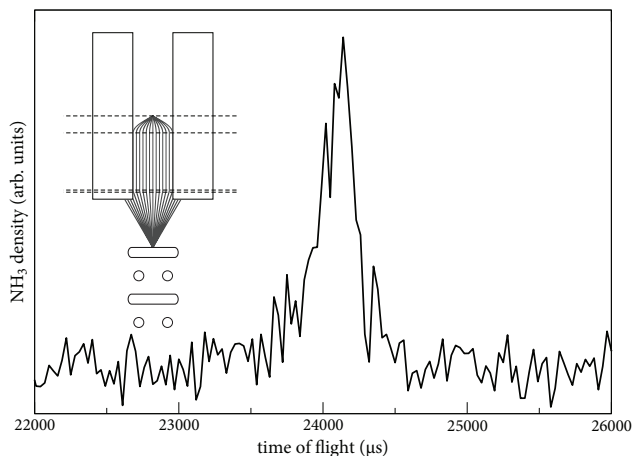


FIGURE 2.8: Time-of-flight profile for molecules decelerated from 300 to 5 m/s and detected at the lower detection zone. The inset shows a schematic drawing of the lowest quadrupole and the effective pulses that were used to focus the molecules together with some simulated trajectories. In this measurement, two pulses were used in order to maximize both the opening angle of the quadrupole lens and the tightness of the focus. Note that these molecules are slow enough to fall back under gravity within the confines of our modest sized apparatus.

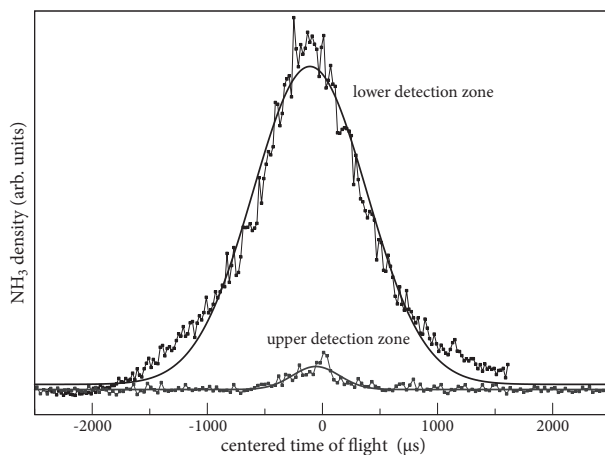


FIGURE 2.9: Time-of-flight profiles recorded at the lower and upper detection zone for molecules decelerated from 300 to 14 m/s. Spatial foci are created at the first and second detection zone and at the center of the cylindrical quadrupole. The intensity at the upper detection zone is about 1.5 times weaker than expected if broadening during time of flight would be the only loss mechanism. The additional loss is attributed to clipping by the quadrupole lenses and a less tight focus at the upper detection zone. Note that the maximum velocity for which the buncher can spatially focus the molecules at the second detection zone is 8 m/s.

such as to create a collimated beam (velocity focus). The second pulse is applied just before the molecules are detected and creates a focus that corresponds to the root of a sine function. The volume of such a focus is much smaller than a focus of a converging beam and hence the ammonia density is higher. Although molecules with a vertical velocity of 5 m/s are slow enough to fall back under gravity within the confines of our modest sized molecular beam machine, it is impossible to detect these molecules due to the residual velocity spread in the vertical direction. In order to increase the density of the molecules as they fall back, the cylindrical quadrupole has to be used in addition to the linear quadrupole.

2.4.2.2 Longitudinal focusing of decelerated molecules

By setting the lower and upper quadrupoles such as to create a first focus at the lower detection zone, a second focus at the center of the buncher and a third focus at the upper detection zone, the velocity spread in the radial direction is compensated for fully. If the pulses applied to the buncher are timed properly the packet of molecules is focused in the vertical direction and an increase in signal at the upper detection zone should be observed. Fig. 2.9 shows two time-of-flight profiles originating from molecules decelerated to 14 m/s and detected at the lower and upper detection zone. As can be seen in the figure, the signal at the upper detection zone is about $\frac{1}{7}$ th of the signal at the lower detection zone. The vertical velocity spread in combination with the longer time of flight accounts for a loss in signal intensity of 80%, while the remaining loss is attributed to clipping by the quadrupole lenses and to a less tight focus at the upper

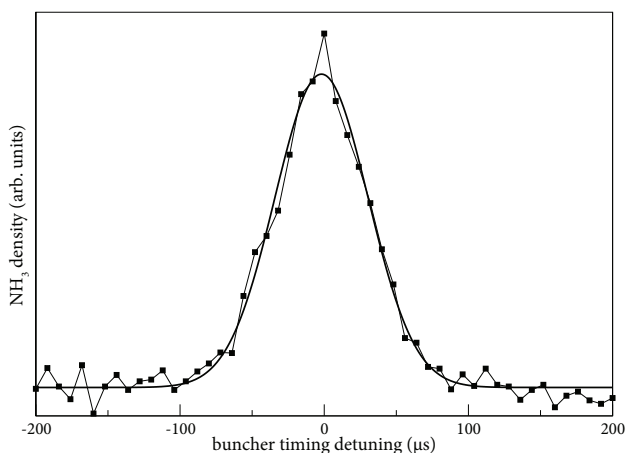


FIGURE 2.10: Simulated density of ammonia molecules with a vertical velocity of 8 m/s at the upper detection zone as a function of the detuning of the buncher timing. These simulations only take the harmonic force into account and ignore nonlinear contributions. The bold solid line is a Gaussian fit with a full width at half maximum of $75 \mu\text{s}$ (0.5 mm). The effective length of the buncher and the upper and lower quadrupole settings are chosen such to produce a maximum signal intensity.

detection zone. The minimum velocity that is still detectable at the upper detection zone is limited by the signal-to-noise ratio and is about 14 m/s.

The maximum voltage difference that can be applied safely between the ring electrode and endcaps, based on the conditioning of the electrodes, is 14 kV, resulting in a longitudinal angular frequency of $\omega/2\pi = 160$ Hz. Assuming a maximum effective buncher length of 25 mm and an object and image distance of 200 and 220 mm, respectively, Eq. (2.5) results in a maximum focusable velocity of 8 m/s. This result has been confirmed by numerical simulations. In order to observe an effect of the buncher, the signal-to-noise ratio for slow molecules should be increased such that velocities below 8 m/s can be detected.

The ability of the buncher to create a space or velocity focus at the upper detection zone depends strongly on a proper timing of the applied electric field pulses. To illustrate this effects for a velocity focus, we have simulated the density of ammonia molecules at the second detection zone as a function of the detuning of the buncher timing. The result of this simulation – ignoring nonlinear contributions – is shown in Fig. 2.10 for a packet of ammonia molecules with a velocity of $v_z = 8$ m/s. The simulated curve has a full width at half maximum of about $75 \mu\text{s}$, which translates into an uncertainty of 0.5 mm for the buncher position. Although such a timing accuracy is, in principle, straightforward to achieve, the optimization of the buncher is complicated significantly due to the fact that the focus settings of the different lens systems depend on each other. In addition to the time at which the buncher is switched on, the effective length of the buncher, as well as the trigger time and effective length of the upper and lower quadrupole, influence the detected signal.

2.5 Conclusions and outlook

In this chapter we have presented the design of a molecular fountain based on a Stark-decelerated molecular beam of ammonia molecules. By using two linear quadrupoles, we demonstrated full control over the radial phase-space distribution of the slow packet of molecules; both spatial and velocity foci were readily obtained in the radial direction. In this way, a packet of ammonia molecules with an upward velocity of 5 m/s was obtained. Although these molecules are – in principle – slow enough to fall back under gravity within the confines of our modest sized molecular beam apparatus, no such molecules were observed. The main reason for this can be found in the inability to observe an effect of the buncher. As a consequence, the velocity spread in the vertical direction could not be compensated for and the slow packet of molecule spreads out during free flight.

We attribute the inability to observe bunched signal to the following two reasons. (i) The lens system that is used to cool and collimate the slow molecules is too complex. For example, the parameter range for which bunching is feasible is rather small and depends critically on the way the slow packet of molecules is coupled into the buncher by the quadrupoles. (ii) The density of the ammonia signal is insufficient at low velocities. These two issues could, in principle, be solved on their own, however their combination obstructed the successful operation of the fountain. The signal-to-

noise ratio at low velocities can be improved by adopting a new detection scheme that discriminates slow ammonia molecules from thermal background and by using a new approach to decelerate the molecules to low velocities. In Chapter 3 the implementation of velocity map imaging is discussed, while in Chapter 4 a traveling-wave decelerator is used to decelerate and trap ammonia molecules. In addition to a larger acceptance at low velocities, this ring-type decelerator allows for phase-space manipulation in the decelerator itself making a buncher obsolete.

VELOCITY MAP IMAGING OF A SLOW BEAM OF AMMONIA MOLECULES INSIDE A QUADRUPOLE GUIDE

Velocity map imaging inside an electrostatic quadrupole guide is demonstrated. By switching the voltages that are applied to the rods, the quadrupole can be used for guiding Stark-decelerated molecules and for extracting the ions. The extraction field is homogeneous along the axis of the quadrupole, while it defocuses the ions in the direction perpendicular to both the axis of the quadrupole and the axis of the ion optics. To compensate for this astigmatism, a series of planar electrodes with horizontal and vertical slits is used. A velocity resolution of 35 m/s is obtained. It is shown that signal due to thermal background can be eliminated, resulting in the detection of slow molecules with an increased signal-to-noise ratio. As an illustration of the resolving power we have used the velocity map imaging system to characterize the phase-space distribution of a Stark-decelerated ammonia beam.

3.1 Introduction

Techniques to decelerate and cool molecules increase the interaction time in spectroscopic experiments and promise to significantly enhance the precision of a number of experiments aimed at testing fundamental laws of physics [51, 81, 93, 94]. As a proof of principle, high-resolution microwave spectroscopy was carried out on Stark-decelerated molecular beams of ND_3 [45] and OH [78]. In these experiments, an interaction time on the order of a millisecond was achieved. In Chapter 2 we discussed the construction of a molecular fountain in our laboratory, in order to increase the interaction time further. Unfortunately, due to the limited efficiency of cooling techniques, the increased interaction time comes at the expense of a decreased signal-to-noise

ratio. Techniques such as resonance-enhanced multiphoton ionization (REMPI) allow detection of very small quantities of molecules. However, if the signal of the decelerated molecules becomes too small, it will be obscured by the signal of the undecelerated part of the beam.

Here, we use velocity map imaging (VMI) to discriminate the signal of slow molecules from thermal background molecules. VMI is a technique that uses ion lenses to focus laser-produced ions onto a position sensitive ion detector [95]. By setting the voltages of the ion lenses correctly, molecules that have the same initial velocity but a different initial position are focused at the same position on the detector. In this way, all velocity information of the particles involved in the experiment is contained in a single image. Ion imaging techniques, such as VMI, have been used extensively for measuring the velocity of product molecules or atoms following a chemical reaction or the photodissociation of a parent molecule [95–97]. State-of-the-art velocity map imaging systems achieve a velocity resolution below 10 m/s [98].

The ion optics used in a conventional VMI setup consist of three or more electrodes with circular apertures. In this chapter, we demonstrate velocity map imaging inside an electrostatic quadrupole guide that is mounted directly behind a Stark decelerator. The main advantage of this configuration is that it allows for detection inside the guide, where the density of molecules is relatively high. As our detection scheme relies on multiphoton transitions using a focused laser beam, a high density of molecules is crucial. In our configuration, the ions are extracted from the guide by applying a small positive voltage to two of the quadrupole rods. This results in a field that is homogeneous along the axis of the quadrupole, while it defocuses the ions in the direction perpendicular to both the axis of the quadrupole and the axis of the ion optics. Here, we show how the astigmatism can be compensated by using a series of planar electrodes with horizontal and vertical slits.

3.2 Experimental setup

Our experiments have been performed in a vertical molecular beam machine that is described in Chapter 2. In brief, a pulsed ($\sim 100 \mu\text{s}$) ammonia beam is released into vacuum from a solenoid valve (GeneralValve series 99) at a 10 Hz repetition rate. By cooling the valve housing to -50°C and seeding the ammonia molecules in xenon, the mean velocity of the beam is lowered to 300 m/s. The ammonia beam is decelerated using a Stark decelerator consisting of an array of 101 deceleration stages. Adjacent stages are 5.5 mm apart. Each deceleration stage is formed by two parallel 3 mm diameter cylindrical rods, spaced 2 mm apart. The two opposite rods are switched to +10 and -10 kV by four independent HV switches that are triggered by a programmable delay generator. The velocity of the molecular beam is controlled completely by the computer generated burst sequence (for details on Stark deceleration, see Refs. [31, 85, 89]). An electrostatic quadrupole, mounted 30 mm behind the decelerator, is used for focusing the slow molecules and to provide an extraction field for the velocity map imaging system. The chamber that houses the quadrupole guide is differentially pumped and kept at a pressure of 3×10^{-8} mbar when the pulsed valve is operating.

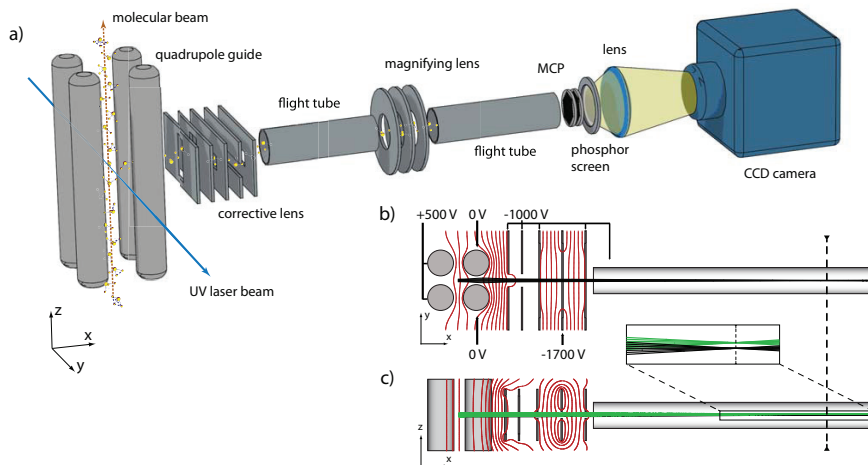


FIGURE 3.1: (a) Schematic view of the ion optics used for performing velocity map imaging inside a quadrupole guide. A set of rectangular electrodes with horizontal and vertical slits (corrective lens) is used to make a position focus approximately 300 mm from the center of the quadrupole, indicated by the vertical dashed line in panels (b) and (c). Using an Einzel lens consisting of three cylindrical electrodes (magnifying lens), this image is mapped onto a Multi-Channel Plate detector mounted in front of a phosphor screen. The image is recorded using a CCD camera. (b) and (c) Equipotential lines in the lens system along the horizontal and vertical plane, respectively. The black and green lines show trajectories of ions starting with a velocity along the z axis of 0 and 300 m/s, respectively.

A schematic view of the quadrupole and ion optics is shown in Fig. 3.1(a). The quadrupole consists of four 20 mm diameter cylindrical rods that are placed on the outside of a 20 mm diameter circle. Alternating positive and negative voltages of up to 6 kV are applied to adjacent rods to focus decelerated ammonia molecules. The molecules are focused 90 mm downstream from the decelerator, where they are ionized using a (2+1) REMPI scheme. The laser radiation (~ 10 mJ in a 5 ns pulse @322 nm) is focused between the rods of the quadrupole using a lens with a focal length of 500 mm. In order to extract the ions, a positive voltage pulse is applied to the left-hand side quadrupole rods while the other two rods are grounded. In this way, ions are pushed towards the corrective lens consisting of five rectangular (80×40 mm²) electrodes, two of which have a vertical slit aperture (10×30 mm²) and three have a horizontal slit aperture (50×10 mm²). The fourth electrode is composed of two parts such that a voltage difference can be applied between the upper and lower part. The first electrode of the corrective lens is placed 40 mm away from the center of the quadrupole, while the next electrodes are separated by 15 mm. After a 220 mm long flight tube, the ions pass a magnifying lens that consists of three circular electrodes with 15 mm circular apertures [99]. Finally, after another 240 mm long flight tube, the ions impinge upon a double Multi-Channel Plate (MCP) mounted in front of a fast response ($1/e$ time ~ 10 ns) Phosphor Screen (Photonis P-47 MgO). The light of the phosphor screen is imaged onto a CCD camera (PCO 1300, 1392×1040 pixels). By applying a timed voltage

pulse with a high-voltage switch (Behlke HTS 31-03-GSM), the gain of the front MCP can be gated to select ammonia ions, thus eliminating background signal due to oil and other residual molecules in the vacuum.

In Fig. 3.1(b and c), the equipotential lines in the lens system are shown along the horizontal and vertical plane, respectively. Also shown in the figure are the trajectories of ions, starting with a velocity along the z -axis of 0 (black lines) or 300 m/s (green lines). These calculations were performed using the SIMION package [100]. With voltages applied to the left-hand side rods of the quadrupole, the ions are defocused in the horizontal plane [Fig. 3.1(b)]. This is compensated by applying a voltage difference between the right-hand side rods of the quadrupole and the first electrode. If an extraction voltage of +500 V is applied, a voltage of -1000 V is required on the first electrode to create a focus slightly before the magnifying lens. From our simulations, molecules starting with a velocity of 300 m/s along the z -axis are displaced from the center by approximately 0.5 mm. The magnifying lens is used to map the image plane onto the position sensitive detector, magnifying the image by a factor of about 6. In the vertical direction (Fig. 3.1(c)), the divergence of the beam is not affected by the quadrupole or the first two electrodes. The ions are focused onto the image plane by applying a voltage of -1700 V to the fourth electrode while keeping the other electrodes and the flight tubes at a voltage of -1000 V.

In our VMI system, the focusing properties along the horizontal plane are determined by the voltage difference between the first electrode and the left-hand side of the quadrupole, while the focusing properties along the vertical plane are determined by the voltage applied to the fourth electrode. Note that the second and third electrodes are kept at the same voltage to ensure that the vertical and horizontal focusing properties are fully uncoupled. In addition, the position of the beam can be steered in the horizontal and vertical plane by applying small voltage differences (typically about 30 V) between the two right-hand side quadrupole rods and between the upper and lower part of the fourth electrode, respectively.

3.3 Characterizing the ion optics

In order to have optimal velocity resolution, the voltages need to be applied such that ions with the same initial velocity but a different initial position are focused at the same position on the detector. In the y direction, ions are collected over a range that is limited by the gap between the quadrupole rods. A position focus is found by changing the voltage applied to the left-hand side rods until the observed ion distribution in the horizontal direction is minimized. In the z direction, the optimal settings are found by scanning the voltage applied to the fourth electrode while the laser focus was located at different heights. In these measurements, shown as the symbols in Fig. 3.2, the beam is decelerated from 300 to 100 m/s and the height of the laser focus was changed over a range of about 0.5 mm. The curves in Fig. 3.2 are the result of trajectory simulations using SIMION [100]. For the measurement shown in Fig. 3.2(a) the magnifying lens was not used, i.e., it was set at the same voltage as the flight tubes. It is seen that for an applied voltage around -1100 V the beam is neither focused nor defocused and the

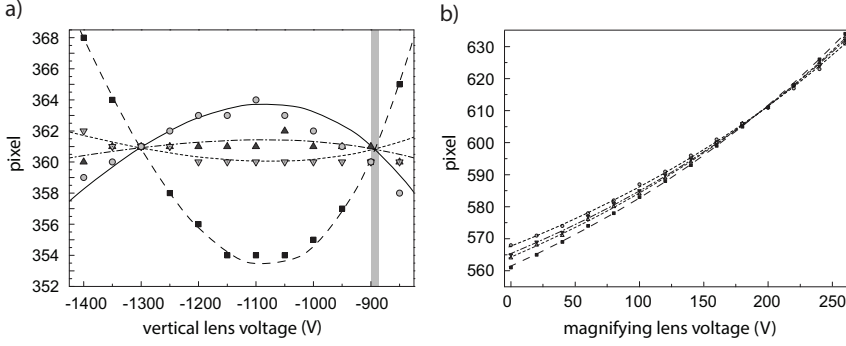


FIGURE 3.2: (a) Measured vertical position of the ions as a function of the voltage applied to the fourth electrode of the corrective lens with the laser focused at four different vertical positions over a range of about 0.5 mm in the quadrupole. A voltage of -500 V is applied to the left-hand side quadrupole rods while a voltage of -1000 V is applied to all other electrodes. The gray-shaded area indicated which position focus had been used. (b) Measured vertical position of the ions as a function of the voltage applied to the magnifying lens. The fourth electrode is kept at -1700 V. The other voltages are set as in (a).

vertical position at which the ions arrive at the detector directly reflects the height of the laser focus (under our conditions, one pixel corresponds to about 0.05 mm). Note that -1100 V is slightly more negative than the expected -1000 V that is applied to the other electrodes. This is attributed to the finite size of the electrodes.

When the voltage applied to the fourth electrode is larger (more negative) than that of the surrounding electrodes, the ions are first accelerated and then decelerated as they pass the fourth electrode. At the same time, they experience a focusing, a defocusing and again a focusing force. As the ions are (on average) faster and closer to the axis when they experience a defocusing force and slower and further away from the axis when they experience a focusing force, the overall effect of the field is focusing. This is the basic operation principle of an Einzel lens [97]. The same argument holds for the situation when the voltage applied to the fourth electrode is smaller (less negative) than that applied to the surrounding electrodes. As a result of this effect, position foci are observed at voltages of -900 V and -1300 V. Either voltage setting can be used to perform velocity map imaging; we chose the lower voltage setting.

When the magnifying lens is used, the focal length of the first horizontal and vertical lens needs to be reduced. When a voltage of $+550$ V is applied to the left-hand side rods of the quadrupole and a voltage of -1730 V is applied to the fourth electrode, the focal plane is situated about 30 mm before the magnifying lens. It is seen from the measurements and simulations shown in Fig. 3.2(b) that the focal plane is imaged onto the detector when a voltage of $+200$ V is applied to the middle electrode of the magnifying lens.

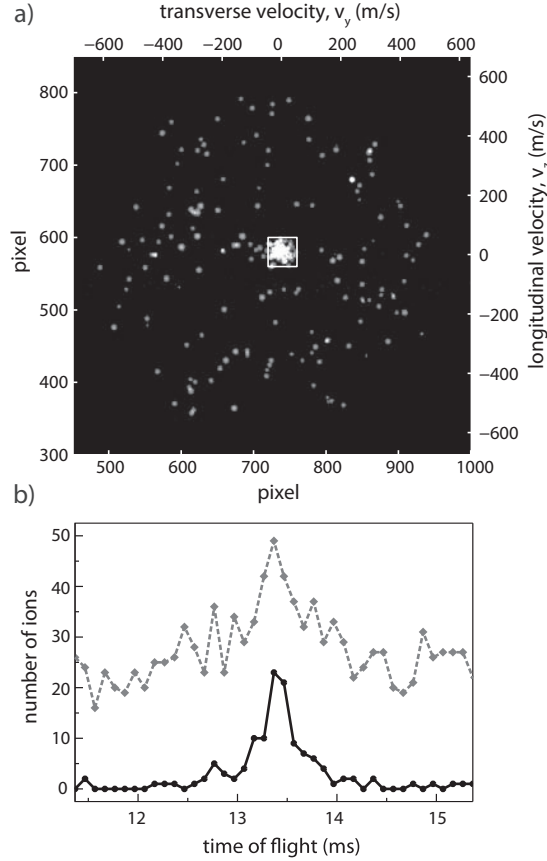


FIGURE 3.3: (a) Camera image showing the distribution of ions. The MCP gate is set to detect ammonia ions only. The bright spot inside the square corresponds to ammonia molecules that are decelerated from 300 to 10 m/s. (b) Time-of-flight distributions for a molecular beam decelerated to 10 m/s. The dashed curve is obtained by counting ions over the entire area of the camera, while the solid curve is obtained by counting ions inside the white square depicted in (a).

3.4 Experimental results

In Fig. 3.3(a), a typical camera image is shown with the voltages set to obtain optimal velocity resolution. In this measurement, the decelerator is set to decelerate ammonia molecules from 300 m/s to 10 m/s. The image is averaged over 256 shots. For each laser shot, pixels below a certain threshold are set to zero before adding up the images. The bright spot at the center of the image corresponds to the decelerated molecules, while the scattered spots result from thermal background ammonia molecules in the vacuum. Note that the ion distribution is clipped by the aperture of the magnifying lens. On the upper side and the right-hand side, the horizontal and vertical position is translated into horizontal and vertical velocity, respectively (*vide infra*).

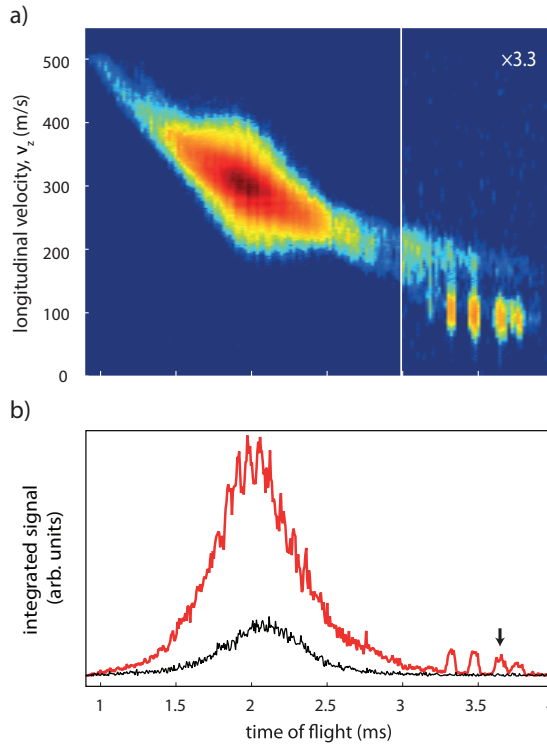


FIGURE 3.4: (a) Longitudinal velocity of the ammonia beam as a function of time. The intensity of the right-hand side panel is scaled by a factor of 3.3 for clarity. (b) Integrated ion signal as a function of time with the decelerator on (red curve) and with the decelerator off (black curve). The arrow indicates the position of the synchronous packet of molecules.

In Fig. 3.3(b), the observed ion signal is shown as a function of time with respect to the start of the burst sequence applied to the decelerator. The lower trace is obtained by counting the ions over the area enclosed by the $100 \times 100 \text{ (m/s)}^2$ white square shown in Fig. 3.3(a), while the upper trace is obtained by counting the ions over the entire area of the camera. Ions are counted using the centroiding method introduced in Ref. [101]. Each data point is averaged over 32 shots. If ions are counted over the entire area of the camera, typically some 20 background ions are detected. By only counting ions within the selected area, this background is reduced by a factor of $550^2 \pi / 100^2 \approx 100$. Note that for a given voltage the quadrupole will focus molecules within a small velocity interval. As a result, the width of the time of flight profile does not reflect the velocity spread of the decelerated packet, but rather the position spread of the packet as it leaves the decelerator.

In Fig. 3.4, the longitudinal velocity of the molecular beam is shown as a function of time with respect to the start of the burst sequence applied to the decelerator. For this image, the decelerator was set to decelerate from 300 to 100 m/s. At every time delay, an image is averaged over 64 shots and the intensity is integrated over the horizontal

direction of the camera. This results in 156 vertical lines which are combined to obtain Fig. 3.4(a). The observed signal follows a hyperbolic curve due to the inverse relation between velocity and time. The most intense part of the beam is observed at short times having an average velocity of 300 m/s. These are molecules that were not in sync with the time sequence and, as a result, they are on average neither decelerated nor accelerated but they do experience a focusing effect in the transverse directions. At later arrival times, four packets are seen that are offset from this hyperbola. The packet arriving at $3700\ \mu\text{s}$ originates from molecules that were at the right position near the entrance of the decelerator at the start of the time sequence and that passed through all 101 deceleration stages in sync with the deceleration fields. These molecules entered the decelerator with a velocity of 300 m/s and exit the decelerator with a velocity of 100 m/s. The earlier peaks originate from molecules that were either one or two periods further inside the decelerator at the start of the time sequence. These molecules also entered the decelerator with a velocity of 300 m/s, but since they missed the last two or four deceleration stages they exit the decelerator with a velocity of 108 or 115 m/s, respectively. The peak that appears at a later time in the time-of-flight distribution originates from molecules entering the decelerator with a lower initial velocity, catching up with the time sequence one period later. Throughout the decelerator, it trails the synchronous packet by 11 mm, exiting the decelerator with the same final velocity of 100 m/s. Although the resolution of our vMI system is insufficient to resolve the difference in velocity between the distinct packets, a small displacement between the first three packets can be observed. Note that the figure resembles the calculation presented in Fig. 2 of Heiner *et al.* [89], the main difference being that here we plot the longitudinal velocity as a function of time at the detection zone, whereas Heiner *et al.* plot the longitudinal velocity as a function of position in the decelerator at specific times.

In Fig. 3.4(b), the ion signal is integrated over the total area of the camera. The red curve shows the time-of-flight with the decelerator on, while the black curve shows the same measurement taken with the decelerator off. Note that the observed oscillations in the undecelerated part of the beam are due to velocity modulations, and are well reproduced in simulations [31].

In order to calibrate the velocity axis, we have recorded vMI images while the velocity of the beam was scanned from 150 to 5 m/s in steps of 1 m/s by changing the burst sequence applied to the Stark decelerator. At every velocity, an image is averaged over 64 shots and the intensity is integrated over the horizontal direction of the camera. This results in 145 vertical lines which are combined to obtain Fig. 3.5(a). Since molecules are ionized using a focused laser beam, the number of detected ions is proportional to the density of the decelerated beam. Due to the increasing time of flight, this density decreases rapidly when the velocity of the beam is lowered. In these measurements, the quadrupole is set to transversely focus molecules of 10 m/s at the position of the laser. As a result, a bright spot at this velocity is observed in Fig. 3.5(a) (shown enlarged in the inset). In Fig. 3.5(b), the ion signal is integrated over the total area of the camera. A peak is observed when molecules are decelerated to 10 m/s corresponding to molecules that are focused 90 mm downstream from the decelerator, where the molecular beam crosses the ionisation laser.

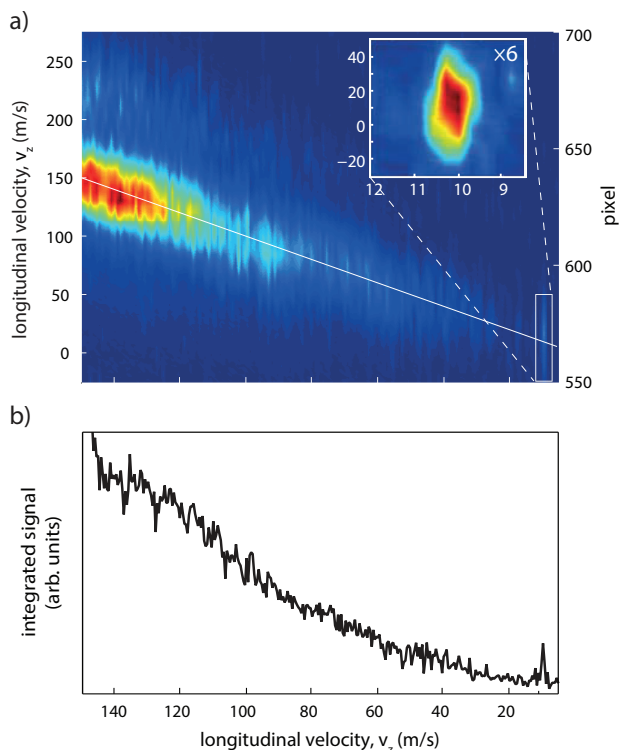


FIGURE 3.5: (a) Longitudinal velocity of the ammonia beam as a function of the velocity set by the burst sequence applied to the decelerator. The quadrupole is set to focus molecules of 10 m/s at the position of the laser. The inset shows an enlarged view of molecules that are focused with the quadrupole. The intensity is scaled by a factor of 6 for clarity. (b) Integrated ion signal as a function of velocity with the burst sequence set to decelerate molecules to different velocities.

The straight line shown in Fig. 3.5(a) is used to translate the position at the camera into a vertical velocity. The FWHM velocity spread of the beam that is inferred from the camera images is 35 m/s (corresponding to 20 pixels on the camera). As, at the used settings of the decelerator, the longitudinal velocity spread of the beam is below 10 m/s [85], we conclude that the velocity resolution of the lens system is on the order of 35 m/s. The instrumental resolution of the system might be better than this as in our case the velocity resolution is limited by the recoil of the photoelectron during the ionization step. Ammonia molecules are ionized using a (2+1) REMPI scheme via the $B(v_2 = 3)$ state, producing ions predominantly in the $v_2 = 3$ state [102].

Since the ionization potential of ammonia is 10.07 eV [103], a velocity of 20 m/s is imparted to the ion in either direction. Note that, in our experiment, the polarization of the laser was parallel to the molecular beam axis. A better velocity resolution may have been obtained if we had chosen the polarization perpendicular to the molecular beam. During the experiment we found that the exact arrival position of ions with a certain velocity changed from day to day which is attributed to charging effects of

nearby isolators used for suspending the quadrupole and the ion optics. These charging effects might contribute to the observed velocity resolution.

3.5 Conclusions

A setup consisting of a series of planar electrodes is used for performing velocity map imaging inside an electrostatic quadrupole guide. We obtain a velocity resolution of 35 m/s, limited by recoil of the photoelectron and by the presence of isolators used for suspending the quadrupole. Our work demonstrates that velocity map imaging can be performed in unconventional electrode configurations while achieving a resolution that is sufficient for most purposes. This should be useful for studies in electrostatic traps [85], storage rings [104, 105] and molecular fountains [51]. An often quoted phrase in the ion imaging community is: “if you do not use VMI, you throw away information”. In this work, the information obtained from VMI is used to detect slow molecules free of any signal from thermal background gas.

DECELERATING AND TRAPPING OF AMMONIA MOLECULES IN A RING DECELERATOR

In Chapter 2, the design of a molecular fountain based on a Stark-decelerated beam of ammonia was discussed. By rapidly switching electric fields between two static geometric configurations of a conventional Stark decelerator, an effective travelling potential well is produced that moves along with the molecules in the beam and that was used to decelerate part of these molecules in a quasi-continuous fashion [31, 33]. However, for low final velocities, the fraction of molecules that can be decelerated in this way is reduced significantly. This is particularly disadvantageous for experiments that require molecules at low final velocities, such as the fountain experiment described earlier. In this chapter we present measurements of decelerated and trapped ammonia molecules that are confined in a true 3D potential well. These measurements were performed in a hybrid Stark decelerator configuration consisting of a conventional Stark decelerator with an adjoined ring-type decelerator. We demonstrate the versatility of this ring-type decelerator by manipulating the phase space distribution of the trapped molecules. In addition, we determine the temperature of the trapped molecules from a measurement in which we excite the trap frequencies.

4.1 Introduction

In conventional Stark decelerators the principle of phase stability is employed, which ensures that molecules experience an ‘effective’ 3D potential well that keeps them in a compact packet during the deceleration process [34, 85]. Whereas the approximations used to derive this effective well are valid at high velocity, where the characteristic wavelength of the longitudinal and transverse motion of the molecules is much larger than the periodicity of the decelerator, they no longer hold at low velocity. As a result

of this breakdown, the number of molecules in the packet as well as its phase-space density drops dramatically at low velocities (see Chapter 2).

Recently, Meek *et al.* [106, 107] demonstrated a chip-based Stark decelerator that provides a true 3D trapping potential. The decelerator presented by these authors consists of a periodic array of electrodes that is used to produce a spatial and temporal modulated electrostatic potential to create the desired field minima. Expanding on this work, Osterwalder and co-workers [108, 109] decelerated CO molecules from 288 to 144 m/s using a series of ring electrodes to which a sinusoidal voltage was applied. In this ring-type decelerator, the molecules experience a ‘genuine’ rather than an effective potential well that moves continuously along with the molecules. The molecules are decelerated by slowly decreasing the velocity of the moving potential well by chirping the frequency of the applied waveform. The lowest velocity that can be reached with the setup of Osterwalder *et al.* is 120 m/s and is limited by the range over which the sinusoidally varying voltages can be varied. Besides avoiding losses at low velocities, a ring-type decelerator has the advantage that molecules can be brought to a complete standstill and trapped without the need to load them in a separate electrode geometry. Furthermore, as the molecules are always close to the zero-point of the electric field, they can be decelerated in states that become high-field seeking at relatively low electric fields. This makes it possible to decelerate heavy molecules such as YbF [110] and SrF [111]. However, in order to decelerate these heavy molecules to a complete standstill, the apparatus needs to be several meters long [111].

We have chosen an approach that combines a conventional Stark decelerator with a ring-type decelerator to slow down ammonia molecules. First, the conventional Stark decelerator is used to decelerate the molecular beam from 300 to 90 m/s. The decelerated packet of ammonia molecules is subsequently coupled into a ring decelerator that is used to remove the remaining kinetic energy of the molecules. The advantages of this approach are twofold: (i) the conventional Stark decelerator is used to remove about 90% of the kinetic energy and is operated in the range where its acceptance is relatively large. In this way, the size of the molecular beam apparatus remains relatively small. (ii) The velocity at which the molecules are coupled into the traveling-wave decelerator corresponds to a frequency of the waveform of 8.3 kHz, which has to be chirped down to zero in order to bring the molecules to a complete standstill. This frequency can be generated by commercially-available HV amplifiers, whereas a frequency of 30 kHz, that is required for molecules travelling at an initial speed of 300 m/s cannot be easily generated.

4.2 Ring decelerator concept

4.2.1 Electric potential

The factors that are responsible for the dramatic decrease in the phase-space acceptance of a conventional Stark decelerator are inherent in its design and solving them requires a new decelerator concept that accounts for the symmetry of the distribution of molecules in the beam and that provides a true 3D-trapping potential. As the distribution of molecules in a molecular beam is cylindrically symmetric around the molecular beam

axis, the most natural choice for a decelerator design is one that produces a electric field distribution that possesses a similar symmetry. A hollow conducting cylinder of infinite length constitutes the simplest of such devices. Here, the derivation of Van de Meerakker *et al.* [31] to derive the electric potential of this cylinder is reproduced. The inner radius of the cylinder is denoted by r_0 and the longitudinal symmetry axis of the cylinder coincides with the molecular-beam axis. The electric potential inside the cylinder, $\Phi(r, \phi, z)$, has to obey Laplace's equation in cylindrical coordinates

$$\nabla^2 \Phi(r, z) = 0, \quad (4.1)$$

where we have made use of cylindrical symmetry ($d\Phi/d\phi = 0$) and it has been assumed that there are no free charges inside the cylinder. The solution of this equation can be readily obtained by separation of variables, that is, $\Phi(r, z)$ is considered to be a product of a radial function $\Phi_r(r)$ that only depends on r , and a longitudinal function $\Phi_z(z)$ that only depends on z . After dividing by $\Phi(r, z)$ and grouping terms that either depend on r or z , two ordinary differential equations are obtained

$$\frac{1}{\Phi_r(r)} \left(\frac{d^2 \Phi_r(r)}{dr^2} + \frac{1}{r} \frac{d\Phi_r(r)}{dr} \right) = - \frac{1}{\Phi_z(z)} \frac{d^2 \Phi_z(z)}{dz^2} = k^2, \quad (4.2)$$

with k a separation constant. The ordinary differential equation for $\Phi_z(z)$ has periodic solutions of the form $\Phi_z(z) = e^{\pm ikz}$ for nonzero and real values of k and these solutions have a period length given by $\lambda = 2\pi/k$. Under the change of variable $x = kr$, the equation for $\Phi_r(r)$ takes the form of the standard modified Bessel's equation and its solutions are proportional to a modified Bessel function of the first kind of order zero [112]. This function, denoted as $I_0(x)$, is symmetric around $x = 0$ where it has the value $I_0(0) = 1$ and increases exponentially with x . Because Laplace's equation is a linear differential equation, linear combinations of its solutions are also solutions. For the infinitely long hollow cylinder considered here, the most general solution is thus given by [31]

$$\Phi(r, z) = \sum_{n=0}^{\infty} A_n \cos(nkz + \delta_n) I_0(nkr). \quad (4.3)$$

When the electric potential on the cylinder ($r = r_0$) is given by $\Phi(r, z) = V_0 \cos(kz)$, the summation reduces to a single term where $n = 1$ and $A_1 = I_0(kr_0)^{-1}$. Since the electric field magnitude is given by $|\vec{E}| = [(\partial\Phi/\partial r)^2 + (\partial\Phi/\partial z)^2]^{1/2}$, the electric field magnitude inside the cylinder, $|\vec{E}(r, z)|$, takes the form [31]

$$|\vec{E}(r, z)| = \frac{V_0 k}{I_0(kr_0)} \sqrt{[I_1(kr) \cos(kz)]^2 + [I_0(kr) \sin(kz)]^2}, \quad (4.4)$$

where the modified Bessel function of the first kind of order one, $I_1(kr)$, is the derivative of $I_0(kr)$ [112]. Again, this function is symmetric around $kr = 0$ and increases exponentially with kr , however $I_1(0) = 0$. By setting $r = 0$ in Eq. (4.4), the electric field magnitude on the molecular beam axis is obtained

$$|\vec{E}(r = 0, z)| = \frac{V_0 k}{I_0(kr_0)} |\sin(kz)|, \quad (4.5)$$

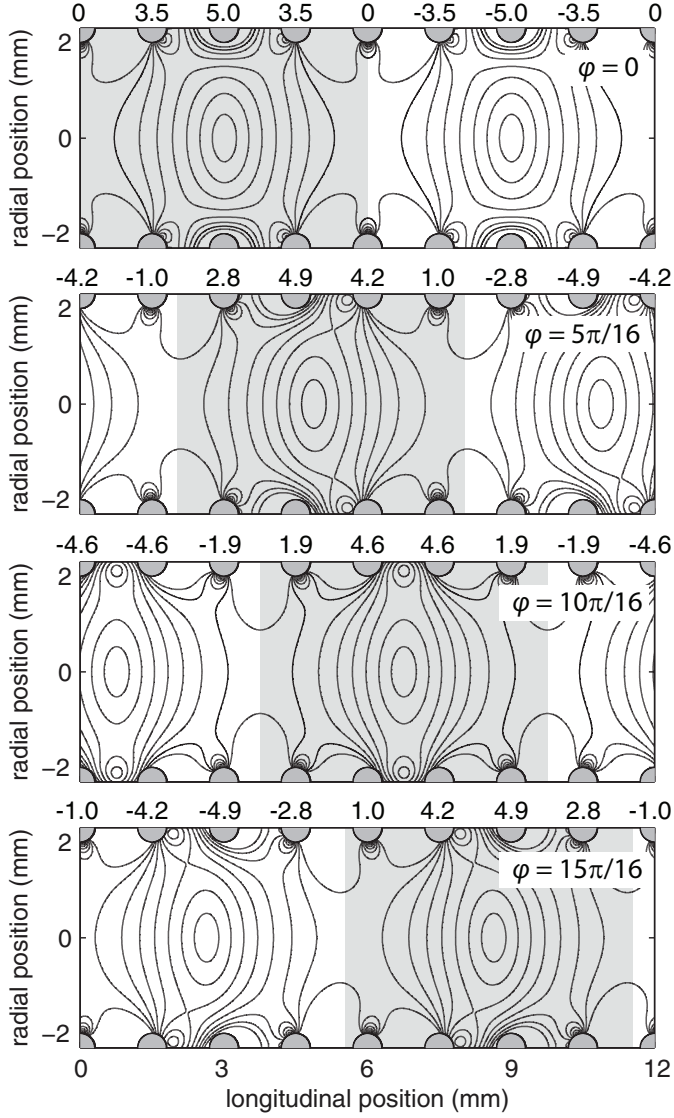


FIGURE 4.1: Contour plots of the electric field magnitude for four different phase offsets ϕ . The electrodes are shown schematically as the gray-shaded hemispheres. The numbers above the upper electrodes in each panel indicate the potential in kV applied to each electrode to produce the shown electric field. Contour lines start at 2.5 kV/cm around the center of the trap and are spaced by 2.5 kV/cm. Gray-shaded areas are used to indicate a typical unit cell that is used in the simulation of the trajectories through the ring-type decelerator

which implies that two electric field minima exist per period of the potential. From comparing this equation with Eq. (4.3) it follows that these minima correspond to positions where the potential has a maximum value. The r dependence of the electric-field strength at the molecular beam axis is obtained by setting $z = 0$ in Eq. (4.4)

$$|\vec{E}(r, z = 0)| = \frac{V_0 k}{I_0(kr_0)} I_1(kr). \quad (4.6)$$

It is interesting to expand $\sin(kz)$ and $I_1(kr)$ around $kz = 0$ and $kr = 0$, respectively

$$\begin{aligned} \sin(kz) &= kz - \frac{(kz)^3}{6} + \dots \\ I_1(kr) &= \frac{kr}{2} + \frac{(kr)^3}{16} + \dots \end{aligned}$$

Thus, almost perfect quadrupole electric traps are created on the molecular beam axis near the electric field minima. As this infinitely long cylinder cannot be implemented in an experimental setup, a decelerator design consisting of a periodic ring-electrode structure is used to mimic the electric-field distribution of the cylinder. Similar to Osterwalder and co-workers [108, 109], we adopt a periodicity for the ring-type decelerator consisting of eight electrodes. It is essential to the operation of the decelerator that the trapping potential maintains a constant shape and depth while it is moved. However, the use of a finite number of electrodes to mimic the sinusoidal potential produces an electric-field geometry that depends on the phase offset of the waveform. This effect is illustrated in Fig. 4.1 in which the electric-field magnitude is shown for several values of the phase offset. The electrode array in this figure has a period of 12 mm and a periodicity $N = 8$. These contour plots were calculated using the SIMION package [100]. In the chosen geometry, the electric field gradients in the bottom of the well, as well as the trap depth in the longitudinal direction are nearly independent of the position of the trap minimum. The trap depth in the transverse direction, however, is 40% deeper when the trap minimum is located in the plane of a ring compared to the situation when the trap minimum is located directly between two rings.

4.2.2 Waveform considerations

The required potential V_n on the individual electrodes n in the ring-type decelerator can be expressed as [109]

$$V_n(t) = V_0 \sin\left(-\phi(t) + \frac{2\pi n}{N}\right), \quad (4.7)$$

where V_0 is the amplitude of the sine-modulated potential and ϕ is a time-dependent phase offset that governs the motion of the traps. In Fig. 4.1, contour plots of the electric field magnitude for four different phase offsets ϕ are shown.

The angular frequency of the wave is given by the time derivative of $\phi(t)$, thus $(d\phi/dt) = 2\pi f(t)$, with $f(t)$ the frequency in Hz. Since one oscillation of the waveform moves the trap over one period, the velocity of the trap is given by $v_z(t) = f(t)L$.

Integrating the angular frequency with respect to time results in the following expression for the phase

$$\phi(t) = \frac{2\pi}{L} \int_0^t v_z(\tau) d\tau, \quad \text{with } v_z(t) = \int_0^t a_z(\tau) d\tau. \quad (4.8)$$

A linear increase of ϕ with time results in a trap that moves with a constant positive velocity along the cylindrical axis. Acceleration or deceleration of the traps can be achieved by applying a chirp to the frequency. It is convenient to describe the equations of motion of the molecules in a coordinate system that moves along with the traps. However, acceleration of the trap does change the effective longitudinal potential experienced by the molecules. In order to account for this pseudoforce an additional term of the form $W_{\text{acc}} = m a_z z$, with m the mass of the molecule and a_z the acceleration along the z axis, must be added to the potential. The resulting effective potential for NH_3 and ND_3 is shown in Fig. 4.2 for various accelerations and a waveform amplitude of $V_0 = 5$ kV. Deceleration of the waveform reduces the volume and depth of the traps and thus decreases the number of molecules that can be confined at higher accelerations. For decelerations above a certain threshold, the potential does not longer contain a minimum and no molecules can be trapped at all. It is interesting to note that the shape of the effective potential for NH_3 and ND_3 displays some distinct characteristics. In the case of NH_3 , the center of the trap is shifted in the positive z direction and remains rather symmetric around the minimum. The minimum of the effective potential for ND_3 , on the other hand, remains close to $z = 0$, while the longitudinal potential is skewed in the positive z direction. This is a direct consequence of the fact that the Stark effect of NH_3 scales quadratically with the electric field magnitude, whereas the Stark effect of ND_3 scales linearly with the electric field magnitude and that for small displacements z the electric field magnitude increases linearly away from the trap center.

4.2.3 Calculation of forces and trajectories

The ring decelerator is described most conveniently in the cylindrical coordinates (r, θ, z) , which in terms of the Cartesian coordinates (x, y, z) are expressed as

$$r = \sqrt{x^2 + y^2}, \quad (4.9)$$

$$\theta = \arctan \frac{y}{x}, \quad (4.10)$$

$$z = z, \quad (4.11)$$

where $r \in [0, \infty)$, $\theta \in [0, 2\pi)$, $z \in (-\infty, \infty)$ and the inverse tangent is defined such to take the correct quadrant of (x, y) into account. Due to the cylindrical symmetry of the array the electric field magnitude is independent of the azimuthal angle θ and only the radial and longitudinal coordinates have to be considered. As a consequence of the repetitive structure of the ring decelerator, a phase increase of $\Delta\phi = +2\pi/N$ corresponds to a translation of the electric fields over $\Delta z = +L/N$. For the computation of the Stark potential, W_{Stark} , the approximate form of Eq. (1.24) suffices

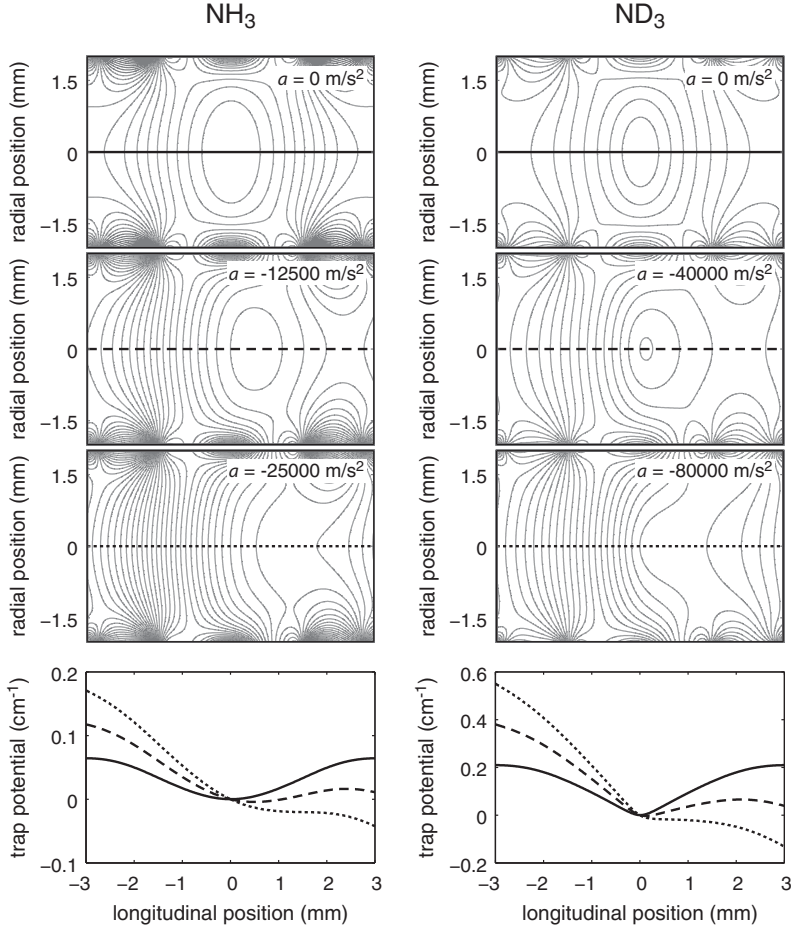


FIGURE 4.2: Effective potentials for NH_3 (left) and ND_3 (right) for various accelerations and a waveform amplitude of $V_0 = 5 \text{ kV}$. A constant acceleration produces a pseudoforce that distorts the Stark potential and reduces the trap volume and depth. Above a certain threshold the potential no longer contains a minimum and no molecules can be trapped. Contour lines are separated by 10 mK for NH_3 and 40 mK for ND_3 . The lower panels show the longitudinal dependence of the effective trapping potential along the beam axis for the different accelerations (relative to $a = 0 \text{ m/s}$). Note the difference in the position of the trap center between NH_3 and ND_3 for $a \neq 0 \text{ m/s}^2$.

$$W_{\text{Stark}} = -\varepsilon \sqrt{\left(\frac{W_{\text{inv}}}{2}\right)^2 + \left(\mu_{\text{el}} |\vec{E}| \frac{MK}{J(J+1)}\right)^2} + \varepsilon \frac{W_{\text{inv}}}{2}. \quad [1.24]$$

The mechanical force experienced by the molecules due to the Stark potential is defined by

$$\vec{F} = -\nabla W_{\text{Stark}}, \quad (4.12)$$

with ∇ the gradient in cylindrical coordinates

$$\nabla = \hat{r} \frac{\partial}{\partial r} + \hat{\theta} \frac{1}{r} \frac{\partial}{\partial \theta} + \hat{z} \frac{\partial}{\partial z}. \quad (4.13)$$

The second term on the right-hand side of Eq. (4.13) cancels due to symmetry. The computed force is directly related to the acceleration on a molecule and can be used to construct the equation of motion of the molecule.

In order to simulate the trajectories of the molecules in the ring decelerator we introduce the reduced phase

$$\phi_{\text{red}}(t) \equiv \phi(t) \pmod{2\pi/N}, \quad (4.14)$$

which defines the shape of the potential at time t (compare Fig. 4.1). Using SIMION, the electric-field magnitude of a unit cell is calculated for four values of the reduced phase for a waveform amplitude of 5 kV. This unit cell is centered around the trap minimum and has a length of $L/2$, as the shape of the trap depends on the absolute value of the potential. In Fig. 4.1 the unit cell is indicated by the gray-shaded area. At $t = 0$ it follows from Eq. (4.7) that the first trap is located at the second ring electrode. The traps advance a full period as the phase is increased by 2π , thus, the position of the trap that moves along with the synchronous molecule is given by

$$z_{\text{trap}}(t) = \frac{\phi(t)}{2\pi} L + \frac{L}{N}, \quad (4.15)$$

where the origin corresponds to the first ring of the decelerator. The distance between a molecule at position z and the nearest trap can be expressed as

$$z_{\text{red}}^* \equiv z - z_{\text{trap}} \pmod{\frac{L}{2}}. \quad (4.16)$$

The force that is experienced by a molecule at position (r, z) at time t is obtained by calculating the Stark energy of the tabulated electric fields and determining the gradient at the position (r, z_{red}^*) . As the electric-field files are calculated for a phase increment of $\pi/16$, interpolation between two of these files is necessary to obtain the force at the desired value of the reduced phase. Note that an additional interpolation is required if the waveform amplitude differs from 5 kV (scaling the electric field in every time step turned out to be too time consuming).

The trajectories are obtained by the Euler method [113], which assumes that the time derivatives are constant between successive integration steps. This crude method is easy to implement, but rather inefficient and therefore requires rather small time steps to reach a reasonable accuracy.

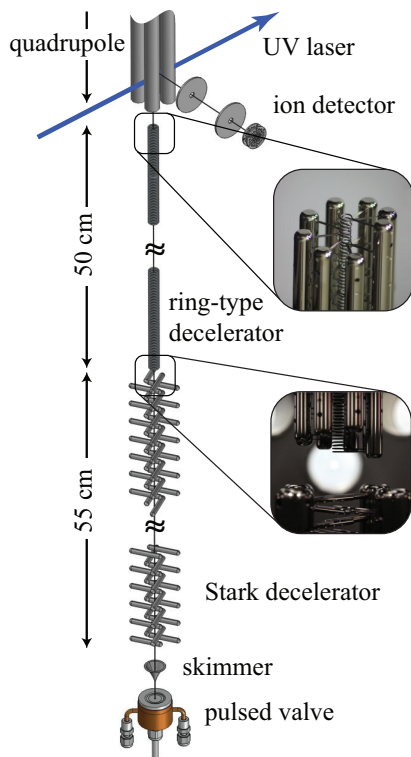


FIGURE 4.3: Schematic view of the experimental setup consisting of a conventional Stark decelerator with an adjoined ring decelerator.

4.3 Experimental setup

Fig. 4.3 shows a schematic view of our vertical molecular beam machine. The experimental setup consists of a conventional Stark decelerator, described in Chapter 2, with a ring-type decelerator attached. In brief, a pulsed ($\sim 100 \mu\text{s}$) ammonia beam is released into vacuum from a solenoid valve (General Valve series 99) at a 10 Hz repetition rate. By cooling the valve housing to typically -50°C and seeding the ammonia molecules in xenon, the mean velocity of the beam is lowered to 300 m/s. The ammonia beam is decelerated using a Stark decelerator consisting of an array of 101 deceleration stages. Adjacent stages are 5.5 mm apart. Each deceleration stage is formed by two parallel 3 mm diameter cylindrical rods, spaced 2 mm apart. The two opposite rods are switched to +10 and -10 kV by four independent HV switches that are triggered by a programmable delay generator. A ring-type decelerator is mounted 24 mm above the last electrode pair. The ring-type decelerator consists of 336 ring electrodes each of which is attached to one of eight 6 mm diameter stainless steel rods, resulting in a periodic array in which every ninth ring electrode is attached to the same rod. The rods are placed on

the circumference of a 13 mm diameter circle, forming a regular octagon. Each rod is mounted by two ceramic posts that are attached to the octagon via an adjustable aluminum bar that allows for fine tuning of the alignment. The ring electrodes are made by bending 0.6 mm thick tantalum wire into the shape of a tennis racket with an inner diameter of 4 mm. Consecutive rings are separated by 1.5 mm (center to center) resulting in a periodic length of 12 mm. This combination of parameters is copied from the design of Osterwalder and co-workers [108, 109]. The relative positioning of the 8 rods determines the final orientation of the ring electrodes and can be adjusted by the alignment tools that support the aluminum mounting bars. To avoid mechanical contact with the electrodes a CCD camera was used to monitor the electrode positions. In this way, the relative positions of the individual rods were set with an estimated accuracy of 0.05 mm. The voltages applied to the eight support bars are generated by amplifying the output of an arbitrary wave generator (Wuntronic DA8150) using eight fast HV-amplifiers (Trek 5/80) up to ± 5 kV. An electrostatic quadrupole, mounted 15 mm behind the ring decelerator, can be used for focusing slow molecules and to provide an extraction field for a Wiley-McLaren type mass spectrometer setup [91]. The molecular beam overlaps with the focus of an UV laser 40 mm behind the last ring electrode of the decelerator to ionize the ammonia molecules. The chamber that houses the two decelerators and quadrupole guide is differentially pumped and kept at a pressure of 3×10^{-8} mbar when the pulsed valve is operating.

4.4 Results

In this section experimental results and Monte Carlo simulations are presented that characterize the combination of the conventional Stark decelerator and ring-type decelerator. Experimental data of guided, decelerated, and trapped ammonia molecules are presented in Sec. 4.4.1. In Sec. 4.4.2 the coupling of molecules in the ring-type decelerator is discussed in the context of phase-space matching between the two decelerators. Phase jumps, which are used to perform phase-space matching within the ring decelerator, are considered in Sec. 4.4.3. Finally, in Sec. 4.4.4 the trapping potential is mapped out by driving parametric resonances of the trapped molecules.

4.4.1 Guiding, deceleration and trapping of ammonia

The simplest experiment that can be performed once a packet of molecules is loaded into the ring decelerator, is guiding the molecules at a constant speed through the decelerator. The time-of-flight profiles of such measurements for NH_3 and ND_3 are shown as the purple traces in the upper left and upper right-hand side of Fig. 4.4, respectively. The ammonia molecules were decelerated from 300 to 90 m/s with the conventional Stark decelerator and guided at this velocity using the ring-type decelerator. The valve is triggered in such a way that the synchronous molecule has a total time-of-flight of 90 ms. For ND_3 , a second smaller peak, in addition to the peak at 90 m/s, is observed that arrives approximately 160 μs earlier than the main peak and is attributed to molecules that are two minima ahead of the synchronous molecule.

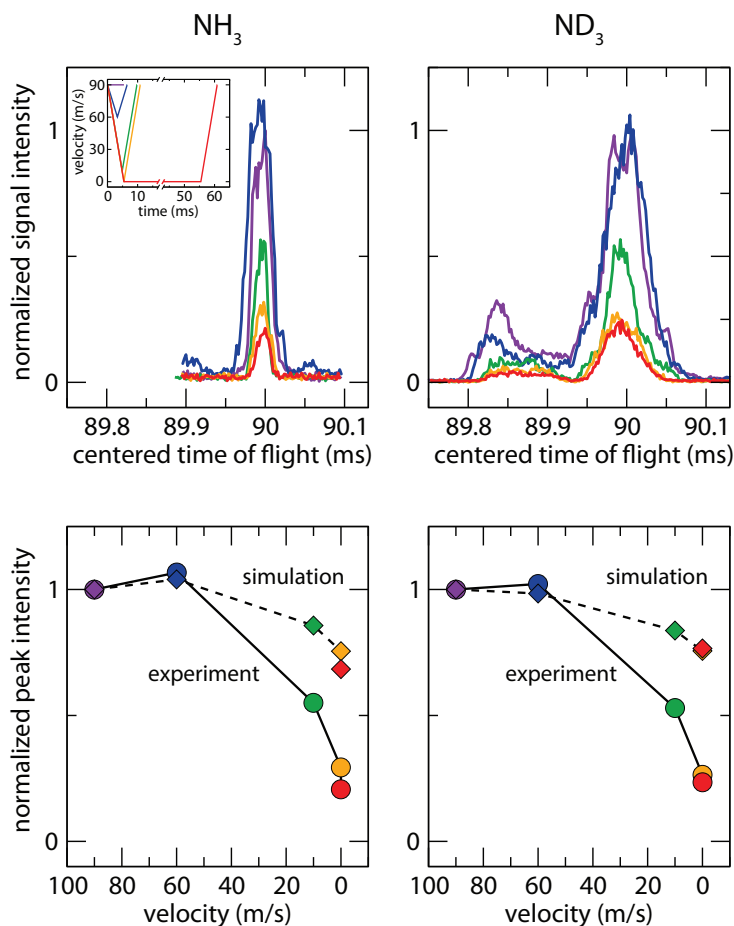


FIGURE 4.4: Upper panels: Measured time-of-flight profiles for NH_3 (left) and ND_3 (right) when molecules are guided at 90 m/s (purple curve), decelerated to 60, 30, and 0 m/s (blue, green and yellow, respectively) and decelerated to 0 m/s and trapped for 50 ms (red curve) before being accelerated back to 90 m/s and detected. The valve was triggered as to obtain a total time-of-flight of 90 ms. The inset shows the velocity of the electric field minimum as a function of time for the different recorded time-of-flight profiles, shown in the corresponding color. Lower panels: Measured and simulated peak intensity as function of the intermediate velocity for NH_3 (left) and ND_3 (right).

By adjusting the waveform that is applied to the electrodes, the molecules can be decelerated to an arbitrary velocity and accelerated back to their initial velocity. The relatively high outcoupling velocity ensures that the spreading of the packet during its free flight to the laser focus remains rather small. The blue, green and yellow traces in the upper left and upper right-hand side of Fig. 4.4 are time-of-flight profiles of NH_3 and ND_3 molecules, respectively, that are decelerated from 90 m/s to 60, 10, and 0 m/s

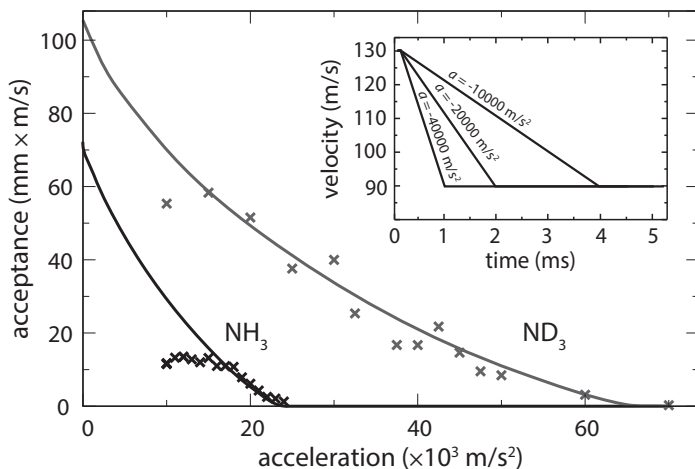


FIGURE 4.5: Integrated time-of-flight distributions for NH_3 and ND_3 shown as a function of acceleration. The solid curves correspond to the 1D acceptance of the ring-type decelerator. The inset displays three typical deceleration schemes.

and accelerated back to 90 m/s. It is seen that the shape of the distribution slightly changes, which can be attributed to the fact that the phase space matching between deceleration and acceleration is not perfect.

The maximum acceptance of the ring decelerator depends on the size of the effective trap and thus on the acceleration applied to the waveform. As a consequence, the signal decreases slightly for velocities lower than 60 m/s, as can be seen in Fig. 4.4. However, almost no additional losses occur once the molecules are trapped by the electric fields of the decelerator. This is illustrated by the red curves in the upper panels of Fig. 4.4, which corresponds to the time-of-flight profile of a packet of NH_3 and ND_3 molecules that were trapped for 50 m/s at the center of the ring-type decelerator. This trapping time is only limited by the current repetition rate of the experiment (10 Hz). In the lower panels of Fig. 4.4, experimental (circles) peak intensities of the time-of-flight profiles are compared to simulated ones (diamonds). It can be seen that the simulated acceptance is up to three times larger than the acceptance of the actual measurement. We attribute the loss mainly to mechanical misalignments that lead to parametric amplification of the motion of the trapped molecules at low velocities. On inspection, we noticed that one of the suspension bars was slightly displaced from its original position when the decelerator was placed in the vacuum chamber. Another loss mechanism comes from the fact that the phase-space distribution of the packet exiting the conventional Stark decelerator is not perfectly matched to the acceptance of the traveling wave decelerator. As a result the trapped packet will perform a (damped) breathing motion, similar to Fig. 4.6. This oscillation explains why the observed TOF profile for deceleration to 60 m/s is wider and more intense than the TOF profile for guided molecules. Both loss mechanisms are not fundamental and we believe they can be eliminated in future work.

The decrease of the effective trap depth with increased acceleration is demonstrated in some more detail in Fig. 4.5. In this figure, the time-integrated density of ammonia molecules is plotted as a function of the applied acceleration. In these measurements, ammonia molecules are guided at 90 m/s for 5 mm before being accelerated to 130 m/s and guided at 130 m/s for the remaining length of the decelerator.

In a ring-type decelerator the acceptance in the transverse direction is almost independent of the used acceleration and in all cases much bigger than the transverse emittance of the conventional Stark decelerator. Hence, we choose to compare the measurement to the numerically determined longitudinal acceptance of the ring-type decelerator shown as the solid curves in Fig. 4.5. As can be observed, at high acceleration the measurements follow the simulated curves quite well. At lower accelerations, however, the measurements are seen to reach a constant value which is consistent with the expected longitudinal acceptance of the conventional Stark decelerator at the used phase angle of 65 degrees [85]. At these accelerations the longitudinal acceptance of the ring-type decelerator is larger than the longitudinal emittance of the packet exiting the Stark decelerator; i.e., all molecules exiting the conventional Stark decelerator are in fact trapped in the ring-type decelerator.

The fraction of molecules that remains confined after the acceleration process has a lower velocity spread than the initial guided packet. In principle, the reduction in the velocity spread of the trapped packet of molecules should be apparent as a narrowing in the time-of-flight profile of the detected packet. However, such a reduction in the width of the time-of-flight distribution has been observed only for NH_3 molecules. This is attributed to imperfect phase-space matching that heats up the ND_3 molecules when they are accelerated from the trap.

4.4.2 Phase-space matching

According to Liouville's theorem, the number of particles per unit volume in six-dimensional phase-space is conserved for conservative and differentiable forces, such as those that derive from time-varying electric fields [114]. Although the density of the phase-space volume is constant in time, it may decrease when the molecules are transferred from the conventional Stark decelerator to the ring decelerator [31]. Hence, in order to maintain the phase-space density of the molecular packet throughout the entire deceleration process, it is important to properly map the phase-space emittance of the conventional Stark decelerator onto the phase-space acceptance of the ring decelerator. The phase-space coupling of the packet of molecules from the conventional Stark decelerator into the ring decelerator is illustrated in Fig. 4.6. Using the conventional decelerator with a typical phase angle of $\phi_0 = 60^\circ$, ammonia molecules are decelerated from 300 to 100 m/s, while the ring decelerator is used for guiding. From the figure it can be seen that the phase-space distribution for a decelerated packet of molecules is highly structured. This effect is well-known and is caused by coupling between longitudinal and transverse motion in the conventional Stark decelerator [115]. In the time that the molecules fly from the end of the conventional Stark decelerator to the entrance of the ring decelerator, the packet rotates in phase space. In Fig. 4.6, the outermost solid curve indicates the phase space acceptance of the ring decelerator

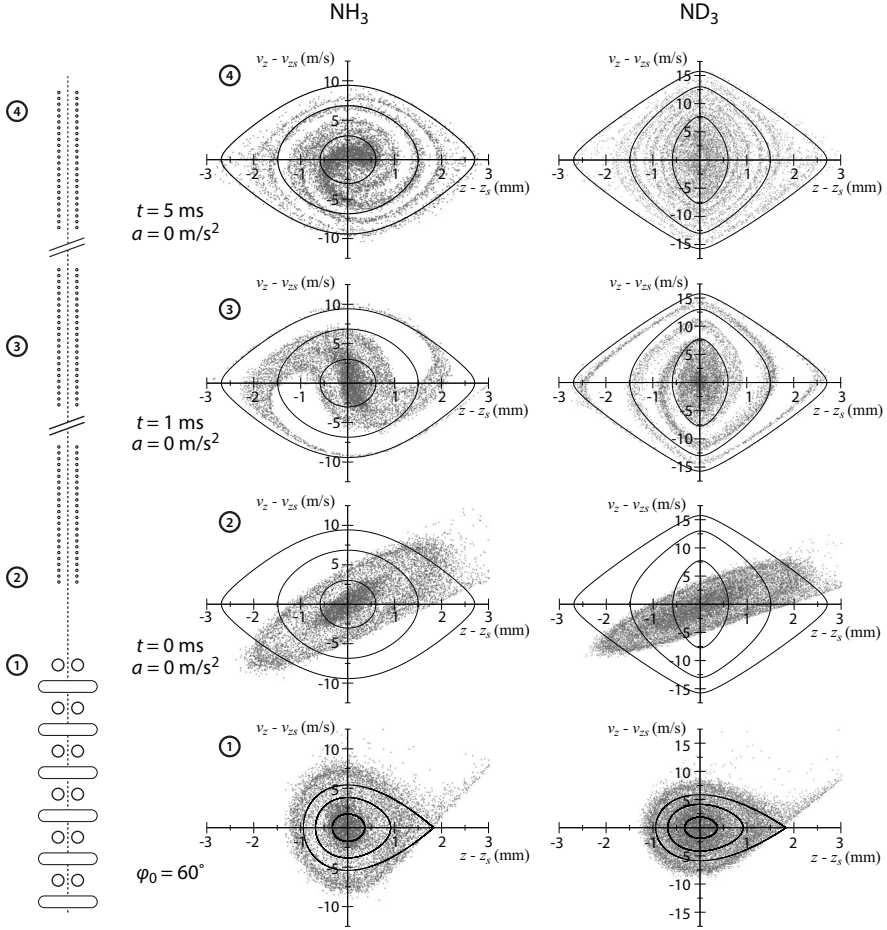


FIGURE 4.6: Phase-space diagrams for NH_3 (left) and ND_3 (right) at different times and positions in the deceleration process. Ammonia molecules are decelerated from 300 to 100 m/s with the conventional Stark decelerator and guided through the ring decelerator at a constant speed of 100 m/s. (1) Longitudinal phase-space diagram for a packet of molecules at the end of the conventional Stark decelerator. (2) During the free flight to the beginning of the ring decelerator the packet of molecules rotates in phase space. (3) After 1 ms of guiding the molecules have clearly spiraled. Note that the angular frequency for ND_3 is much larger than that of NH_3 resulting in more evolutions of the packet in phase space. (4) At the end of the ring decelerator, the spiral structure is still apparent for NH_3 , whereas for ND_3 all substructure is blurred almost entirely.

and from this it can be seen that the loading process of the slow packet into the ring decelerator is imperfect in two different ways: (i) The emittance of the conventional decelerator is (slightly) larger than the acceptance of the potential. This leads to a loss of molecules, but not to a decrease in phase-space density [31]. (ii) The emittance of

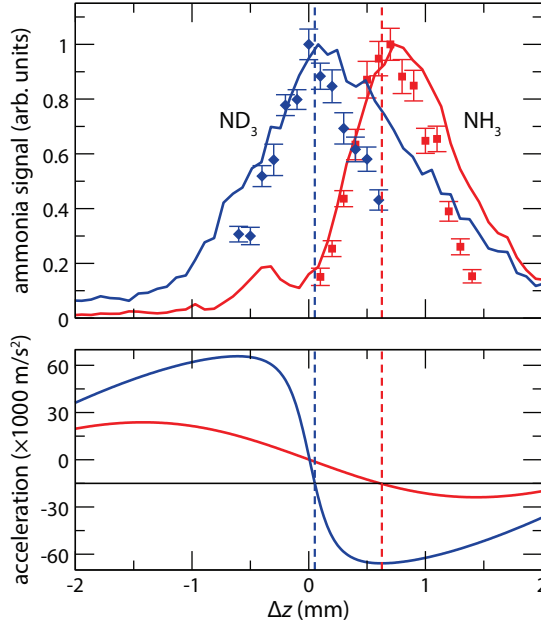


FIGURE 4.7: The effect of phase jumps for an acceleration of $-15\,000 \text{ m/s}^2$ are illustrated in the upper panel for NH_3 (squares) and ND_3 (diamonds). Solid curves show the result of a 1D numerical simulation. The lower panel shows the longitudinal acceleration along the beam axis for NH_3 and ND_3 molecules using a waveform amplitude of 5 kV. The dashed vertical lines indicate the phase jumps that are derived from the acceleration curves in the lower panel.

the conventional decelerator and the acceptance of the ring decelerator have a different shape in phase-space. As a result, the beam will start to spiral in the potential well, which will lead to an effective decrease in phase-space density [31]. Moreover, the spiralling of the packet introduces an oscillation in the detected signal as a function of time. This can be explained by the fact that as the packet evolves for different times in the trap, it creates effective spatial or velocity foci at the detector.

4.4.3 Phase jumps

Phase-space matching is not only important when the molecules are coupled into the ring decelerator, it is also required when the molecules are located inside the ring decelerator and a time-dependent acceleration is applied to the waveform. The shape of the effective potential, and hence the phase-space acceptance of the ring decelerator, depends strongly on the acceleration applied to the waveform and on the Stark energy of the investigated molecules. This effect should be taken into account when the acceleration is not constant but a function of time, for instance, when the molecules are decelerated to a standstill, trapped and accelerated again to their initial velocity. When the molecules are guided, the effective trap center is located at the position of

maximum electric field strength. However, when the waveform is set to decelerate the molecules, the position of the effective trap center shifts in the positive z direction. As a consequence, the phase space distribution of the guided packet of molecules is not properly matched to the phase-space acceptance of the deceleration process. The shift in effective trap position with respect to the synchronous molecule, Δz , can be compensated for by sweeping instantly the phase of the waveform in such a way that the trapping potential shifts an equal amount in the opposite direction. We will refer to this sweep as a “phase jump”. However, in practice this phase jump cannot be applied instantaneous and a finite time t_{jump} is required to adjust the waveform. During this time the synchronous molecule will travel a distance $v_z t_{\text{jump}}$, and this distance needs to be accounted for. Hence, the total phase jump follows from

$$z_{\text{jump}} = v_z t_{\text{jump}} - \Delta z. \quad (4.17)$$

The value of Δz depends on the Stark energy of the molecules and can be deduced from a simple one-dimensional model involving the longitudinal acceleration along the molecular beam axis. The lower panels in Fig. 4.7 show the acceleration for NH_3 (left panel) and ND_3 (right panel) molecules as a function of the displacement from the center of the trap. The horizontal lines correspond to accelerations of $\pm 10\,000$ and $\pm 15\,000$ m/s^2 for NH_3 and ND_3 , respectively. The values of Δz follow from the intercepts of these lines with the acceleration curve and are indicated by the dashed vertical lines.

The upper panel of Fig. 4.7 illustrates the effect of the applied phase jump on the signal intensity for NH_3 (squares) and ND_3 (diamonds). In these measurements, ammonia molecules were initially guided at 70 m/s and decelerated to a standstill using an acceleration of $-15\,000$ m/s^2 . The molecules were decelerated back to 70 m/s using the opposite acceleration and guided through the remainder of the traveling-wave decelerator. A phase jump was applied every time the chirp of the waveform changed. From the figure it can be seen that both isotopologues require a different phase jump to obtain the highest signal density. For ND_3 the optimal phase jump corresponds to a shift in the position of the trap center of about $50\ \mu\text{m}$, whereas for NH_3 the optimal phase jump corresponds to a shift of $0.6\ \text{mm}$. This effect can be explained by the differences in the trap depth and shape between NH_3 and ND_3 . The lower panel of Fig. 4.7 shows the longitudinal acceleration along the beam axis for NH_3 and ND_3 molecules using a waveform amplitude of 5 kV . The electric field increases linearly away from the center of the trap resulting in a harmonic potential for NH_3 , which experience a quadratic Stark shift, and a strong and anharmonic potential for ND_3 , which experiences a linear Stark shift. Hence, the shift of the effective trap center for NH_3 molecules at a certain acceleration is much larger than the shift of the effective trap center for ND_3 molecules at the same acceleration. The dashed vertical lines in Fig. 4.7 indicate the phase jumps that are derived from the acceleration curves in the lower panel.

The solid curves in the upper panel Fig. 4.7 show the result of a 1D numerical simulation. Although the simulations seem to slightly overestimate the width of the observed peaks, the maximum and overall shape correspond fairly well with the experiment.

4.4.4 Parametric resonances

Parametric excitation [116] is a technique that is routinely applied to characterize atom and ion traps [117–120]. Here we apply this technique to a sample of polar molecules trapped in static electric fields. The classical theory of parametric excitation in the context of a harmonic oscillator with time-varying potential is presented by Landau and Lifshitz [116], here we only summarize their results. If a particle in a one-dimensional harmonic potential along the z direction is driven by an additional time-dependent force, the equation of motion takes the form

$$\frac{d^2z}{dt^2} + \omega_z^2 z = F_z \cos(\omega t)z, \quad (4.18)$$

where ω_z is the Eigen frequency of the potential, F_z is the amplitude of the time-dependent force, and ω is its frequency. This equation can be transformed into the Mathieu equation, which has well-known stable and unstable regions for different parameter values. Evaluation of Eq. (4.18) predicts the existence of a primary resonance at $2\omega_z$ and higher-order resonances at a fraction of the primary resonance, that is $2\omega_z/n$, with $n = 2, 3, 4, \dots$. Note that anharmonicities in the trapping potential may give rise to combination frequencies at sufficient excitation [116].

A one-dimensional excitation like this can be realized in the ring-type decelerator by varying the phase of the waveform sinusoidally once the molecules are trapped. In this way the trap is effectively shaking in the longitudinal direction, and only the longitudinal motion is excited. However, it is much more interesting to excite the radial and longitudinal motions in the trap simultaneously, which can be accomplished by varying the amplitude of the waveform once the molecules are trapped. Note that this excitation scheme may also give rise to coupled resonances.

The trapping potential of the ring decelerator approximates a quadrupole field and therefore accommodates a longitudinal eigen frequency that is about a factor of two larger than the radial eigen frequency. Away from the center of the trap, these frequencies decrease or increase slightly, depending on the longitudinal position of the trap center. Recall that the radial eigen frequency is a periodic function of the phase, whereas the longitudinal eigen frequency remains rather constant over the entire length of the decelerator.

Typical spectra for NH_3 (upper) and ND_3 (lower, offset for clarity) molecules that are trapped in the plane of a ring are shown as the solid squares in Fig. 4.8. These spectra were obtained by modulating the DC amplitude of the waveform with an external oscillatory voltage while the molecules are trapped. For the measurements of NH_3 and ND_3 the amplitude of the sinusoidal voltage was set to 400 and 800 V, respectively. In this way both the longitudinal and radial resonances are excited, resulting in a number of mixed resonances. When the frequency of the external voltage matches a characteristic frequency of a trapped molecule, the amplitude of the motion of the molecule inside the trap is increased. As a result, molecules are lost from the trap. The excitation scans are recorded in two situations. In the first case, shown as the red data points, molecules are decelerated and subsequently trapped for 30 ms before the excitation voltages are applied, after which they are accelerated and detected. In the second case, shown as the

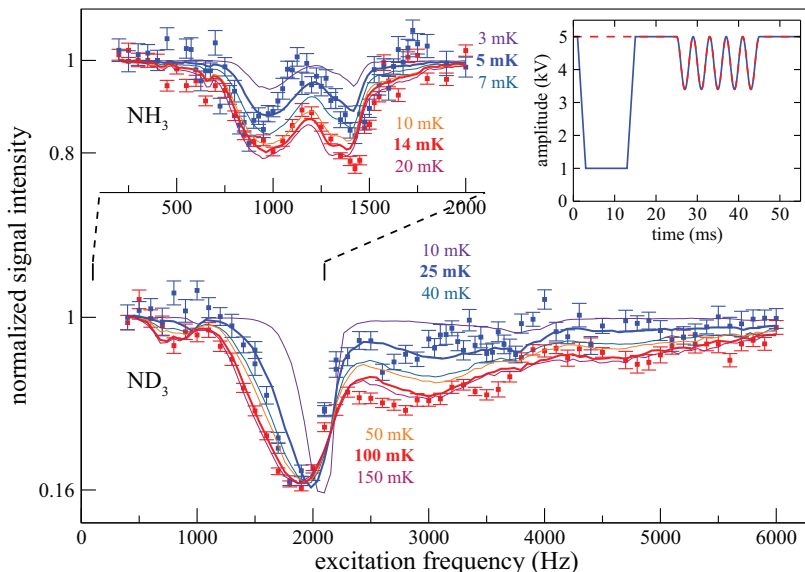


FIGURE 4.8: Fractional trap loss as a function of excitation frequency for ND_3 (lower) and NH_3 (upper, offset for clarity). The blue and red data points correspond to the amplitude manipulation shown in the inset. The solid curves are 3D simulations that assume a (truncated) thermal distribution with temperatures as indicated in the figure.

blue data points, the trap voltages are first lowered to 1 kV for a period of 10 ms before the excitation voltages are applied, allowing the hottest molecules to escape the trap. The amplitude and frequency of the waveform for both cases is shown in the inset.

Due to the anharmonicity of the trap, the width of the observed resonances depends strongly on the effective temperature of the trapped ensemble of molecules. The solid red and blue curves, show a simulation assuming a (truncated) thermal distribution with temperatures as indicated in the figure. Note that, strictly speaking, a temperature is not defined as the densities are not large enough to have thermalization on the timescales of the experiment. We use temperature here only as a convenient means to describe the distribution. From these simulations we assign a temperature of 14 mK to the trapped NH_3 molecules. By lowering the trap depth this temperature decreases to about 5 mK. In the case of ND_3 the estimated temperatures are much higher (100 mK and 25 mK) due to the fact that the traps for ND_3 are much steeper than for NH_3 . Note that, when the trap center is located in the plane of a ring electrode, a waveform amplitude of 5 kV results in a trapping potential with a depth of 30 mK for NH_3 and 160 mK for ND_3 . The simulations thus seem to indicate that the trap for ND_3 molecules is almost saturated. Further it should be noted that the estimated temperatures depend slightly on the adopted parameters for the simulation.

4.5 Conclusions

In this chapter, we demonstrated decelerating and trapping of NH_3 and ND_3 molecules in a ring decelerator. Observed trapping times are limited only by the current repetition rate of the experiment. The deceleration of a supersonic beam of ammonia molecules is performed in two steps; in the first step, the molecules are decelerated from 300 to 100 m/s using a conventional Stark decelerator, while in the second step, the ring decelerator is used to remove the remaining kinetic energy from the molecules. The advantages of such a system are that the requirements imposed on the electronics of the ring decelerator remain rather low and that the combined length of both decelerators is less than 2 m.

Once the molecules are loaded into the ring decelerator, the motion of the molecules can be controlled completely by computer generated waveforms. As an example of the possibilities offered by this setup, we characterized the trapping potential of the ring decelerator before and after manipulating the phase-space distribution of the trapped molecules. In addition we assign a temperature to the trapped sample of molecules before and after the phase-space manipulation.

The main motivation for this setup is to use the combination of the two Stark decelerators as a source of cold molecules for a molecular fountain. Previous attempts to create a fountain using a conventional Stark decelerator were unsuccessful due to losses at low velocities and a complex lens system for applying phase manipulation. The presented setup should solve both of these issues.

METHANOL AS A SENSITIVE PROBE FOR SPATIAL AND TEMPORAL VARIATIONS OF THE PROTON-TO-ELECTRON MASS RATIO

The 6.7 and 12.2 GHz masers, corresponding to the $5_1 \rightarrow 6_0 A^+$ and $2_0 \rightarrow 3_{-1} E$ transitions in methanol (CH_3OH), respectively, are among the brightest radio objects in the sky. We present calculations for the sensitivity of these and other transitions in the ground state of methanol to a variation of the proton-to-electron mass ratio. We show that the sensitivity is greatly enhanced due to a cancellation of energies associated with the hindered internal rotation and the overall rotation of the molecule. We find sensitivities of $K_\mu = -42$ and $K_\mu = -33$, for the $5_1 \rightarrow 6_0 A^+$ and $2_0 \rightarrow 3_{-1} E$ transitions, respectively. The sensitivities of other transitions in the different isotopologues of methanol range from -88 to 330 . This makes methanol a sensitive probe for spatial and temporal variations of the proton-to-electron mass ratio.

5.1 Introduction

A possible spatial or temporal variation of the fine structure constant, α , or the proton-to-electron mass ratio, μ , can be detected by comparing transitions in atoms and molecules as a function of time and/or position. As these transitions have, in general, a different dependence on α and μ , a possible variation might be observed as a shift of the transition frequencies [65, 121]. In astrophysical searches, the frequencies of two or more atomic and molecular absorptions from distant objects are compared with the frequencies as measured in the laboratory. This allows one to determine the apparent redshift – and hence distance to the object – and a possible variation. In this Chapter, we discuss the use of molecules to detect a variation of μ . The sensitivity of an experiment searching for a frequency shift $\Delta\nu$ due to the variation of μ depends both on the size of

the shift, i.e., the inherent sensitivity of the molecular transition, and on the ability to measure this shift. As a measure for the inherent sensitivity of a transition, the sensitivity coefficient K_μ is defined via

$$\frac{\Delta\nu}{\nu} = K_\mu \frac{\Delta\mu}{\mu}. \quad (5.1)$$

For a sensitive test, one needs molecular transitions that are observed with a good signal to noise, and that exhibit high K_μ . Transitions in hydrogen, the most abundant molecule in outer space, and observed at high redshift ($z = 3$), have sensitivities that range from $K_\mu = -0.02$ to $+0.05$ [11, 65, 122]. Rotational transitions in CO, the second most abundant molecule in space, have a sensitivity of $K_\mu = -1$. The inversion frequency in ammonia is exponentially dependent on μ . As a consequence, the inversion frequency in ammonia has a sensitivity of $K_\mu = -4.2$ [45, 46, 71].

It was noticed by Flambaum [123], Flambaum and Kozlov [124], DeMille *et al.* [125], and Bethlem and Ubachs [126] that the sensitivity to a variation of α and μ is enhanced when an accidental degeneracy occurs between levels which have substantially different dependences on α and μ – for instance, when rotational splittings are equal to a hyperfine structure splitting [123] or fine structure splitting [126] or when a vibrational splitting is equal to a fine structure splitting [124] or an electronic splitting [125]. However, the molecular transitions discussed in these papers are unlikely to be observed in interstellar objects. In this chapter, we show that a significant enhancement occurs in methanol due to a cancellation of energies associated with the hindered internal rotation and the overall rotation of the molecule. This is particularly relevant as methanol is abundantly present in the Universe.

5.2 Molecular structure of methanol

Methanol is one of the simplest molecules that exhibits hindered internal rotation and has, therefore, been the subject of numerous experimental and theoretical studies [127–133]. The structure of methanol, depicted on the right-hand side of Fig. 5.1, consists of a methyl group, with a hydroxyl group attached. The center of mass of the OH group is slightly displaced from the symmetry axis of the methyl group. The overall rotation is described by three rotational constants A , B , and C , associated with the moments of inertia I_a , I_b , and I_c , respectively, along the three principal axes. The total angular momentum of the molecule is given by the quantum number J , while the projection of J onto the molecule fixed axis is given by K .

In addition to the overall rotation, methanol has internal rotation; the OH group rotates with respect to the methyl group. The angle between the two parts of the molecule is denoted by γ . The rotation is severely hindered, due to the repulsion of a threefold torsional potential energy curve, shown on the left-hand side of Fig. 5.1. The vibrational levels in this well are denoted by ν_t . In lowest order – neglecting higher orders in the potential and centrifugal distortions – the Hamiltonian can be written as [127]

$$H = \frac{1}{2} \frac{P_a^2}{I_a} + \frac{1}{2} \frac{P_b^2}{I_b} + \frac{1}{2} \frac{P_c^2}{I_c} + \frac{1}{2} \frac{1}{I_{\text{red}}} p_\gamma^2 + \frac{1}{2} V_3 (1 - \cos 3\gamma), \quad \text{with} \quad I_{\text{red}} = \frac{I_a I_{a2}}{I_a}. \quad (5.2)$$

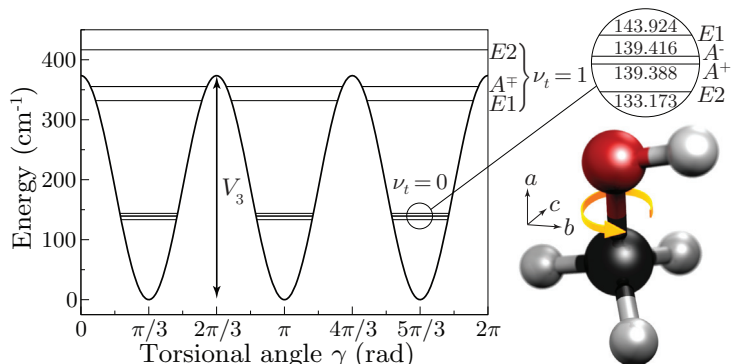


FIGURE 5.1: Variation of the potential energy of methanol with the relative rotation γ of the OH group with respect to the methyl group about the molecular axis. Shown are the $J = 1, |K| = 1$ energies of the lowest torsion-vibrational levels. The splitting between the different symmetry levels is due to tunneling through the potential barriers. The A symmetry species are split further due to the asymmetry of the molecule (K splitting).

The first three terms describe the overall rotation around the a , b , and c axis, respectively. The fourth term describes the internal rotation around the a axis, with I_{red} the reduced moment of inertia along the a axis, I_{a2} the moment of inertia of the methyl group along its own symmetry axis, and I_{a1} the part of I_a that is attributed to the OH group; $I_{a1} = I_a - I_{a2}$. The fifth term is the lowest order term arising from the torsional potential. If the torsional potential were infinitely high, the threefold barrier would result in three separate harmonic potentials, with rotational energies corresponding to the harmonic oscillator eigenvalues. In the case of a finite barrier, quantum-mechanical tunneling mixes the levels in the different wells of the potential. As a result, every K level is split into three levels, which can be labeled according to torsional symmetry, T_s , as A, E1, or E2. Following Lees [129], E1 and E2 symmetries are labeled by the sign of K ; i.e., levels with E1 symmetry are denoted by a positive K value, whereas levels with E2 symmetry are denoted by a negative K value. For $K \neq 0$, A levels are further split into + and – components by molecular asymmetry. For $K = 0$, only single E and A⁺ levels exist. The tunneling motion in the torsional potential is similar to the inversion motion in ammonia, which exhibits an increased sensitivity to a possible variation of the proton-to-electron mass ratio [45, 46]. This similarity prompted us to study the methanol spectrum. In Fig. 5.2, the lowest energy levels of $^{12}\text{CH}_3^{16}\text{OH}$ are shown.

5.3 Sensitivity coefficients

The splitting between the different symmetry levels is related to the tunneling frequency between the different torsional potential wells, and, hence, it is very sensitive to the reduced moment of inertia. In Fig. 5.3, the energy splittings between A and E levels of the $J = 0, K = 0$ and the energy splitting between E1 and E2 levels in the $J = 1, |K| = 1$ are plotted as a function of the reduced moment of inertia I_{red} along the a axis for six

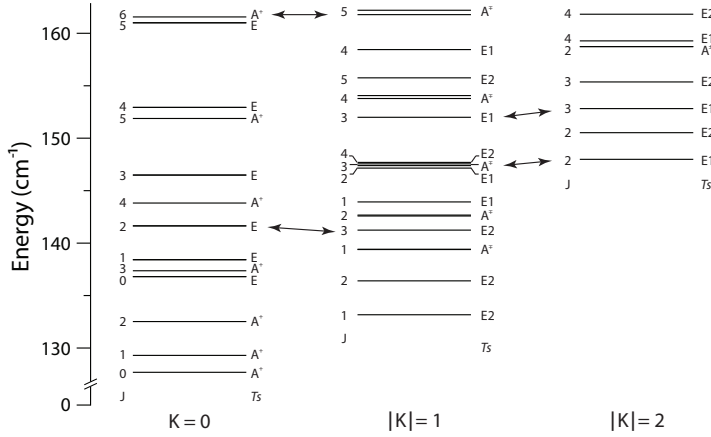


FIGURE 5.2: Energy of the lowest rotational levels in the torsion-vibrational ground state ($v_t = 0$) of methanol [133]. The levels are denoted by J and K and by their torsional symmetry T_s .

different isotopologues of methanol [133]. In analogy with ammonia [45], we expect the tunneling splitting to follow the formula

$$W_\gamma = \frac{a_0}{\sqrt{I_{\text{red}}}} e^{-a_1 \sqrt{I_{\text{red}}}}, \quad (5.3)$$

with W_γ the energy splitting due to hindered rotation and a_0 and a_1 constants. The fitted lines in Fig. 5.3 correspond to $a_0 = 316$ and $433 \text{ cm}^{-1}(\text{amu} \text{ \AA}^2)^{1/2}$ and $a_1 = 4.9$ and $5.1(\text{amu} \text{ \AA}^2)^{-1/2}$ for $K = 0$ and $|K| = 1$, respectively.

If we assume that possible variations of the proton and neutron masses scale in a similar manner, the reduced moment of inertia is directly proportional to μ . Thus, the sensitivity coefficient is given by

$$K_\mu^{\text{tors}} = \frac{I_{\text{red}}}{W_\gamma} \frac{\partial W_\gamma}{\partial I_{\text{red}}}. \quad (5.4)$$

From the above fits, we find for the $K = 0$ and $|K| = 1$ splitting a sensitivity coefficient of $K_\mu^{\text{tors}} = -2.4$ and $K_\mu^{\text{tors}} = -2.5$, respectively.

In the case of ammonia, the tunneling frequency can be directly measured by inducing a transition between the two inversion levels. In the case of methanol, however, the different torsional levels of a specific J, K state have different torsional symmetries, and transitions between these levels are not allowed. Hence, we look for rotational transitions between levels which differ in K and/or J . The sensitivity coefficients of these transitions are given by

$$K_\mu (v_t'', J'', K'', Ts'' \rightarrow v_t', J', K', Ts') = \frac{\mu (\partial E / \partial \mu)_{v_t'', J'', K'', Ts''} - \mu (\partial E / \partial \mu)_{v_t', J', K', Ts'}}{E(v_t'', J'', K'', Ts'') - E(v_t', J', K', Ts')}, \quad (5.5)$$

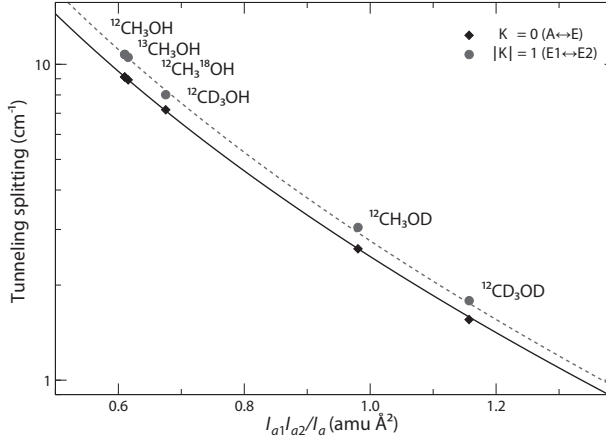


FIGURE 5.3: Energy splitting between A and E levels of the $J = 0, K = 0$ (diamonds) and the energy splitting between $E1$ and $E2$ levels of the $J = 1, |K| = 1$ (circles) as a function of the reduced moment of inertia along the a axis for six different isotopologues of methanol [133]. The solid and dashed lines are fits according to Eq. (5.3).

with

$$\mu \left(\frac{\partial E}{\partial \mu} \right)_{v_t, J, K, T_s} = K_{\mu}^{\text{vib}} E_{\text{vib}} + K_{\mu}^{\text{rot}} E_{\text{rot}} + K_{\mu}^{\text{tors}} E_{\text{tors}}, \quad (5.6)$$

where K_{μ}^{vib} , K_{μ}^{rot} , and K_{μ}^{tors} are the sensitivities to a possible variation of the proton-to-electron mass ratio of a vibrational, rotational, and torsional energy level, respectively. In the first-order approximation $K_{\mu}^{\text{vib}} = -\frac{1}{2}$ and $K_{\mu}^{\text{rot}} = -1$. Equation (5.5) suggests that the sensitivity is enhanced for transitions between near degenerate levels. In Fig. 5.2 some of these transitions have been indicated. Let us, for instance, look at the $5_1 \rightarrow 6_0 A^+$ transition, which corresponds to the strong 6.7 GHz maser line that is observed in many interstellar objects. Using the known energies of the rotational levels and $K_{\mu}^{\text{tors}} = -2.4$, we find $K_{\mu} = -41$. Similarly, for the $2_0 \rightarrow 3_{-1} E$ transition, which corresponds to the 12.2 GHz maser line, we find $K_{\mu} = -33$.

5.4 Numerical results

In order to validate this simple model, we have simulated the methanol level energies using BELGI [134]. This code was modified and improved by Xu *et al.* in a number of ways useful for treating the large data sets available for the methanol molecule [133]. Note that, rather than the Hamiltonian given in Eq. (5.2), BELGI uses an axis transformation (the so-called "Rho-Axis Method" or RAM) to simplify the calculation. This Hamiltonian is diagonalized in a two-step process to obtain the level energies. By

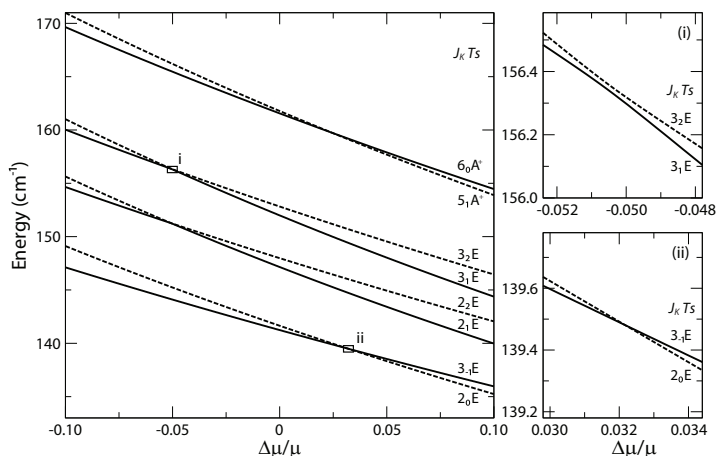


FIGURE 5.4: Energies of selected rotational levels as a function of the fractional change in the proton-to-electron mass ratio. The panels on the right-hand side of the figure show enlargements of selected crossings. It is seen that levels with same J give rise to avoided crossings, whereas levels with different J do not interact.

using a set of 119 molecular constants for $^{12}\text{CH}_3^{16}\text{OH}$ and 53 or more for the other isotopologues taken from Ref. [133], the lower energy levels are found typically with an accuracy < 50 kHz. In order to obtain the sensitivity to a variation of the proton-to-electron mass ratio of each level, the molecular constants are scaled using the relations given in Appendix A.

In Fig. 5.4, the energies of selected states (indicated in Fig. 5.2) are shown as a function of the fractional change of the proton-to-electron mass ratio. As expected, the energies of all rotational levels decrease for larger values of $\Delta\mu/\mu$. However, levels that have different J and K are seen to have a different dependence. The sensitivity coefficient for a transition connecting different levels is given by the difference of the slopes divided by their energy difference – in accordance with Eq. (5.5). Large sensitivity coefficients are expected when different levels cross in the vicinity of $\Delta\mu/\mu = 0$. If the levels cross at $\Delta\mu/\mu < 0$, K_μ will be positive; if the levels cross at $\Delta\mu/\mu > 0$, K_μ will be negative. Note that the behavior of the sensitivity coefficient very close to the resonance depends on the quantum numbers of the levels involved. For equal J , the levels will mix and K_μ goes to zero, whereas if the levels have unequal J , K_μ goes to infinity.

We have calculated the sensitivity coefficients for several transitions in the most common isotopologues of methanol. The most sensitive transitions involving levels with $J \leq 10$ are listed in Table 5.1. The error in the last digit of the K_μ coefficients is quoted in brackets. The error has 3 sources: (i) errors due to the uncertainty in the determination of the molecular constants, (ii) errors due to inexactness of the scaling relations of higher order constants, (iii) errors due to neglecting the μ dependence of the torsional potential. We estimate the error to be below 5% when $K_\mu \geq 1$ or below 0.05

when $K_\mu < 1$. It is seen that the values of the sensitivity coefficients for the $5_1 \rightarrow 6_0 A^+$ and $2_0 \rightarrow 3_{-1} E$ transitions agree well with those found using Eq. (5.5).

TABLE 5.1: Selected transitions and K_μ coefficients for different isotopologues of methanol, calculated with BELGI. All lines listed for $^{12}\text{CH}_3^{16}\text{OH}$ are observed as maser lines [132], except for the two lines marked with an asterisk. The error in the last digit(s) is quoted within brackets.

Isotopologue	Transition, J_K	Transition (MHz)	K_μ
$^{12}\text{CH}_3^{16}\text{OH}$	$1_1 \rightarrow 1_1 A^\mp$	834.280	-1.03(5)
	$3_1 \rightarrow 3_1 A^\mp$	5 005.302	-1.03(5)
	$5_1 \rightarrow 6_0 A^+$	6 668.567	-42.(2)
	$9_{-1} \rightarrow 8_{-2} E$	9 936.137	11.5(6)
	$5_2 \rightarrow 4_3 A^+$	9 978.718*	53.(3)
	$5_2 \rightarrow 4_3 A^-$	10 058.295*	52.(3)
	$2_0 \rightarrow 3_{-1} E$	12 178.587	-33.(2)
	$2_1 \rightarrow 3_0 E$	19 967.376	-5.9(3)
	$9_2 \rightarrow 10_1 A^+$	23 120.916	-11.7(6)
	$3_2 \rightarrow 3_1 E$	24 928.726	17.9(9)
	$2_2 \rightarrow 2_1 E$	24 934.399	17.9(9)
	$8_2 \rightarrow 9_1 A^-$	28 969.965	-9.5(6)
	$4_{-1} \rightarrow 3_0 E$	36 169.259	9.7(5)
	$6_2 \rightarrow 5_3 A^-$	38 293.273	-15.1(8)
	$6_2 \rightarrow 5_3 A^+$	38 452.632	-15.0(8)
	$7_0 \rightarrow 6_1 A^+$	44 069.364	5.2(3)
	$1_0 \rightarrow 2_{-1} E$	60 531.477	-7.4(4)
	$1_1 \rightarrow 2_0 E$	68 305.629	-2.4(1)
$^{12}\text{CD}_3^{16}\text{OH}$	$1_1 \rightarrow 2_2 E$	1 202.296	330.(20)
	$2_0 \rightarrow 1_1 E$	1 424.219	-42.(2)
	$9_2 \rightarrow 8_3 E$	2 827.262	43.(2)
	$5_1 \rightarrow 6_0 A^+$	2 971.067	93.(5)
	$4_{-1} \rightarrow 3_0 E$	4 011.340	-73.(4)
	$6_4 \rightarrow 5_5 E$	6 723.841	167.(8)
	$9_6 \rightarrow 10_5 A^+$	20 088.522	-88.(4)
	$9_6 \rightarrow 10_5 A^-$	20 088.522	-88.(4)
$^{12}\text{CH}_3^{18}\text{OH}$	$9_2 \rightarrow 10_1 A^-$	2 604.912	93.(5)
	$2_0 \rightarrow 3_{-1} E$	11 629.591	-34.(2)
$^{12}\text{CD}_3^{16}\text{OD}$	$1_0 \rightarrow 1_{-1} E$	2 237.883	45.(2)
	$7_{-4} \rightarrow 8_{-3} E$	2 329.088	-80.(4)
$^{13}\text{CH}_3^{16}\text{OH}$	$9_{-1} \rightarrow 8_{-2} E$	1 989.502	-63.(3)

5.5 Conclusions

It is important to note that the sensitivity coefficients of the transitions in Table 5.1 have both large positive and large negative values; i.e., if the proton-to-electron mass ratio varies, some transitions will shift to higher frequencies while others shift to lower frequencies. This makes it possible to perform a test of the variation of the proton-to-electron mass ratio using transitions in methanol only, thus avoiding the many systematic effects that plague tests based on comparing transitions in different molecules. Detection of methanol at even modest redshift will facilitate more stringent bounds on a possible variation of μ over cosmological time-scales. Darling *et al.* [131] have performed a dedicated survey for 6.7 GHz methanol maser emission in OH megamaser galaxies at $0.11 < z < 0.27$. No detections were made in the 25 observed objects.

The high sensitivity coefficients in methanol are also beneficial for probing variation of μ as a result of chameleonlike scalar fields. These fields predict a dependence of μ on the local matter density. Recently, Levshakov *et al.* [135] compared ammonia spectra taken at high (terrestrial) and low (interstellar) densities of baryonic matter and observed a statistically significant variation of μ . Using methanol, rather than ammonia, in these tests should result in an at least 1 order of magnitude increase in sensitivity.

Furthermore, methanol is a promising candidate for laboratory tests on a possible variation of μ . For instance, when combined, the $1_1 \rightarrow 2_2 E$ transition and the $4_{-1} \rightarrow 3_0 E$ transition in CD_3OH have a sensitivity that is more than 400 times larger than a pure rotational transition. Note that the large dipole moment and low mass make it possible to manipulate methanol molecules by using electric fields. The enhanced sensitivity for a variation of μ , due to a cancellation of energies associated with the hindered internal rotation and the overall rotation for methanol, should in principle occur in every molecule that exhibits internal rotation.

SENSITIVITY OF TRANSITIONS IN INTERNAL ROTOR MOLECULES TO A POSSIBLE VARIATION OF THE PROTON-TO-ELECTRON MASS RATIO

In Chapter 5, methanol was identified as a sensitive target system to probe variations of the proton-to-electron mass ratio μ . The high sensitivity of methanol originates from the interplay between overall rotation and hindered internal rotation of the molecule, that is, transitions that convert internal rotation energy into overall rotation energy, or vice versa, have an enhanced sensitivity coefficient, K_μ . As internal rotation is a common phenomenon in polyatomic molecules, it is likely that other molecules display similar or even larger effects. In this chapter we generalize the concepts that form the foundation of the high sensitivity in methanol and use this to construct an approximate model which makes it possible to estimate the sensitivities of transitions in internal rotor molecules with C_{3v} symmetry, without performing a full calculation of energy levels. We find that a reliable estimate of transition sensitivities can be obtained from the three rotational constants (A , B , and C) and three torsional constants (F , V_3 and ρ). This model is verified by comparing obtained sensitivities for methanol, acetaldehyde, acetamide, methyl formate and acetic acid with a full analysis of the molecular Hamiltonian. Of the molecules considered, methanol is by far the most suitable candidate for laboratory and cosmological tests searching for a possible variation of μ .

6.1 Introduction

Physical theories extending the Standard Model have presented scenarios that allow for, or even predict, spatiotemporal variations of the constants of nature [136]. Currently, a number of laboratory experiments and astronomical observations are conducted to search for signatures of such variations [137]. One of the dimensionless constants that

are hypothesized to vary is the proton-to-electron mass ratio, $\mu = m_p/m_e$. A variation of μ can be detected by comparing frequencies of spectral lines in molecules as a function of time and/or position. A fractional change in μ will manifest itself as a fractional frequency shift. As a measure for the inherent sensitivity of a transition, the sensitivity coefficient, K_μ , is defined by

$$\frac{\Delta\nu}{\nu} = K_\mu \frac{\Delta\mu}{\mu}. \quad (6.1)$$

From the mass dependence of the rotational and vibrational constants one can derive that $K_\mu = -1$ for pure rotational transitions and $K_\mu = -\frac{1}{2}$ for pure vibrational transitions, while $K_\mu = 0$ for pure electronic transitions [122]. Transitions between the inversion levels of ammonia [45, 46] and hydronium (H_3O^+) [138] have a sensitivity of $K_\mu = -4.2$ and $K_\mu = -2.5$, respectively. It was shown that the sensitivity of a transition between two near-degenerate levels that have a different functional dependence on μ is enhanced significantly [123–126, 138]. In Chapter 5, we discussed such an enhancement for torsional-rotational transitions in methanol.

Methanol (CH_3OH), schematically depicted in Fig. 6.1, consists of an OH group attached to a methyl group. The OH and methyl group may rotate with respect to each other about the C–O bond. On the left-hand side of the figure, the potential energy curve is shown as a function of the torsional angle, γ . The interaction between the OH and methyl group results in a threefold barrier. Tunneling between the three wells results in a splitting of each rotational level into three levels of different torsional symmetries [127]. Transitions between the different torsional levels have a sensitivity coefficient, $K_\mu = -2.5$. As the torsional levels *A* and *E* belong to different symmetries, transitions between them are not allowed. It was shown in Chapter 5 that transitions converting internal rotation energy into overall rotation energy, or vice versa, have sensitivity coefficients, K_μ , that range from -88 to +330 in the different isotopologues of methanol.

Hindered internal rotation is a common phenomenon found in many polyatomic molecules. Hence, other molecules may have similar or larger sensitivities to a variation of μ . In this chapter we calculate the sensitivities for methanol, acetaldehyde, acetamide, methyl formate, and acetic acid, five relatively small molecules that have a group of C_{3v} symmetry that rotates with respect to the remainder of the molecule. These five molecules have been detected in the interstellar medium of the local galaxy [139] and some at high redshift [64]. Methylamine, another relatively small internal rotor molecule is computationally more complex and will be treated in Chapter 7.

This chapter is organized as follows. In Section 6.2, we give a brief review of the theory of internal rotor molecules and outline how the torsional-rotational levels are numerically calculated using the BELGI code [134]. In addition, we present approximate expressions for obtaining the torsional energy splitting as function of the barrier height and the reduced moment of inertia, and compare this to the output of numerical calculations of a full Hamiltonian. In Section 6.3, we will discuss how the molecular constants that appear in the torsional-rotational Hamiltonian scale with μ . These scaling relations are then used to determine the sensitivities of selected transitions in five different internal rotor molecules using BELGI. In Section 6.4 the analytical expressions

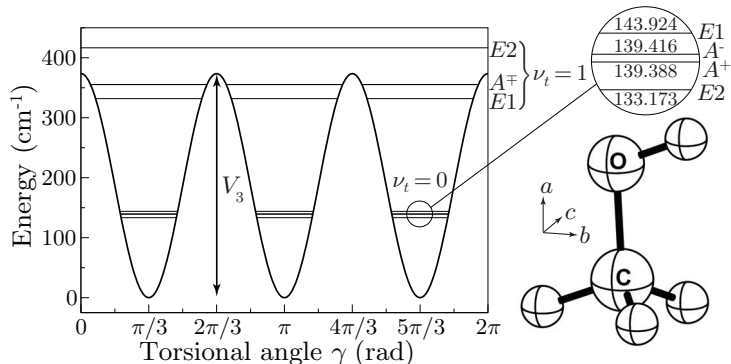


FIGURE 6.1: Variation of the potential energy of methanol as function of the relative rotation γ of the OH group with respect to the methyl group about the molecular axis. Shown are the $J = 1, |K| = 1$ energies of the lowest torsion-vibrational levels. The splitting between the different symmetry levels is due to tunneling through the potential barriers. The A-symmetry species are split further due to the asymmetry of the molecule (K splitting).

for the torsional energy splitting presented in Section 6.2 are used to construct a simple model for obtaining K_μ from the three rotational constants (A , B and C) and three torsional constants (F , V_3 and ρ). This model provides an intuitive picture of the physics involved and makes it straightforward to estimate the sensitivity of other internal rotor molecules.

6.2 Hindered internal rotation

A review of hindered internal rotation can be found in the seminal paper by Lin and Swalen [127], while a recent review of various effective Hamiltonians, methods, and codes dealing with asymmetric-top molecules containing one internal rotor with C_{3v} (or close to C_{3v}) symmetry can be found in the paper by Kleiner [140]. In this section we will summarize those results that are relevant for obtaining the sensitivity coefficients.

6.2.1 Hamiltonian

The potential energy of an internal rotor molecule is a periodic function of the torsional angle γ between the C_{3v} group and the remainder of the molecule, as shown in Fig. 6.1. Hence, it can be expanded in a Fourier series as

$$V(\gamma) = \frac{V_3}{2} (1 - \cos 3\gamma) + \frac{V_6}{2} (1 - \cos 6\gamma) + \dots, \quad (6.2)$$

where typically V_6 is about 100 times smaller than V_3 , but provides information on the shape of the torsional potential. If only the first term of the expansion is taken into account, the torsional wave functions and energies follow from the solutions of the Mathieu equation [127].

TABLE 6.1: Some low-order Hamiltonian terms for an asymmetric top containing a C_{3v} internal rotor and a partial parameter list as used in the BELGI code (taken from Kleiner [140] and rationalized by Xu). The μ dependence of the molecular constants is given in parenthesis. The product of the parameter and operator from a given row and column yields the term actually used in the torsion-rotation Hamiltonian of the fitting program, except for F , ρ , and A , which occur in the Hamiltonian in the form $F(P_\gamma + \rho P_a)^2 + AP_a^2$ (see text).

	Torsional/Potential						
	1 (μ^0)	$1 - \cos 3\gamma$ (μ^0)	P_γ^2 (μ^{-1})	$P_a P_\gamma$ (μ^0)	$1 - \cos 6\gamma$ (μ^0)	P_γ^4 (μ^{-2})	$P_a P_\gamma^3$ (μ^{-1})
Rotational							
1	(μ^0)	$V_3/2$	F	ρ	$V_6/2$	k_4	k_3
P^2	(μ^{-1})	$\frac{1}{2}(B+C)$	F_v	G_v	N_v	M_v	k_{3J}
P_a^2	(μ^{-1})	$A - \frac{B+C}{2}$	k_5	k_2	K_2	K_1	k_{3K}
$P_b^2 - P_c^2$	(μ^{-1})	$\frac{1}{2}(B-C)$	c_2	c_1	c_4	c_3	c_{12}
$P_a P_b + P_b P_a$	(μ^{-1})	D_{ab}	d_{ab}	Δ_{ab}	d_{ab6}	$\Delta \Delta_{ab}$	$\delta \delta_{ab}$

To express the kinetic part of the Hamiltonian an axis system (a, b, c) must be defined. The symmetric part of the molecule is defined as the internal rotor or top, whereas the remainder of the molecule is referred to as the frame, which for all molecules presented here has a plane of symmetry. The origin of the coordinate system coincides with the center of mass of the molecule. The a axis is chosen parallel to the symmetry axis of the top, and the b axis lies in the plane of symmetry. The c axis follows from the definition of a right-handed coordinate system. The inertia tensor then takes the form

$$\mathbf{I} = \begin{bmatrix} I_c & 0 & 0 \\ 0 & I_b & -I_{ab} \\ 0 & -I_{ab} & I_a \end{bmatrix}, \quad (6.3)$$

with $I_a = \sum_i m_i (b_i^2 + c_i^2)$ being the moment of inertia of the molecule about the a axis. The subscript i runs over all atoms with mass m_i in the molecule. Expressions for I_b and I_c , the moments of inertia around the b and c axis, respectively, can be found by cyclic permutation of the a , b and c labels. $I_{ab} = \sum_i m_i a_i b_i$ is the product of inertia about the a and b axis. The kinetic energy can be expressed as [127]

$$T = \frac{1}{2} I_a \omega_a^2 + \frac{1}{2} I_b \omega_b^2 + \frac{1}{2} I_c \omega_c^2 - I_{ab} \omega_a \omega_b + \frac{1}{2} I_{a2} \dot{\gamma}^2 + I_{a2} \omega_a \dot{\gamma}, \quad (6.4)$$

with ω_a , ω_b , and ω_c the angular velocity components around the a , b , and c axis, respectively, and I_{a2} the moment of inertia of the top along its own symmetry axis. For a given vibrational state, the zeroth-order torsion-rotation Hamiltonian can be separated into a symmetric top part, an asymmetric top part and a torsional part [130, 141]

$$H^0 = H_{\text{RS}}^0 + H_{\text{RA}}^0 + H_{\text{tors}}^0, \quad (6.5a)$$

where

$$H_{\text{RS}}^0 = \frac{1}{2} (B + C) (P_b^2 + P_c^2) + AP_a^2, \quad (6.5b)$$

$$H_{\text{RA}}^0 = \frac{1}{2} (B - C) (P_b^2 - P_c^2) + D_{ab} (P_a P_b + P_b P_a), \quad (6.5c)$$

$$H_{\text{tors}}^0 = F (p_\gamma + \rho P_a)^2 + V(\gamma). \quad (6.5d)$$

P_a , P_b , and P_c are the usual angular momentum operators along the a , b and c axis, respectively, and $p_\gamma = -i\partial/\partial\gamma$ is the angular momentum operator associated with the internal rotation of the top with respect to the frame. The coupling between the internal rotation and overall rotation in Eq. (6.5d) can be eliminated partly by transforming to a different axis system, the so-called “Rho-Axis System”. In the resultant “Rho-Axis Method” (RAM), which is implemented in the BELGI code used hereafter, the torsional Hamiltonian operator contains only the $+2F\rho P_a p_\gamma$ term. It is important to note here that two sign conventions are used in the literature for the torsion-rotation operator in Eq. (6.5d), that is, $F(p_\gamma + \rho P_a)^2$ and $F(p_\gamma - \rho P_a)^2$. If the latter convention is adopted the $\pm K$ labeling of the E levels (*vide infra*) is reversed [142]. Here, we adopt the convention with the “+” sign, that is, $F(p_\gamma + \rho P_a)^2$. The effective rotational and torsional constants are defined by

$$A = \frac{1}{2} \hbar^2 \left(\frac{I_a + I_b}{I_a I_b - I_{ab}^2} - \frac{I_b}{I_b^2 + I_{ab}^2} \right), \quad (6.6)$$

$$B = \frac{1}{2} \hbar^2 \frac{I_b}{I_b^2 + I_{ab}^2}, \quad (6.7)$$

$$C = \frac{1}{2} \hbar^2 \frac{1}{I_c}, \quad (6.8)$$

$$D_{ab} = \frac{1}{2} \hbar^2 \frac{I_{ab}}{I_b^2 + I_{ab}^2}, \quad (6.9)$$

$$F = \frac{1}{2} \hbar^2 \frac{I_a I_b - I_{ab}^2}{I_{a2} (I_{a1} I_b - I_{ab}^2)}, \quad (6.10)$$

where I_{a1} is the moment of inertia attributed to the frame, defined by $I_{a1} = I_a - I_{a2}$. A dimensionless parameter ρ is introduced by the axis transformation described earlier. For a symmetric top, ρ is simply defined as the ratio between the moment of inertia of the top divided by the moment of inertia of the molecule along the a -axis, that is, $\rho = I_{a2}/I_a$. For asymmetric molecules ρ is a more complicated function of the various moments of inertia:

$$\rho = \frac{I_{a2} \sqrt{I_b^2 + I_{ab}^2}}{I_a I_b - I_{ab}^2}. \quad (6.11)$$

The Hamiltonian of Eq. (6.5) can be expanded by adding additional distortion and interaction terms. Many of these higher-order constants multiply torsional operators by rotational operators and can be considered as effective constants after the van Vleck

transformations of the torsion-rotation Hamiltonian [128, 130, 140]. Some low-order symmetry-allowed torsion-rotation terms for an asymmetric top containing a C_{3v} internal rotor are listed in Table 6.1.

The overall Hamiltonian can now be written as

$$H = H^0 + H_{\text{int}} + H_{\text{c.d.}}, \quad (6.12)$$

where $H_{\text{c.d.}}$ corresponds to the centrifugal distortion Hamiltonian and H_{int} contains higher-order torsional-rotation interaction terms.

6.2.2 Eigenfunctions and eigenvalues

6.2.2.1 Torsion

Herbst *et al.* [130] suggested to evaluate the Hamiltonian of Eq. (6.12) in two steps. In the first step, the torsional Hamiltonian H_{tors}^0 is diagonalized in a product basis set composed of free rotor torsional eigenfunctions of p_γ and eigenfunctions $|K\rangle = (2\pi)^{-1/2} \times \exp(-iK\chi)$ of P_a , where χ is the Euler angle:

$$|Kk\sigma\rangle = \frac{1}{\sqrt{2\pi}} |K\rangle \exp(i[3k + \sigma]\gamma), \quad (6.13)$$

where σ can take the values -1 , 0 , or $+1$ and k can be any integer. The eigenvalues of p_γ are $3k + \sigma$ as required by the periodicity of the potential. Due to the symmetry of the torsional Hamiltonian, basis functions of different σ do not mix. Moreover, basis functions of different K do not mix either, as P_a and H_{tors}^0 commute. The resulting Hamiltonian matrix for each value of σ and K is infinite in size, but it was found that truncating it to a 21×21 matrix ($-10 \leq k \leq 10$) is sufficient to obtain experimental accuracy for the molecules under study here [130]. The torsional eigenfunctions can be written as

$$|K\nu_t\sigma\rangle = \frac{1}{\sqrt{2\pi}} |K\rangle \sum_{k=-10}^{10} A_{3k+\sigma}^{K,\nu_t} \exp(i[3k + \sigma]\gamma), \quad (6.14)$$

where ν_t is the torsional vibration quantum number and $A_{3k+\sigma}^{K,\nu_t}$ are expansion coefficients. States with $\sigma = 0$ are labeled as A , and states with $\sigma = +1$ and $\sigma = -1$ are labeled as $E1$ and $E2$, respectively. For A torsional states, $\pm K$ levels are degenerate, whereas for E states a degeneracy exists between $E1$, K and $E2$, $-K$ levels. Although the torsional $E1$ and $E2$ state have different labels, transitions between these two states are allowed. It was therefore suggested by Lees [129] to refer to $E1$ and $E2$ levels as E levels where the sign of K distinguishes the two symmetries.

The eigenvalues of the torsional Hamiltonian for methanol, acetaldehyde, and acetic acid are depicted in Fig. 6.2 as a function of K for the ground torsional state ($\nu_t = 0$) of those molecules. The solid circles, open circles, and open triangles represent values numerically calculated using the BELGI code [133, 134, 143, 144] for the A , $E1$, and $E2$ torsional states, respectively. It is seen that the torsional energies are periodic functions

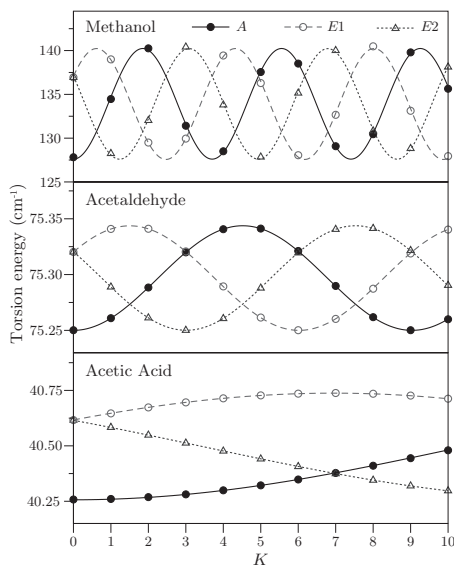


FIGURE 6.2: Torsional energies obtained with BELGI for A (solid circles), E1 (open circles), and E2 (open triangles) levels as function of K for methanol (CH_3OH), acetaldehyde (CH_3COH), and acetic acid (CH_3COOH) for $\nu_t = 0$. The solid curves are fits to Eq. (6.15) for A, E1, and E2 states. Note that only integer values of K have physical meaning.

of K with a period that is proportional to ρ^{-1} ($\rho = 0.81, 0.33$, and 0.07 for methanol, acetaldehyde, and acetic acid, respectively).

In order to obtain an analytical model for estimating the sensitivities of transitions in internal rotor molecules, discussed in Section 6.4, we now derive approximate solutions to the torsional Hamiltonian. It is clear from Eq. (6.14) that substituting σ with $\sigma + 3$ results in identical eigenvalues; consequently, the eigenvalues may be regarded as periodic functions which can be expanded in a Fourier series as [127]

$$E_{\text{tors}} = F \left[a_0 + a_1 \cos \left\{ \frac{2\pi}{3} (\rho K + \sigma) \right\} + \dots \right], \quad (6.15)$$

where a_0, a_1 and higher order terms are (dimensionless) expansion coefficients. It can be shown [127] that these coefficients are functions of the reduced barrier height s , with

$$s = \frac{4V_3}{9F}, \quad (6.16)$$

and that in the moderate-to-high-barrier limit, the series converges quickly. The solid curves shown in Fig. 6.2 are obtained by fitting the first two terms of Eq. (6.15) for A ($\sigma = 0$), E1 ($\sigma = +1$), and E2 ($\sigma = -1$) states. The resulting coefficients for methanol, acetaldehyde, and acetic acid, as well as those for acetamide and methyl formate, are plotted as the open diamonds in Fig. 6.3. By diagonalizing H_{tors}^0 for several values of s and $\rho > 0$, while all other constants are set to zero, and fitting the torsional energies according to Eq. (6.15), a_1 coefficients were obtained for each value of s . These

generic coefficients are plotted as the solid diamonds in Fig. 6.3. According to Lin and Swalen [127] the a_1 coefficients are given by the following equation:

$$a_1 = A_1 s^{B_1} e^{-C_1 \sqrt{s}}. \quad (6.17)$$

The solid line shown in Fig. 6.3 is obtained by fitting Eq. (6.17) to the generic a_1 values, using $A_1 = -5.296$, $B_1 = 1.111$, and $C_1 = 2.120$. Note that these fit parameters deviate from those given in Table IV of Ref. [127], but the curves agree with the curves shown in Fig 7 of the same paper. Small differences between the curves and the a_1 coefficients obtained for the different molecules can be attributed to higher order torsional terms which were not taken into account to obtain the fits.

6.2.2.2 Rotation

At this point the torsional Hamiltonian is diagonalized and the first step of the approach by Herbst *et al.* is complete. The second step of the approach consists of evaluating the remainder of the full Hamiltonian, that is, overall rotation and coupling terms, in the basis set [130]

$$|JKv_t\sigma\rangle = |JK\rangle|Kv_t\sigma\rangle, \quad (6.18)$$

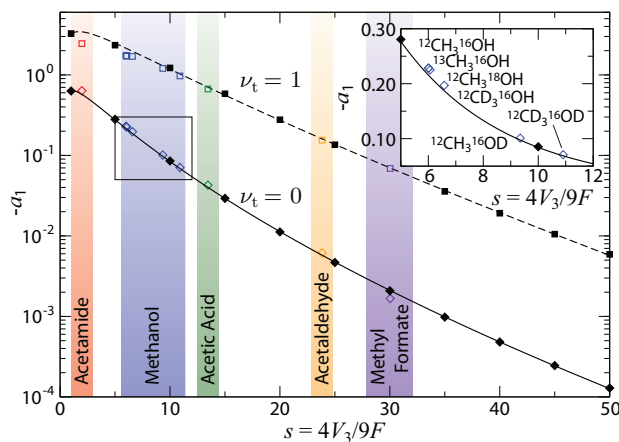


FIGURE 6.3: The a_1 expansion coefficients of Eq. (6.15) as a function of the reduced barrier height s for the ground torsional state $v_t = 0$ and first excited torsional state $v_t = 1$. Solid diamonds and squares represent a_1 coefficients in $v_t = 0$ and $v_t = 1$, respectively, determined by fitting the eigenvalues of Eq. (6.5d) obtained with BELGI for different values of s according to the expansion of Eq. (6.15). The solid and dashed curves are fits according to Eq. (6.17) and Eq. (6.29), respectively. Open diamonds and squares are a_1 expansion coefficients for several molecules taking into account higher-order torsional parameters. The inset shows an enlargement of the $v_t = 0$ curve near the values for the six isotopologues of methanol.

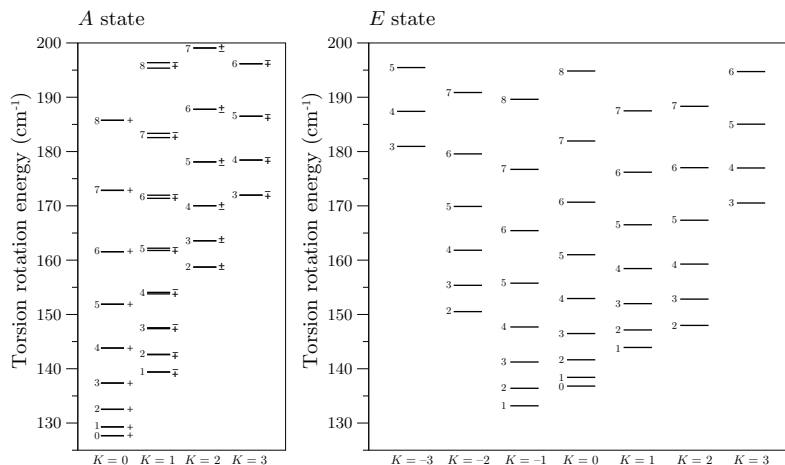


FIGURE 6.4: Energy of the lowest rotational levels in the torsion-vibrational groundstate ($\nu_t = 0$) of methanol ($^{12}\text{CH}_3^{16}\text{OH}$) [133]. The levels are denoted by J (indicated on the left side of each level), K . For the A levels the so-called parity quantum number (+/-) is also used. The panel on the left displays the A state levels, whereas the panel on the right displays the E state levels. High sensitivities are expected for transitions that connect near degenerate levels with different K .

with $|JK\rangle$ the symmetric top rotational eigenfunctions. The eigenvalues of the Hamiltonian of Eq. (6.5b) are

$$\langle JK\nu_t\sigma|H_{\text{Rsym}}^0|JK\nu_t\sigma\rangle = \frac{1}{2}(B+C)J(J+1) + \left(A - \frac{B+C}{2}\right)K^2. \quad (6.19)$$

Note that, in the case of an asymmetric top, torsional A levels are split in \pm components for $K > 0$ due to the asymmetry of the molecule.

6.2.3 Level schemes and selection rules

In Fig. 6.4 the lowest energy levels of $^{12}\text{CH}_3^{16}\text{OH}$ are shown for the A and E species. A and E symmetry species can be considered as two different molecular species in the same sense as para- and ortho-hydrogen: Radiative transitions between A and E species do not occur. The arrangement of energy levels within a symmetry state is quite similar to the structure of the K ladders in a (prolate) symmetric top; however, in the case of internal rotation each K ladder attains an additional offset, $E_{\text{tors}}(K)$, induced by the tunneling splitting. The + or - component of the A state refers to the $|J, K, \nu_t, 0\rangle \pm |J, -K, \nu_t, 0\rangle$ and $|J, K, \nu_t, 0\rangle \mp |J, -K, \nu_t, 0\rangle$ linear combinations of basis functions for K even and K odd respectively. The overall parity of the levels is given by $\pm(-1)^{J+\nu_t}$ [130]. The selection rules for allowed transitions within a torsion-rotational state are [130]

$$\begin{array}{llll}
A \text{ levels:} & \pm \leftrightarrow \mp & \Delta J = 0 & |\Delta K| = 0 \ (K \neq 0), 1 \\
& \pm \leftrightarrow \pm & |\Delta J| = 1 & |\Delta K| = 0, 1 \\
E \text{ levels:} & & \Delta J = 0 & |\Delta K| = 1 \\
& & |\Delta J| = 1 & |\Delta K| = 0, 1
\end{array}$$

where K is only a good quantum number in the limit of a symmetric top. As a consequence, transitions with $|\Delta K| > 1$ are allowed in asymmetric top molecules.

6.3 Scaling and sensitivity coefficients

The sensitivity to a variation of μ of a transition between states $|v_t'', J'', K'', Ts''\rangle$ and $|v_t', J', K', Ts'\rangle$ is given by

$$K_\mu(v_t'', J'', K'', Ts'' \rightarrow v_t', J', K', Ts') = \frac{\mu (\partial E / \partial \mu)_{v_t'', J'', K'', Ts''} - \mu (\partial E / \partial \mu)_{v_t', J', K', Ts'}}{E(v_t'', J'', K'', Ts'') - E(v_t', J', K', Ts')}. \quad (6.20)$$

Thus, in order to calculate the K_μ coefficients, the energy of each level and its dependence on μ has to be obtained. This translates into knowing the values of the molecular constants that go into BELGI and how these constants scale with μ .

We first examine the scaling relations for the lowest-order constants. We implicitly assume that the neutron-electron mass ratio follows the same behavior as the proton-electron mass ratio and that no effects depending on quark structure persist [66]. As a consequence, the atomic masses and hence the moments of inertia are directly proportional to μ . The rotational, centrifugal, and torsional constants A, B, C, D_{ab} , and F and the factor ρ are explicit functions of I_a, I_b, I_c , and I_{ab} , their μ dependence is obtained from Eqs. (6.6)–(6.11). Within the Born-Oppenheimer approximation, the torsional potential V_3 is independent of the mass of the nuclei and hence of μ .

The scaling relations for higher-order constants are derived from combinations of lower-order torsional and rotational operators. Some symmetry-allowed torsion-rotation terms are listed in Table 6.1. Let us, for example, inspect the constant M_v , which can be considered as a product of the torsional operator p_y^4 with the rotational operator P^2 . As the term with p_y^4 scales as μ^{-2} and the term with P^2 scales as μ^{-1} , we expect M_v to scale as μ^{-3} . The scaling relations of constants associated with other operators follow in a similar manner. The supplementary material of Ref. [145] lists the scaling relations for all constants used for methanol.

In this chapter, as well as in Chapter 5, we interpreted higher-order terms multiplying operators with powers of $P_\gamma P_a$ [such as $\rho_J(L_v), \rho_K(k_1), \rho_m(k_3)$] as the J, K , and m dependence of ρ (hence, we assumed these terms should be scaled as μ^{-1}). It was, however, kindly brought to our attention [146] that those terms might have been interpreted as powers of $2F\rho$ (in which case they should be scaled as μ^{-2}). Interestingly, when we use these alternative scaling relations, the obtained sensitivities for the

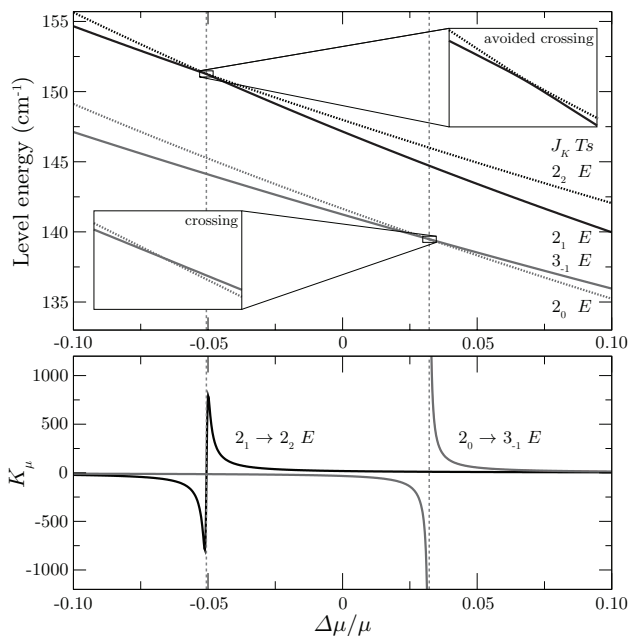


FIGURE 6.5: Energies of selected rotational levels in methanol ($^{12}\text{CH}_3^{16}\text{OH}$) as a function of the fractional change in the proton-to-electron mass ratio. The insets in the top panel show magnifications of the regions where the levels cross. It can be seen that levels with same J give rise to avoided crossings, whereas levels with different J do not. The bottom panel depicts the sensitivity coefficients of the $2_1 \rightarrow 2_2 E$ and $2_0 \rightarrow 3_1 E$ transitions as a function of $\Delta\mu/\mu$. For transitions between levels with same J , K_μ goes to zero at the (avoided) crossing, whereas transitions between levels with different J K_μ diverges to infinity at the crossing.

various transitions calculated using 119 constants are much closer to the values found when using only 7 constants (A , B , C , D_{ab} , F , and V_3). This might be taken as an indication (but not a proof) that the scaling relations are, in fact, the correct ones. To fully understand the implications of this finding, a careful study is needed where (i) proper expressions for the higher order terms should be derived explicitly as functions of the mass (or the moment of inertia) and (ii) a consistent set of axis system must be assured for all parameters to be scaled. Although understanding the physical meaning of the higher-order constants is relevant in its own right, the exact scaling relations do not alter the obtained sensitivities significantly.

In order to determine the sensitivity coefficients, we have written a computer code that generates the molecular constants as a function of μ using the discussed scaling relations, calls BELGI with these constants as input, and subsequently stores the computed level energies.

As an example, the upper panel of Fig. 6.5 shows the energies of the $2_2 E$, $2_1 E$, $3_1 E$, and $2_0 E$ levels in methanol as a function of $\Delta\mu/\mu$. The sensitivity coefficient of the $2_0 \rightarrow 3_1 E$ and $2_1 \rightarrow 2_2 E$ transitions can be obtained by dividing the difference in slope by the

difference in energy [cf. Eq. (6.20)]. The sensitivity coefficients of these transitions as a function of the relative variation of the proton-electron mass ratio, $\Delta\mu/\mu$, are shown in the lower panel of Fig. 6.5. As expected from Eq. (6.20), the sensitivity is strongly enhanced when the energy difference between the levels becomes small.

The behavior of the sensitivity coefficient close to the resonance depends on the quantum numbers of the levels involved. For instance, in methanol, K is not a good quantum number due to the asymmetry of the molecule, and levels with equal J mix. As a consequence, the $2_2 E$ and $2_1 E$ levels shown in Fig. 6.5 display an avoided crossing, and the sensitivity coefficient for the $2_1 \rightarrow 2_2 E$ transition is zero at the resonance. In contrast, J is a good quantum number and levels of different J will not mix. As a consequence, the sensitivity coefficient for the $2_0 \rightarrow 3_{-1} E$ transition becomes infinite at the resonance. In practice, we are only interested in the value of K_μ at $\Delta\mu/\mu < 10^{-5}$ and the effects of avoided crossings is relevant only if the levels cross extremely close to $\Delta\mu/\mu = 0$. In our study we have only come across one transition that has a significantly reduced sensitivity coefficient as a result of mixing of the energy levels involved, namely, the $8_0 \rightarrow 8_{-1} E$ transition in $^{12}\text{CD}_3^{16}\text{OD}$ at 4.2 GHz with $K_\mu = 0.7$. Note that the sign of the sensitivity coefficients at $\Delta\mu/\mu = 0$ is positive if the levels cross at $\Delta\mu/\mu < 0$, and negative if the levels cross at $\Delta\mu/\mu > 0$.

Using the recipe described above, the sensitivity coefficient of any desired transition in a molecule containing a C_{3v} symmetry group can be calculated. We have calculated the sensitivity coefficients of many (> 1000) transitions in methanol, acetaldehyde, acetamide, methyl formate, and acetic acid, using the constants listed in Refs. [133, 143, 144, 147, 148], respectively. In Table 6.2 sensitivity coefficients of selected transitions in the vibrational ground state ($\nu_t = 0$) of these molecules are listed. For methanol, the most sensitive transitions involving levels with $J \leq 10$ are listed. For the other molecules no large sensitivities were found for the vibrational ground state and the eight lowest transition frequencies that have been observed in the interstellar medium have been listed [69]. From the table, we see in particular that transitions in methanol are much more sensitive to a variation of μ than the transitions listed for the other molecules. Except for the $1_{-1} \rightarrow 1_1 E$ transition in acetaldehyde with $K_\mu = -3.7$, all transitions in acetaldehyde, acetamide, methyl formate, and acetic acid have $-1.57 \leq K_\mu \leq -0.74$.

The error in the last digit of the K_μ -coefficients is quoted in brackets, and is conservatively taken to be 5% if $|K_\mu| \geq 1$ or 0.05 if $|K_\mu| < 1$. The error in the sensitivity coefficients has 3 sources. (i) The first consists of errors due to the uncertainty in the determination of the molecular constants. As the simulations reproduce almost all transitions < 100 kHz, this error is negligible small. (ii) The second source consists of errors due to inexactness of the scaling relations of higher-order constants. Many of the higher-order constants are products of torsional and rotational operators and may also be fairly correlated. Therefore, the exact relationships between the higher order parameters and the moments of inertia (and masses) are not obvious. For methanol we have investigated the influence of the higher order parameters by comparing K_μ coefficients calculated by scaling only the first 7 and the first 31 constants to K_μ coefficients obtained by scaling all 119 constants. Sensitivity coefficients were found to typically agree within 5% or 0.5% if 7 or 31 constants were scaled, respectively. The

TABLE 6.2: Selected transitions [69] and K_μ coefficients for different molecules, calculated with BELGI (fourth column) using the constants from Refs. [133, 143, 144, 147, 148] and the approximate model (fifth column) discussed in the text. For methanol the most sensitive lines are shown, whereas for the other molecules the eight lowest transitions that have been observed in the interstellar medium as listed in the review by Lovas [69] are given. The error in the last digit(s) is given within brackets. Molecules marked with an asterisk (*) are labeled according to the sign convention opposite to the one as used in the text to be consistent with literature, that is, $F(p_\gamma - \rho p_a)^2$ instead of $F(p_\gamma + \rho p_a)^2$. As a consequence, the sign of the $\pm K$ labeling of the E transitions is reversed for these molecules.

Molecule	Transition, J_K	Transition (MHz)	K_μ^{BELGI}	K_μ^{toy}
Methanol	$5_1 \rightarrow 6_0 A^+$	6 668.5192(8)	-42.(2)	-46
	$9_{-1} \rightarrow 8_{-2} E$	9 936.202(4)	11.5(6)	16.7
	$5_2 \rightarrow 4_3 A^+$	9 978.686(4)	53.(3)	35
	$5_2 \rightarrow 4_3 A^-$	10 058.257(12)	52.(3)	35
	$2_0 \rightarrow 3_{-1} E$	12 178.593(4)	-33.(2)	-32
	$2_1 \rightarrow 3_0 E$	19 967.396(2)	-5.9(3)	-5.0
	$9_2 \rightarrow 10_1 A^+$	23 121.024(2)	-11.7(6)	-10.8
	$3_2 \rightarrow 3_1 E$	24 928.715(14)	17.9(9)	15.2
	$2_2 \rightarrow 2_1 E$	24 934.382(5)	17.9(9)	15.2
	$8_2 \rightarrow 9_1 A^-$	28 969.954(20)	-9.5(6)	-8.8
	$4_{-1} \rightarrow 3_0 E$	36 169.290(14)	9.7(5)	9.6
	$6_2 \rightarrow 5_3 A^-$	38 293.292(14)	-15.1(8)	-10.4
	$6_2 \rightarrow 5_3 A^+$	38 452.653(14)	-15.0(8)	-10.4
	$7_0 \rightarrow 6_1 A^+$	44 069.476(15)	5.2(3)	5.9
	$1_0 \rightarrow 2_{-1} E$	60 531.489(10)	-7.4(4)	-7.3
	$1_1 \rightarrow 2_0 E$	68 305.680(7)	-2.4(1)	-2.2
Acetaldehyde	$1_{-1} \rightarrow 1_1 E$	1 849.634(7)	-3.7(2)	-4.2
	$1_1 \rightarrow 2_{0A^+}$	8 243.462(3)	-1.11(6)	-1.15
	$1_0 \rightarrow 0_0 E$	19 262.140(4)	-1.00(5)	-1.00
	$1_0 \rightarrow 0_0 A^+$	19 265.137(1)	-1.00(5)	-1.00
	$2_0 \rightarrow 1_0 E$	38 506.035(3)	-1.00(5)	-1.00
	$2_0 \rightarrow 1_0 A^+$	38 512.081(3)	-1.00(5)	-1.00
	$1_{-1} \rightarrow 1_0 E$	47 746.980(5)	-1.03(5)	-0.93
	$1_1 \rightarrow 1_0 A^+$	47 820.620(4)	-1.02(5)	-1.03
Acetamide*	$2_2 \rightarrow 2_1 A^\pm$	9 254.418(4)	-1.04(5)	-1.12
	$1_0 \rightarrow 1_1 E$	13 388.703(4)	-1.57(8)	-1.34
	$4_3 \rightarrow 4_2 A^\mp$	14 210.349(4)	-1.03(5)	-1.12
	$3_3 \rightarrow 3_2 A^\mp$	14 441.705(4)	-1.05(5)	-1.12
	$2_0 \rightarrow 2_1 E$	15 115.748(4)	-1.43(7)	-1.30
	$2_2 \rightarrow 1_1 E$	22 095.527(4)	-0.74(5)	-0.78
	$3_3 \rightarrow 3_2 A^\pm$	22 769.635(4)	-1.03(5)	-1.08
	$4_2 \rightarrow 3_3 E$	47 373.320(4)	-1.04(5)	-1.11
Methyl Formate*	$1_1 \rightarrow 1_{-1} E$	1 610.900(2)	-1.00(5)	-0.70
	$2_{-1} \rightarrow 1_{-1} E$	22 827.741(8)	-1.00(5)	-1.00
	$2_1 \rightarrow 1_1 A^+$	22 828.134(8)	-1.00(5)	-1.00
	$2_0 \rightarrow 1_0 E$	24 296.491(8)	-1.00(5)	-1.00
	$2_0 \rightarrow 1_1 A^+$	24 298.481(8)	-1.00(5)	-1.00
	$2_1 \rightarrow 1_1 E$	26 044.796(8)	-1.00(5)	-1.00
	$2_1 \rightarrow 1_1 A^-$	26 048.534(8)	-1.00(5)	-1.00
	$4_0 \rightarrow 3_0 E$	47 534.069(16)	-1.00(5)	-1.00
Acetic Acid*	$8_{-1} \rightarrow 7_{-1} E$	90 203.444(20)	-1.00(5)	-1.00
	$8_{-1} \rightarrow 7_0 E$	90 203.444(20)	-1.00(5)	-0.97
	$8_0 \rightarrow 7_{-1} E$	90 203.444(20)	-1.00(5)	-1.03
	$8_0 \rightarrow 7_0 E$	90 203.444(20)	-1.00(5)	-1.00
	$8_0 \rightarrow 7_0 A^+$	90 246.250(50)	-1.00(5)	-1.00
	$8_0 \rightarrow 7_1 A^+$	90 246.250(50)	-1.00(5)	-1.00
	$8_1 \rightarrow 7_0 A^+$	90 246.250(50)	-1.00(5)	-1.00
	$8_1 \rightarrow 7_1 A^+$	90 246.250(50)	-1.00(5)	-1.00

TABLE 6.3: Rotational and torsional energy differences and associated sensitivity coefficients. Expressions for differences in rotational energy are only valid in the limit of a symmetric top molecule.

			ΔE	K_μ
Rotation	$\Delta J = 0$	$\Delta K = \pm 1$	$\left[A - \frac{1}{2}(B + C)\right](1 \pm 2K)$	-1
	$\Delta J = \pm 1$	$\Delta K = 0$	$\pm(B + C)\left[J + \frac{1}{2}(1 \pm 1)\right]$	-1
	$\Delta J = \pm 1$	$\Delta K = \pm 1$	$\pm(B + C)\left[J + \frac{1}{2}(1 \pm 1)\right] + \left[A - \frac{1}{2}(B + C)\right](1 \pm 2K)$	-1
	$\Delta J = \pm 1$	$\Delta K = \mp 1$	$\pm(B + C)\left[J + \frac{1}{2}(1 \pm 1)\right] + \left[A - \frac{1}{2}(B + C)\right](1 \mp 2K)$	-1
Torsion		$\Delta K = 0^a$	$\pm\sqrt{3}Fa_1 \sin\left(\frac{2\pi}{3}\left[\rho K \mp \frac{1}{2}\right]\right)$	$(B_1 - 1) - \frac{1}{2}C_1\sqrt{s}$
		$\Delta K = \pm 1$	$\mp 2Fa_1 \sin\left(\frac{\pi}{3}\rho\right) \sin\left[\frac{2\pi}{3}\left\{\rho\left(K \pm \frac{1}{2}\right) - \sigma\right\}\right]$	$(B_1 - 1) - \frac{1}{2}C_1\sqrt{s}$

^a Note that the transitions involving different overall symmetry species of the torsional levels ($A \leftrightarrow E$) are forbidden, thus transitions with $\Delta K = 0$, $\Delta J = 0$ do not occur.

results of Levshakov *et al.* [149] are exactly identical to ours if only 7 constants are scaled. Differences in calculated K_μ coefficients due to alternative scaling relations for some higher-order terms (*vide supra*) are therefore expected to be small. (iii) The third source consists of errors due to neglecting the μ dependence of the torsional potential. Within the Born-Oppenheimer approximation the torsional potential, V_3 , is independent of the mass of the nuclei and hence of μ . It is known, however, that V_3 does vary between isotopologues. For instance for $^{12}\text{CH}_3^{16}\text{OH}$ the torsional potential $V_3 \approx 373 \text{ cm}^{-1}$, and for $^{12}\text{CD}_3^{16}\text{OD}$ $V_3 \approx 362 \text{ cm}^{-1}$. A reliable model for this variation is not available. As a check, we have assumed V_3 to be a linear function of $I_{\text{red}} = I_{a1}I_{a2}/I_a$; $V_3 = V_3(^{12}\text{CH}_3^{16}\text{OH}) - 19.4[I_{\text{red}} - I_{\text{red}}(^{12}\text{CH}_3^{16}\text{OH})]$. As I_{red} is directly proportional to μ , this introduces a μ dependence in the potential. We found that the K_μ coefficients for $^{12}\text{CH}_3^{16}\text{OH}$ calculated by including the linear scaling for V_3 are typically 3% smaller than those obtained when the potential is assumed to be independent of μ .

6.4 “Toy” model

Although the numerical calculations described in the previous section yield the sensitivity coefficient for any desired transition, they provide limited insight. In this section, we devise a simple model which provides an intuitive picture of the physics involved and aids in the identification of other internal rotor molecules that possibly exhibit large sensitivity coefficients. In this model, we neglect coupling between vibrational, rotational, and torsional motion. In this case, the μ dependence of the energy of a certain state $|\nu_t, J, K, Ts\rangle$ can be written as

$$\mu \left(\frac{\partial E}{\partial \mu} \right)_{\nu_t, J, K, Ts} = K_\mu^{\text{vib}} E_{\text{vib}} + K_\mu^{\text{rot}} E_{\text{rot}} + K_\mu^{\text{tors}} E_{\text{tors}}, \quad (6.21)$$

where K_μ^{vib} , K_μ^{rot} , and K_μ^{tors} are the sensitivities to a possible variation of the proton-to-electron mass ratio of a vibrational, rotational, and torsional transition, respectively. We neglect vibrational excitation and use Eq. (6.21) to rewrite Eq. (6.20) as

$$K_\mu = \frac{K_\mu^{\text{rot}} \Delta E_{\text{rot}} + K_\mu^{\text{tors}} \Delta E_{\text{tors}}}{\Delta E_{\text{rot}} + \Delta E_{\text{tors}}}, \quad (6.22)$$

with ΔE_{rot} and ΔE_{tors} being the difference in rotational and torsional energy between the two energy levels involved, respectively. From this equation it immediately follows that K_μ diverges for $\Delta E_{\text{rot}} = -\Delta E_{\text{tors}}$ and $K_\mu^{\text{rot}} \neq K_\mu^{\text{tors}}$. This implies that the highest sensitivities are expected for transitions that convert overall rotation into internal rotation or vice versa. Furthermore, Eq. (6.22) indicates that the K_μ coefficients are proportional to the amount of energy that is cancelled. We now derive approximate analytical expressions for ΔE_{rot} , ΔE_{tors} , K_μ^{rot} , and K_μ^{tors} using the results of Sec. 6.2.

The rotational energy is given by Eq. (6.19), from which it is straightforward to calculate the energy differences for different transitions. The results are listed in Table 6.3. Note that these expressions are valid only for a nearly symmetric molecule.

K_μ^{rot} follows from the μ dependence of the rotational constants. From Eqs. (6.6)–(6.8) A , B , and C are inversely proportional to the moments of inertia that are proportional to μ . Consequently, in first order approximation $K_\mu^{\text{rot}} = -1$.

The torsional energy is given by Eq. (6.15), from which the splitting between the A ($\sigma = 0$) and E ($\sigma = \pm 1$) states can be calculated:

$$\begin{aligned} \Delta E_{\text{tors}}^{A \leftrightarrow E} &= F a_1 \left[\cos \left\{ \frac{2\pi}{3} (\rho K \pm 1) \right\} - \cos \left(\frac{2\pi}{3} \rho K \right) \right] \\ &= \pm \sqrt{3} F a_1 \sin \left(\frac{2\pi}{3} \left[\rho K \pm \frac{1}{2} \right] \right). \end{aligned} \quad (6.23)$$

Analogously, the splitting between $E1$ ($\sigma = +1$) and $E2$ ($\sigma = -1$) levels is given by

$$\Delta E_{\text{tors}}^{E1 \leftrightarrow E2} = \sqrt{3} F a_1 \sin \left(\frac{2\pi}{3} \rho K \right). \quad (6.24)$$

Equations (6.23) and (6.24) are plotted in Fig. 6.6 as function of s for $K = 0$ and $|K| = 1$, respectively, using the A_1 , B_1 , and C_1 parameters obtained in Sec. 6.2. Also shown

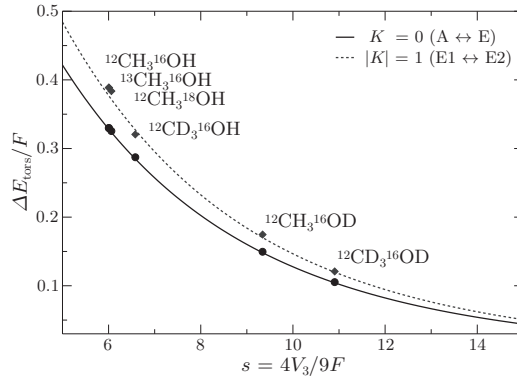


FIGURE 6.6: Torsional energy splitting between A and E $J = 0, K = 0$ (solid line) and $E1$ and $E2$ $J = 1, |K| = 1$ levels (dashed line) as function of s from Eqs. (6.23) and (6.24). For the curve representing the splitting between the $E1$ and $E2$ states, ρ is fixed at $\rho = 0.8$. Also shown are the torsional splittings for the different isotopologues of methanol.

are data points for the various isotopologues of methanol derived from experiments. Within the Born-Oppenheimer approximation s is proportional to $I_{\text{red}} \simeq \frac{1}{2} \hbar^2 F^{-1}$.

As transitions between different symmetry states ($A \leftrightarrow E$) are not allowed, we are interested in transitions within the same torsional states that differ in K . The difference in torsional energy for such transition with $\Delta K = \pm 1$ can be derived from Eq. (6.15) to be

$$\Delta E_{\text{tors}} = \mp 2Fa_1 \sin\left(\frac{\pi}{3}\rho\right) \sin\left(\frac{2\pi}{3}\left\{\rho\left(K \pm \frac{1}{2}\right) + \sigma\right\}\right). \quad (6.25)$$

Due to the a_1 coefficient appearing in Eqs. (6.23)-(6.25) all torsional splittings have the same dependence on s , and hence on μ . The sensitivity of a torsional transition, K_μ^{tors} , can be obtained from Eq. (6.1) by writing

$$\begin{aligned} K_\mu^{\text{tors}} &= \left(\frac{\partial \Delta E_{\text{tors}}}{\partial s}\right) \left(\frac{\partial s}{\partial \mu}\right) \frac{\mu}{\Delta E_{\text{tors}}} \\ &= \frac{\partial (\Delta E_{\text{tors}}/F)}{\partial s} \frac{sF}{\Delta E_{\text{tors}}} - 1, \end{aligned} \quad (6.26)$$

where we have used the fact that F scales with μ^{-1} . The -1 appearing in the second line is introduced by the substitution of ΔE_{tors} with $\Delta E_{\text{tors}}/F$. By inserting Eq. (6.25) in Eq. (6.26) we obtain

$$\begin{aligned} K_\mu^{\text{tors}} &= (B_1 - 1) - \frac{1}{2}C_1\sqrt{s} \\ &\simeq 0.111 - 1.060\sqrt{s}, \end{aligned} \quad (6.27)$$

where we have used the dimensionless fit values for B_1 and C_1 obtained in Sec. 6.2. Hence, within our approximations, K_μ^{tors} is only a function of s . For $^{12}\text{CH}_3^{16}\text{OH}$, with $s = 6.01$, this results in $K_\mu^{\text{tors}} = -2.5$, in agreement with the value found in Chapter 5.

With the help of Eq. (6.22) and the expressions for ΔE_{rot} , ΔE_{tors} , K_μ^{rot} , and K_μ^{tors} as listed in Table 6.3, we can now determine which transitions are likely to have an enhanced sensitivity and estimate the K_μ coefficients of these transitions. From Eq. (6.22), we saw that the highest sensitivities are expected when $\Delta E_{\text{rot}} \simeq -\Delta E_{\text{tors}}$. In Fig. 6.7 the difference in rotational energy, ΔE_{rot} , (solid curves) and negated torsional energy, $-\Delta E_{\text{rot}}$ (dashed curves), are shown for $|J, K\rangle \rightarrow |J+1, K-1\rangle A^+$ transitions in methanol. The highest sensitivities are expected when the lines representing the difference in rotational energy ΔE_{rot} and the negated difference in torsional energy $-\Delta E_{\text{tors}}$ cross. For this to happen at low J and K it requires that the rotational constants A , B , and C are of the same order as the difference in torsional energy. If the rotational constants are much smaller or larger than ΔE_{tors} , the crossings will only occur for high J and/or K quantum numbers. With the help of Fig. 6.7, it is straightforward to select transitions that are likely to have a large K_μ coefficient. For instance, the solid line representing the difference in rotational energy for $K = 1$ (solid circles) crosses the dashed line representing the negated difference in torsional energy near $J = 5$. As the lines cross near the maximum of torsional energy that may be attained, represented by the border of the gray shaded area, we may expect a large K_μ for the $5_1 \rightarrow 6_0 A^+$ transition. Indeed, this transition has $K_\mu = -42$.

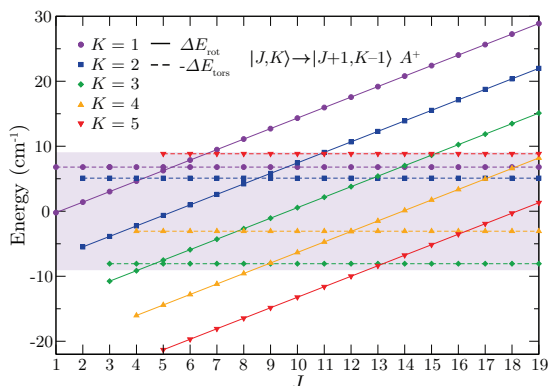


FIGURE 6.7: Difference in rotational energy, ΔE_{rot} (solid lines), and negated difference in torsional energy, $-\Delta E_{\text{tors}}$ (dashed lines), between levels connected by a $|J, K\rangle \rightarrow |J+1, K-1\rangle A^+$ type transition in methanol. The curves are obtained by the expressions in Table 6.3 and the molecular constants of methanol [133]. The highest sensitivities are expected when torsional energy is converted into rotational energy or vice versa, that is, when the two curves cross. The shaded area represents the maximum torsional energy that can be attained by the molecule. Note that the amount of energy that is cancelled is proportional to the K_μ coefficient.

The sensitivity coefficients K_μ of the transitions can be estimated using Eq. (6.22). Unfortunately, we found that the agreement between the K_μ coefficients obtained from this simple model and the values found from the full calculation was unsatisfactory, mainly as a result of neglecting the asymmetry of the molecules. Hence, we chose to use the experimental energy difference between the levels, $h\nu$, rather than $(\Delta E_{\text{rot}} + \Delta E_{\text{tors}})$. In this case, Eq. (6.22) can be written as

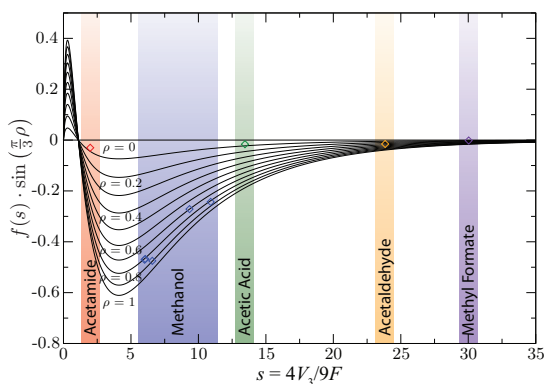


FIGURE 6.8: The product $f(s) \sin\left(\frac{\pi}{3}\rho\right)$ (see text) in the ground torsional state as a function of the effective barrier height, s , using Eq. (6.28) with ρ as indicated in the figure. Also shown are data points for each molecule investigated in this chapter; values of s and ρ can be found in Table 6.4.

$$\begin{aligned}
K_\mu &= (K_\mu^{\text{rot}} (h\nu - \Delta E_{\text{tors}}) + K_\mu^{\text{tors}} \Delta E_{\text{tors}}) / h\nu \\
&= K_\mu^{\text{rot}} + \Delta E_{\text{tors}} (K_\mu^{\text{tors}} - K_\mu^{\text{rot}}) / h\nu \\
&= -1 \mp 2FA_1 s^{B_1} e^{-C_1 \sqrt{s}} \left(B_1 - \frac{1}{2} C_1 \sqrt{s} \right) \sin\left(\frac{\pi}{3}\rho\right) \sin\left(\frac{2\pi}{3}\left\{\rho\left(K \pm \frac{1}{2}\right) + \sigma\right\}\right) / h\nu \\
&\equiv -1 + Ff(s) \sin\left(\frac{\pi}{3}\rho\right) g(\rho, K, \sigma) / h\nu,
\end{aligned} \tag{6.28}$$

The calculated K_μ coefficients from this model for selected transitions are listed in Table 6.2 and are seen to agree rather well with the numerical calculations.

We are now ready for a qualitative discussion of the sensitivity coefficients obtained for the different molecules. In the last line of Eq. (6.28), we have separated the expression for the sensitivity coefficient in four parts: the molecular constant F ; a function $f(s)$ that depends only on s ; a function that depends only on ρ ; and a function $g(\rho, K, \sigma)$ that depends on the rotational quantum number K , on the torsional symmetry σ , and on ρ . This last function takes on a value between -1 and 1 for the different σ , K levels. Although this function determines the sensitivity of a specific level, it is not important for comparing different molecules. The product $f(s) \sin\left(\frac{\pi}{3}\rho\right)$ can be used as a means to compare the sensitivity for different molecules. In Fig. 6.8 this product is plotted as a function of s with ρ as indicated in the figure. The curves can be regarded as the maximum sensitivity one may hope to find in a molecule with a certain F and transition energy $h\nu$. The maximum sensitivity peaks at $s = 4$ and $\rho = 1$. Recall that ρ is defined as the moment of inertia of the top over the moment of inertia of the whole molecule ($\rho \simeq I_{a2}/I_a$), and cannot be greater than unity.


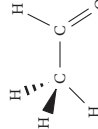
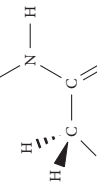
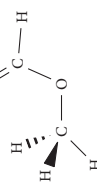
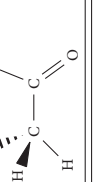
In Table 6.4 the structure and lowest order molecular constants of the molecules investigated in this chapter are listed as well as the results from our analytical model. The last column lists the generic maximum sensitivity K_μ^{gen} that may be expected for a hypothetical transition with a frequency of 1 GHz. For methanol, this number is 10–100 times larger than for the other investigated molecules, following from the fact that methanol has a large F , an effective barrier close to the optimal value of 4, and a relatively large ρ .

Application of the toy model to excited torsional states

So far, we have limited the discussion to transitions in the ground torsional state ($\nu_t = 0$). In this paragraph we discuss the application of the model to excited torsional states. Transitions within excited torsional states are both unlikely to be observed in the interstellar medium and of less interest for laboratory tests due to the added complexity of the experiment; hence, the following discussion is merely intended for providing a more complete picture. In excited torsional states the splitting between the different torsional symmetry levels becomes larger as tunneling through the torsional potential becomes more likely. This implies that the energy that can be cancelled also becomes larger, but, at the same time, the sensitivity coefficient of a pure torsional transition, K_μ^{tors} , becomes smaller. As we will see, the first effect is more important.

In Fig. 6.3 the solid squares represent a_1 coefficients for the $\nu_t = 1$ state obtained by fitting the second eigenvalues of the torsional Hamiltonian as function of K to the

TABLE 6.4: Structure and some lower-order constants of the molecules investigated in this chapter. The $A \leftrightarrow E$ $K = 0$ torsional splitting from Eq. (6.23) is listed for the vibrational ground state $v_t = 0$ of these molecules. Note that the magnitude of the torsional splitting only depends on the reduced barrier height $s = 4V_3/9F$. The magnitude of K_μ^{ors} for each molecule follows from Eq. (6.26). The K_μ^{gen} values given in the last column of the table are hypothetical sensitivities that may be expected for transitions of 1 GHz and with $g(\rho, K, \sigma) = 1$. Molecular constants are taken from Refs. [133, 143, 144, 147, 148].

Structure	Isotopologue	V_3 (cm^{-1})	F (cm^{-1})	s	ρ	$\Delta E_{\text{tors}}^{A \leftrightarrow E}$ (cm^{-1})	K_μ^{ors}	$K_\mu^{\text{gen}} + 1$
 Methanol	$^{12}\text{CH}_3^{16}\text{OH}$	373.555	27.647	6.01	0.810	9.07	-2.5	± 398
	$^{13}\text{CH}_3^{16}\text{OH}$	373.777	27.642	6.01	0.810	9.06	-2.5	± 397
	$^{12}\text{CH}_3^{18}\text{OH}$	374.067	27.428	6.06	0.809	8.88	-2.5	± 392
	$^{12}\text{CD}_3^{16}\text{OH}$	370.055	24.994	6.58	0.895	7.12	-2.6	± 363
	$^{12}\text{CH}_3^{16}\text{OD}$	366.340	17.428	9.34	0.699	2.58	-3.1	± 145
 Acetaldehyde	$^{12}\text{CD}_3^{16}\text{OD}$	362.122	14.758	10.91	0.822	1.54	-3.4	± 110
	$^{12}\text{CH}_3^{12}\text{C}^{16}\text{OH}$	407.716	7.600	23.84	0.332	0.065	-5.1	± 3.6
 Acetamide	$^{12}\text{CH}_3^{12}\text{C}^{16}\text{O}^{14}\text{NH}_2$	25.044	5.617	1.98	0.068	4.85	-1.4	± 5.2
 Methyl Formate	$^{12}\text{CH}_3^{16}\text{O}^{12}\text{C}^{16}\text{OH}$	370.924	5.490	30.03	0.084	0.017	-5.7	± 0.3
 Acetic Acid	$^{12}\text{CH}_3^{12}\text{C}^{16}\text{O}^{16}\text{OH}$	170.174	5.622	13.45	0.072	0.34	-3.8	± 2.8

Fourier expansion of Eq. (6.15). The dashed line in Fig. 6.3 represents a fit using an expression similar to Eq. (6.17) with an additional term, that is,

$$a_1^{\nu_t=1} = A_1 s^{B_1} e^{-C_1 \sqrt{s} + D_1 s}, \quad (6.29)$$

with $A_1 = 10.388$, $B_1 = 0.829$, $C_1 = 1.108$, and $D_1 = -0.058$. The open squares, also shown in Fig. 6.3, are a_1 coefficients for the first excited torsional state of the five molecules investigated in this chapter. The additional term modifies Eq. (6.28) only slightly. With the known coefficients, A_1 , B_1 , C_1 , and D_1 , we can again plot the parts that depend only on s and ρ , as was done for $\nu_t = 0$ shown in Fig. 6.8. As compared to the $\nu_t = 0$, the curves for the $\nu_t = 1$ are broadened and the center of the peak is shifted from $s = 4$ to $s = 7$. Moreover, the generic sensitivity is 5 times larger at the peak. As a consequence, the generic sensitivity, that is, the sensitivity for a transition with $\nu = 1$ GHz and $g(\rho, K, \sigma) = 1$, of molecules with unfavorable s and ρ in the ground torsional state, can be large in the $\nu_t = 1$ state. For instance, acetaldehyde in the $\nu_t = 1$ state has a generic sensitivity $K_\mu^{\text{gen}} + 1 = \pm 82$ as compared to $K_\mu^{\text{gen}} + 1 = \pm 3.6$ in the torsional ground state. For methanol, the generic sensitivity will also increase; however, as the torsional splitting in the $\nu_t = 1$ state is much larger than the rotational splittings, resonances are expected to occur only at high J and K values. Note that the sensitivities for transitions from the $\nu_t = 0$ to the $\nu_t = 1$ state will not be significantly enhanced as compared to ordinary vibrational transitions, that is, $K_\mu \approx -0.5$.

6.5 Conclusion and outlook

In the present study we have demonstrated that transitions in internal rotor molecules that convert internal rotation energy into overall rotation energy of the molecule exhibit an enhanced sensitivity to a possible variation of the proton-to-electron mass ratio. We have calculated the K_μ coefficients for five, relatively small, internal rotor molecules that are of astrophysical relevance: methanol, acetaldehyde, acetamide, methyl formate, and acetic acid. In addition to full calculations using advanced codes, such as the BELGI program, that achieve spectroscopic accuracy on the level energies, we have developed an approximate model, dubbed as the “toy” model, in which the molecular structure is described by the six most relevant molecular parameters. Based on this model we produce insight in the question as to why certain molecules of C_{3v} symmetry with hindered internal rotation are sensitive to μ variation. In particular, molecules in the torsional ground state are expected to have large K_μ coefficients if they have (i) an effective barrier height, s , around 4, (ii) a ratio between the moment of inertia of the top and the whole molecule, ρ , close to unity, and (iii) a large value for the molecular constant that relates to the internal rotation, F . If the torsional splittings are of the same order as the rotational constants, sensitive transitions will occur between levels with low J and K quantum numbers.

From the approximate toy model we learn that of the five molecules studied, methanol has by far the largest sensitivity, due to its favorable value of the effective barrier s and the fact that in methanol ρ is near unity. Moreover methanol has a fairly large value of F . The other investigated molecules either have too large a barrier (acetaldehyde),

have too heavy a frame attached to the methyl group and consequently a very small ρ (acetamide and acetic acid), or have both a high barrier and a small ρ (methyl formate). Based on these criteria, other interesting molecules containing a C_{3v} symmetry group include mercaptan, CH_3SH , ($F = 15 \text{ cm}^{-1}$, $V_3 = 439 \text{ cm}^{-1}$, and $\rho = 0.65$ [150], resulting in $K_\mu^{\text{gen}} + 1 = \pm 67$) and methylamine (which will be treated in Chapter 7). Other interesting candidate molecules, although of C_2 symmetry, are H_2O_2 (recently treated by Kozlov [151]) and H_2S_2 . These molecules require a modification in the definition of s and will have different A_1 , B_1 , and C_1 coefficients.

The high sensitivities of internal rotor molecules, particularly methanol, make them excellent target species to search for a variation of the proton-to-electron mass ratio over cosmological time scales. It is important to note that the sensitivity coefficients of the transitions in these molecules have both large positive and large negative values, that is, if μ varies, some transitions will shift to higher frequencies while others shift to lower frequencies. This makes it possible to perform a test of the variation of μ using transitions pertaining to a single species, thus avoiding the many systematic effects that plague tests based on comparing transitions in different molecules.

Currently, the most stringent bounds on a cosmological variation of μ is set by observations of hydrogen molecules in high ($z = 2 - 3$) redshift objects [152, 153] and a comparison between the ammonia tunneling frequencies and rotational transitions in anchor molecules at intermediate redshift ($z = 0.5 - 1$) objects [67, 68, 71]. Methanol provides a system that should result in more stringent bounds for μ variation. Recently, methanol, as well as methylamine and acetaldehyde have been observed in the gravitationally lensed system PKS 1830-211 at $z = 0.89$ [64, 154]. The $1_0 \rightarrow 2_{-1} E$ transition in methanol reported by Muller *et al.* was calculated to have $K_\mu = -7.4$. We have also calculated the K_μ coefficients for the nine observed transitions in acetaldehyde and found that all lines have sensitivities of $K_\mu \simeq -1$. Sensitivity coefficients for methylamine, for which three lines were observed in the same survey, will be calculated in Chapter 7.

The high-sensitivity coefficients in methanol are also beneficial for probing variation of μ as a result of chameleonlike scalar fields. These fields predict a dependence of μ on the local matter density. Note that the physical origin of these chameleonlike theories is very different from theories describing temporal μ variation. Levshakov *et al.* [135] compared ammonia spectra taken at high (terrestrial) and low (interstellar) densities of baryonic matter, and observed a statistically significant variation of μ . Recently, a preliminary test using methanol was performed by Levshakov *et al.* [149]. This test obtained similar results as for ammonia but can be further improved if more accurate laboratory data become available.

Methanol is also a promising candidate for laboratory tests on a possible variation of μ . Laboratory experiments can make use of rare isotopologues (in contrast to cosmological searches). Hence, the most sensitive transitions deriving from the present calculations can be targeted; a combined measurement of the $2_1 \rightarrow 1_1 E$ and $3_0 \rightarrow 4_{-1} E$ lines in CD_3OH exhibit a sensitivity spread ΔK_μ that is more than 400 times larger than a pure rotational transition [145]. Measurements of these transitions in slow (Stark decelerated [33, 51]) molecular beams may result in more stringent bounds on the variation of the proton-to-electron mass ratio in the current epoch.

SENSITIVITY TO A POSSIBLE VARIATION OF THE PROTON-TO-ELECTRON MASS RATIO OF TORSION-WAGGING-ROTATION TRANSITIONS IN METHYLAMINE (CH_3NH_2)

We determine the sensitivity to a possible variation of the proton-to-electron mass ratio μ for torsion-wagging-rotation transitions in the ground state of methylamine (CH_3NH_2). Our calculation uses an effective Hamiltonian based on a high-barrier tunneling formalism combined with extended-group ideas. The μ dependence of the molecular parameters that are used in this model are derived, and the most important ones of these are validated using the spectroscopic data of different isotopologues of methylamine. We find a significant enhancement of the sensitivity coefficients due to energy cancellations between internal rotational, overall rotational, and inversion energy splittings. The sensitivity coefficients of the different transitions range from -19 to $+24$. The sensitivity coefficients of the 78.135, 79.008, and 89.956 GHz transitions that were recently observed in the disk of a $z = 0.89$ spiral galaxy located in front of the quasar PKS 1830-211[64] were calculated to be -0.87 for the first two and -1.4 for the third transition. From these transitions a preliminary upper limit for a variation of the proton-to-electron mass ratio of $\Delta\mu/\mu < 9 \times 10^{-6}$ is deduced.

7.1 Introduction

Recently, it was shown that transitions between accidentally degenerate levels that correspond to different motional states in polyatomic molecules are very sensitive to a possible variation of the proton-to-electron mass ratio, $\mu = m_p/m_e$. Kozlov *et al.* [138] showed that transitions that convert rotational motion into inversion motion, and vice

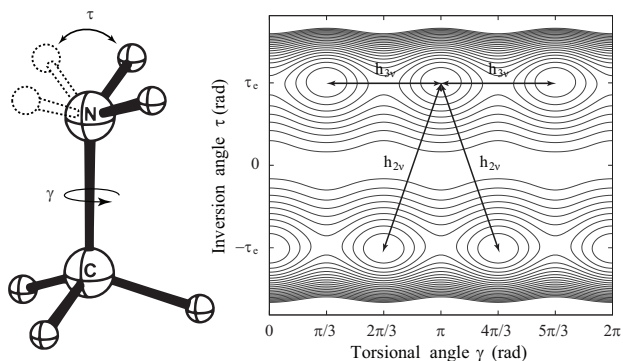


FIGURE 7.1: Schematic representation of methylamine and variation of the potential energy of methylamine as function of the relative rotation γ of the CH_3 group with respect to the amino group about the CN bond, and the angle τ of the two hydrogen atoms of the NH_2 group with respect to the CN bond. The two large-amplitude motions, corresponding to inversion (h_{2v}) and hindered rotation (h_{3v}) are schematically indicated by the arrows. Note that inversion of the NH_2 group is accompanied by a $\pi/3$ rotation about the CN bond of the CH_3 group with respect to the amino group.

versa, in the different isotopologues of hydronium (H_3O^+) have K_μ coefficients ranging from -219 to $+11$ ¹. Similarly, in Chapter 5 we showed that transitions that convert internal rotation into overall rotation in the different isotopologues of methanol have K_μ coefficients ranging from -88 to $+330$. Here, the sensitivity coefficient K_μ is defined by

$$\frac{\Delta\nu}{\nu} = K_\mu \frac{\Delta\mu}{\mu}. \quad (7.1)$$

For comparison, pure rotational transitions have $K_\mu = -1$, while pure vibrational transitions have $K_\mu = -\frac{1}{2}$ and pure electronic transitions have $K_\mu = 0$.

Accidental degeneracies between different motional states in polyatomic molecules are likely to occur if the energies associated with the different types of motions are similar. In this chapter, we present a calculation of the sensitivity coefficients for microwave transitions in methylamine (CH_3NH_2). Methylamine is an interesting molecule for several reasons: (i) it displays two large amplitude motions; hindered internal rotation of the methyl (CH_3) group with respect to the amino group (NH_2), and tunneling associated with wagging of the amino group. The coupling between the internal rotation and overall rotation in methylamine is rather strong resulting in a strong dependence of the torsional energies on the K quantum number, which is favorable for obtaining large enhancements of the K_μ coefficients [155]. (ii) Methylamine is a relatively small and stable molecule that is abundantly present in our galaxy and easy to work with in

¹In Kozlov *et al.* [138], μ is defined as the electron-to-proton mass ratio, consequently, the signs of the sensitivity coefficients used in that work are opposite to the signs of the sensitivity coefficient used here, $Q_\mu = -K_\mu$.

the laboratory. Recently it was also detected in the disk of a high redshift ($z = 0.89$) spiral galaxy located in front of the quasar PKS 1830-211[64].

This chapter is organized as follows. In Section 7.2, we introduce the effective Hamiltonian used for calculating the level energies in the vibrational ground state of methylamine. In Section 7.3 we derive how the constants that appear in this Hamiltonian scale with μ . Finally, in Section 7.4 we use the Hamiltonian and the scaling relations to determine the sensitivity coefficients of selected transitions.

7.2 Hamiltonian and energy level structure

Methylamine, schematically depicted in Fig. 7.1, is a representative of molecules exhibiting two coupled large-amplitude motions, the torsional motion of a methyl group and the wagging (or inversion) motion of an amine group. A combination of intermediate heights of the potential barriers with a leading role of the light hydrogen atoms in the large-amplitude motions results in relatively large tunneling splittings even in the ground vibrational state. On the right-hand side of Fig. 7.1, a contour plot of the potential energy is shown with the relative angle between the methyl and the amino group, γ , on the horizontal axis and the angle between the NH_2 plane and the CN bond, τ , on the vertical axis. The methyl torsion motion is indicated with the arrow labeled by h_{3v} whereas the amino wagging motion is indicated with the arrow labeled by h_{2v} . From the contour plot, it is seen that amino wagging motion of the NH_2 group is accompanied by a $\pi/3$ rotation of the CH_3 group about the CN bond with respect to the NH_2 group. Consequently, the amino wagging motion is strongly coupled to the hindered methyl top internal rotation resulting in a rather complicated computational problem.

In Fig. 7.2 the lowest rotational levels of the ground vibrational state of CH_3NH_2 are shown. The level ordering resembles that of a near-prolate asymmetric top molecule. In addition to the usual asymmetric splitting, every J, K level is split due to the different tunneling motions. The internal rotation tunneling splits each rotational level into one doubly degenerate and one nondegenerate sublevel. Each of these sublevels are further split into two due to the inversion motion. Together, this results in eight levels with overall symmetry $A_1, A_2, B_1, B_2, E_1 + 1, E_2 + 1, E_1 - 1$, and $E_2 - 1$ for $K > 0$ and four levels for $K = 0$. The $+1$ and -1 levels in the E_1 and E_2 symmetry species correspond to $K > 0$ and $K < 0$, respectively. Because of nuclear-spin statistics, in the ground vibrational state the nondegenerate levels of $J = \text{even}, K = 0$ are only allowed to possess the overall symmetry A_1, B_1 , whereas levels with $J = \text{odd}, K = 0$ are only allowed to possess the overall symmetry A_2, B_2 . The $K = 0$ doubly degenerate levels of E_1 and E_2 symmetry are denoted by $+1$ levels, i.e. by $E_1 + 1, E_2 + 1$ levels. The exact ordering of the different symmetry levels within a certain J, K level is determined by the relative contributions of the h_{3v} and h_{2v} parameters (see, for example, Fig. 3 of Ref. [156]). The internal motions are strongly coupled to the overall rotation resulting in a strong dependence of the torsional-wagging energies on the K quantum number. Thus the level ordering may differ from one K ladder to another. This turns out to be important for obtaining large

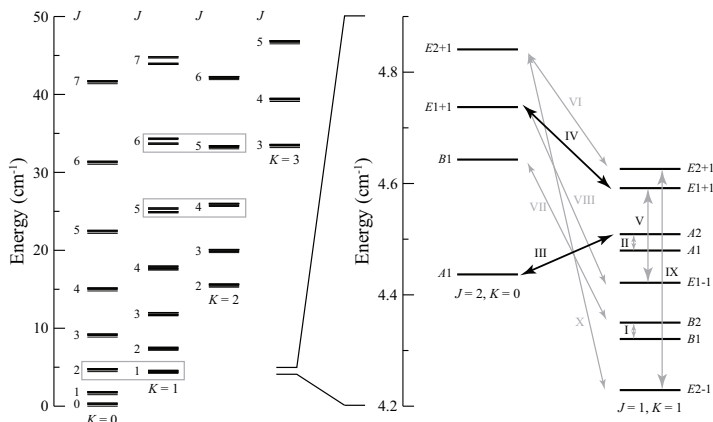


FIGURE 7.2: Energy of the lowest rotational levels in the ground state of methylamine ($^{12}\text{CH}_3^{14}\text{NH}_2$). The levels are denoted by J , K and the overall symmetry. The panel on the right-hand side of the figure shows an enlarged view of the $J = 2, K = 0$ and $J = 1, K = 1$ levels, with all symmetry allowed transitions assigned with roman numerals. The sensitivities of these transitions are listed in Table 7.3. The two transitions that are designated with bold arrows and are labeled by III and IV have sensitivity coefficients equal to $K_\mu = -19$ and $+2$, respectively.

enhancement factors, as it may result in closely spaced energy levels with a different functional dependence on μ that are connected by a symmetry allowed transition.

The panel on the right-hand side of Fig. 7.2 shows an enlarged view of the $J = 2, K = 0$ and $J = 1, K = 1$ levels, with all symmetry allowed transitions assigned with roman numerals. Note that transitions with $\Delta J = 0$ in the $K = 0$ manifold are not allowed. The transitions labeled by III, IV, VI, VII, VIII and X are of particular interest as these connect the closely spaced levels of different K manifolds and have an enhanced sensitivity to a variation of μ . A similar enhancement occurs for transitions between the $J = 5, K = 1$, and $J = 4, K = 2$ levels as well as for transitions between the $J = 6, K = 1$, and $J = 5, K = 2$ levels. In what follows, we will outline the procedure to calculate the sensitivities of these transitions. The resulting sensitivity coefficients are presented in Table 7.2 and Table 7.3 and discussed in Sec. 7.4.

In the present work, we use the group-theoretical high-barrier tunneling formalism developed for methylamine by Ohashi and Hougen [157], which is capable of reproducing observations of the rotational spectrum of the ground vibrational state of CH_3NH_2 to within a few tens of kilohertz [158, 159]. The high-barrier formalism assumes that the molecule is confined to one of n equivalent equilibrium potential minima for many vibrations, but that it occasionally tunnels from one of these n minima to another. The formalism fits in between the infinite-barrier approximation, where no tunneling splittings are observed, and the low-barrier approximation, where the present formalism breaks down. A backward rotation of the whole molecule is introduced to cancel the angular momentum generated by one of the large amplitude motions – the so-called internal axis method – requiring the usage of extended group ideas. The reader

is referred to Refs. [156–160] for a detailed description of the high-barrier tunneling formalism and the used Hamiltonian.

Table 7.1 lists the molecular constants used in our calculations. It includes three types of parameters: “nontunneling” or pure rotational parameters; parameters associated with pure methyl torsion motion (odd numerical subscripts n); and parameters associated with the NH_2 wagging motion (even numerical subscripts n). The obtained μ -scaling relations for the different parameters of the high-barrier tunneling formalism of methylamine are listed in the 2nd, 5th, and 8th column of Table 7.1. In the next sections, we discuss the scaling relations for the lowest-order parameters. The scaling relations for the higher-order parameters, and the problems encountered in determining these, are discussed in the supplemental material of Ref. [161].

7.3 Scaling relations of the molecular parameters

We use two different approaches for determining the μ dependence of the molecular constants that appear in the Hamiltonian:

(i) The first approach is based on the fact that the tunneling model essentially assumes that for each large-amplitude tunneling motion the system point travels along some path in coordinate space. In zeroth approximation, we may represent each large amplitude motion as a one-dimensional mathematical problem after parameterizing the potential along the path and the effective mass that moves along it. Thus, for each large amplitude motion, we will set up a Hamiltonian that contains one position coordinate and its momentum conjugate. The parameters of this one dimensional Hamiltonian may be connected with the observed splittings which are fitting parameters of the high-barrier tunneling formalism. The parameters of the one-dimensional Hamiltonians are functions of the moments of inertia and the potential barrier only, and their μ dependence can be found in a similar fashion as was done for methanol and other internal rotors [145, 155]. Application of this approach is straightforward in the case of the leading tunneling parameters of methylamine but some ambiguities appear for the J and K dependences of the main terms, because there are several ways of representing these dependences in a one-dimensional model.

(ii) In the second approach, we use the spectroscopic data of different isotopologues of methylamine to estimate the dependence of the tunneling constants. In analogy with methanol, we expect the tunneling splittings to follow the formula [145]:

$$W_{\text{splitting}} = \frac{a_0}{\sqrt{I_{\text{red}}}} e^{-a_1 \sqrt{I_{\text{red}}}}. \quad (7.2)$$

This formula originates from the semi-classical [Wentzel-Kramers-Brillouin (WKB)] approximation that assumes that the effective tunneling mass, which is represented by I_{red} , changes with isotopic substitution, but that the barrier between different wells remains unchanged. This expression was successfully applied to the $J = 0$, $K = 0$ $A - E$ splittings and the $J = 1$, $|K| = 1$ splittings in methanol [145]. In methylamine, the h_{nv} parameters correspond to the splittings in the $J = 0$, $K = 0$ due to tunneling between framework $|1\rangle$ and framework $|n\rangle$ (the set of frameworks represent the equivalent potential wells between which the system can tunnel), and application of the WKB

TABLE 7.1: Molecular parameters P_s of the ground torsional state of methylamine CH_3NH_2 [158], and their sensitivity to a variation of the proton-to-electron mass ratio μ defined as $K_\mu^{P_s} = \frac{\mu}{P_s} \frac{\partial P_s}{\partial \mu}$. All molecular parameters are in MHz, except ρ and ρ_K , which are dimensionless.

	Rotation ^a		Inversion ^b		Torsion ^c	
	$K_\mu^{P_s}$		$K_\mu^{P_s}$		$K_\mu^{P_s}$	
\tilde{B}	-1	22 169.36636(30)	-5.5	-1 549.18621(77)	-4.7	-2 493.5140(12)
$A - \tilde{B}$	-1	80 986.3823(11)	-8.2	2.73186(96)	-8.8	2.88398(55)
$B - C$	-1	877.87717(53)	-5.5	0.101759(11)	-4.7	-0.052546(20)
D_J	-2	0.0394510(18)	-5.5	1.73955(16)	-8.8	0.0002282(55)
D_{JK}	-2	0.170986(15)	-8.2	-0.004778(37)	-4.7	1.16676(22)
D_K	-2	0.701044(24)	-6.5	-0.000005466(88)	-8.8	-0.002667(73)
δ_J	-2	0.00175673(17)	-6.5	-0.0009016(63)	-5.7	-0.000017296(44)
δ_K	-2	-0.33772(13)	-6.5	-0.00015400(94)	-5.7	-0.0002995(42)
Φ_J	-3	-0.000000485(16)	-7.5	0.0000001923(56)	-6.7	-0.0000004702(67)
Φ_{JK}	-3	0.000002442(50)	-5.5	21.54923(52)	-4.7	-0.173439(24)
Φ_{KJ}	-3	-0.00000855(10)	-8.2	-0.03071(20)	-5.7	-0.00000261(13)
Φ_K	-3	0.0000322(29)	-6.5	-0.0037368(45)	-5.7	-0.0001359(32)
ϕ_K	-3	0.0002366(48)	-6.5	-0.019676(43)	-6.7	-0.0000000646(27)
			-7.5	0.000002098(62)	-5.7	-0.000003021(89)
			-7.5	0.00001023(54)	-6.7	0.00000000220(13)
ρ	0	0.64976023(13)	-5.5	-0.096739(38)		
ρ_K	-1	-0.0000011601(77)	-8.2	0.0002153(39)		
			-6.5	0.000004452(67)		
			-6.5	0.001188(37)		
			-7.5	-0.000001600(47)		
			-6.5	-0.000002443(55)		
			-5.5	10.979(37)		
			-6.5	-0.7206(73)		

^a These parameters do not involve tunneling motions.

^b These parameters arise from the NH_2 inversion tunneling motion.

^c These parameters arise from the CH_3 torsional tunneling motions.

approach to these parameters is straightforward. Moreover, since in fact all tunneling parameters in methylamine may be related to the same type of overlap integral as the h_{nv} parameters, we may expect that the isotopologue dependence of all tunneling terms can be described by Eq. (7.2). Unfortunately, ambiguities appear again when we apply this approach to higher order terms in the methylamine Hamiltonian. These ambiguities are connected to the fact that vibrational basis set functions $|n\rangle$ localized near various minima are not orthogonal, but in fact have nonzero overlap integrals with each other. The correlation problems that arise in the high-barrier tunneling formalism due to nonorthogonality of the basis functions are discussed in some detail in Ref. [162]. The main consequence which affects the isotopologue approach is that there may be “leakage” from one parameter to another; each fitted parameter appears as a sum of the “true” parameter value plus a small linear combination of all other parameters with a coefficient that goes to zero when the overlap integral goes to zero. While this effect should be insignificant for the main tunneling parameters of methylamine, it may be important for higher-order terms because even a small leakage of the low order parameters may be comparable in magnitude with the true values of the higher-order parameters.

In order to verify the mass-dependent coefficients of the parameters of the methylamine Hamiltonian, we have refitted available data on the CH_3ND_2 [163], CD_3NH_2 [164], and CD_3ND_2 [165] isotopologues of methylamine using the high-barrier tunneling formalism. Unfortunately, the amount of data available in the literature was rather limited: 66 transitions for CH_3ND_2 [163], 41 transition for CD_3NH_2 [164] and 49 transitions for CD_3ND_2 [165]. Therefore, many of the higher-order terms were not determined in the fits, while some low-order parameters were determined with a few significant digits only. As a result, it was possible to obtain the μ dependence of the main tunneling parameters h_{2v} and h_{3v} only. In order to obtain information on higher-order terms, we have undertaken a new investigation of the CH_3ND_2 spectrum with the Kharkov millimeter wave spectrometer. The newly obtained dataset for CH_3ND_2 contains 614 transitions, comparable to the number of microwave transitions available for CH_3NH_2 (696 transitions). The CH_3NH_2 and CH_3ND_2 fits have an almost equal number of varied parameters and obtained similar weighted root-mean-square deviations. The results of the CH_3ND_2 investigation will be published elsewhere [166]; here we will use only those results necessary for obtaining the scaling relations.

7.3.1 Pure rotational constants

The pure rotational or nontunneling parameters in the model are connected to the usual moments of inertia of the molecule and to the centrifugal distortion parameters. Therefore, we will assume the same μ -dependence for these parameters as used for methanol [155].

7.3.2 CH_3 torsion and the h_{3v} parameter

The h_{3v} parameter in the high-barrier tunneling formalism corresponds to a pure torsion motion. The quantity $|3h_{3v}|$ may be related to the usual $A - E$ internal rotation

splitting in a molecule that contains a group of C_{3v} symmetry. Assuming that the potential barrier is described by a cosine function and taking the moment of inertia of the methyl top to represent the mass that tunnels, we may set up a one-dimensional internal rotation Hamiltonian

$$H_{\text{tors}} = F_{\gamma} p_{\gamma}^2 + \frac{V_n}{2} (1 - \cos n\gamma), \quad (7.3)$$

with $p_{\gamma} = -i\partial/\partial\gamma$ is the angular momentum operator associated with the internal rotation coordinate, F_{γ} is the internal rotation parameter, and V_n the barrier height. For a threefold barrier $n = 3$. Using a value for F_{γ} derived from the molecular constants, we may fit the barrier height V_3 to the observed value for $|3h_{3v}|$ and estimate the μ dependence of h_{3v} .

In the used axis system, the off-diagonal contribution to the inertia tensor is represented by the s_1 parameter. For methylamine, this parameter is set to zero as it is not required by the fit. Thus, we may assume that the methyl top axis coincides with the principal axis a , hence $\rho = I_{\gamma}/I_a$, and $F_{\gamma} = C_{\text{conv}}/[(1 - \rho)I_{\gamma}]$, with C_{conv} being a conversion factor ($C_{\text{conv}} = 16.8576291 \text{ amu } \text{\AA} \text{ cm}^{-1}$). Using values for ρ and I_a (recalculated from rotational parameters) from Table 7.1, we obtain $I_{\gamma} = 3.18 \text{ amu } \text{\AA}^2$ and $F_{\gamma} = 15.12 \text{ cm}^{-1}$ (*ab initio* value 15.1684 cm^{-1} [167]). The value for I_{γ} is close to the expected one which supports the validity of the present analysis. Now, using this value for F_{γ} and the value for h_{3v} from Table 7.1, a fit to Eq. (7.3) yields the effective barrier height $V_3 = 683.7 \text{ cm}^{-1}$ (*ab initio* value 708.64 cm^{-1} [167]). The one-dimensional model with this value for V_3 predicts values for the first torsional band and the $A - E$ splitting in the first excited torsional state that are in a good agreement with the observed values (269 versus 264 cm^{-1} [168] for the band origin and 186 versus 180 GHz [168] for the splitting in the $\nu_t=1$). All this indicates that the one-dimensional model is physically sound and sufficiently accurate for our purposes.

Finally, we obtain the μ dependence of h_{3v} via

$$K_{\mu}^{h_{3v}} = \frac{\mu}{h_{3v}} \frac{\partial(h_{3v})}{\partial\mu} = -\frac{F_{\gamma}}{h_{3v}} \frac{\partial(h_{3v})}{\partial F_{\gamma}},$$

where we have used the fact that F_{γ} scales as μ^{-1} , i.e., we assume that the neutron mass has a similar variation as the proton mass. The numerical evaluation $\partial(h_{3v})/\partial F_{\gamma}$ using Eq. (7.4) yields $K_{\mu}^{h_{3v}} = -4.66$.

In the left panel of Fig. 7.3, the value of the h_{3v} parameter is plotted as a function of the reduced moment of inertia, $I_{\text{red}}^{\gamma} = C_{\text{conv}}/F_{\gamma}$, for four different isotopologues of methylamine. As mentioned, the quantity $|3h_{3v}|$ corresponds to the usual $A - E$ internal rotation splitting in a methyl top molecule; hence, we expect the tunneling splitting to follow Eq. (7.2). The solid line in the left panel of Fig. 7.3, corresponds to $a_0 = 10.3 \text{ THz (amu } \text{\AA}^2)^{1/2}$ and $a_1 = 7.84 \text{ (amu } \text{\AA}^2)^{-1/2}$, obtained using the CH_3NH_2 and CH_3ND_2 data. The reduced moment of inertia is directly proportional to μ . Thus, the sensitivity coefficient is given by:

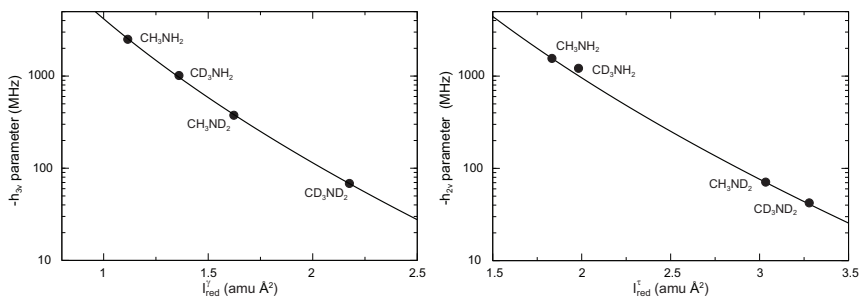


FIGURE 7.3: h_{2v} and h_{3v} parameters as a function of the reduced moment of inertia for the torsional and inversion motion for four different isotopologues of methylamine. The solid lines are fits according to Eq. (7.2) through the values of CH₃NH₂ and CH₃ND₂.

$$K_\mu^{h_{3v}} = \frac{I_{red}^y}{h_{3v}} \frac{\partial(h_{3v})}{\partial I_{red}^y} = -\frac{1}{2} - \frac{a_1 \sqrt{I_{red}^y}}{2}.$$

From the above expression, we find for the h_{3v} parameter of CH₃NH₂ a sensitivity coefficient of $K_\mu^{h_{3v}} = -4.64$, in excellent agreement with the value found from the one-dimensional Hamiltonian model.

7.3.3 Inversion and the h_{2v} parameter

The interpretation of the h_{2v} parameter in terms of an effective mass moving in a one-dimensional effective potential is not straightforward. For instance, *ab initio* calculations of the kinetic parameter for the inversion motion in the equilibrium geometry range from 9.6017 [167] to 26.7291 cm⁻¹ [169], while the barrier height in different studies varies from 1686 [170] to 2081 cm⁻¹ [171]. Since the system needs to tunnel six times in order to return to its initial configuration, we will treat this large amplitude motion as a six-fold periodic well problem, following Ohashi *et al.* [172]. Furthermore, we assume that the potential along the path can be represented by a rapidly converging Fourier series. Thus, we use Eq. (7.3) with γ replaced by τ and $n = 6$ as a zeroth order model. The effective inversion-torsion constant F_τ and barrier height V_6 can be determined from the splittings in the ground state and NH₂ wagging band origin (780 cm⁻¹ [173]). From this, we obtain $F_\tau = 9.19$ cm⁻¹ and $V_6 = 2322$ cm⁻¹, close to the values obtained by Ohashi *et al.* [172]. Following the same procedure as for h_{3v} , we obtain the μ dependence of h_{2v} , $K_\mu^{h_{2v}} = -5.49$.

In the right panel of Fig. 7.3, the value of the h_{2v} parameter is plotted as a function of the reduced moment of inertia, $I_{red}^\tau = C_{conv}/F_\tau$, for four different isotopologues of methylamine. The solid line in Fig. 7.3 corresponds to $a_0 = 44.4$ THz (amu Å²)^{1/2} and $a_1 = 7.35$ (amu Å²)^{-1/2}, obtained using the CH₃NH₂ and CH₃ND₂ data. From this fit, we find for the h_{2v} parameter of CH₃NH₂ a sensitivity coefficient equal to $K_\mu^{h_{2v}} = -5.48$, again in excellent agreement with the one-dimensional Hamiltonian model.

7.3.4 q_2 and r_2 parameters

The linear terms q and r correspond to the interaction of components of the total angular momentum with the angular momentum generated in the molecule-fixed axis system by the two large-amplitude motions. In methylamine, q_2 and r_2 represent the interaction of the angular momentum generated by the NH_2 inversion and the “corrective” $\pi/3$ rotation of the CH_3 group with the J_z and J_y components of the total angular momentum, respectively. It can be shown in different ways that q_2 has the same dependence on μ as h_{2v} . For instance, it follows from a study of the correlations between the q_2 , q_3 , and ρ parameters carried out by Ohashi and Hougen [157]. In methylamine, two possible choices exist for ρ . ρ can be chosen such that Coriolis coupling due to the inversion plus corrective rotation is eliminated (q_2 fixed to zero), or such that Coriolis coupling due to the internal rotation of the CH_3 group is eliminated (q_3 fixed to zero). These two choices result in a difference $\Delta\rho = (3/\pi)q_2/h_{2v}$ [157]. Since ρ is in both cases a (dimensionless) ratio between different moments of inertia and independent of μ , the above equation implies that q_2 and h_{2v} should have the same μ dependence.

From the CH_3ND_2 isotopologue data, a sensitivity coefficient $K_\mu^{q_2} = -5.53$ was found, in good agreement with the $K_\mu^{q_2} = -5.50$ obtained from the one-dimensional model and close to the value for $K_\mu^{h_{2v}}$. The r_2 term is expected to have the same μ dependence as q_2 . We were not able to check the isotopologue dependence for this term, since it was not required by the CH_3ND_2 fit.

7.3.5 Higher order terms

The μ dependence of the higher order terms, including the J and K dependences of the h_{2v} and h_{3v} parameters, was determined in a similar fashion (see the supplemental material of Ref. [161]). Unfortunately, some ambiguities and discrepancies between the different approaches appeared in the determination of the scaling relations for some higher-order terms, which is reflected by the rather large error for these parameters (see Sec. 7.4). This is not a serious concern as the higher order tunneling parameters only marginally affect the K_μ coefficients of the considered transitions.

7.4 Sensitivity of selected transitions

Using the scaling relations for the high-barrier tunneling Hamiltonian determined in the previous section, we are now able to calculate the sensitivity coefficient of any desired transition in the ground state of methylamine. In order to do numerical calculations, we rewrite Eq. (7.1) as

$$K_\mu^{v_{mn}} = \frac{v_{mn}^+ - v_{mn}^-}{2\varepsilon v_{mn}}, \quad (7.4)$$

with v_{mn} the transition frequency between state m and n for the present value of μ and v_{mn}^\pm the transition frequency when μ is replaced by $\mu(1 \pm \varepsilon)$ with ε a number much smaller than 1 (in our calculations, we typically use $\varepsilon = 0.0001$). v_{mn} is calculated using

TABLE 7.2: Transitions in methylamine (CH_3NH_2) that are detected in astrophysical objects in our local galaxy as listed in Lovas *et al.* [69]. The fourth column lists the transition strength multiplied by the electric dipole moment μ_e squared. The last column lists the sensitivity of the transitions to a possible variation of the proton-to-electron mass ratio.

Upper state			Lower state			Transition (MHz)	$S\mu_e^2$ (D^2)	K_μ
J	K	Sym	J	K	Sym			
2	0	B_1	1	1	B_2	8 777.827	0.779	-2.14(6)
5	1	B_1	5	0	B_2	73 044.474	9.024	-0.86(3)
4	1	B_2	4	0	B_1	75 134.858	7.290	-0.87(3)
3	1	B_1	3	0	B_2	76 838.932	5.611	-0.87(3)
1	1	B_1	1	0	B_2	79 008.693	2.373	-0.87(3)
5	1	A_1	5	0	A_2	83 978.941	9.024	-1.47(4)
2	1	$E_1 + 1$	2	0	$E_1 + 1$	84 598.202	1.065	-1.14(3)
4	1	A_2	4	0	A_1	86 074.729	7.290	-1.45(4)
3	1	A_1	3	0	A_2	87 782.494	5.613	-1.45(4)
2	0	B_1	1	0	B_2	88 667.906	0.189	-1.00(3)
2	0	$E_2 + 1$	1	0	$E_2 + 1$	88 668.681	0.189	-1.00(3)
2	0	$E_1 + 1$	1	0	$E_1 + 1$	88 669.543	0.188	-1.00(3)
2	0	A_1	1	0	A_2	88 669.626	0.188	-1.00(3)
8	2	$E_1 - 1$	8	1	$E_1 + 1$	219 151.221	3.519	-0.84(3)
7	0	B_2	6	1	B_1	220 826.705	4.295	-1.05(3)
9	2	$E_2 + 1$	9	1	$E_2 + 1$	220 888.443	7.496	-0.94(3)
5	0	$E_2 + 1$	4	0	$E_2 + 1$	221 527.438	0.472	-1.00(3)
5	0	$E_1 + 1$	4	0	$E_1 + 1$	221 530.404	0.470	-1.00(3)
5	0	B_2	4	0	B_1	221 530.481	0.473	-1.00(3)
5	0	A_2	4	0	A_1	221 536.285	0.470	-1.00(3)
5	2	$E_2 + 1$	4	2	$E_2 + 1$	221 717.567	0.395	-1.00(3)
5	2	$E_1 + 1$	4	2	$E_1 + 1$	221 721.771	0.396	-1.00(3)
5	2	$E_1 - 1$	4	2	$E_1 - 1$	221 724.256	0.395	-1.00(3)
5	2	$E_2 - 1$	4	2	$E_2 - 1$	221 728.700	0.396	-1.00(3)
10	2	B_2	10	1	B_1	227 545.019	8.759	-1.15(3)
8	2	$E_1 + 1$	8	1	$E_1 + 1$	227 997.002	3.320	-1.00(3)
4	2	$E_1 - 1$	4	1	$E_1 + 1$	229 310.604	0.848	-0.83(3)
7	2	$E_2 - 1$	7	1	$E_2 + 1$	229 452.729	0.628	-0.96(3)
9	2	B_1	9	1	B_2	231 844.268	7.784	-1.16(3)
5	2	$E_2 + 1$	5	1	$E_2 + 1$	232 003.755	3.580	-0.89(3)
7	2	A_1	7	1	A_2	233 368.424	5.922	-1.03(3)
14	6	A_1	15	5	A_2	235 337.423	2.367	-1.17(4)
14	6	A_2	15	5	A_1	235 337.540	2.367	-1.17(4)
8	2	B_2	8	1	B_1	235 734.967	6.840	-1.14(3)
6	2	A_2	6	1	A_1	236 408.779	5.020	-1.03(3)
2	2	$E_1 - 1$	2	1	$E_1 - 1$	237 143.512	1.230	-0.88(3)
4	2	$E_1 - 1$	4	1	$E_1 - 1$	239 427.017	2.299	-0.87(3)
3	2	$E_1 + 1$	3	1	$E_1 + 1$	239 446.258	1.937	-0.98(3)
5	2	$E_1 - 1$	5	1	$E_1 - 1$	241 501.243	2.554	-0.87(3)
6	2	B_2	6	1	B_1	242 261.957	5.020	-1.14(3)
6	2	$E_1 - 1$	6	1	$E_1 - 1$	244 151.624	2.725	-0.87(3)
10	5	B_1	11	4	B_2	245 463.443	1.506	-1.09(3)
10	5	B_2	11	4	B_1	245 464.483	1.506	-1.09(3)
2	2	A_1	2	1	A_2	246 924.172	1.298	-1.03(3)
4	2	B_2	4	1	B_1	247 080.140	3.235	-1.14(3)
7	2	$E_1 - 1$	7	1	$E_1 - 1$	247 362.353	2.807	-0.86(3)
3	2	B_1	3	1	B_2	248 838.499	2.317	-1.14(3)
3	2	$E_2 - 1$	3	1	$E_2 - 1$	248 999.871	2.182	-1.09(3)
8	0	A_1	7	1	A_2	250 702.202	4.891	-0.84(3)

TABLE 7.2: *Continued.*

Upper state			Lower state			Transition (MHz)	$S\mu_e^2$ (D ²)	K_μ
J	K	Sym	J	K	Sym			
6	2	$E_1 + 1$	6	1	$E_1 - 1$	252 908.786	1.740	-1.01(3)
6	2	$E_2 - 1$	6	1	$E_2 - 1$	253 768.569	3.999	-1.06(3)
4	1	$E_1 - 1$	3	0	$E_1 + 1$	254 055.766	0.259	-1.01(3)
9	2	$E_1 - 1$	9	1	$E_1 - 1$	255 444.689	2.612	-0.87(3)
4	2	B_1	4	1	B_2	255 997.777	3.065	-1.13(3)
5	2	B_2	5	1	B_1	258 349.240	3.804	-1.13(3)
7	2	A_2	7	1	A_1	258 857.426	5.080	-1.03(3)
10	2	$E_1 - 1$	10	1	$E_1 - 1$	260 293.984	2.308	-0.87(3)
11	1	B_2	10	2	B_1	260 963.400	3.943	-0.87(3)
4	1	$E_2 + 1$	3	0	$E_2 + 1$	261 024.312	3.128	-1.00(3)
4	1	B_1	3	0	B_2	261 219.282	3.924	-0.96(3)
8	0	B_1	7	1	B_2	261 562.178	4.881	-1.04(3)
8	0	$E_2 + 1$	7	1	$E_2 + 1$	263 377.814	4.613	-1.04(3)

values for the molecular constants as listed in Table 7.1, ν_{mn}^+ and ν_{mn}^- are calculated using the molecular constants scaled according to the relations that were determined in the previous section. We have calculated the K_μ coefficients for all rotational transitions in the ground state of methylamine with $J < 30$, $K_a < 15$, and ν_{mn} below 500 GHz. The two largest coefficients $K_\mu \approx -19$ and $K_\mu \approx +24$ were found for the $1_1A_2 \leftarrow 2_0A_1$ and $13_3E_1 + 1 \leftarrow 12_4E_1 + 1$ transitions at 2166 and 1458 MHz, respectively.

In Table 7.2, the transitions of methylamine that are detected in astrophysical objects in our local galaxy are listed together with their transition strengths and sensitivity coefficients. Table 7.3 lists transitions involving levels that have an excitation energy below 10 cm^{-1} , i.e., transitions involving levels that are expected to be populated in cold molecular clouds. The rotational transitions labeled with an asterisk have recently been detected by Muller *et al.* [64] via absorption in a cold cloud at a redshift $z = 0.89$. Due to their rather large transition frequency, their sensitivity coefficients are only slightly enhanced.

The transitions in Table 7.3 that are labeled by the roman numerals i-x, correspond to transitions in the $J = 1, K = 1$ and $J = 2, K = 0$ levels that are shown in the right hand side panel of Fig. 7.2. The transitions labeled by i and ii correspond to transitions between the levels of K doublets; hence these have sensitivities of approximately -1. The transitions labeled by v and ix are transitions between levels which splittings are significantly affected by tunneling motions. The sensitivities of these transitions are on the order of -5, comparable to the sensitivity of the h_{2v} and h_{3v} parameters. The transitions labeled by iii, iv, vi, vii, viii, and x are of particular interest as these are transitions between levels that differ in overall rotational energy as well as torsional-wagging energy. Consequently, cancellations may occur that lead to an enhancement of the sensitivity coefficients. Of these, the transition labeled by iii has the smallest transition frequency (2166 MHz) and the highest sensitivity coefficient ($K_\mu = -19$). The transition labeled by iv at 4364 MHz has a sensitivity coefficient equal to $K_\mu = +2$.

TABLE 7.3: Transitions in methylamine (CH_3NH_2) involving levels with an excitation energy lower than 10 cm^{-1} (i.e., both the upper and lower level of the transition have an excitation energy below 10 cm^{-1}). The fourth column lists the transition strength multiplied by the electric dipole moment μ_e squared. The last column lists the sensitivity of the transitions to a possible variation of the proton-to-electron mass ratio. The transitions labeled by roman numerals correspond to the ones depicted in Fig. 7.2. The transitions labeled with an asterisk have recently been detected by Muller *et al.* [64] in a cold cloud at $z = 0.89$.

	Upper state			Lower state			Transition (MHz)	$S\mu_e^2 (\text{D}^2)$	K_μ
	<i>J</i>	<i>K</i>	Sym	<i>J</i>	<i>K</i>	Sym			
I	1	1	A_2	1	1	A_1	879.859	0.141	-1.02(3)
II	1	1	B_2	1	1	B_1	881.386	0.142	-1.02(3)
III	1	1	A_2	2	0	A_1	2 166.305	0.779	-19.1(6)
	2	1	A_1	2	1	A_2	2 639.491	0.078	-0.99(3)
	2	1	B_1	2	1	B_2	2 644.073	0.080	-0.98(3)
IV	2	0	$E_1 + 1$	1	1	$E_1 + 1$	4 364.348	0.456	1.95(6)
V	1	1	$E_1 + 1$	1	1	$E_1 - 1$	5 094.897	0.004	-4.0(1)
	2	1	$E_1 + 1$	2	1	$E_1 - 1$	5 669.477	0.017	-3.5(1)
VI	2	0	$E_2 + 1$	1	1	$E_2 + 1$	6 437.552	0.418	-0.42(3)
VII	2	0	B_1	1	1	B_2	8 777.827	0.779	-2.14(6)
VIII	2	0	$E_1 + 1$	1	1	$E_1 - 1$	9 459.246	0.322	-1.29(4)
IX	1	1	$E_2 + 1$	1	1	$E_2 - 1$	11 911.000	0.001	-4.9(1)
	2	1	$E_2 + 1$	2	1	$E_2 - 1$	12 167.419	0.004	-4.8(1)
X	2	0	$E_2 + 1$	1	1	$E_2 - 1$	18 348.552	0.360	-3.3(1)
	3	0	A_2	2	1	A_1	41 263.780	1.541	-0.05(3)
	1	0	B_2	0	0	B_1	44 337.938	0.095	-1.00(3)
	1	0	$E_2 + 1$	0	0	$E_2 + 1$	44 338.468	0.094	-1.00(3)
	1	0	A_2	0	0	A_1	44 338.755	0.094	-1.00(3)
	1	0	$E_1 + 1$	0	0	$E_1 + 1$	44 338.876	0.094	-1.00(3)
	3	0	$E_1 + 1$	2	1	$E_1 + 1$	48 385.595	1.128	-0.75(3)
	3	0	$E_2 + 1$	2	1	$E_2 + 1$	50 615.856	0.936	-0.94(3)
	3	0	B_2	2	1	B_1	52 202.362	1.540	-1.19(4)
	3	0	$E_1 + 1$	2	1	$E_1 - 1$	54 055.072	0.412	-1.04(3)
	3	0	$E_2 + 1$	2	1	$E_2 - 1$	62 783.275	0.603	-1.68(5)
	2	1	$E_2 - 1$	2	0	$E_2 + 1$	70 199.113	2.420	-0.40(3)
	1	1	$E_2 - 1$	1	0	$E_2 + 1$	70 320.128	1.274	-0.39(3)
	2	1	$E_2 - 1$	1	1	$E_2 + 1$	76 636.665	0.001	-0.40(3)
	2	1	B_2	2	0	B_1	78 135.504*	3.976	-0.87(3)
	2	1	$E_1 - 1$	2	0	$E_1 + 1$	78 928.726	2.914	-0.98(3)
	1	1	B_1	1	0	B_2	79 008.693*	2.373	-0.87(3)
	1	1	$E_1 - 1$	1	0	$E_1 + 1$	79 210.297	1.392	-0.97(3)
	1	1	$E_2 + 1$	1	0	$E_2 + 1$	82 231.128	1.099	-1.05(3)
	2	1	$E_2 + 1$	2	0	$E_2 + 1$	82 366.532	1.558	-1.04(3)
	2	1	$E_1 - 1$	1	1	$E_1 + 1$	83 293.074	0.003	-0.82(3)
	1	1	$E_1 + 1$	1	0	$E_1 + 1$	84 305.195	0.982	-1.15(3)
	2	1	$E_1 + 1$	2	0	$E_1 + 1$	84 598.202	1.065	-1.14(3)
	2	1	B_2	1	1	B_1	87 794.717	0.141	-1.00(3)
	2	1	A_2	1	1	A_1	87 795.016	0.141	-1.00(3)
	2	1	$E_1 - 1$	1	1	$E_1 - 1$	88 387.971	0.138	-1.01(3)
	2	1	$E_2 - 1$	1	1	$E_2 - 1$	88 547.665	0.140	-1.01(3)
	2	0	B_1	1	0	B_2	88 466.906	0.189	-1.00(3)
	2	0	$E_2 + 1$	1	0	$E_2 + 1$	88 668.681	0.189	-1.00(3)
	2	0	$E_1 + 1$	1	0	$E_1 + 1$	88 669.543	0.188	-1.00(3)
	2	0	A_1	1	0	A_2	88 669.626	0.188	-1.00(3)
	2	1	$E_2 + 1$	1	1	$E_2 + 1$	88 804.084	0.141	-0.99(3)

TABLE 7.3: *Continued.*

Upper state			Lower state			Transition (MHz)	$S\mu_e^2$ (D ²)	K_μ
J	K	Sym	J	K	Sym			
2	1	$E_1 + 1$	1	1	$E_1 + 1$	88 962.550	0.138	-0.99(3)
2	1	A_2	2	0	A_1	89 081.463	3.978	-1.44(4)
2	1	A_1	1	1	A_2	89 554.649	0.141	-1.00(3)
2	1	B_1	1	1	B_2	89 557.404	0.141	-1.00(3)
1	1	A_1	1	0	A_2	89 956.072*	2.374	-1.44(4)
2	1	$E_1 + 1$	1	1	$E_1 - 1$	94 057.448	0.003	-1.16(3)
2	1	$E_2 + 1$	1	1	$E_2 - 1$	100 715.084	0.001	-1.46(4)
1	1	$E_2 - 1$	0	0	$E_2 + 1$	114 658.597	0.733	-0.63(3)
1	1	$E_1 - 1$	0	0	$E_1 + 1$	123 549.174	0.655	-0.98(3)
1	1	B_2	0	0	B_1	124 228.018	1.582	-0.92(3)
1	1	$E_2 + 1$	0	0	$E_2 + 1$	126 569.597	0.850	-1.03(3)
1	1	$E_1 + 1$	0	0	$E_1 + 1$	128 644.071	0.928	-1.10(3)
3	0	B_2	2	0	B_1	132 981.939	0.284	-1.00(3)
3	0	$E_2 + 1$	2	0	$E_2 + 1$	132 982.388	0.283	-1.00(3)
3	0	$E_1 + 1$	2	0	$E_1 + 1$	132 983.797	0.282	-1.00(3)
3	0	A_2	2	0	A_1	132 984.734	0.282	-1.00(3)
1	1	A_2	0	0	A_1	135 174.686	1.583	-1.29(4)
2	1	$E_2 - 1$	1	0	$E_2 + 1$	158 867.793	0.929	-0.73(3)
2	1	$E_1 - 1$	1	0	$E_1 + 1$	167 598.269	0.636	-0.99(3)
2	1	B_1	1	0	B_2	169 447.483	2.373	-0.94(3)
2	1	$E_2 + 1$	1	0	$E_2 + 1$	171 035.212	1.444	-1.02(3)
2	1	$E_1 + 1$	1	0	$E_1 + 1$	173 267.745	1.739	-1.07(3)
2	1	A_1	1	0	A_2	180 390.580	2.374	-1.22(4)

The estimated uncertainties of the K_μ coefficients are quoted in brackets in units of the last digits. There are two sources of the uncertainty in the K_μ coefficients: (i) the uncertainty in the determination of the molecular constants and (ii) the inexactness of the scaling relations of the Hamiltonian parameters including errors due to neglecting the μ dependence of the torsion-wagging potential of the molecule. We have assumed the error in the scaling coefficients to be ± 0.02 for the rotational parameters, ± 0.1 for the tunneling parameters h_{2v} , h_{3v} , q_2 , r_2 , and ± 1 for higher order tunneling terms. Since the uncertainties for the measured transition frequencies in the ground torsional state of methylamine are less than 10^{-4} (and below 5×10^{-6} for the low- J transitions of interest in the present study [159]), we assume that the main errors in sensitivity coefficients are due to the inexactness of the scaling relations of the Hamiltonian parameters. Therefore, similarly to the procedure adopted in Ref. [149], the K_μ coefficients were calculated taking either the upper or the lower bound for the scaling relations, corresponding to the upper and lower bounds of the assumed uncertainties. The difference was taken as an estimate of the uncertainty of the K_μ coefficients. In spite of the large uncertainties of the scaling relations for the higher-order terms, the resulting errors in the K_μ coefficients of the different transitions are below 3%. To test the influence of the uncertainties in the scaling relations of the higher-order terms, we have performed an additional calculation where only the nontunneling parameters and h_{2v} , h_{3v} , q_2 , and r_2 were used to calculate the K_μ coefficients for different transitions. The difference between this calculation and the calculation with the full set of scaling relations was less than 1.7%, i.e., within the uncertainties presented in Table 7.2 and 7.3.

It is interesting to note that almost identical values for the sensitivity coefficients

are obtained by using an equation that directly connects the sensitivity coefficient of a transition with the sensitivity coefficients of the Hamiltonian parameters:

$$K_{\mu}^{v_{mn}} = \frac{1}{v_{mn}} \sum_s K_{\mu}^{P_s} P_s \left[\frac{\partial E_n}{\partial P_s} - \frac{\partial E_m}{\partial P_s} \right], \quad (7.5)$$

where

$$\frac{\partial E_m}{\partial P_s} = \langle m | \hat{O}_s | m \rangle \quad (7.6)$$

is the derivative of the energy level E_m with respect to the Hamiltonian parameter P_s used in the program to build up the least-squares-fit matrix, and $K_{\mu}^{P_s}$ is the sensitivity coefficient with respect to the s th Hamiltonian parameter. Eq. (7.5) is based on the assumption that the energy of state $|m\rangle$ may be represented as $E_m = \sum_s P_s \langle m | \hat{O}_s | m \rangle$. This assumption is valid when the Hamiltonian depends linearly on the parameters, i.e. that the Hamiltonian may be written as $H = \sum_s P_s \hat{O}_s$. The high-barrier tunneling Hamiltonian used for methylamine depends nonlinearly on ρ , but as $K_{\mu}^{\rho} = 0$, the transition sensitivity coefficients calculated using Eq. (7.5) agree well with the results obtained by using Eq. (7.4); the $\approx 0.4\%$ difference is attributed to the ρ_K term, which is also nonlinear and whose scaling coefficient is nonzero.

From Eq. (7.5) it is seen that contributions to $K_{\mu}^{v_{mn}}$ from different terms in the Hamiltonian are proportional to the relative contributions of these terms to the transition frequency. From this fact, it is obvious that the resulting sensitivity coefficients are mainly determined by the largest terms in the Hamiltonian, and uncertainties in the scaling relations for the high-order parameters do not significantly affect our results.

Eq. (7.5) illustrates that the largest enhancement is obtained for transitions that connect two near degenerate levels that have substantially different dependences on μ . The different dependence on μ is provided when the two levels contain nonequal contributions from different types of motions in the molecule. In that case, a transition “converts” one superposition of rotation-torsion-wagging motion to another superposition of rotation-torsion-wagging motion. A significant enhancement is obtained when a “cancellation” takes place, i.e. when two levels have nearly the same total energy due to quantitatively different contributions from various types of motion in the molecule.

From Eq. (7.5), it is possible to obtain an upper limit for the sensitivity coefficient that we may hope to find in the ground vibrational state of methylamine. Considering the main, low-order terms, the maximum splitting due to the tunneling motions, i.e., the maximum torsional-wagging energy difference between levels n and m may be roughly taken to be $4(h_{2v} + h_{3v})$. Large enhancements of the sensitivity are expected for transitions that convert a considerable fraction of this energy into rotational energy. Using Eq. (7.5) and the values and sensitivities of the molecular parameters as listed in Table 7.1, the maximum sensitivity that we may hope to find is

$$\begin{aligned} K_{\mu} &= K_{\mu}^{\text{rot}} \pm \frac{1}{v_{nm}} \left(4h_{2v} [K_{\mu}^{h_{2v}} - K_{\mu}^{\text{rot}}] + 4h_{3v} [K_{\mu}^{h_{3v}} - K_{\mu}^{\text{rot}}] \right) \\ &\approx -1 \pm 64\,800/v_{nm}, \end{aligned} \quad (7.7)$$

with $K_\mu^{\text{rot}} = -1$ (i.e. that the K_μ of a rotational parameters) and ν_{nm} the transition frequency in MHz. The sensitivities obtained from our numerical calculations are indeed found within these bounds.

7.5 Conclusion

Spectra of molecular hydrogen in highly redshifted objects have been used to constrain a possible variation of the proton-electron mass ratio μ since the 1970s. However, as the observed absorptions in H_2 correspond to transitions between different electronic states, these are rather insensitive to μ ; the sensitivity coefficients K_μ fall in the range -0.01 to $+0.05$ [11, 66, 122]. For this reason even the highest quality H_2 absorption spectra involving over 90 lines, observed with the large dish Keck Telescope [152] and the Very Large Telescope [153] yield constraints $|\Delta\mu/\mu|$ of only 5×10^{-6} at a redshift $z \sim 2$.

The notion that specific molecules exhibit an enhanced sensitivity to μ variation is changing the paradigm for searching drifting constants on cosmological time scales from the optical to the radio domain. The use of NH_3 inversion transitions in the microwave range that have K_μ coefficients of -4.2 [45, 46], has led to much tighter constraints [71], with currently the lowest limit on temporal variations in μ of $|\Delta\mu/\mu| < 0.4 \times 10^{-6}$ at $z = 0.68$ [68]. In Chapter 5 we pointed out that microwave transitions in the methanol molecule (CH_3OH) have sensitivity coefficients in the range -42 to $+53$ [145, 149], which was used to obtain a limit on $|\Delta\mu/\mu| < 0.3 \times 10^{-6}$ at $z \sim 0.89$ based on two methanol lines at 12.2 and 60.5 GHz [63]. In the Milky Way, the methanol method was used to test the variation of μ by looking at the 9.9 and 104 GHz maser transitions resulting in $|\Delta\mu/\mu| < 0.03 \times 10^{-6}$ [149]. This limit can be improved one order of magnitude if new and more accurate laboratory rest frequencies of methanol transitions are measured. Improvements beyond the level of $\sim 10^{-9}$ are hindered by segregation effects within the methanol emitters [174].

In this chapter, we showed that the sensitivity of microwave transitions in methylamine, CH_3NH_2 , are in the range -19 to $+24$. Methylamine is particularly relevant as it was recently observed at $z = 0.8859$ in the intervening galaxy towards the quasar PKS 1830–211 [64]. The sensitivity coefficients of the observed transitions at 78.135, 79.008, and 89.956 GHz were calculated to be $K_\mu = -0.87$ for the first two and $K_\mu = -1.4$ for the third transition (see Table 7.3). These three methylamine lines have a mean radial velocity of $\nu_{\text{CH}_3\text{NH}_2} = -6.2 \pm 1.6 \text{ km s}^{-1}$ [64]. With $|\Delta K_\mu| = 0.563$ and the uncertainty interval $\Delta\nu = 1.6 \text{ km s}^{-1}$, we obtain a preliminary estimate of $\Delta\mu/\mu$:

$$\left| \frac{\Delta\mu}{\mu} \right| = \left| \frac{\Delta\nu}{c\Delta K_\mu} \right| < 9 \times 10^{-6}, \quad (7.8)$$

where c is the speed of light.

A tighter constraint on $\Delta\mu/\mu$ is obtained from the comparison of $\nu_{\text{CH}_3\text{NH}_2}$ with the radial velocity of the methanol line at 60.531 GHz, also detected at $z = 0.8859$; $\nu_{\text{CH}_3\text{OH}} = -5.3 \pm 0.5 \text{ km s}^{-1}$ [64]. This transition has a sensitivity coefficient $K_\mu = -7.4$. In this case, we have $|\Delta K_\mu| = 6.5$ and $\Delta\nu = 0.9 \pm 1.7 \text{ km s}^{-1}$, which yields $|\Delta\mu/\mu| < 10^{-6}$.

This estimate contains an unknown input due to possible noncospatial distribution of CH_3OH and CH_3NH_2 . More robust constraints on $\Delta\mu/\mu$ are derived from observations of lines of the same molecule. In this approach the low frequency transitions of CH_3NH_2 at 2166 and 4364 MHz would be particularly attractive as the difference of their sensitivity coefficients is $\Delta K_\mu \approx 21$.

SAMENVATTING

Veelatomige moleculen als instrument om een mogelijke verandering in de massaverhouding tussen het proton en het elektron te detecteren

Sinds Pythagoras het verband ontdekte tussen de lengte van een snaar en de toon die deze snaar voortbrengt, heeft de wetenschap zich toegelegd op het ontdekken van de wetmatigheden in de natuur en deze beschreven in de vorm van zogenaamde “natuurwetten”. Deze wetten hebben twee algemene eigenschappen: (i) ze zijn geschreven in de vorm van mathematische vergelijkingen en (ii) ze bevatten empirische parameters, de natuurconstanten.

Een eenvoudig voorbeeld is de zwaartekracht aan het aardoppervlak, $F_z = mg$. Wiskundig gezien zegt deze vergelijking dat de zwaartekracht, op bijvoorbeeld een appel, recht evenredig is met de massa van de appel, terwijl de “koppelingsconstante” g bepaalt dat een vallende appel een versnelling ondervindt van ongeveer -10 m/s^2 . De constante g is echter geen fundamentele natuurconstante, want uit nauwkeurige metingen volgt dat g varieert over het aardoppervlak. Newtons algemene gravitatiewet is in staat de waarde van g en de kleine variaties daarin te verklaren op een meer fundamenteel niveau; g kan worden geschreven als functie van de massa van de aarde, de afstand tot het (massa)middelpunt van de aarde, en de gravitatieconstante G . Een logische vraag is nu of we de waarde van G ook kunnen verklaren op een dieper niveau. Dit blijkt (nog) niet het geval te zijn en G kan dus worden beschouwd als een echte fundamentele natuurconstante. Dat de waarde van G ook echt constant is, volgt niet uit de zwaartekrachttheorie of enige andere theorie, maar is een aanname die gebaseerd is op observaties en een sterk geloof in het principe dat de resultaten van een experiment onafhankelijk zijn van ruimte en tijd (locale positie-invariantie). Een van de eerste wetenschappers die speculeerde over een mogelijke variatie in de waarde van G was Dirac. In zijn “Large Number Hypothesis” (1937) stelt hij dat de waarde van G omgekeerd evenredig is met de leeftijd van het heelal. Hoewel Diracs theorie onjuist bleek, opende het toetsen ervan aan paleontologische en kosmologische waarnemingen de zoektocht naar veranderende natuurconstanten.

Voor de atoom- en molecuulfysica zijn in het bijzonder de fijnstructuurconstante, $\alpha = 1/137,03599974(44)$, en de massaverhouding tussen het proton en het elektron, $\mu = 1836,15267245(75)$, van belang. Deze twee constanten bepalen in grote mate de stabiliteit van atomen en moleculen. In dit proefschrift wordt exclusief gekeken naar manieren om een mogelijke verandering in μ te detecteren. Een kleine verandering in μ (of α) heeft vergaande consequenties voor de natuurkunde, scheikunde en biologie. Bij een verandering in de orde van een procent zouden er bijvoorbeeld geen elementen zwaarder dan helium kunnen worden gevormd. Toch is het juist deze afhankelijkheid die ons in staat stelt een mogelijke verandering waar te nemen. Een verandering in μ verandert namelijk ook de kleuren licht die door een molecuul kunnen worden geabsorbeerd (en uitgezonden). Niet alle geabsorbeerde kleuren veranderen evenveel

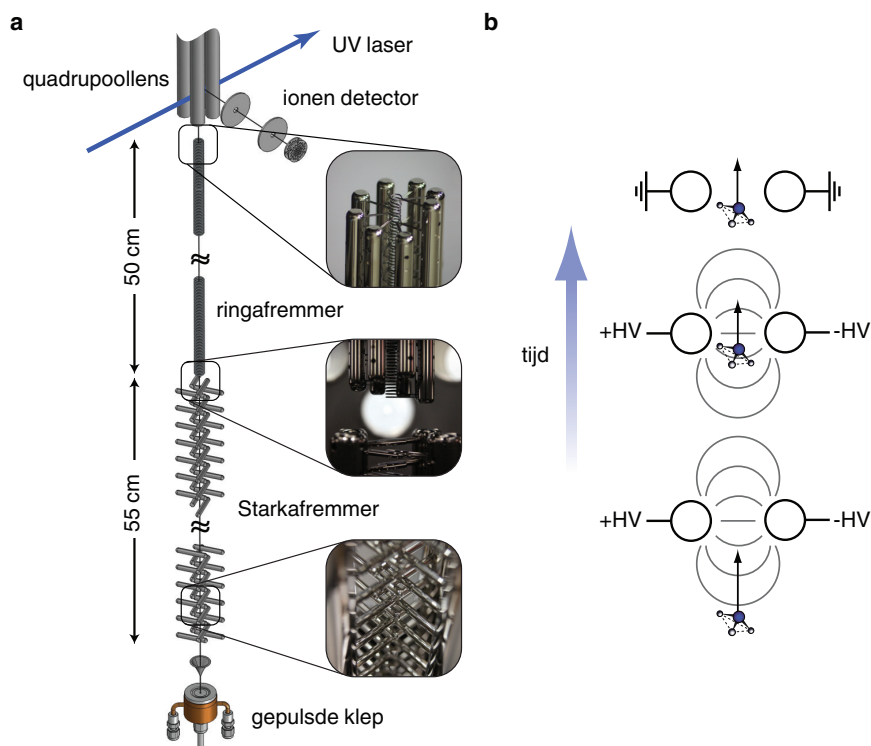
of op dezelfde manier; sommige kleuren worden veel roder, terwijl andere juist een klein beetje blauwer worden en weer andere helemaal niet veranderen. De manier waarop een bepaalde absorptieovergang verandert wordt aangegeven door middel van een gevoeligheidsfactor, K_μ . Een gevoeligheidsfactor van -1 betekent dat als μ 1% groter wordt, de energie van het geabsorbeerde licht 1% kleiner (roder) wordt.

Als de waarde van μ daadwerkelijk verandert dan zal de verandering in μ – en daarmee ook de verandering in het spectrum van een molecuul – onvoorstelbaar klein zijn. In de praktijk worden er drie strategieën gebruikt om zo'n onvoorstelbaar kleine verandering in het spectrum van een molecuul te detecteren. De eerste methode is gebaseerd op het vergelijken van astrofysische waarnemingen met nauwkeurige laboratoriummetingen en de aanname dat de waarde van μ elk jaar een beetje verandert. Licht dat (gedeeltelijk) is geabsorbeerd door moleculen in het vroege universum doet er namelijk miljarden jaren over om de aarde te bereiken. De tweede methode maakt gebruik van extreem nauwkeurige metingen op aarde over een periode van een paar jaar om een verandering in μ te detecteren. Het voordeel van deze studies is de experimentele controle die mogelijk is in het lab. De derde methode is gebaseerd op redelijk nauwkeurige metingen in combinatie met een molecuul dat een spectrum heeft dat extreem gevoelig is voor een verandering in μ , dus een molecuul met hoge gevoeligheidsfactoren.

Dit proefschrift bestaat grofweg uit twee delen. Het eerste deel beschrijft een experiment dat als doel heeft om in het lab extreem nauwkeurige metingen te verrichten aan ammoniak moleculen (NH_3). In het tweede deel worden de gevoeligheidsfactoren van een aantal moleculen berekend. Sommige overgangen in deze moleculen – met name die in methanol (CH_3OH) – zijn uitermate gevoelig voor een verandering in μ . Aangezien methanolmoleculen zijn gedetecteerd in een gaswolk in het vroege universum is dit molecuul met name relevant voor astrofysische waarnemingen.

Een moleculaire fontein

Het tellen van een aantal gebeurtenissen in een bepaalde tijd, ofwel de frequentie, is de fysische grootte die met de hoogste nauwkeurigheid kan worden bepaald. Niet voor niets is de seconde gedefinieerd als de duur van 9 192 631 770 perioden van de straling die correspondeert met een specifieke overgang in het cesiumatoom. De precisie van een frequentiemeting, zoals die aan het cesiumatoom, wordt uiteindelijk gelimiteerd door de totale meettijd. Deze meettijd wordt bepaald door de grootte van de interactiezone en de snelheid waarmee de deeltjes door de interactiezone vliegen. Een heel precieze meting vraagt dus een lange interactiezone en een lage snelheid. Een opstelling die deze twee eigenschappen combineert is een atomaire fontein. In een fontein worden atomen met een hele lage snelheid omhoog geschoten en vallen daarna onder invloed van de zwaartekracht weer naar beneden. Tijdens deze vlucht komen de atomen tweemaal door dezelfde interactiezone. Het bijzondere van deze techniek, Ramsey spectroscopie genaamd, is dat de tijd tussen het tweemaal passeren van de interactiezone geldt als de totale meettijd. Hoewel het idee voor een atomaire fontein in de jaren 50 van de vorige eeuw is ontstaan duurde het tot 1989 voor er een



FIGUUR 1: (a) Schematische weergave van de experimentele opstelling die is gebruikt om ammoniakmoleculen af te remmen en op te sluiten. Door ammoniakgas te laten expanderen in vacuüm ontstaat er een bundel moleculen met een snelheid van ongeveer 300 m/s. Met behulp van hoge elektrische velden in de Starkafremmer worden deze moleculen afgeremd tot 100 m/s. De langzame moleculen vliegen vervolgens de ringafremmer in. Door oscillerende spanningen op de ringvormige elektrodes te zetten ontstaat er een val die met de moleculen meereist. Het verlagen van de frequentie van de oscillerende spanningen verlaagt eveneens de snelheid van de val en remt de ammoniakmoleculen verder af. Op deze manier kunnen de ammoniakmoleculen zelfs worden opgesloten op een willekeurige plaats in de ringafremmer. (b) *Het principe van de Starkafremmer.* Wanneer een ammoniakmolecuul een inhomogeen elektrisch veld invliegt, ondervindt het molecuul een kracht waarvan de richting en grootte afhankelijk zijn van de energietoestand waarin het molecuul zich bevindt. Voor bepaalde energietoestanden van ammoniak leidt het elektrisch veld dat gevormd wordt door twee cilindervormige elektrodes ertoe dat het molecuul wordt afgeremd bij het invliegen van het veld en weer versneld bij het uitvliegen van het veld. Er is dus geen netto effect op de snelheid. Als het veld echter wordt uitgeschakeld als het molecuul zich nog tussen de elektrodes bevindt, zal het molecuul zijn lagere snelheid behouden. In onze Starkafremmer herhalen we dit principe honderd keer om de ammoniakmoleculen af te remmen.

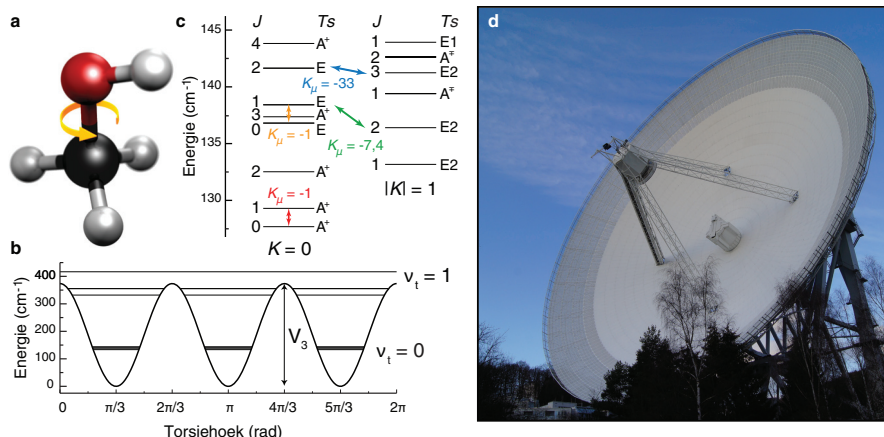
werkende fontein kon worden gerealiseerd. De cruciale stap in de verwezenlijking van een fontein was de ontwikkeling van laserkoeling van atomen, waardoor extreem koude en langzame pakketjes atomen met een hoge dichtheid beschikbaar werden.

In Hoofdstuk 2 wordt uitgelegd hoe wij met hoge elektrische velden ammoniak-moleculen proberen af te remmen om een koud en langzaam pakketje moleculen te maken dat gebruikt kan worden in een moleculaire fontein. Het afgeremde pakketje moleculen wordt omhoog geschoten en met behulp van elektrostatische lenzen bij elkaar gehouden. Ammoniak is om meerdere redenen een geschikt molecuul voor dit experiment. Allereerst is ammoniak een licht molecuul met een relatief groot dipoolmoment waardoor de beweging betrekkelijk eenvoudig te manipuleren is met behulp van elektrische velden. Daarnaast is er een overgang in ammoniak die redelijk gevoelig is voor een verandering in μ ($K_\mu = -4, 2$).

Hoewel in de opstelling die beschreven staat in Hoofdstuk 2 moleculen met een snelheid van 300 m/s konden worden afgeremd tot 5 m/s is het helaas nog niet gelukt om deze moleculen terug te zien vallen. De belangrijkste redenen hiervoor zijn (i) de lage dichtheid van het pakketje langzame moleculen, (ii) een relatief hoog achtergrondsignaal en (iii) de complexiteit van het lenzensysteem. Om deze problemen te verhelpen is de opstelling op twee punten aangepast. Deze aanpassingen worden beschreven in de Hoofdstukken 3 en 4. Een schematische weergave van de aangepaste opstelling is te zien in Figuur 1a. Ten eerste is er voor een detectiemethode gekozen die onderscheid maakt tussen langzame en snelle moleculen. Hierdoor is het mogelijk alleen naar de langzame moleculen te kijken en deze bijna zonder achtergrond te detecteren (Hoofdstuk 3). Bij de tweede aanpassing, beschreven in Hoofdstuk 4, is het complexe lenzensysteem vervangen door een nieuw type afremmer, bestaande uit een serie ringelektroden, die recht boven de oorspronkelijke afremmer is geplaatst. De eerste afremmer wordt gebruikt om de snelheid van de moleculen terug te brengen tot 100 m/s (zie Figuur 1b). In de ringafremmer kan dit pakketje moleculen vervolgens verder worden afgeremd en zelfs worden opgesloten. Doordat de elektrische spanningen op de ringelektroden willekeurig aan te passen zijn geeft deze afremmer een ongekende controle over de beweging van de moleculen. Daarnaast is de nieuwe afremmer veel stabiel bij lage snelheden dan de oude conventionele afremmer. Deze aanpassingen zouden de realisatie van een moleculaire fontein mogelijk moeten maken.

Een alcoholtest voor zwalkende constanten

Methanol, weergegeven in Figuur 2a en uitvoerig beschreven in Hoofdstuk 5, is het kleinste alcoholmolecuul en bestaat uit een methylgroep (CH_3) met daaraan een hydroxylgroep (OH). De CO-binding is niet star, zodat de methylgroep kan draaien ten opzichte van de hydroxylgroep. Deze zogenaamde interne rotatie wordt sterk gehinderd door de waterstofatomen op beide groepen met als gevolg dat er bij een volledige rotatie drie energiebarrières moeten worden overwonnen, zoals te zien in Figuur 2b. In het extreme geval dat de barrières oneindig hoog zijn, vindt er geen interne rotatie plaats, maar oscilleert de hydroxylgroep in een van de drie equivalente energiminima. De oplossingen van de Schrödingervergelijking komen in dit geval overeen met die van



FIGUUR 2: (a) Schematische weergave van de structuur van een methanolmolecuul. De zwarte en rode bol stellen respectievelijk een koolstof- en zuurstofatoom voor, terwijl de witte bollen de waterstofatomen representeren. De gele pijl geeft de interne rotatie aan tussen de OH- en CH₃-groep. (b) Potentiële energie als functie van de hoek tussen de hydroxyl- (OH) en methylgroep (CH₃) (c) Energie van de laagste torsie-rotatietoestanden van methanol. De overgangen die zijn aangegeven met de gekleurde pijlen zijn gemeten in een gaswolk op 7 miljard lichtjaar van de aarde. (d) Foto van de radiotelescoop in Effelsberg die gebruikt is om de overgangen in methanol te meten.

een drievoudig ontaarde harmonische oscillator. In het andere uiterste is de barrière verwaarloosbaar laag en kunnen de groepen vrij links- of rechtsom draaien ten opzichte van elkaar en zijn de energieniveaus tweevoudig ontaard. De hoogte van de barrière in methanol ligt tussen deze twee extremen in. Klassiek gezien kan de interne rotatie alleen plaatsvinden wanneer de rotatie-energie hoog genoeg is om de barrière te overwinnen. Dankzij het quantummechanische tunneleffect kan het waterstofatoom door de barrière heen “tunnelen” om zich zo van het ene naar het andere minimum te verplaatsen. Als gevolg van deze tunnelbeweging worden de energieniveaus van de harmonische oscillator in drieën gesplitst. Deze drie niveaus worden aangeduid met de symmetrielabels A, E1 en E2. Naast interne rotatie (of torsie) van de methyl- en hydroxylgroep langs de CO-binding kan het methanolmolecuul draaien langs zijn drie ruimteassen. De totale energie is de som van de torsie- en algehele rotatie-energie.

De grootte van de splitsing van de energieniveaus in methanol hangt exponentieel af van de hoogte van de barrière en van de “effectieve massa” die door de barrière heen tunnelt. Het ligt dus voor de hand dat het energieverschil tussen bijvoorbeeld een A- en een E1-niveau of tussen een E1- en E2-niveau erg gevoelig is voor een verandering in μ . Het blijkt dat het energieverschil tussen de niveaus in methanol 2,5% kleiner wordt, als μ 1% groter wordt, dus $K_{\mu} = -2,5$. Helaas volgt uit quantummechanische selectieregels dat er geen overgangen mogelijk zijn tussen de A-, E1- en E2-niveaus omdat deze een andere symmetrie hebben. Alleen overgangen tussen dezelfde symmetrietoestand zijn

toegestaan. Interessant genoeg zal blijken dat juist deze overgangen extreem gevoelig zijn voor een variatie in de waarde van μ .

In Figuur 2c staan de laagste torsie-rotatietoestanden van methanol schematisch weergegeven. De gekleurde pijlen geven een aantal mogelijke overgangen aan. Om de verschillende overgangen in methanol te karakteriseren wordt, naast de symmetrie van de niveaus, gebruikgemaakt van de twee quantumgetallen J en K . Bij een overgang tussen niveaus met verschillende J maar gelijke K (rode en gele pijl), verandert alleen de rotatie-energie van het molecuul (de torsie-energie blijft gelijk). De gevoeligheidsfactor van deze overgangen is $K_\mu = -1$. Wanneer ook de waarde van K verandert, verandert naast de rotatie-energie ook de torsie-energie. Omdat rotatie- en torsie-energie beiden op een andere manier afhankelijk zijn van μ , zal een verandering in μ altijd een absolute verandering in de overgangsenergie teweegbrengen. Voor sommige overgangen gebeurt er iets interessants: het verschil in rotatie-energie wordt grotendeels gecompenseerd door het verschil in torsie-energie en de twee niveaus hebben bijna dezelfde energie. Hierdoor wordt de relatieve verandering in de overgangsenergie enorm versterkt. Overgangen waarbij algehele rotatie wordt omgezet in interne rotatie (of andersom) vertonen dus de grootste gevoeligheid voor μ -variatie. De gevoeligheidsfactoren voor de overgangen aangegeven met de groene en blauwe pijl zijn respectievelijk -7 , 4 en -33 . Wat methanol erg bijzonder maakt is de aanwezigheid van overgangen die compleet anders reageren op een verandering in μ . Het is dus mogelijk om variatie van μ te onderzoeken door enkel gebruik te maken van overgangen in methanol, waardoor een groot aantal systematische effecten te vermijden is. Met de 100 m radiotelescoop in Effelsberg (Figuur 2d) hebben wij de vier aangegeven overgangen in Figuur 2c geobserveerd in een gaswolk op 7 miljard lichtjaar van de aarde. Door de posities van deze lijnen te vergelijken met metingen op aarde konden wij vaststellen dat een verandering in μ op deze tijdschaal kleiner moet zijn dan éénhonderdduizendste procent.

In Hoofdstuk 6 van dit proefschrift wordt onderzocht in hoeverre moleculen die vergelijkbaar zijn met methanol geschikt zijn bij de zoektocht naar μ -variatie. Uit deze analyse blijkt dat methanol de hoogste gevoeligheidsfactoren heeft en dat het onwaarschijnlijk is dat er een ander molecuul wordt gevonden met interne rotatie met hogere gevoeligheidsfactoren. In Hoofdstuk 7 worden de gevoeligheidsfactoren bepaald voor methylamine. Dit molecuul ondergaat zowel interne rotatie als inversie en lijkt daarom op methanol en ammoniak.



SCALING OF MOLECULAR CONSTANTS

TABLE A.1: Molecular constants used to simulate the torsional groundstate of $^{12}\text{CH}_3^{16}\text{OH}$, taken from Ref. [133]. The last column shows the dependence of these constants to the proton-to-electron mass ratio, μ . The rotational, centrifugal and torsional constants A, B, C, D_{ab}, F and ρ are explicit functions of I_a, I_b , and I_c and are given in Ref. [127]. The dependence of these constants on μ can be obtained by realizing that all moments of inertia are directly proportional to μ . Within the Born-Oppenheimer approximation the torsional potential, V_3 , is independent of the mass of the nuclei and hence of μ . The higher order constants can be considered as products of the first 7 constants.

Term order $\{nlm\}$	Operator	Parameter		$^{12}\text{CH}_3^{16}\text{OH}$	μ dependence
		In BELGI	Literature		
{220}	P_γ^2	FPARA	F	27.64684641(28)	μ^{-1}
	$(1 - \cos 3\gamma)/2$	V3	V_3	373.554746(12)	μ^0
{211}	$P_\gamma P_a$	RHORHO	ρ	0.8102062230(37)	μ^0
{202}	P_a^2	OA	A	4.2537233(71)	μ^{-1}
	P_b^2	B	B	0.8236523(70)	μ^{-1}
	P_c^2	C	C	0.7925575(71)	μ^{-1}
	$\{P_a, P_b\}$	DAB	D_{ab}	-0.0038095(38)	μ^{-1}
{440}	P_γ^4	AK4	$F_m(k_4)$	-8.976763(48) $\times 10^{-3}$	μ^{-2}
	$(1 - \cos 6\gamma)/2$	V6	V_6	-1.319650(85)	μ^0
{431}	$P_\gamma^3 P_a$	AK3	$\rho_m(k_3)$	-3.504714(14) $\times 10^{-2}$	μ^{-1}
{422}	$P_\gamma^2 P^2$	GV	$F_J(G_v)$	-1.373(31) $\times 10^{-4}$	μ^{-2}
	$P_\gamma^2 P_a^2$	AK2	$F_K(k_2)$	-5.188031(18) $\times 10^{-2}$	μ^{-2}
	$P_\gamma \{P_a, P_b\}$	DELTA	$F_{ab}(\Delta_{ab})$	3.112(23) $\times 10^{-3}$	μ^{-2}
	$2P_\gamma^2(P_b^2 - P_c^2)$	C1	$F_{bc}(c_1)$	-0.1955(97) $\times 10^{-4}$	μ^{-2}
	$(1 - \cos 3\gamma)P^2$	FV	$V_{3J}(F_v)$	-2.4324(69) $\times 10^{-3}$	μ^{-1}
	$(1 - \cos 3\gamma)P_a^2$	AK5	$V_{3K}(k_5)$	1.117844(23) $\times 10^{-2}$	μ^{-1}
	$(1 - \cos 3\gamma)\{P_a, P_b\}$	ODAB	$V_{3ab}(d_{ab})$	9.07791(65) $\times 10^{-3}$	μ^{-1}
	$(1 - \cos 3\gamma)(P_b^2 - P_c^2)$	C2	$V_{3bc}(c_2)$	-8.698(21) $\times 10^{-5}$	μ^{-1}
	$\sin 3\gamma\{P_a, P_c\}$	DAC	$D_{3ac}(D_{ac})$	5.177(29) $\times 10^{-2}$	μ^{-1}
	$\sin 3\gamma\{P_b, P_c\}$	DBC	$D_{3bc}(D_{bc})$	0.538(12) $\times 10^{-3}$	μ^{-1}
	$P_\gamma P_a P^2$	ALV	$\rho_J(L_v)$	-2.305(54) $\times 10^{-4}$	μ^{-1}
{413}					

TABLE A.1: *Continued.*

Term order $\{nlm\}$	Operator	Parameter		$^{12}\text{CH}_3^{16}\text{OH}$	μ dependence
		In BELGI	Literature		
{404}	$P_\gamma P_a^3$	AK1	$\rho_K(k_1)$	$-3.4254(13) \times 10^{-2}$	μ^{-1}
	$P_\gamma(P_a^2 P_b + P_b P_a^2)$	ODELTA	$\rho_{ab}(\delta_{ab})$	$4.496(33) \times 10^{-3}$	μ^{-1}
	$P_\gamma\{P_a, (P_b^2 - P_c^2)\}$	C4	$\rho_{bc}(c_4)$	$-0.7047(94) \times 10^{-4}$	μ^{-1}
	$-P^4$	DJ	Δ_J	$1.688465(31) \times 10^{-6}$	μ^{-2}
	$-P^2 P_a^2$	DJK	Δ_{JK}	$9.20(25) \times 10^{-5}$	μ^{-2}
	$-P^4$	DK	Δ_K	$8.524(10) \times 10^{-3}$	μ^{-2}
	$-2P^2(P_b^2 - P_c^2)$	ODELN	δ_J	$5.9414(33) \times 10^{-8}$	μ^{-2}
	$-\{P_a^2, (P_b^2 - P_c^2)\}$	ODELK	δ_K	$5.7361(89) \times 10^{-5}$	μ^{-2}
	$\{P_a, P_b\} P^2$	DABJ	D_{abJ}	$-0.548(23) \times 10^{-7}$	μ^{-2}
	$\{P_a^3, P_b\}$	DABK	D_{abK}	$1.443(11) \times 10^{-3}$	μ^{-2}
{660}	P_γ^6	AK4B	$F_{mm}(k_{4B})$	$1.01639(75) \times 10^{-5}$	μ^{-3}
	$(1 - \cos 9\gamma)/2$	V9	V_9	$-0.05126(34)$	μ^0
{651}	$P_\gamma^5 P_a$	AK3B	$\rho_{mm}(k_{3B})$	$6.7042(35) \times 10^{-5}$	μ^{-2}
{642}	$P_\gamma^4 P^2$	AMV	$F_{mJ}(M_\gamma)$	$9.215(14) \times 10^{-8}$	μ^{-3}
	$P_\gamma^4 P_a^2$	BK1	$F_{mK}(K_1)$	$1.79670(69) \times 10^{-4}$	μ^{-3}
{633}	$P_\gamma^4\{P_a, P_b\}$	DELTAB	$F_{mab}(\Delta\Delta_{ab})$	$0.773(54) \times 10^{-6}$	μ^{-3}
	$2P_\gamma^4(P_b^2 - P_c^2)$	C3	$F_{mbc}(c_3)$	$0.214(18) \times 10^{-7}$	μ^{-3}
	$\{(1 - \cos 3\gamma), P_\gamma^2\} P^2$	AK7J	$V_{3mJ}(k_{7J})$	$9.4(16) \times 10^{-6}$	μ^{-2}
	$(1 - \cos 6\gamma) P^2$	ANV	$V_{6J}(N_\gamma)$	$2.64(53) \times 10^{-5}$	μ^{-1}
	$(1 - \cos 6\gamma) P_a^2$	BK2	$V_{6K}(K_2)$	$-1.3905(25) \times 10^{-4}$	μ^{-1}
	$(1 - \cos 6\gamma)\{P_a, P_b\}$	ODAB6	$V_{6ab}(d\Delta_{ab})$	$-0.388(16) \times 10^{-4}$	μ^{-1}
	$(1 - \cos 6\gamma)(P_b^2 - P_c^2)$	C11	$V_{6bc}(c_{11})$	$-3.3840(70) \times 10^{-5}$	μ^{-1}
	$\sin 6\gamma\{P_a, P_c\}$	DAC6	D_{6ac}	$3.401(58) \times 10^{-4}$	μ^{-1}
	$P_\gamma^3 P_a P^2$	AK3J	$\rho_{mJ}(k_{3J})$	$7.875(69) \times 10^{-7}$	μ^{-2}
	$P_\gamma^3 P_a^3$	AK3K	$\rho_{mK}(k_{3K})$	$2.51512(70) \times 10^{-4}$	μ^{-2}
{624}	$P_\gamma^3\{P_a^2, P_b\}$	ODELTB	$\rho_{mab}(\delta\delta_{ab})$	$1.61(11) \times 10^{-6}$	μ^{-2}
	$P_\gamma^3\{P_a, (P_b^2 - P_c^2)\}$	C12	$\rho_{mbc}(c_{12})$	$6.903(52) \times 10^{-7}$	μ^{-2}
	$\{(1 - \cos 3\gamma), P_a P^2 P_\gamma\}$	AK6J	$\rho_{3J}(k_{6J})$	$2.11(27) \times 10^{-5}$	μ^{-1}
	$\{(1 - \cos 3\gamma), P_a^2 P_\gamma\}$	AK6K	$\rho_{3K}(k_{6K})$	$0.385(63) \times 10^{-4}$	μ^{-1}
	$P^2 P^4$	GVJ	$F_{JJ}(g_\gamma)$	$0.5243(22) \times 10^{-9}$	μ^{-3}
	$P_\gamma^2 P_a^2 P^2$	AK2J	$F_{JK}(k_{2J})$	$1.769(19) \times 10^{-6}$	μ^{-3}
	$P_\gamma^2\{P_a, P_b\} P^2$	DELTAJ	F_{Jab}	$2.75(21) \times 10^{-9}$	μ^{-3}
	$P_\gamma^2 P_a^4$	AK2K	$F_{KK}(k_{2K})$	$1.94907(47) \times 10^{-4}$	μ^{-3}
	$P_\gamma^2\{P_a^3, P_b\}$	DELTAK	F_{Kab}	$8.29(59) \times 10^{-7}$	μ^{-3}
	$P_\gamma^2\{P_a^2, (P_b^2 - P_c^2)\}$	C1K	$F_{Kbc}(c_8)$	$1.518(15) \times 10^{-6}$	μ^{-3}
{615}	$(1 - \cos 3\gamma) P^4$	OFV	$V_{3JJ}(f_\gamma)$	$9.149(21) \times 10^{-9}$	μ^{-2}
	$(1 - \cos 3\gamma) P_a^2 P^2$	AK5J	$V_{3JK}(k_{5J})$	$7.6(26) \times 10^{-6}$	μ^{-2}
	$(1 - \cos 3\gamma)\{P_a, P_b\} P^2$	ODABJ	$V_{3Jab}(d_{abJ})$	$-2.027(17) \times 10^{-7}$	μ^{-2}
	$2(1 - \cos 3\gamma)(P_b^2 - P_c^2) P^2$	C2J	$V_{3Jbc}(c_{2J})$	$1.251(43) \times 10^{-9}$	μ^{-2}
	$(1 - \cos 3\gamma) P_a^4$	AK5K	$V_{3KK}(f_k)$	$0.78(10) \times 10^{-4}$	μ^{-2}
	$(1 - \cos 3\gamma)\{P_a^3, P_b\}$	ODABK	$V_{3Kab}(d_{abK})$	$-1.538(79) \times 10^{-7}$	μ^{-2}
	$(1 - \cos 3\gamma)\{P_a^2, (P_b^2 - P_c^2)\}$	C2K	$V_{3Kbc}(c_9)$	$7.232(86) \times 10^{-6}$	μ^{-2}
	$\sin 3\gamma P^2\{P_a, P_c\}$	DACJ	D_{3acJ}	$-2.888(23) \times 10^{-7}$	μ^{-2}
	$\sin 3\gamma P^2\{P_b, P_c\}$	DBCJ	D_{3bcJ}	$-1.070(58) \times 10^{-8}$	μ^{-2}
	$\sin 3\gamma\{P_a^3, P_c\}$	DACK	D_{3acK}	$0.70(10) \times 10^{-6}$	μ^{-2}
{606}	$\sin 3\gamma\{P_a^2, \{P_b, P_c\}\}$	DBCK	D_{3bcK}	$-0.585(70) \times 10^{-6}$	μ^{-2}
	$P_\gamma P_a P^4$	OLV	$\rho_{JJ}(l_\gamma)$	$0.8961(62) \times 10^{-9}$	μ^{-2}
	$P_\gamma^3 P_a^2 P^2$	AK1J	$\rho_{JK}(l_\gamma)$	$1.231(14) \times 10^{-6}$	μ^{-2}
	$P_\gamma P^2\{P_a^2, P_b\}$	DAGJ	ρ_{Jab}	$1.91(18) \times 10^{-9}$	μ^{-2}
	$P_\gamma P^2\{P_a, (P_b^2 - P_c^2)\}$	C4J	$\rho_{Jbc}(c_7)$	$0.426(33) \times 10^{-9}$	μ^{-2}
	$P_\gamma P_a^5$	AK1K	$\rho_{KK}(l_k)$	$7.9805(24) \times 10^{-5}$	μ^{-2}
	$P_\gamma\{P_a^3, (P_b^2 - P_c^2)\}$	C4K	$\rho_{Kbc}(c_{7K})$	$1.119(16) \times 10^{-6}$	μ^{-2}
	P^6	HJ	H_J	$-1.191(16) \times 10^{-12}$	μ^{-3}

TABLE A.1: Continued.

Term order	Operator	Parameter		$^{12}\text{CH}_3^{16}\text{OH}$	μ dependence
$\{nlm\}$		In BELGI	Literature		
{880}	$P_a^4 P_a^2$	HJK	H_{JK}	$4.781(40) \times 10^{-10}$	μ^{-3}
	$P_a^4 p^2$	HKJ	H_{KJ}	$2.336(37) \times 10^{-7}$	μ^{-3}
	P_a^6	HK	H_K	$1.35675(51) \times 10^{-5}$	μ^{-3}
	$P_a^2 \{P_a^2, (P_b^2 - P_c^2)\}$	OHJK	h_{JK}	$0.427(31) \times 10^{-9}$	μ^{-3}
	$\{P_a^4, (P_b^2 - P_c^2)\}$	OHK	h_K	$2.928(54) \times 10^{-7}$	μ^{-3}
	P_a^8	AK4C	$F_{mmm}(k_{4BB})$	$-0.5887(30) \times 10^{-7}$	μ^{-4}
	$P_a^7 P_a$	AK3C	$\rho_{mmm}(k_{3BB})$	$-0.3447(19) \times 10^{-6}$	μ^{-3}
	$P_a^6 p^2$	AK4BJ	F_{mmj}	$-0.4129(60) \times 10^{-9}$	μ^{-4}
	$P_a^6 P_a^2$	AK4BK	F_{mmK}	$-0.8527(55) \times 10^{-6}$	μ^{-4}
	$(1 - \cos 9\gamma) P^2$	V9J	V_{9J}	$-1.31(66) \times 10^{-6}$	μ^{-1}
{853}	$(1 - \cos 9\gamma) \{P_a, P_b\}$	ODAB9	V_{9ab}	$-0.819(43) \times 10^{-4}$	μ^{-1}
	$P_a^5 P_a P^2$	AK3BJ	ρ_{mmj}	$-1.635(26) \times 10^{-9}$	μ^{-3}
	$P_a^5 p^3$	AK3BK	ρ_{mmK}	$-1.1548(88) \times 10^{-6}$	μ^{-3}
	$P_a^4 P_a^2 P^2$	G4J2K2	$F_{mJK}(K_{1J})$	$-2.097(63) \times 10^{-9}$	μ^{-4}
{844}	$P_a^4 P^2 \{P_a, P_b\}$	DG4J	F_{mJab}	$-8.67(73) \times 10^{-12}$	μ^{-4}
	$P_a^4 P_a^4$	G4K4	$F_{mKK}(K_{1K})$	$-0.9220(84) \times 10^{-6}$	μ^{-4}
	$P_a^4 \{P_a^2, (P_b^2 - P_c^2)\}$	G4BCK	F_{mKbc}	$0.886(95) \times 10^{-10}$	μ^{-4}
	$(1 - \cos 6\gamma) P_a^4$	C6J4	$V_{6JJ}(N_{vJ})$	$4.44(32) \times 10^{-10}$	μ^{-2}
	$(1 - \cos 6\gamma) P^2 P_a^2$	C6J2K2	V_{6JK}	$1.953(61) \times 10^{-7}$	μ^{-2}
	$(1 - \cos 6\gamma) P^2 \{P_a, P_b\}$	CABJ	V_{6Jab}	$3.50(15) \times 10^{-8}$	μ^{-2}
	$2(1 - \cos 6\gamma) P^2 (P_b^2 - P_c^2)$	C6BCJ	V_{6Jbc}	$1.326(52) \times 10^{-9}$	μ^{-2}
	$(1 - \cos 6\gamma) P_a^4$	C6K4	V_{6KK}	$-3.143(66) \times 10^{-7}$	μ^{-2}
	$(1 - \cos 6\gamma) \{P_a^3, P_b\}$	CABK	$V_{6Kab}(dd_{abK})$	$2.26(21) \times 10^{-7}$	μ^{-2}
	$(1 - \cos 6\gamma) \{P_a^2, (P_b^2 - P_c^2)\}$	C6BCK	$V_{6Kbc}(c_{11K})$	$-1.351(43) \times 10^{-7}$	μ^{-2}
{835}	$P_a^3 p^3 P^2$	GAJ2K2	ρ_{mJK}	$-1.062(64) \times 10^{-9}$	μ^{-3}
	$P_a^3 p^5$	GAK4	ρ_{mKK}	$-4.305(48) \times 10^{-7}$	μ^{-3}
	$P_a^3 \{P_a^3, (P_b^2 - P_c^2)\}$	AG3BCK	ρ_{mKbc}	$8.66(94) \times 10^{-11}$	μ^{-3}
	$\{(1 - \cos 3\gamma), P_a^3 P_a\} P^2$	AK6JK	ρ_{3JK}	$5.58(22) \times 10^{-8}$	μ^{-2}
{826}	$P_a^2 p^2 P^4$	GJ4K2	F_{JJK}	$1.477(32) \times 10^{-12}$	μ^{-4}
	$P_a^2 P_a^4 P^2$	GJ2K4	F_{JKK}	$-1.90(20) \times 10^{-10}$	μ^{-4}
	$P_a^2 p^2 \{P_a^3, P_b\}$	DELTJK	F_{JKab}	$4.53(59) \times 10^{-12}$	μ^{-4}
	$P_a^2 P_a^6$	GK6	F_{KKK}	$-1.068(15) \times 10^{-7}$	μ^{-4}
	$P_a^2 \{P_a^5, P_b\}$	DELTKK	F_{KKab}	$-0.89(11) \times 10^{-11}$	μ^{-4}
	$(1 - \cos 3\gamma) P^2 P_a^4$	FJ2K4	V_{3JKK}	$0.914(36) \times 10^{-7}$	μ^{-3}
	$(1 - \cos 3\gamma) P_a^6$	FK6	V_{3KKK}	$-1.00(46) \times 10^{-10}$	μ^{-3}
	$\sin 3\gamma P^4 \{P_a, P_c\}$	DACJJ	D_{3acJJ}	$-0.717(46) \times 10^{-11}$	μ^{-3}
	$\sin 3\gamma P^2 \{P_a^3, P_c\}$	DACJK	D_{3acJK}	$-1.593(30) \times 10^{-9}$	μ^{-3}
	$P_a^3 p^3 P^4$	AGJ4K2	ρ_{JJK}	$1.192(20) \times 10^{-12}$	μ^{-3}
{817}	$P_a^3 P_a^7$	AGK6	$\rho_{KKK}(I_{KK})$	$-1.033(21) \times 10^{-8}$	μ^{-3}
	P_a^{10}	AK4D	F_{mmmm}	$-0.940(20) \times 10^{-10}$	μ^{-5}
{10100}	P_a^9	AK3D	ρ_{mmmm}	$-4.663(92) \times 10^{-10}$	μ^{-4}
{1091}	$P_a^8 P_a$	AK4CK	F_{mmmmK}	$-0.939(17) \times 10^{-9}$	μ^{-5}
{1082}	$P_a^8 p^2$	AK4CK	F_{mmmmK}	$-0.939(17) \times 10^{-9}$	μ^{-5}
{1073}	$P_a^7 P_a^3$	AK3CK	ρ_{mmmmK}	$-0.957(17) \times 10^{-9}$	μ^{-4}
{1064}	$P_a^6 P_a^4$	AK4BK4	F_{mmKK}	$-4.915(82) \times 10^{-10}$	μ^{-5}
{1055}	$P_a^5 p^5$	AK3BK4	ρ_{mmKK}	$-1.017(16) \times 10^{-10}$	μ^{-4}

SENSITIVITY COEFFICIENTS OF SELECTED TRANSITIONS IN METHANOL (CH₃OH)

TABLE B.1: Selected transitions in methanol (CH₃OH) with a lower-level excitation energy below 100 cm⁻¹. The fourth and fifth column list the excitation temperature of the lower state and the transition strength multiplied by the electric dipole moment squared, μ_e^2 , respectively. Sensitivity coefficients of the transitions to a possible variation of the proton-to-electron mass ratio are quoted in the last column. Transition frequencies are calculated with BELGI [134] using the parameters and line list of Xu *et al.* [133]

Upper state			Lower state			Transition (MHz)	Excitation (K)	$S\mu_e^2$ (D ²)	K_μ
<i>J</i>	<i>K</i>	Sym	<i>J</i>	<i>K</i>	Sym				
1	1	A ⁻	1	1	A ⁺	834.280	16.8	1.213	-1.0
2	1	A ⁻	2	1	A ⁺	2 502.768	21.4	0.673	-1.0
3	1	A ⁻	3	1	A ⁺	5 005.302	28.3	0.469	-1.0
5	1	A ⁺	6	0	A ⁺	6 668.567	48.7	5.077	-42.1
4	1	A ⁻	4	1	A ⁺	8 341.590	37.6	0.361	-1.0
9	-1	E	8	-2	E	9 936.137	101.6	2.776	11.3
4	3	A ⁺	5	2	A ⁺	9 978.718	72.5	0.568	53.7
4	3	A ⁻	5	2	A ⁻	10 058.295	72.5	0.568	53.3
2	0	E	3	-1	E	12 178.587	11.6	1.985	-32.8
5	1	A ⁻	5	1	A ⁺	12 511.159	49.1	0.293	-1.0
6	1	A ⁻	6	1	A ⁺	17 513.281	62.9	0.246	-1.0
2	1	E	3	0	E	19 967.376	13.9	0.924	-5.9
9	2	A ⁺	10	1	A ⁺	23 120.916	141.1	3.146	-11.6
7	1	A ⁻	7	1	A ⁺	23 346.879	79.0	0.211	-1.0
10	1	A ⁻	9	2	A ⁻	23 444.760	142.1	3.542	9.5
3	2	E	3	1	E	24 928.726	21.9	2.807	18.0
4	2	E	4	1	E	24 933.502	31.1	3.927	18.0
2	2	E	2	1	E	24 934.399	14.9	1.594	18.0
5	2	E	5	1	E	24 959.120	42.7	5.025	17.9
6	2	E	6	1	E	25 018.173	56.7	6.127	17.9
7	2	E	7	1	E	25 124.929	72.9	7.247	17.8
8	2	E	8	1	E	25 294.480	91.5	8.389	17.6
9	2	E	9	1	E	25 541.464	112.4	9.555	17.4
10	2	E	10	1	E	25 878.334	135.6	10.738	17.1
4	0	E	3	1	E	28 316.085	21.9	1.403	2.5
8	2	A ⁻	9	1	A ⁻	28 969.965	119.9	3.023	-9.5

TABLE B.1: *Continued.*

Upper state			Lower state			Transition (MHz)	Excitation (K)	$S\mu_c^2$ (D ²)	K_μ
J	K	Sym	J	K	Sym				
8	1	A^-	8	1	A^+	30 010.418	97.4	0.185	-1.0
8	1	A^-	8	1	A^+	30 010.418	97.4	0.185	-1.0
4	-1	E	3	0	E	36 169.259	19.2	2.518	9.7
9	1	A^-	9	1	A^+	37 501.779	118.1	0.164	-1.0
9	1	A^-	9	1	A^+	37 501.779	118.1	0.164	-1.0
7	-2	E	8	-1	E	37 703.761	81.2	2.405	-4.3
6	2	A^-	5	3	A^-	38 293.273	84.6	0.948	-15.3
6	2	A^+	5	3	A^+	38 452.632	84.6	0.949	-15.2
7	0	A^+	6	1	A^+	44 069.364	62.9	6.138	5.2
10	1	A^-	10	1	A^+	45 818.114	141.1	0.147	-1.0
9	3	E	10	2	E	45 843.559	136.8	2.653	0.8
1	0	A^+	0	0	A^+	48 372.460	0.0	0.808	-1.0
1	0	E	0	0	E	48 376.887	0.0	0.808	-1.0
4	1	A^+	5	0	A^+	57 032.986	34.8	4.035	-5.8
10	-1	E	9	-2	E	57 292.879	122.5	3.115	1.1
3	3	A^+	4	2	A^+	58 394.958	60.9	0.236	8.3
3	3	A^-	4	2	A^-	58 429.034	60.9	0.236	8.3
1	0	E	2	-1	E	60 531.477	4.6	1.474	-7.4
8	2	A^+	9	1	A^+	66 947.797	118.1	2.745	-4.7
1	1	E	2	0	E	68 305.629	7.0	0.457	-2.4
5	0	E	4	1	E	76 509.685	31.1	1.894	0.3
7	2	A^-	8	1	A^-	80 993.245	98.8	2.522	-4.0
5	-1	E	4	0	E	84 521.170	28.4	3.083	3.6
6	-2	E	7	-1	E	85 568.137	62.7	2.006	-2.4
7	2	A^-	6	3	A^-	86 615.578	98.5	1.357	-7.3
7	2	A^+	6	3	A^+	86 902.919	98.5	1.358	-7.3
8	3	E	9	2	E	94 541.790	113.6	2.235	-0.2
8	0	A^+	7	1	A^+	95 169.388	79.0	7.221	1.9
2	1	A^+	1	1	A^+	95 914.311	16.8	1.214	-1.0
2	-1	E	1	-1	E	96 739.359	0.0	1.213	-1.0
2	0	A^+	1	0	A^+	96 741.371	2.3	1.617	-1.0
2	0	E	1	0	E	96 744.546	2.3	1.616	-1.0
2	1	E	1	1	E	96 755.502	10.2	1.244	-1.0
2	1	A^-	1	1	A^-	97 582.799	16.9	1.214	-1.0
4	-2	E	4	1	E	101 101.739	36.4	0.003	2.6
5	-2	E	5	1	E	101 126.861	48.0	0.009	2.6
6	-2	E	6	1	E	101 185.457	61.9	0.021	2.6
7	-2	E	7	1	E	101 293.419	78.2	0.046	2.6
8	-2	E	8	1	E	101 469.808	96.7	0.091	2.5
9	-2	E	9	1	E	101 737.296	117.6	0.168	2.5
10	-2	E	10	1	E	102 122.779	140.8	0.292	2.5
3	1	A^+	4	0	A^+	107 013.836	23.2	3.009	-3.6
0	0	E	1	-1	E	108 893.948	0.0	0.978	-4.6
7	2	A^+	8	1	A^+	111 289.454	97.4	2.336	-3.2
3	1	E	2	2	E	120 197.466	16.1	0.316	-4.9
2	2	E	1	1	E	121 689.901	10.2	2.829	2.9
6	0	E	5	1	E	124 570.037	42.7	2.399	-0.2
6	2	A^-	7	1	A^-	132 621.824	80.1	2.037	-2.9
6	-1	E	5	0	E	132 890.759	40.0	3.687	1.9
10	-1	E	9	2	E	133 488.712	118.8	0.014	-0.9
5	-2	E	6	-1	E	133 605.445	46.4	1.589	-1.9
8	2	A^-	7	3	A^-	134 896.889	114.8	1.784	-5.1
8	2	A^+	7	3	A^+	135 376.818	114.8	1.787	-5.0
7	-4	E	8	-3	E	137 903.063	138.4	1.164	3.7
7	3	E	8	2	E	143 169.523	92.7	1.813	-0.5
3	1	A^+	2	1	A^+	143 865.796	21.4	2.158	-1.0
3	0	E	2	0	E	145 093.755	7.0	2.424	-1.0
3	-1	E	2	-1	E	145 097.436	4.6	2.157	-1.0
3	0	A^+	2	0	A^+	145 103.186	7.0	2.425	-1.0
3	2	A^-	2	2	A^-	145 124.333	44.7	1.356	-1.0
3	2	E	2	2	E	145 126.192	16.1	1.332	-1.0
3	-2	E	2	-2	E	145 126.387	25.0	1.349	-1.0
3	1	E	2	1	E	145 131.865	14.9	2.212	-1.0
3	2	A^+	2	2	A^+	145 133.417	44.7	1.356	-1.0
3	1	A^-	2	1	A^-	146 368.329	21.6	2.158	-1.0

TABLE B.1: *Continued.*

Upper state			Lower state			Transition (MHz)	Excitation (K)	$S\mu_e^2$ (D ²)	K_μ
J	K	Sym	J	K	Sym				
9	0	A^+	8	1	A^+	146 618.695	97.4	8.329	0.9
10	0	E	10	-1	E	155 320.897	125.3	7.463	-3.5
9	0	E	9	-1	E	155 997.527	102.1	7.181	-3.5
6	2	A^+	7	1	A^+	156 127.545	79.0	1.920	-2.6
8	0	E	8	-1	E	156 488.905	81.2	6.783	-3.5
2	1	A^+	3	0	A^+	156 602.400	13.9	1.996	-2.8
7	0	E	7	-1	E	156 828.520	62.7	6.275	-3.5
6	0	E	6	-1	E	157 048.621	46.4	5.664	-3.5
5	0	E	5	-1	E	157 178.991	32.5	4.959	-3.5
4	0	E	4	-1	E	157 246.066	20.9	4.173	-3.5
1	0	E	1	-1	E	157 270.836	0.0	1.461	-3.5
3	0	E	3	-1	E	157 272.342	11.6	3.318	-3.5
2	0	E	2	-1	E	157 276.023	4.6	2.409	-3.5
1	1	E	1	0	E	165 050.175	2.3	1.347	-1.6
2	1	E	2	0	E	165 061.131	7.0	2.237	-1.6
3	1	E	3	0	E	165 099.241	13.9	3.117	-1.6
4	1	E	4	0	E	165 190.476	23.2	3.981	-1.6
5	1	E	5	0	E	165 369.342	34.8	4.823	-1.6
6	1	E	6	0	E	165 678.651	48.7	5.637	-1.6
7	1	E	7	0	E	166 169.099	65.0	6.416	-1.6
8	1	E	8	0	E	166 898.568	83.5	7.153	-1.6
9	1	E	9	0	E	167 931.059	104.3	7.840	-1.6
4	1	E	3	2	E	168 577.835	23.0	0.707	-3.8
10	1	E	10	0	E	169 335.221	127.5	8.472	-1.6
3	2	E	2	1	E	170 060.591	14.9	3.120	1.8
7	0	E	6	1	E	172 445.840	56.7	2.917	-0.4
7	-1	E	6	0	E	181 295.971	54.0	4.339	1.1
4	-2	E	5	-1	E	181 771.045	32.5	1.161	-1.7
9	2	A^-	8	3	A^-	183 123.788	133.4	2.223	-4.0
5	2	A^-	6	1	A^-	183 852.766	63.7	1.570	-2.3
9	2	A^+	8	3	A^+	183 879.874	133.4	2.230	-4.0
6	-4	E	7	-3	E	186 300.912	119.8	0.796	2.5
6	3	E	7	2	E	191 732.984	74.1	1.392	-0.6
4	1	A^+	3	1	A^+	191 810.504	28.3	3.035	-1.0
4	0	E	3	0	E	193 415.325	13.9	3.232	-1.0
4	-1	E	3	-1	E	193 441.601	11.6	3.033	-1.0
4	0	A^+	3	0	A^+	193 454.360	13.9	3.234	-1.0
4	3	A^+	3	3	A^+	193 471.436	63.7	1.413	-1.0
4	3	A^-	3	3	A^-	193 471.547	63.7	1.413	-1.0
4	3	E	3	3	E	193 474.416	48.5	1.417	-1.0
4	2	A^-	3	2	A^-	193 488.049	51.6	2.441	-1.0
4	-3	E	3	-3	E	193 488.965	68.7	1.423	-1.0
4	1	E	3	1	E	193 506.561	21.9	3.110	-1.0
4	2	A^+	3	2	A^+	193 510.752	51.6	2.441	-1.0
4	-2	E	3	-2	E	193 511.227	31.9	2.429	-1.0
4	2	E	3	2	E	193 511.337	23.0	2.399	-1.0
4	1	A^-	3	1	A^-	195 146.792	28.6	3.035	-1.0
10	0	A^+	9	1	A^+	198 403.066	118.1	9.464	0.4
5	2	A^+	6	1	A^+	201 445.494	62.9	1.502	-2.2
1	1	A^+	2	0	A^+	205 791.276	7.0	0.994	-2.3
1	1	E	0	0	E	213 427.063	0.0	0.894	-1.5
1	1	E	0	0	E	213 427.063	0.0	0.894	-1.5
5	1	E	4	2	E	216 945.525	32.3	1.123	-3.2
4	2	E	3	1	E	218 440.063	21.9	3.476	1.2
8	0	E	7	1	E	220 078.563	72.9	3.447	-0.6
8	0	E	7	1	E	220 078.563	72.9	3.447	-0.6
8	-1	E	7	0	E	229 758.757	70.2	5.048	0.7
3	-2	E	4	-1	E	230 027.055	20.9	0.734	-1.5
4	2	A^-	5	1	A^-	234 683.371	49.7	1.121	-2.1
5	-4	E	6	-3	E	234 698.519	103.6	0.463	1.7
5	1	A^+	4	1	A^+	239 746.221	37.6	3.885	-1.0
5	3	E	6	2	E	240 241.497	57.9	0.981	-0.7
5	0	E	4	0	E	241 700.161	23.2	4.040	-1.0
5	-1	E	4	-1	E	241 767.236	20.9	3.883	-1.0
5	0	A^+	4	0	A^+	241 791.355	23.2	4.042	-1.0

TABLE B.1: *Continued.*

Upper state			Lower state			Transition (MHz)	Excitation (K)	$S\mu_e^2$ (D ²)	K_μ
J	K	Sym	J	K	Sym				
5	4	A^-	4	4	A^-	241 806.526	103.6	1.457	-1.0
5	4	A^+	4	4	A^+	241 806.527	103.6	1.457	-1.0
5	-4	E	4	-4	E	241 813.257	103.2	1.455	-1.0
5	4	E	4	4	E	241 829.631	106.1	1.463	-1.0
5	3	A^+	4	3	A^+	241 832.720	73.0	2.583	-1.0
5	3	A^-	4	3	A^-	241 833.108	73.0	2.583	-1.0
5	2	A^-	4	2	A^-	241 842.286	60.9	3.417	-1.0
5	3	E	4	3	E	241 843.606	57.8	2.591	-1.0
5	-3	E	4	-3	E	241 852.301	78.0	2.602	-1.0
5	1	E	4	1	E	241 879.027	31.1	3.980	-1.0
5	2	A^+	4	2	A^+	241 887.676	60.9	3.417	-1.0
5	-2	E	4	-2	E	241 904.149	41.2	3.400	-1.0
5	2	E	4	2	E	241 904.646	32.3	3.358	-1.0
5	1	A^-	4	1	A^-	243 915.791	38.0	3.885	-1.0
4	2	A^+	5	1	A^+	247 228.588	49.1	1.086	-2.0
7	4	A^-	8	3	A^-	249 443.304	133.4	1.232	0.4
7	4	A^+	8	3	A^+	249 451.845	133.4	1.232	0.4
9	3	A^-	9	2	A^+	251 359.888	142.2	8.314	1.2
8	3	A^-	8	2	A^+	251 517.309	121.3	7.304	1.2
7	3	A^-	7	2	A^+	251 641.787	102.7	6.276	1.2
6	3	A^-	6	2	A^+	251 738.437	86.5	5.221	1.2
5	3	A^-	5	2	A^+	251 811.955	72.5	4.123	1.2
4	3	A^-	4	2	A^+	251 866.523	60.9	2.952	1.2
5	3	A^+	5	2	A^-	251 890.886	72.5	4.122	1.2
6	3	A^+	6	2	A^-	251 895.727	86.5	5.218	1.2
4	3	A^+	4	2	A^-	251 900.452	60.9	2.952	1.2
3	3	A^-	3	2	A^+	251 905.729	51.6	1.640	1.2
3	3	A^+	3	2	A^-	251 917.065	51.6	1.640	1.2
7	3	A^+	7	2	A^-	251 923.701	102.7	6.268	1.2
8	3	A^+	8	2	A^-	251 984.837	121.3	7.288	1.2
9	3	A^+	9	2	A^-	252 090.409	142.1	8.287	1.2
2	0	E	1	-1	E	254 015.382	0.0	0.499	-2.5
2	1	E	1	0	E	261 805.677	2.3	1.334	-1.4
6	1	E	5	2	E	265 289.567	43.9	1.546	-2.8
5	2	E	4	1	E	266 838.148	31.1	3.847	0.8
9	0	E	8	1	E	267 403.473	91.5	3.987	-0.6
9	-1	E	8	0	E	278 304.514	88.7	5.820	0.4
2	-2	E	3	-1	E	278 342.269	11.6	0.329	-1.4
4	-4	E	5	-3	E	283 094.959	89.6	0.185	1.3
3	2	A^-	4	1	A^-	285 111.113	38.0	0.696	-1.9
8	1	E	7	-2	E	285 683.712	83.0	0.020	-2.3
6	1	A^+	5	1	A^+	287 670.770	49.1	4.721	-1.0
4	3	E	5	2	E	288 705.632	43.9	0.592	-0.7
6	0	E	5	0	E	289 939.379	34.8	4.847	-1.0
6	-1	E	5	-1	E	290 069.750	32.5	4.718	-1.0
6	0	A^+	5	0	A^+	290 110.640	34.8	4.850	-1.0
6	4	A^-	5	4	A^-	290 161.351	115.2	2.699	-1.0
6	4	A^+	5	4	A^+	290 161.354	115.2	2.699	-1.0
6	-4	E	5	-4	E	290 162.359	114.8	2.695	-1.0
6	4	E	5	4	E	290 183.292	117.7	2.710	-1.0
6	2	A^-	5	2	A^-	290 184.676	72.5	4.340	-1.0
6	3	A^+	5	3	A^+	290 189.518	84.6	3.633	-1.0
6	3	A^-	5	3	A^-	290 190.552	84.6	3.633	-1.0
6	-3	E	5	-3	E	290 209.698	89.6	3.659	-1.0
6	3	E	5	3	E	290 213.183	69.4	3.643	-1.0
6	1	E	5	1	E	290 248.688	42.7	4.835	-1.0
6	2	A^+	5	2	A^+	290 264.071	72.5	4.340	-1.0
6	-2	E	5	-2	E	290 307.283	52.8	4.318	-1.0
6	2	E	5	2	E	290 307.741	43.9	4.266	-1.0
6	1	A^-	5	1	A^-	292 672.892	49.7	4.721	-1.0
3	2	A^+	4	1	A^+	293 464.057	37.6	0.681	-1.8
6	4	A^-	7	3	A^-	297 820.920	114.8	0.847	0.2
6	4	A^+	7	3	A^+	297 824.800	114.8	0.847	0.2
3	0	E	2	-1	E	302 369.778	4.6	1.014	-2.3
1	1	A^-	1	0	A^+	303 366.928	2.3	2.966	-1.9

TABLE B.1: *Continued.*

Upper state			Lower state			Transition (MHz)	Excitation (K)	$S\mu_e^2$ (D ²)	K_μ
J	K	Sym	J	K	Sym				
2	1	A^-	2	0	A^+	304 208.355	7.0	4.934	-1.9
3	1	A^-	3	0	A^+	305 473.498	13.9	6.887	-1.9
4	1	A^-	4	0	A^+	307 165.930	23.2	8.820	-1.9
5	1	A^-	5	0	A^+	309 290.366	34.8	10.728	-1.9
3	1	E	2	0	E	310 192.996	7.0	1.773	-1.3
6	1	A^-	6	0	A^+	311 852.618	48.7	12.604	-1.9
7	1	E	6	2	E	313 596.766	57.9	1.966	-2.5
10	0	E	9	1	E	314 351.073	112.4	4.531	-0.7
10	0	E	9	1	E	314 351.073	112.4	4.531	-0.7
7	1	A^-	7	0	A^+	314 859.535	65.0	14.442	-1.9
6	2	E	5	1	E	315 266.861	42.7	4.215	0.5
8	1	A^-	8	0	A^+	318 318.926	83.5	16.237	-1.9
9	1	A^-	9	0	A^+	322 239.468	104.4	17.984	-1.9
10	1	A^-	10	0	A^+	326 630.589	127.6	19.677	-1.8
10	1	A^-	10	0	A^+	326 630.589	127.6	19.677	-1.8
10	-1	E	9	0	E	326 961.234	109.6	6.666	0.2
10	-1	E	9	0	E	326 961.234	109.6	6.666	0.2
8	-3	E	9	-2	E	330 793.891	122.5	2.174	-1.8
9	1	E	8	-2	E	333 864.723	101.6	0.035	-2.1
2	2	A^-	3	1	A^-	335 133.572	28.6	0.307	-1.7
7	1	A^+	6	1	A^+	335 582.020	62.9	5.549	-1.0
3	3	E	4	2	E	337 135.861	32.3	0.248	-0.8
7	0	E	6	0	E	338 124.491	48.7	5.653	-1.0
7	-1	E	6	-1	E	338 344.591	46.4	5.546	-1.0
7	0	A^+	6	0	A^+	338 408.701	48.7	5.659	-1.0
7	-4	E	6	-4	E	338 504.068	128.7	3.811	-1.0
7	4	A^-	6	4	A^-	338 512.635	129.1	3.817	-1.0
7	4	A^+	6	4	A^+	338 512.647	129.1	3.817	-1.0
7	2	A^-	6	2	A^-	338 512.856	86.5	5.231	-1.0
7	4	E	6	4	E	338 530.261	131.6	3.833	-1.0
7	3	A^+	6	3	A^+	338 540.830	98.5	4.613	-1.0
7	3	A^-	6	3	A^-	338 543.155	98.5	4.613	-1.0
7	-3	E	6	-3	E	338 559.966	103.6	4.646	-1.0
7	3	E	6	3	E	338 583.219	83.3	4.626	-1.0
7	1	E	6	1	E	338 614.939	56.7	5.681	-1.0
7	2	A^+	6	2	A^+	338 639.805	86.5	5.231	-1.0
7	2	E	6	2	E	338 721.696	57.9	5.143	-1.0
7	-2	E	6	-2	E	338 722.902	66.8	5.204	-1.0
2	2	A^+	3	1	A^+	340 141.145	28.3	0.303	-1.7
7	1	A^-	6	1	A^-	341 415.618	63.7	5.550	-1.0
5	4	A^-	6	3	A^-	346 202.724	98.5	0.496	0.0
5	4	A^+	6	3	A^+	346 204.276	98.5	0.496	0.0
4	0	E	3	-1	E	350 687.667	11.6	1.554	-2.1
1	1	A^+	0	0	A^+	350 905.108	0.0	1.977	-1.8
4	1	E	3	0	E	358 605.802	13.9	2.212	-1.3
8	1	E	7	2	E	361 852.201	74.1	2.379	-2.3
7	2	E	6	1	E	363 739.869	56.7	4.572	0.3
7	-3	E	8	-2	E	379 493.994	101.6	1.749	-1.7
10	1	E	9	-2	E	381 948.998	122.5	0.057	-1.9
8	1	A^+	7	1	A^+	383 477.896	79.0	6.372	-1.0
8	0	E	7	0	E	386 247.662	65.0	6.459	-1.0
8	-1	E	7	-1	E	386 587.277	62.7	6.369	-1.0
8	0	A^+	7	0	A^+	386 682.044	65.0	6.467	-1.0
8	2	A^-	7	2	A^-	386 824.466	102.7	6.102	-1.0
8	3	A^+	7	3	A^+	386 885.602	114.8	5.551	-1.0
8	3	A^-	7	3	A^-	386 890.250	114.8	5.551	-1.0
8	-3	E	7	-3	E	386 901.917	119.8	5.590	-1.0
8	3	E	7	3	E	386 953.783	99.6	5.566	-1.0
8	1	E	7	1	E	386 977.131	72.9	6.520	-1.0
8	2	A^+	7	2	A^+	387 014.728	102.7	6.102	-1.0
8	2	E	7	2	E	387 146.681	74.1	6.001	-1.0
8	-2	E	7	-2	E	387 153.520	83.0	6.071	-1.0
8	1	A^-	7	1	A^-	390 141.435	80.1	6.373	-1.0
4	4	A^-	5	3	A^-	394 586.749	84.6	0.199	-0.1
4	4	A^-	5	3	A^-	394 586.749	84.6	0.199	-0.1

TABLE B.1: *Continued.*

Upper state			Lower state			Transition (MHz)	Excitation (K)	$S\mu_e^2$ (D ²)	K_μ
J	K	Sym	J	K	Sym				
4	4	A^+	5	3	A^+	394 587.267	84.6	0.199	-0.1
4	4	A^+	5	3	A^+	394 587.267	84.6	0.199	-0.1
3	3	A^+	2	2	A^+	397 039.127	44.7	4.661	0.4
3	3	A^-	2	2	A^-	397 041.417	44.7	4.661	0.4
2	1	A^+	1	0	A^+	398 446.958	2.3	2.966	-1.7
5	0	E	4	-1	E	398 946.227	20.9	2.128	-2.0
5	1	E	4	0	E	407 069.504	23.2	2.653	-1.2
9	1	E	8	2	E	410 040.052	92.7	2.782	-2.1
8	2	E	7	1	E	412 271.611	72.9	4.914	0.1
2	-2	E	2	-1	E	423 439.705	4.6	1.675	-1.3
3	-2	E	3	-1	E	423 468.656	11.6	2.953	-1.3
4	-2	E	4	-1	E	423 538.281	20.9	4.137	-1.3
5	-2	E	5	-1	E	423 675.194	32.5	5.302	-1.3
6	-2	E	6	-1	E	423 912.728	46.4	6.475	-1.3
7	-2	E	7	-1	E	424 291.038	62.7	7.671	-1.3
8	-2	E	8	-1	E	424 857.281	81.2	8.896	-1.3
9	-2	E	9	-1	E	425 665.882	102.1	10.154	-1.3
10	-2	E	10	-1	E	426 778.898	125.3	11.442	-1.3
6	-3	E	7	-2	E	428 087.548	83.0	1.334	-1.6
9	1	A^+	8	1	A^+	431 356.384	97.4	7.192	-1.0
9	0	E	8	0	E	434 302.041	83.5	7.265	-1.0
9	-1	E	8	-1	E	434 793.419	81.2	7.189	-1.0
9	0	A^+	8	0	A^+	434 927.203	83.5	7.275	-1.0
9	2	A^-	8	2	A^-	435 117.150	121.3	6.961	-1.0
9	3	A^+	8	3	A^+	435 222.721	133.4	6.459	-1.0
9	3	A^-	8	3	A^-	435 231.238	133.4	6.459	-1.0
9	-3	E	8	-3	E	435 234.361	138.4	6.504	-1.0
9	3	E	8	3	E	435 324.933	118.2	6.477	-1.0
9	1	E	8	1	E	435 334.532	91.5	7.353	-1.0
9	2	A^+	8	2	A^+	435 388.658	121.3	6.961	-1.0
9	2	E	8	2	E	435 581.515	92.7	6.847	-1.0
9	-2	E	8	-2	E	435 602.019	101.6	6.926	-1.0
9	1	A^-	8	1	A^-	438 847.746	98.8	7.194	-1.0
7	-2	E	6	1	E	439 908.358	61.9	0.012	-0.2
4	3	A^+	3	2	A^+	445 377.146	51.6	4.885	0.2
4	3	A^-	3	2	A^-	445 388.630	51.6	4.885	0.2
3	1	A^+	2	0	A^+	445 571.383	7.0	3.959	-1.6
6	0	E	5	-1	E	447 118.370	32.5	2.744	-1.9
6	1	E	5	0	E	455 618.030	34.8	3.097	-1.2
10	1	E	9	2	E	458 144.830	113.6	3.176	-2.0
9	2	E	8	1	E	460 875.995	91.5	5.241	0.0
10	2	A^+	10	1	A^-	461 064.174	143.3	9.900	-1.5
5	-5	E	6	-4	E	462 241.574	128.7	0.165	0.6
9	2	A^+	9	1	A^-	464 834.677	119.9	8.840	-1.5
8	2	A^+	8	1	A^-	468 293.764	98.8	7.799	-1.5
7	2	A^+	7	1	A^-	471 420.471	80.1	6.774	-1.5
7	2	A^+	7	1	A^-	471 420.471	80.1	6.774	-1.5
6	2	A^+	6	1	A^-	474 196.284	63.7	5.759	-1.5
5	-3	E	6	-2	E	476 600.752	66.8	0.934	-1.6
5	2	A^+	5	1	A^-	476 605.105	49.7	4.747	-1.5
4	2	A^+	4	1	A^-	478 633.220	38.0	3.727	-1.5
10	1	A^+	9	1	A^+	479 215.540	118.1	8.010	-1.0
3	2	A^+	3	1	A^-	480 269.260	28.6	2.673	-1.5
2	2	A^+	2	1	A^-	481 504.172	21.6	1.523	-1.5
10	0	E	9	0	E	482 282.131	104.3	8.070	-1.0
10	-1	E	9	-1	E	482 958.761	102.1	8.006	-1.0
10	0	A^+	9	0	A^+	483 140.755	104.4	8.083	-1.0
10	2	A^-	9	2	A^-	483 388.564	142.1	7.810	-1.0
10	1	E	9	1	E	483 686.294	112.4	8.180	-1.0
10	3	E	9	3	E	483 696.719	139.0	7.368	-1.0
10	2	A^+	9	2	A^+	483 761.373	142.2	7.811	-1.0
2	2	A^-	2	1	A^+	484 004.670	21.4	1.513	-1.5
10	2	E	9	2	E	484 023.164	113.6	7.684	-1.0
10	-2	E	9	-2	E	484 071.777	122.5	7.771	-1.0
3	2	A^-	3	1	A^+	485 263.207	28.3	2.640	-1.5

TABLE B.1: *Continued.*

Upper state			Lower state			Transition (MHz)	Excitation (K)	$S\mu_e^2$ (D ²)	K_μ
J	K	Sym	J	K	Sym				
4	2	A^-	4	1	A^+	486 940.752	37.6	3.650	-1.5
10	1	A^-	9	1	A^-	487 531.875	119.9	8.012	-1.0
8	-2	E	7	1	E	488 446.939	78.2	0.023	-0.3
5	2	A^-	5	1	A^+	489 036.817	49.1	4.603	-1.5
6	2	A^-	6	1	A^+	491 550.723	62.9	5.517	-1.5
4	1	A^+	3	0	A^+	492 278.701	13.9	4.958	-1.6
5	3	A^+	4	2	A^+	493 699.114	60.9	5.201	0.1
5	3	A^-	4	2	A^-	493 733.689	60.9	5.201	0.1
7	2	A^-	7	1	A^+	494 481.559	79.0	6.400	-1.5
7	0	E	6	-1	E	495 173.112	46.4	3.410	-1.8
8	2	A^-	8	1	A^+	497 828.129	97.4	7.253	-1.5
9	2	A^-	9	1	A^+	501 588.895	118.1	8.079	-1.5
7	1	E	6	0	E	504 293.590	48.7	3.544	-1.2
10	2	A^-	10	1	A^+	505 761.918	141.1	8.877	-1.5
10	2	E	9	1	E	509 564.628	112.4	5.553	-0.1
2	-2	E	1	-1	E	520 179.064	0.0	2.979	-1.2
8	-4	E	8	-3	E	524 740.213	138.4	6.460	0.2
7	-4	E	7	-3	E	524 804.980	119.8	5.380	0.2
6	-4	E	6	-3	E	524 860.878	103.6	4.242	0.2
5	-4	E	5	-3	E	524 908.216	89.6	3.018	0.2
4	-4	E	4	-3	E	524 947.260	78.0	1.647	0.2
4	-3	E	5	-2	E	525 055.734	52.8	0.560	-1.5
10	3	E	10	2	E	529 540.278	136.8	10.347	-0.8
9	3	E	9	2	E	529 866.723	113.6	9.181	-0.8
8	3	E	8	2	E	530 123.306	92.7	8.017	-0.8
7	3	E	7	2	E	530 316.204	74.1	6.850	-0.9
6	3	E	6	2	E	530 454.680	57.9	5.669	-0.9
5	3	E	5	2	E	530 549.238	43.9	4.456	-0.9
4	3	E	4	2	E	530 610.277	32.3	3.178	-0.9
3	3	E	3	2	E	530 647.198	23.0	1.760	-0.9
9	-2	E	8	1	E	537 071.828	96.7	0.038	-0.3
5	1	A^+	4	0	A^+	538 570.562	23.2	5.967	-1.5
6	3	A^+	5	2	A^+	542 000.956	72.5	5.563	0.0
6	3	A^-	5	2	A^-	542 081.955	72.5	5.561	0.0
8	0	E	7	-1	E	543 076.182	62.7	4.135	-1.7
5	5	E	6	4	E	544 820.589	131.6	0.152	0.5
8	1	E	7	0	E	553 146.230	65.0	3.994	-1.2
3	-2	E	2	-1	E	568 566.093	4.6	3.290	-1.2
3	-3	E	4	-2	E	573 470.918	41.2	0.233	-1.5
2	2	A^-	1	1	A^-	579 084.700	16.9	2.724	-1.4
2	2	A^+	1	1	A^+	579 921.252	16.8	2.718	-1.4
6	1	A^+	5	0	A^+	584 449.977	34.8	6.989	-1.5
10	-2	E	9	1	E	585 809.073	117.6	0.058	-0.4
7	3	A^+	6	2	A^+	590 277.715	86.5	5.951	-0.1
7	3	A^-	6	2	A^-	590 440.433	86.5	5.947	-0.1
9	0	E	8	-1	E	590 790.946	81.2	4.927	-1.6
9	1	E	8	0	E	602 233.099	83.5	4.446	-1.2
4	-2	E	3	-1	E	616 979.883	11.6	3.668	-1.2
7	4	E	8	3	E	619 074.389	118.2	1.190	-1.2
3	2	A^-	2	1	A^-	626 626.235	21.6	3.027	-1.4
3	2	A^+	2	1	A^+	629 140.358	21.4	3.008	-1.4
7	1	A^+	6	0	A^+	629 921.357	48.7	8.026	-1.4
8	4	A^+	8	3	A^-	636 303.139	133.4	7.170	-0.5
8	4	A^-	8	3	A^+	636 311.612	133.4	7.170	-0.5
7	4	A^+	7	3	A^-	636 333.571	114.8	5.947	-0.5
7	4	A^-	7	3	A^+	636 337.431	114.8	5.947	-0.5
6	4	A^+	6	3	A^-	636 364.079	98.5	4.673	-0.5
6	4	A^-	6	3	A^+	636 365.625	98.5	4.673	-0.5
5	4	A^+	5	3	A^-	636 393.277	84.6	3.314	-0.5
5	4	A^-	5	3	A^+	636 393.793	84.6	3.314	-0.5
4	4	A^+	4	3	A^-	636 419.858	73.0	1.804	-0.5
4	4	A^-	4	3	A^+	636 419.987	73.0	1.804	-0.5
10	0	E	9	-1	E	638 279.659	102.1	5.794	-1.6
8	3	A^+	7	2	A^+	638 523.513	102.7	6.355	-0.1
8	3	A^-	7	2	A^-	638 817.827	102.7	6.347	-0.1

TABLE B.1: *Continued.*

Upper state			Lower state			Transition (MHz)	Excitation (K)	$S\mu_e^2$ (D ²)	K_μ
J	K	Sym	J	K	Sym				
10	1	E	9	0	E	651 617.352	104.3	4.896	-1.1
5	-2	E	4	-1	E	665 442.431	20.9	4.061	-1.2
6	4	E	7	3	E	667 497.911	99.6	0.817	-1.2
4	2	A^-	3	1	A^-	673 745.955	28.6	3.409	-1.4
8	1	A^+	7	0	A^+	674 990.552	65.0	9.081	-1.4
3	3	E	2	2	E	675 773.390	16.1	4.986	-0.9
4	2	A^+	3	1	A^+	678 785.314	28.3	3.367	-1.4
9	3	A^+	8	2	A^+	686 731.506	121.3	6.770	-0.2
9	3	A^-	8	2	A^-	687 224.599	121.3	6.755	-0.2
6	-2	E	5	-1	E	713 982.478	32.5	4.446	-1.2
4	-4	E	3	-3	E	718 436.226	68.7	6.379	-0.1
9	1	A^+	8	0	A^+	719 664.892	83.5	10.157	-1.4
5	2	A^-	4	1	A^-	720 441.448	38.0	3.827	-1.3
4	3	E	3	2	E	724 121.614	23.0	5.219	-0.9
5	2	A^+	4	1	A^+	728 862.485	37.6	3.747	-1.3
10	3	A^+	9	2	A^+	734 893.852	142.2	7.192	-0.3
10	3	A^-	9	2	A^-	735 673.043	142.1	7.168	-0.3
6	-5	E	6	-4	E	752 359.362	128.7	3.388	-0.0
6	-5	E	6	-4	E	752 359.362	128.7	3.388	-0.0
5	-5	E	5	-4	E	752 403.933	114.8	1.823	-0.0
5	-5	E	5	-4	E	752 403.933	114.8	1.823	-0.0
7	-2	E	6	-1	E	762 635.630	46.4	4.812	-1.2
7	-2	E	6	-1	E	762 635.630	46.4	4.812	-1.2
10	1	A^+	9	0	A^+	763 953.229	104.4	11.257	-1.4
4	4	E	5	3	E	764 281.390	69.4	0.191	-1.2
9	-3	E	9	-2	E	766 028.253	122.5	8.268	-1.4
9	-3	E	9	-2	E	766 028.253	122.5	8.268	-1.4
8	-3	E	8	-2	E	766 395.911	101.6	7.268	-1.4
8	-3	E	8	-2	E	766 395.911	101.6	7.268	-1.4
7	-3	E	7	-2	E	766 647.514	83.0	6.246	-1.4
7	-3	E	7	-2	E	766 647.514	83.0	6.246	-1.4
6	2	A^-	5	1	A^-	766 710.334	49.7	4.266	-1.3
5	-4	E	4	-3	E	766 760.517	78.0	6.554	-0.2
5	-4	E	4	-3	E	766 760.517	78.0	6.554	-0.2
6	-3	E	6	-2	E	766 810.449	66.8	5.195	-1.4
6	-3	E	6	-2	E	766 810.449	66.8	5.195	-1.4
5	-3	E	5	-2	E	766 908.035	52.8	4.101	-1.4
5	-3	E	5	-2	E	766 908.035	52.8	4.101	-1.4
4	-3	E	4	-2	E	766 959.883	41.2	2.935	-1.4
4	-3	E	4	-2	E	766 959.883	41.2	2.935	-1.4
3	-3	E	3	-2	E	766 982.145	31.9	1.630	-1.4
3	-3	E	3	-2	E	766 982.145	31.9	1.630	-1.4
5	3	E	4	2	E	772 453.883	32.3	5.545	-0.9
6	2	A^+	5	1	A^+	779 380.335	49.1	4.133	-1.3
8	-2	E	7	-1	E	811 444.559	62.7	5.150	-1.2
7	2	A^-	6	1	A^-	812 550.298	63.7	4.721	-1.3
7	2	A^-	6	1	A^-	812 550.298	63.7	4.721	-1.3
6	-4	E	5	-3	E	815 070.575	89.6	6.821	-0.2
6	-4	E	5	-3	E	815 070.575	89.6	6.821	-0.2
6	3	E	5	2	E	820 762.421	43.9	5.910	-0.9
4	4	A^-	3	3	A^-	829 891.404	63.7	6.970	-0.6
4	4	A^-	3	3	A^-	829 891.404	63.7	6.970	-0.6
4	4	A^+	3	3	A^+	829 891.423	63.7	6.970	-0.6
4	4	A^+	3	3	A^+	829 891.423	63.7	6.970	-0.6
7	2	A^+	6	1	A^+	830 349.370	62.9	4.516	-1.3
10	2	E	9	-1	E	833 493.214	102.1	0.027	-1.0
6	5	E	6	4	E	834 959.482	131.6	3.061	-0.0
6	5	E	6	4	E	834 959.482	131.6	3.061	-0.0
5	5	E	5	4	E	835 003.881	117.7	1.649	-0.0
5	5	E	5	4	E	835 003.881	117.7	1.649	-0.0
10	-3	E	10	2	E	841 757.030	142.1	0.007	-1.5
9	-3	E	9	2	E	842 224.085	118.8	0.003	-1.5
8	2	A^-	7	1	A^-	857 959.146	80.1	5.191	-1.3
8	2	A^-	7	1	A^-	857 959.146	80.1	5.191	-1.3
9	-2	E	8	-1	E	860 459.301	81.2	5.452	-1.1

TABLE B.1: *Continued.*

Upper state			Lower state			Transition (MHz)	Excitation (K)	$S\mu_e^2$ (D ²)	K_μ
J	K	Sym	J	K	Sym				
9	-2	E	8	-1	E	860 459.301	81.2	5.452	-1.1
7	-4	E	6	-3	E	863 364.946	103.6	7.140	-0.3
7	-4	E	6	-3	E	863 364.946	103.6	7.140	-0.3
7	3	E	6	2	E	869 037.900	57.9	6.293	-0.9
5	4	A^-	4	3	A^-	878 226.384	73.0	7.157	-0.6
5	4	A^-	4	3	A^-	878 226.384	73.0	7.157	-0.6
5	4	A^+	4	3	A^+	878 226.514	73.0	7.157	-0.6
5	4	A^+	4	3	A^+	878 226.514	73.0	7.157	-0.6
8	2	A^+	7	1	A^+	881 782.078	79.0	4.891	-1.3
8	2	A^+	7	1	A^+	881 782.078	79.0	4.891	-1.3
9	2	A^-	8	1	A^-	902 934.861	98.8	5.677	-1.3
9	2	A^-	8	1	A^-	902 934.861	98.8	5.677	-1.3
5	5	A^+	6	4	A^+	909 074.192	129.1	0.162	-0.8
5	5	A^-	6	4	A^-	909 074.197	129.1	0.162	-0.8
10	-2	E	9	-1	E	909 737.659	102.1	5.711	-1.1
10	-2	E	9	-1	E	909 737.659	102.1	5.711	-1.1
8	-4	E	7	-3	E	911 642.130	119.8	7.492	-0.3
8	-4	E	7	-3	E	911 642.130	119.8	7.492	-0.3
3	-3	E	2	-2	E	912 108.532	25.0	4.639	-1.3
3	-3	E	2	-2	E	912 108.532	25.0	4.639	-1.3
8	3	E	7	2	E	917 269.987	74.1	6.681	-0.9
8	3	E	7	2	E	917 269.987	74.1	6.681	-0.9
6	4	A^-	5	3	A^-	926 554.626	84.6	7.440	-0.6
6	4	A^-	5	3	A^-	926 554.626	84.6	7.440	-0.6
6	4	A^+	5	3	A^+	926 555.148	84.6	7.439	-0.6
6	4	A^+	5	3	A^+	926 555.148	84.6	7.439	-0.6
9	2	A^+	8	1	A^+	933 692.840	97.4	5.255	-1.3
9	2	A^+	8	1	A^+	933 692.840	97.4	5.255	-1.3
10	2	A^-	9	1	A^-	947 475.679	119.9	6.177	-1.3
10	2	A^-	9	1	A^-	947 475.679	119.9	6.177	-1.3
9	-4	E	8	-3	E	959 900.584	138.4	7.866	-0.3
9	-4	E	8	-3	E	959 900.584	138.4	7.866	-0.3
4	-3	E	3	-2	E	960 471.110	31.9	4.864	-1.3
4	-3	E	3	-2	E	960 471.110	31.9	4.864	-1.3
9	3	E	8	2	E	965 448.238	92.7	7.065	-0.9
9	3	E	8	2	E	965 448.238	92.7	7.065	-0.9
7	4	A^-	6	3	A^-	974 876.709	98.5	7.774	-0.6
7	4	A^+	6	3	A^+	974 878.277	98.5	7.774	-0.6
10	2	A^+	9	1	A^+	986 097.829	118.1	5.606	-1.2
5	-5	E	4	-4	E	994 217.190	103.2	8.901	-0.3
9	4	E	9	3	E	1 005 818.528	139.0	7.887	-1.1
9	4	E	9	3	E	1 005 818.528	139.0	7.887	-1.1
8	4	E	8	3	E	1 005 943.809	118.2	6.779	-1.1
8	4	E	8	3	E	1 005 943.809	118.2	6.779	-1.1
7	4	E	7	3	E	1 006 028.171	99.6	5.635	-1.1
7	4	E	7	3	E	1 006 028.171	99.6	5.635	-1.1
6	4	E	6	3	E	1 006 081.130	83.3	4.436	-1.1
6	4	E	6	3	E	1 006 081.130	83.3	4.436	-1.1
5	4	E	5	3	E	1 006 111.021	69.4	3.150	-1.1
5	4	E	5	3	E	1 006 111.021	69.4	3.150	-1.1
4	4	E	4	3	E	1 006 124.996	57.8	1.717	-1.1
4	4	E	4	3	E	1 006 124.996	57.8	1.717	-1.1
5	-3	E	4	-2	E	1 008 812.184	41.2	5.180	-1.3
10	3	E	9	2	E	1 013 563.442	113.6	7.440	-0.9
8	4	A^-	7	3	A^-	1 023 193.338	114.8	8.140	-0.7
8	4	A^+	7	3	A^+	1 023 197.265	114.8	8.140	-0.7
6	-5	E	5	-4	E	1 042 521.722	114.8	9.056	-0.3
6	-3	E	5	-2	E	1 057 117.732	52.8	5.540	-1.3
6	-3	E	5	-2	E	1 057 117.732	52.8	5.540	-1.3
9	4	A^-	8	3	A^-	1 071 505.283	133.4	8.523	-0.7
9	4	A^-	8	3	A^-	1 071 505.283	133.4	8.523	-0.7
9	4	A^+	8	3	A^+	1 071 513.940	133.4	8.523	-0.7
9	4	A^+	8	3	A^+	1 071 513.940	133.4	8.523	-0.7
5	5	E	4	4	E	1 076 833.512	106.1	8.067	-0.2
5	5	E	4	4	E	1 076 833.512	106.1	8.067	-0.2

TABLE B.1: *Continued.*

Upper state			Lower state			Transition (MHz)	Excitation (K)	$S\mu_e^2$ (D ²)	K_μ
J	K	Sym	J	K	Sym				
7	-5	E	6	-4	E	1 090 815.901	128.7	9.303	-0.3
7	-5	E	6	-4	E	1 090 815.901	128.7	9.303	-0.3
7	-3	E	6	-2	E	1 105 370.415	66.8	5.924	-1.2
7	-3	E	6	-2	E	1 105 370.415	66.8	5.924	-1.2
6	5	E	5	4	E	1 125 142.774	117.7	8.211	-0.3
6	5	E	5	4	E	1 125 142.774	117.7	8.211	-0.3
8	-3	E	7	-2	E	1 153 549.431	83.0	6.321	-1.2
8	-3	E	7	-2	E	1 153 549.431	83.0	6.321	-1.2
9	3	E	8	0	E	1 157 641.286	83.5	0.012	-0.6
7	5	E	6	4	E	1 173 434.712	131.6	8.440	-0.3
7	5	E	6	4	E	1 173 434.712	131.6	8.440	-0.3
6	5	A^-	6	4	A^+	1 199 219.280	129.1	3.317	-0.9
6	5	A^-	6	4	A^+	1 199 219.280	129.1	3.317	-0.9
6	5	A^+	6	4	A^-	1 199 219.285	129.1	3.317	-0.9
6	5	A^+	6	4	A^-	1 199 219.285	129.1	3.317	-0.9
5	5	A^-	5	4	A^+	1 199 235.547	115.2	1.785	-0.9
5	5	A^-	5	4	A^+	1 199 235.547	115.2	1.785	-0.9
5	5	A^+	5	4	A^-	1 199 235.548	115.2	1.785	-0.9
5	5	A^+	5	4	A^-	1 199 235.548	115.2	0.000	-0.9
5	5	A^+	5	4	A^-	1 199 235.548	115.2	1.785	-0.9
4	4	E	3	3	E	1 199 599.412	48.5	6.651	-1.1
4	4	E	3	3	E	1 199 599.412	48.5	6.651	-1.1
9	-3	E	8	-2	E	1 201 630.272	101.6	6.724	-1.2
5	4	E	4	3	E	1 247 954.627	57.8	6.833	-1.1
10	-3	E	9	-2	E	1 249 584.362	122.5	7.128	-1.2
6	4	E	5	3	E	1 296 294.313	69.4	7.109	-1.1
7	4	E	6	3	E	1 344 611.391	83.3	7.438	-1.1
8	4	E	7	3	E	1 392 897.591	99.6	7.798	-1.1
5	5	A^-	4	4	A^-	1 441 042.074	103.6	8.723	-0.9
5	5	A^+	4	4	A^+	1 441 042.074	103.6	8.723	-0.9
9	4	E	8	3	E	1 441 143.461	118.2	8.178	-1.1
10	4	E	9	3	E	1 489 338.366	139.0	8.571	-1.1
10	4	E	9	3	E	1 489 338.366	139.0	8.571	-1.1
6	5	A^+	5	4	A^+	1 489 380.634	115.2	8.878	-0.9
6	5	A^+	5	4	A^+	1 489 380.634	115.2	8.878	-0.9
6	5	A^-	5	4	A^-	1 489 380.635	115.2	8.878	-0.9
6	5	A^-	5	4	A^-	1 489 380.635	115.2	8.878	-0.9
7	5	A^+	6	4	A^+	1 537 705.605	129.1	9.123	-0.9
7	5	A^-	6	4	A^-	1 537 705.610	129.1	9.123	-0.9

BIBLIOGRAPHY

- [1] E. Crone, E. J. Dijksterhuis, R. Forbes, M. G. J. Minnaert, and A. Pannekoek, *The Principal Works of Simon Stevin, Mechanics*, vol. 1 (Swets & Zeitlinger, 1955).
- [2] P. A. M. Dirac, *The Cosmological Constants*, Nature p. 323 (1937).
- [3] E. Teller, *On the Change of Physical Constants*, Phys. Rev. **73**, 801 (1948).
- [4] R. Gold, *Time Invariance of the Elementary Charge*, Phys. Rev. Lett. **20**, 219 (1968).
- [5] P. J. Mohr, B. N. Taylor, and D. B. Newell, *CODATA recommended values of the fundamental physical constants: 2010*, Rev. Mod. Phys. **84**, 1527 (2012).
- [6] C. T. H. Davies et al., *Precise Charm to Strange Mass Ratio and Light Quark Masses from Full Lattice QCD*, Phys. Rev. Lett. **104**, 132003 (2010).
- [7] S. Dürer et al., *Lattice QCD at the physical point: Light quark masses*, Physics Letters B **701**, 265 (2011).
- [8] D. N. F. Dunbar, R. E. Pixley, W. A. Wenzel, and W. Whaling, *The 7.68-MeV State in C^{12}* , Phys. Rev. **92**, 649 (1953).
- [9] F. Hoyle, D. N. F. Dunbar, R. E. Pixley, W. A. Wenzel, and W. Whaling, *A state in C^{12} predicted from astrophysical evidence*, Phys. Rev. **92**, 1095 (1953), conference abstract.
- [10] H. Oberhummer, A. Csótó, and H. Schlattl, *Stellar Production Rates of Carbon and Its Abundance in the Universe*, Science **289**, 88 (2000).
- [11] R. I. Thompson, *The determination of the electron to proton inertial mass ratio via molecular transitions*, Astrophys. Lett. **16**, 3 (1975).
- [12] V. V. Flambaum, D. B. Leinweber, A. W. Thomas, and R. D. Young, *Limits on variations of the quark masses, QCD scale, and fine structure constant*, Phys. Rev. D **69**, 115006 (2004).
- [13] J. Bagdonaite, M. T. Murphy, L. Kaper, and W. Ubachs, *Constraint on a variation of the proton-to-electron mass ratio from H_2 absorption towards quasar Q2348-011*, Mon. Not. R. Astron. Soc. **421**, 419 (2012).
- [14] I. I. Rabi, J. R. Zacharias, S. Millman, and P. Kusch, *A New Method of Measuring Nuclear Magnetic Moment*, Phys. Rev. **53**, 318 (1938).
- [15] I. I. Rabi, S. Millman, P. Kusch, and J. R. Zacharias, *The Molecular Beam Resonance Method for Measuring Nuclear Magnetic Moments.*, Phys. Rev. **55**, 526 (1939).
- [16] N. F. Ramsey, *Molecular Beams* (Oxford University Press, 1956).
- [17] N. F. Ramsey, *A New Molecular Beam Resonance Method*, Phys. Rev. **76**, 996 (1949).
- [18] N. F. Ramsey, *A Molecular Beam Resonance Method with Separated Oscillating Fields*, Phys. Rev. **78**, 695 (1950).

- [19] R. P. Feynman, J. Frank L. Vernon, and R. W. Hellwarth, *Geometrical Representation of the Schrödinger Equation for Solving Maser Problems*, J. App. Phys. **28**, 49 (1957).
- [20] J. R. Zacharias, *Proposed precision magnetic resonance experiment*, MIT, Res. Lab. Electron., Quarterly Progr. Rep. **28**, 19 (1953).
- [21] P. Forman, *Atomichron®: The atomic clock from concept to commercial product*, Proc. IEEE **73**, 1181 (1985).
- [22] N. F. Ramsey, *History of atomic clocks*, J. Res. Nat. Bur. Stand. **88**, 301 (1983).
- [23] A. de Marchi, *The Optically Pumped Caesium Fountain: 10^{-15} Frequency Accuracy?*, Metrologia **18**, 103 (1982).
- [24] R. G. Beausoleil and T. W. Hänsch, *Ultrahigh-resolution two-photon optical Ramsey spectroscopy of an atomic fountain*, Phys. Rev. A **33**, 1661 (1986).
- [25] M. A. Kasevich, E. Riis, S. Chu, and R. G. DeVoe, *rf spectroscopy in an atomic fountain*, Phys. Rev. Lett. **63**, 612 (1989).
- [26] A. Clairon, C. Salomon, S. Guellati, and W. D. Phillips, *Ramsey Resonance in a Zacharias Fountain*, Europhys. Lett. **16**, 165 (1991).
- [27] G. K. Campbell and W. D. Phillips, *Ultracold atoms and precise time standards*, Philos. Trans. R. Soc. London, Ser. A **369**, 4078 (2011).
- [28] W. Gerlach and O. Stern, *Das magnetische Moment des Silberatoms*, Z. Phys. A **9**, 353 (1922).
- [29] H. G. Bennewitz, W. Paul, and C. Schlier, *Fokussierung polarer Moleküle*, Z. Phys. A **141**, 6 (1955).
- [30] J. P. Gordon, H. J. Zeiger, and C. H. Townes, *The Maser – New Type of Microwave Amplifier, Frequency Standard, and Spectrometer*, Phys. Rev. **99**, 1264 (1955).
- [31] S. Y. T. van de Meerakker, H. L. Bethlem, N. Vanhaecke, and G. Meijer, *Manipulation and Control of Molecular Beams*, Chem. Rev. **112**, 4828 (2012).
- [32] J. G. King and J. R. Zacharias, *Linear decelerator for molecules*, MIT, Res. Lab. Electron., Quarterly Progr. Rep. **48**, 56 (1958).
- [33] S. Y. T. van de Meerakker, H. L. Bethlem, and G. Meijer, *Taming molecular beams*, Nat. Phys. **4**, 595 (2008).
- [34] H. L. Bethlem, G. Berden, and G. Meijer, *Decelerating Neutral Dipolar Molecules*, Phys. Rev. Lett. **83**, 1558 (1999).
- [35] S. D. Hogan, M. Motsch, and F. Merkt, *Deceleration of supersonic beams using inhomogeneous electric and magnetic fields*, Phys. Chem. Chem. Phys. **13**, 18705 (2011).
- [36] C. H. Townes and A. L. Schawlow, *Microwave Spectroscopy* (Dover Publications, 1975).
- [37] B. H. Bransden and C. J. Joachain, *Physics of atoms and molecules* (Pearson Education, 2003), 2nd ed.
- [38] D. M. Dennison and G. E. Uhlenbeck, *The Two-Minima Problem and the Ammonia Molecule*, Phys. Rev. **41**, 313 (1932).

-
- [39] P. F. Bernath, *Spectra of atoms and molecules* (Oxford University Press, 1995).
 - [40] J. J. H. B. Schleipen, *State-to-state cross sections for rotational excitation of NH₃ and OH by collisions with He, Ar, and H₂*, Ph.D. thesis, University of Nijmegen (1992).
 - [41] R. N. Zare, *Angular Momentum* (John Wiley & Sons, 1988).
 - [42] C. M. Western, *PGOPHER, a Program for Simulating Rotational Structure*, <http://pgopher.chm.bris.ac.uk>.
 - [43] M. N. R. Ashfold, R. N. Dixon, N. Little, R. J. Stickland, and C. M. Western, *The \tilde{B}^1E'' state of ammonia: Sub-Doppler spectroscopy at vacuum ultraviolet energies*, J. Chem. Phys. **89**, 1754 (1988).
 - [44] G. Herzberg, *Molecular spectra and molecular structure*, vol. III. Electronic spectra and electronic structure of polyatomic molecules (Van Nostrand Reinhold Company, 1966).
 - [45] J. van Veldhoven, J. Küpper, H. L. Bethlem, B. Sartakov, A. J. A. van Roij, and G. Meijer, *Decelerated molecular beams for high-resolution spectroscopy*, Eur. Phys. J. D **31**, 337 (2004).
 - [46] V. V. Flambaum and M. G. Kozlov, *Limit on the Cosmological Variation of m_p/m_e from the Inversion Spectrum of Ammonia*, Phys. Rev. Lett. **98**, 240801 (2007).
 - [47] P. Helminger, F. C. De Lucia, W. Gordy, H. W. Morgan, and P. A. Staats, *Microwave rotation-inversion spectrum of NT₃*, Phys. Rev. A **9**, 12 (1974).
 - [48] J. van Veldhoven, R. T. Jongma, B. Sartakov, W. A. Bongers, and G. Meijer, *Hyperfine structure of ND₃*, Phys. Rev. A **66**, 032501 (2002).
 - [49] S. G. Kukolich, *Measurement of Ammonia Hyperfine Structure with a Two-Cavity Maser*, Phys. Rev. **156**, 83 (1967).
 - [50] J. T. Hougen, *Reinterpretation of Molecular Beam Hyperfine Data for ¹⁴NH₃ and ¹⁵NH₃*, J. Chem. Phys. **57**, 4207 (1972).
 - [51] H. L. Bethlem, M. Kajita, B. Sartakov, G. Meijer, and W. Ubachs, *Prospects for precision measurements on ammonia molecules in a fountain*, Eur. Phys. J. Spec. Top. **163**, 55 (2008).
 - [52] Š. Urban, V. Špirko, D. Papoušek, J. Kauppinen, S. Belov, L. Gershtein, and A. Krupnov, *A simultaneous analysis of the microwave, submillimeterwave, far infrared, and infrared-microwave two-photon transitions between the ground and ν_2 inversion-rotation levels of ¹⁴NH₃*, J. Mol. Spectrosc. **88**, 274 (1981).
 - [53] D. Laughton, S. Freund, and T. Oka, $\Delta K = \pm 3$ "Forbidden" infrared transitions in the ν_2 -band of NH₃, J. Mol. Spectrosc. **62**, 263 (1976).
 - [54] S. Belov, L. Gershtein, A. Krupnov, A. Maslovskij, Š. Urban, V. Špirko, and D. Papoušek, *Inversion and inversion-rotation spectrum of ¹⁴NH₃ in the ν_2 excited state*, J. Mol. Spectrosc. **84**, 288 (1980).
 - [55] I. Perlman, A. Ghiorso, and G. T. Seaborg, *Systematics of Alpha-Radioactivity*, Phys. Rev. **77**, 26 (1950).
 - [56] R. Eisberg and R. Resnick, *Quantum physics of atoms, molecules, solids, nuclei, and particles* (John Wiley & Sons, 1985), 2nd ed.

- [57] H. Geiger and J. M. Nuttall, *The ranges of the α particles from various radioactive substances and a relation between range and period of transformation*, Philos. Mag. **22**, 613 (1911).
- [58] D. Park, *Introduction to the quantum theory* (McGraw-Hill, 1974), 2nd ed.
- [59] G. Gamow, *Zur Quantentheorie des Atomkernes*, Z. Phys. A **51**, 204 (1928).
- [60] R. W. Gurney and E. U. Condon, *Quantum Mechanics and Radioactive Disintegration*, Phys. Rev. **33**, 127 (1929).
- [61] Y. Hatsukawa, H. Nakahara, and D. C. Hoffman, *Systematics of alpha decay half-lives*, Phys. Rev. C **42**, 674 (1990).
- [62] G. Audi, O. Bersillon, J. Blachot, and A. Wapstra, *The Nubase evaluation of nuclear and decay properties*, Nucl. Phys. A **729**, 3 (2003).
- [63] S. P. Ellingsen, M. A. Voronkov, S. L. Breen, and J. E. J. Lovell, *First Cosmological Constraints on the Proton-to-electron Mass Ratio from Observations of Rotational Transitions of Methanol*, Astrophys. J. Lett **747**, L7 (2012).
- [64] S. Muller et al., *Molecules at $z = 0.89$: A 4-mm-rest-frame absorption line survey toward PKS 1830-211*, Astron. Astrophys. **535**, A103 (2011).
- [65] E. Reinhold, R. Buning, U. Hollenstein, A. Ivanchik, P. Petitjean, and W. Ubachs, *Indication of a Cosmological Variation of the Proton-Electron Mass Ratio Based on Laboratory Measurement and Reanalysis of H_2 Spectra*, Phys. Rev. Lett. **96**, 151101 (2006).
- [66] W. Ubachs, R. Buning, K. S. E. Eikema, and E. Reinhold, *On a possible variation of the proton-to-electron mass ratio: H_2 spectra in the line of sight of high-redshift quasars and in the laboratory*, J. Mol. Spectrosc. **241**, 155 (2007).
- [67] C. Henkel et al., *The density, the cosmic microwave background, and the proton-to-electron mass ratio in a cloud at redshift 0.9*, Astron. Astrophys. **500**, 725 (2009).
- [68] N. Kanekar, *Constraining Changes in the Proton-Electron Mass Ratio with Inversion and Rotational Lines*, Astroph. J. Lett. **728**, L12 (2011).
- [69] F. J. Lovas, *NIST Recommended Rest Frequencies for Observed Interstellar Molecular Microwave Transitions—2002 Revision*, J. Phys. Chem. Ref. Data **33**, 177 (2004).
- [70] T. Wiklind and F. Combes, *The redshift of the gravitational lens of PKS1830-211 determined from molecular absorption lines*, Nature **379**, 139 (1996).
- [71] M. T. Murphy, V. V. Flambaum, S. Muller, and C. Henkel, *Strong Limit on a Variable Proton-to-Electron Mass Ratio from Molecules in the Distant Universe*, Science **320**, 1611 (2008).
- [72] S. Bize et al., *Cold atom clocks and applications*, J. Phys. B. **38**, S449 (2005).
- [73] T. P. Heavner, S. R. Jefferts, E. A. Donley, J. H. Shirley, and T. E. Parker, *NIST-F1: recent improvements and accuracy evaluations*, Metrologia **42**, 411 (2005).
- [74] M. M. Boyd, A. D. Ludlow, S. Blatt, S. M. Foreman, T. Ido, T. Zelevinsky, and J. Ye, *^{87}Sr Lattice Clock with Inaccuracy below 10^{-15}* , Phys. Rev. Lett. **98**, 083002 (2007).
- [75] W. H. Oskay et al., *Single-Atom Optical Clock with High Accuracy*, Phys. Rev. Lett.

- 97, 020801 (2006).
- [76] C. W. Chou, D. B. Hume, J. C. J. Koelemeij, D. J. Wineland, and T. Rosenband, *Frequency Comparison of Two High-Accuracy Al^+ Optical Clocks*, Phys. Rev. Lett. **104**, 070802 (2010).
 - [77] J. Doyle, B. Friedrich, R. V. Krems, and F. Masnou-Seeuws, *Editorial: Quo vadis, cold molecules?*, Eur. Phys. J. D **31**, 149 (2004).
 - [78] E. R. Hudson, H. J. Lewandowski, B. C. Sawyer, and J. Ye, *Cold Molecule Spectroscopy for Constraining the Evolution of the Fine Structure Constant*, Phys. Rev. Lett. **96**, 1 (2006).
 - [79] J. J. Hudson, B. E. Sauer, M. R. Tarbutt, and E. A. Hinds, *Measurement of the Electron Electric Dipole Moment Using YbF Molecules*, Phys. Rev. Lett. **89**, 023003 (2002).
 - [80] E. R. Meyer and J. L. Bohn, *Prospects for an electron electric-dipole moment search in metastable ThO and ThF^+* , Phys. Rev. A **78**, 010502 (2008).
 - [81] D. DeMille, S. B. Cahn, D. Murphree, D. A. Rahmlow, and M. G. Kozlov, *Using Molecules to Measure Nuclear Spin-Dependent Parity Violation*, Phys. Rev. Lett. **100**, 1 (2008).
 - [82] C. Daussy, T. Marrel, A. Amy-Klein, C. T. Nguyen, C. J. Bordé, and C. Chardonnet, *Limit on the Parity Nonconserving Energy Difference between the Enantiomers of a Chiral Molecule by Laser Spectroscopy*, Phys. Rev. Lett. **83**, 1554 (1999).
 - [83] A. Shelkovnikov, R. J. Butcher, C. Chardonnet, and A. Amy-Klein, *Stability of the Proton-to-Electron Mass Ratio*, Phys. Rev. Lett. **100**, 150801 (2008).
 - [84] V. V. Flambaum, *Variation of fundamental constants in space and time: Theory and observations*, Eur. Phys. J. Spec. Top. **163**, 159 (2008).
 - [85] H. L. Bethlem, F. M. H. Crompvoets, R. T. Jongma, S. Y. T. van de Meerakker, and G. Meijer, *Deceleration and trapping of ammonia using time-varying electric fields*, Phys. Rev. A **65**, 1 (2002).
 - [86] G. Herzberg, *Molecular spectra and molecular structure*, vol. II. Infrared and Raman spectra of polyatomic molecules (Van Nostrand Reinhold Company, 1956).
 - [87] F. M. H. Crompvoets, R. T. Jongma, H. L. Bethlem, A. J. A. van Roij, and G. Meijer, *Longitudinal Focusing and Cooling of a Molecular Beam*, Phys. Rev. Lett. **89**, 093004 (2002).
 - [88] S. Stolte, J. Reuss, and H. Schwartz, *Orientalional anisotropy in the total collision cross section of state-selected NO on CCl_4 using crossed molecular beams*, Physica **57**, 254 (1972).
 - [89] C. E. Heiner, H. L. Bethlem, and G. Meijer, *Molecular beams with a tunable velocity*, Phys. Chem. Chem. Phys. **8**, 2666 (2006).
 - [90] W. Paul, *Electromagnetic traps for charged and neutral particles*, Rev. Mod. Phys. **62**, 531 (1990).
 - [91] W. C. Wiley and I. H. McLaren, *Time-of-Flight Mass Spectrometer with Improved Resolution*, Rev. Sci. Instr. **26**, 1150 (1955).

- [92] B. Sawyer, Ph.D. thesis, University of Colorado (2010).
- [93] J. J. Hudson, D. M. Kara, I. J. Smallman, B. E. Sauer, M. R. Tarbutt, and E. A. Hinds, *Improved measurement of the shape of the electron.*, Nature **473**, 493 (2011).
- [94] M. R. Tarbutt, J. J. Hudson, B. E. Sauer, and E. A. Hinds, *Prospects for measuring the electric dipole moment of the electron using electrically trapped polar molecules*, Farad. Disc. **142**, 37 (2009).
- [95] A. T. J. B. Eppink and D. H. Parker, *Velocity map imaging of ions and electrons using electrostatic lenses: Application in photoelectron and photofragment ion imaging of molecular oxygen*, Rev. Sci. Instrum. **68**, 3477 (1997).
- [96] D. W. Chandler and P. L. Houston, *Two-dimensional imaging of state-selected photodissociation products detected by multiphoton ionization*, J. Chem. Phys. **87**, 1445 (1987).
- [97] B. J. Whitaker, *Imaging in Molecular Dynamics: Technology and Applications* (Cambridge University Press, Cambridge, 2003).
- [98] M. L. Lipciuc, J. B. Buijs, and M. H. M. Janssen, *High resolution slice imaging of a molecular speed distribution.*, Phys. Chem. Chem. Phys. **8**, 219 (2006).
- [99] H. L. Offerhaus, C. Nicole, F. Lefhpine, C. Bordas, F. Rosca-Pruna, and M. J. J. Vrakking, *A magnifying lens for velocity map imaging of electrons and ions*, Rev. Sci. Instrum. **72**, 3245 (2001).
- [100] D. A. Dahl, J. E. Delmore, and A. D. Appelhans, *SIMION PC/PS2 electrostatic lens design program*, Rev. Sci. Instrum. **61**, 607 (1990).
- [101] B. Y. Chang, R. C. Hoetzlein, J. A. Mueller, J. D. Geiser, and P. L. Houston, *Improved two-dimensional product imaging: The real-time ion-counting method*, Rev. Sci. Instrum. **69**, 1665 (1998).
- [102] W. E. Conaway, R. J. Morrison, and R. N. Zare, *Vibrational state selection of ammonia ions using resonant 2 + 1 multiphoton ionization*, Chem. Phys. Lett. **113**, 429 (1985).
- [103] R. Rüede, H. Troxler, C. Beglinger, and M. Jungen, *The dissociation energies of the positive ions NH_3^+ , NF_3^+ , PH_3^+ , PF_3^+ and PCl_3^+* , Chem. Phys. Lett. **203**, 477 (1993).
- [104] C. E. Heiner, D. Carty, G. Meijer, and H. L. Bethlem, *A molecular synchrotron*, Nat. Phys. **3**, 115 (2007).
- [105] P. C. Zieger, S. Y. T. van de Meerakker, C. E. Heiner, H. L. Bethlem, A. J. A. van Roij, and G. Meijer, *Multiple Packets of Neutral Molecules Revolving for over a Mile*, Phys. Rev. Lett. **105**, 1 (2010).
- [106] S. A. Meek, H. Conrad, and G. Meijer, *A Stark decelerator on a chip*, N. J. Phys. **11**, 055024 (2009).
- [107] S. A. Meek, H. Conrad, and G. Meijer, *Trapping Molecules on a Chip*, Science **324**, 1699 (2009).
- [108] A. Osterwalder, S. A. Meek, G. Hammer, H. Haak, and G. Meijer, *Deceleration of neutral molecules in macroscopic traveling traps*, Phys. Rev. A **81**, 051401 (2010).
- [109] S. A. Meek, M. F. Parsons, G. Heyne, V. Platschkowski, H. Haak, G. Meijer, and A. Osterwalder, *A traveling wave decelerator for neutral polar molecules*, Rev. Sci.

-
- Instrum. **82**, 093108 (2011).
- [110] N. E. Bulleid, R. J. Hendricks, E. A. Hinds, S. A. Meek, G. Meijer, A. Osterwalder, and M. R. Tarbutt, *Traveling-wave deceleration of heavy polar molecules in low-field-seeking states*, Phys. Rev. A **86**, 021404 (2012).
 - [111] J. van den Berg, S. Turkesteen, E. Prinsen, and S. Hoekstra, *Deceleration and trapping of heavy diatomic molecules using a ring-decelerator*, Eur. Phys. J. D **66**, 235 (2012).
 - [112] M. Abramowitz and I. A. Stegun (Eds.), *Handbook of Mathematical Functions with Formulas, Graphs, and Mathematical Tables* (Dover Publications, 1972), 9 ed., page 374–377.
 - [113] E. Kreyszig, *Advanced engineering mathematics* (John Wiley & Sons, 2006), 9th. ed.
 - [114] W. Ketterle and D. E. Pritchard, *Atom cooling by time-dependent potentials*, Phys. Rev. A **46**, 4051 (1992).
 - [115] S. Y. T. van de Meerakker, N. Vanhaecke, H. L. Bethlem, and G. Meijer, *Transverse stability in a Stark decelerator*, Phys. Rev. A **73**, 023401 (2006).
 - [116] L. D. Landau and E. M. Lifshitz, *Mechanics*, vol. 1 (Pergamon, Oxford, 1976).
 - [117] D. Wineland, P. Ekstrom, and H. Dehmelt, *Monoelectron Oscillator*, Phys. Rev. Lett. **31**, 1279 (1973).
 - [118] S. Friebe, C. D’Andrea, J. Walz, M. Weitz, and T. W. Hänsch, *CO₂-laser optical lattice with cold rubidium atoms*, Phys. Rev. A **57**, R20 (1998).
 - [119] M. A. N. Razvi, X. Z. Chu, R. Alheit, G. Werth, and R. Blümel, *Fractional frequency collective parametric resonances of an ion cloud in a Paul trap*, Phys. Rev. A **58**, R34 (1998).
 - [120] J. Wu, R. Newell, M. Hausmann, D. J. Vieira, and X. Zhao, *Loading dynamics of optical trap and parametric excitation resonances of trapped atoms*, Journal of Applied Physics **100**, 054903 (2006).
 - [121] J. K. Webb, V. V. Flambaum, C. W. Churchill, M. J. Drinkwater, and J. D. Barrow, *Search for Time Variation of the Fine Structure Constant*, Phys. Rev. Lett. **82**, 884 (1999).
 - [122] D. Varshalovich and S. Levshakov, *On a time dependence of physical constants*, JETP Lett. **58**, 231 (1993).
 - [123] V. V. Flambaum, *Enhanced effect of temporal variation of the fine-structure constant in diatomic molecules*, Phys. Rev. A **73**, 034101 (2006).
 - [124] V. V. Flambaum and M. G. Kozlov, *Enhanced Sensitivity to the Time Variation of the Fine-Structure Constant and m_p/m_e in Diatomic Molecules*, Phys. Rev. Lett. **99**, 150801 (2007).
 - [125] D. DeMille *et al.*, *Enhanced Sensitivity to Variation of m_e/m_p in Molecular Spectra*, Phys. Rev. Lett. **100**, 043202 (2008).
 - [126] H. L. Bethlem and W. Ubachs, *Testing the time-invariance of fundamental constants using microwave spectroscopy on cold diatomic radicals*, Farad. Disc. **142**, 25 (2009).

- [127] C. C. Lin and J. D. Swalen, *Internal Rotation and Microwave Spectroscopy*, Rev. Mod. Phys. **31**, 841 (1959).
- [128] B. Kirtman, *Interactions between Ordinary Vibrations and Hindered Internal Rotation. I. Rotational Energies*, J. Chem. Phys. **37**, 2516 (1962).
- [129] R. M. Lees, *On the E_1-E_2 Labeling of Energy Levels and the Anomalous Excitation of Interstellar Methanol*, Astrophys. J. **184**, 763 (1973).
- [130] E. Herbst, J. K. Messer, F. C. D. Lucia, and P. Helminger, *A new analysis and additional measurements of the millimeter and submillimeter spectrum of methanol*, J. Mol. Spectrosc. **108**, 42 (1984).
- [131] J. Darling, P. Goldsmith, D. Li, and R. Giovanelli, *A Search for 6.7 GHz Methanol Masers in OH Megamaser Galaxies at $0.11 < z < 0.27$* , Astrophys. J. **125**, 1177 (2003).
- [132] H. S. P. Müller, K. M. Menten, and H. Mäder, *Accurate rest frequencies of methanol maser and dark cloud lines*, Astron. Astrophys. **428**, 1019 (2004).
- [133] L.-H. Xu et al., *Torsion-rotation global analysis of the first three torsional states ($v_t = 0, 1, 2$) and terahertz database for methanol*, J. Mol. Spectrosc. **251**, 305 (2008), and references therein.
- [134] J. T. Hougen, I. Kleiner, and M. Godefroid, *Selection Rules and Intensity Calculations for a C_s Asymmetric Top Molecule Containing a Methyl Group Internal Rotor*, J. Mol. Spectrosc. **163**, 559 (1994), (program available through: <http://www.ifpan.edu.pl/~kisiel/introt/introt.htm#belgi>).
- [135] S. A. Levshakov et al., *Searching for chameleon-like scalar fields with the ammonia method**, Astron. Astrophys. **512**, A44 (2010).
- [136] J.-P. Uzan, *The fundamental constants and their variation: observational and theoretical status*, Rev. Mod. Phys. **75**, 403 (2003), and references therein.
- [137] J. C. Berengut and V. V. Flambaum, *Astronomical and laboratory searches for space-time variation of fundamental constants*, J. Phys. Conf. Ser. **264**, 012010 (2011).
- [138] M. G. Kozlov and S. A. Levshakov, *Sensitivity of the H_3O^+ Inversion-Rotational Spectrum to Changes in the Electron-to-proton Mass Ratio*, Astrophys. J. **726**, 65 (2011).
- [139] E. Herbst and E. F. van Dishoeck, *Complex Organic Interstellar Molecules*, Ann. Rev. of Astron. Astroph. **47**, 427 (2009).
- [140] I. Kleiner, *Asymmetric-top molecules containing one methyl-like internal rotor: Methods and codes for fitting and predicting spectra*, J. Mol. Spectrosc. **260**, 1 (2010).
- [141] R. M. Lees and J. G. Baker, *Torsion-Vibration-Rotation Interactions in Methanol. I. Millimeter Wave Spectrum*, J. Chem. Phys. **48**, 5299 (1968).
- [142] V. V. Ilyushin et al., *The Ground and First Excited Torsional States of Acetic Acid*, J. Mol. Spectrosc. **205**, 286 (2001).
- [143] I. Kleiner, J. T. Hougen, J. U. Grabow, S. P. Belov, M. Y. Tretyakov, and J. Cosléou, *The Third and Fourth Torsional States of Acetaldehyde*, J. Mol. Spectrosc. **179**, 41 (1996).

-
- [144] V. V. Ilyushin, I. Kleiner, and F. J. Lovas, *Microwave Spectra of Molecules of Astrophysical Interest. XXVI. Acetic Acid (CH_3COOH)*, J. Phys. Chem. Ref. Data **37**, 97 (2008).
- [145] P. Jansen, L.-H. Xu, I. Kleiner, W. Ubachs, and H. L. Bethlem, *Methanol as a Sensitive Probe for Spatial and Temporal Variations of the Proton-to-Electron Mass Ratio*, Phys. Rev. Lett. **106**, 100801 (2011).
- [146] V. V. Ilyushin, Private Communication.
- [147] V. V. Ilyushin, E. Alekseev, S. Dyubko, I. Kleiner, and J. Hougen, *Ground and first excited torsional states of acetamide*, J. Mol. Spectrosc. **227**, 115 (2004).
- [148] M. Carvajal, F. Willaert, J. Demaison, and I. Kleiner, *Reinvestigation of the ground and first torsional state of methylformate*, J. Mol. Spectrosc. **246**, 158 (2007).
- [149] S. A. Levshakov, M. G. Kozlov, and D. Reimers, *Methanol as A Tracer of Fundamental Constants*, Astrophys. J. **738**, 26 (2011).
- [150] F. L. Bettens, K. V. L. N. Sastry, E. Herbst, S. Albert, L. C. Oesterling, and F. C. D. Lucia, *The Millimeter- and Submillimeter-Wave Spectrum of Methyl Mercaptan (CH_3SH)*, Astrophys. J. **510**, 789 (1999).
- [151] M. G. Kozlov, *Sensitivity of microwave transitions in H_2O_2 to variation of the electron-to-proton mass ratio*, Phys. Rev. A **84**, 042120 (2011).
- [152] A. L. Malec et al., *Keck telescope constraint on cosmological variation of the proton-to-electron mass ratio*, Mon. Not. R. Astron. Soc. **403**, 1541 (2010).
- [153] F. van Weerdenburg, M. T. Murphy, A. L. Malec, L. Kaper, and W. Ubachs, *First Constraint on Cosmological Variation of the Proton-to-Electron Mass Ratio from Two Independent Telescopes*, Phys. Rev. Lett. **106**, 180802 (2011).
- [154] C. Henkel, Private Communication.
- [155] P. Jansen, I. Kleiner, L.-H. Xu, W. Ubachs, and H. L. Bethlem, *Sensitivity Coefficients to a possible variation of the Proton-to-Electron Mass Ratio of Torsion-Rotation Transitions in Internal Rotor Molecules*, Phys. Rev. A **84**, 062505 (2011).
- [156] V. V. Ilyushin, E. A. Cloessner, Y.-C. Chou, L. B. Picraux, J. T. Hougen, and R. Lavrich, *A microwave study of hydrogen-transfer-triggered methyl-group rotation in 5-methyltropolone*, J. Chem. Phys. **133**, 184307 (2010).
- [157] N. Ohashi and J. T. Hougen, *The torsional-wagging tunneling problem and the torsional-wagging-rotational problem in methylamine*, J. Mol. Spectrosc. **121**, 474 (1987).
- [158] V. Ilyushin, E. Alekseev, S. Dyubko, R. Motiyenko, and J. Hougen, *The rotational spectrum of the ground state of methylamine*, J. Mol. Spectrosc. **229**, 170 (2005).
- [159] V. Ilyushin and F. J. Lovas, *Microwave Spectra of Molecules of Astrophysical Interest. XXV. Methylamine*, J. Phys. Chem. Ref. Data **36**, 1141 (2007).
- [160] J. T. Hougen and B. M. DeKoven, *The application of extended permutation-inversion groups to internal rotation of a symmetric rotor top in a symmetric or asymmetric rotor molecule*, J. Mol. Spectrosc. **98**, 375 (1983).
- [161] V. V. Ilyushin, P. Jansen, M. G. Kozlov, S. A. Levshakov, I. Kleiner, W. Ubachs, and H. L. Bethlem, *Sensitivity to a possible variation of the proton-to-electron mass*

- ratio of torsion-wagging-rotation transitions in methylamine* CH_3NH_2 , Phys. Rev. A **85**, 032505 (2012).
- [162] N. Ohashi and J. T. Hougen, *The torsional-wagging tunneling problem and the torsional-wagging-rotational problem in hydrazine*, J. Mol. Spectrosc. **112**, 384 (1985).
- [163] K. Takagi and T. Kojima, *Microwave Spectrum of Methylamine*, J. Phys. Soc. Jpn **30**, 1145 (1971).
- [164] M. Kréglewski, W. Jager, and H. Dreizler, *The rotational spectrum of methylamine-d3*, J. Mol. Spectrosc. **144**, 334 (1990).
- [165] M. Kréglewski, D. Stryjewski, and H. Dreizler, *Hyperfine quadrupole structure of the rotational spectrum of methylamine-d5*, J. Mol. Spectrosc. **139**, 182 (1990).
- [166] V. V. Ilyushin *et al.*, in preparation .
- [167] Y. G. Smeyers, M. Villa, and M. L. Senent, *Ab Initio Determination of the Torsional and Wagging FIR Spectrum of Methylamine*, J. Mol. Spectrosc. **177**, 66 (1996).
- [168] M. Kréglewski and G. Wlodarczak, *The rotational spectrum of methylamine in a submillimeter-wave range*, J. Mol. Spectrosc. **156**, 383 (1992).
- [169] Y. G. Smeyers, M. Villa, and M.-L. Senent, *Ab Initio Determination of the Torsion-Wagging and Wagging-Bending Infrared Band Structure Spectrum of Methylamine*, J. Mol. Spectrosc. **191**, 232 (1998).
- [170] M. Tsuboi, A. Y. Hirakawa, and K. Tamagake, *An Infrared Analysis of Intra-Molecular Motions of Methylamine*, Proc. Japan Acad. **42**, 795 (1966).
- [171] L. Sztraka, *Determination of the Inversion Potential Function and the Geometry of Methylamine from Microwave and Infrared Data*, Acta Chim. Hung. **6**, 865 (1987).
- [172] N. Ohashi, K. Takagi, J. T. Hougen, W. Olson, and W. J. Lafferty, *Far-infrared spectrum of methyl amine: Assignment and analysis of the first torsional state*, J. Mol. Spectrosc. **132**, 242 (1988).
- [173] M. Tsuboi, A. Y. Hirakawa, T. Ino, T. Sasaki, and K. Tamagake, *Amino Wagging and Inversion in Methylamines*, J. Chem. Phys. **41**, 2721 (1964).
- [174] S. Ellingsen, M. Voronkov, and S. Breen, *Practical Limitations on Astrophysical Observations of Methanol to Investigate Variations in the Proton-to-Electron Mass Ratio*, Phys. Rev. Lett. **107**, 270801 (2011).

DANKWOORD

“What comes up, must go down...” Het moet zo’n beetje de eerste borrel zijn geweest na mijn aanstelling als promovendus dat ik dit - naïef en onbezorgd - tegen Jacques zei. De mensen die Jacques een beetje kennen weten dat hij niet alleen een uitstekende technicus is, maar bovenal ook een bijna encyclopedische kennis bezit op het gebied van classic rock. Hij antwoordde dan ook snel: “Weet je van wie dat nummer is? Dat komt uit *Spinning Wheel* van *Blood, Sweat & Tears*. Dat belooft wat jongen.” En natuurlijk kreeg Jacques gelijk. Dat er nu, vier jaar later, alsnog een proefschrift is van mijn hand is dan ook mede te danken aan de hulp en inspanning van een heleboel mensen, maar van een aantal in het bijzonder. Het doet me veel genoegen om hen hier te bedanken voor hun bijdrage aan het werk dat beschreven is in mijn proefschrift.

Allereerst gaat mijn dank uit naar onze technicus Jacques die altijd bereid was zijn soep koud te laten worden om te helpen bij het zoeken van een lek in de vacuümkamer of om mee te denken over het (ver)bouwen van de opstelling. Jacques, jouw vermogen om snel praktische oplossingen voor lastige problemen te vinden is van onschatbare waarde geweest als het experiment weer eens vast liep. Daarnaast zorgde jij samen met Joost, die regelmatig hielp bij het programmeren in C++, voor een gezellige sfeer in de koffiekamer van het lasercentrum. De pick-up speler en lp’s die jullie daar hebben neergezet hebben vele borrels van een unieke sound voorzien. Heren, bedankt voor de gezellige tijd. Graag wil ik ook Rob bedanken voor zijn hulp en gezellige gesprekken bij de koffie (al dan niet met sompige blokken). Rob, ik ben erg blij dat jij na Jacques’ pensioen onze technicus bent geworden.

Eind 2007 kreeg ik een email van Rick met de vraag of ik eens wilde komen praten over de mogelijkheden om onderzoek bij hem te komen doen in het lab tegenover de koffiemachine. Eén jaar later kon ik aan de slag als AiO. Rick, ik wil je heel erg bedanken voor het sturen van deze email. De afgelopen jaren heb ik enorm veel van je geleerd, maar ook de ruimte gekregen om zelf dingen te leren. In het nawoord van je “blauwe bijbel” schrijf je over Gerard dat zijn instinct voor interessante fysica moeilijk aan te leren is; ik denk dat het je toch aardig gelukt is om je dit eigen te maken. Heel erg bedankt voor je begeleiding, betrokkenheid en enthousiasme, vooral ook op de dagen dat je misschien wat meer had willen slapen.

Wim Ubachs wil ik bedanken voor zijn niet aflatende enthousiasme en voor de vele goede ideeën. Wim, jouw manier om nieuwe samenwerkingsverbanden aan te gaan heeft een diepe indruk op mij gemaakt. Nog voor het wegsturen van het methanolartikel had jij al contact gelegd met de radioastronomen in Bonn, waarmee je de concurrentie de pas afsneed. Ik ben zeer trots om straks te kunnen zeggen dat ik in jouw groep ben gepromoveerd.

My sincere thanks are due to Marina who worked with me on the fountain experiment. Dear Marina thank you so much for the patience you must have had to work with me. I really enjoyed working with you the past years and I especially recall our

happiness when we saw trapped signal for the first time. I am also very grateful to Thomas who joined our team last year. Thomas, you told me once that your brother is teaching English in Vietnam, I am happy that you've chosen to do the same thing here in Amsterdam. Julija, it was great to travel with you to Effelsberg to perform the observations on methanol. Mijn dank gaat daarnaast uit naar Ruud van Putten, oud masterstudent, die voor ik begon als AiO een belangrijke bijdrage heeft geleverd aan de bouw van de opstelling en mij wegwijs heeft gemaakt in het lab.

Ook de andere leden van de koude moleculen subgroep wil ik hartelijk bedanken voor hun gezelligheid en inspiratie. Adrian, bedankt voor de vele gesprekken over spectroscopie en voor het zijn van een gezellige kamergenoot. Also thanks to Chris and Peter, although their stay in Amsterdam was short, it was not less memorable. Aernout, veel succes met de botsingen in de ring.

Since the beginning of my PhD, the size of our group is doubled in size. Despite this rapid growth the good and productive atmosphere that prevails in the group blossomed. I would like to thank all colleagues, students and guests that have contributed to this atmosphere. Thank you for the scientific discussions, but also for the comic relief during coffee breaks or borrels. It has been a great pleasure to have worked with you. The quality of our weekly group seminars could often compete with the most prestigious conferences.

I would also like to thank the members of the department of Physical Chemistry who always made me feel welcome. Steven, bedankt dat ik altijd bij je langs kon lopen om een boek te lenen of om gewoon een praatje te maken. Ook de door jouw georganiseerde kerstdiners aan de Keizergracht waren altijd erg gezellig. Ik vind het erg leuk dat je als lid van de leescommissie en als opponent bij mijn promotie betrokken bent. I would also like to express my appreciation and thanks to the other members of the reading committee for their time and valuable suggestions to improve the manuscript.

Chère Isabelle, merci beaucoup pour la coopération très agréable. C'était super que vous m'avez enseigné la physique de la rotation interne. I am also indebted to Li-Hong Xu, who shared her great knowledge and work on methanol with us. In addition, I would like to thank Vadim Ilyushin, Mikhail Kozlov and Sergei Levshakov for the work on methylamine. Gerne möchte ich auch Christian Henkel und Karl Menten für die gute Zusammenarbeit bei den Radiobeobachtungen danken.

De naam die zeker niet in dit dankwoord mag ontbreken is die van Stefan Lehmann. Stefan, ik ben erg blij dat we de afgelopen jaren regelmatig experimentele tegenslag konden relativeren onder het genot van een biertje. Ook al promoveerde je in een andere groep, je was altijd bereid om te helpen als dat nodig was. Ik ben blij dat je mijn paranimf wilt zijn.

Verder wil ik nog mijn familie en vrienden bedanken voor hun geduld en begrip wanneer ik niet de tijd of energie had die ik graag zou willen hebben. Vooral mijn ouders, mijn zusjes Elisa en Sophie, en Hans en Marijke ben ik dankbaar omdat hun steun verder gaat dan de afgelopen vier jaar. Marit, bedankt dat je er voor me bent, "without you, life would be like a broken pencil. Pointless."

PUBLICATIONS

- *Methanol as a sensitive probe for spatial and temporal variations of the proton-to-electron mass ratio.*
Paul Jansen, Li-Hong Xu, Isabelle Kleiner, Wim Ubachs, and Hendrick L. Bethlem.
Phys. Rev. Lett. **106**, 100801 (2011).
- *Sensitivity of transitions in internal rotor molecules to a possible variation of the proton-to-electron mass ratio.*
Paul Jansen, Isabelle Kleiner, Li-Hong Xu, Wim Ubachs, and Hendrick L. Bethlem.
Phys. Rev. A **84**, 062505 (2011).
- *Sensitivity to a possible variation of the proton-to-electron mass ratio of torsion-wagging-rotation transitions in methylamine CH_3NH_2 .*
Vadim V. Ilyushin, Paul Jansen, Mikhail G. Kozlov, Sergei A. Levshakov, Isabelle Kleiner, Wim Ubachs, and Hendrick L. Bethlem.
Phys. Rev. A **85**, 032505 (2012).
- *Velocity map imaging of a slow beam of ammonia molecules inside a quadrupole guide.*
Marina Quintero-Pérez[†], Paul Jansen[†], and Hendrick L. Bethlem.
Phys. Chem. Chem. Phys. **14**, 9630 (2012).
- *A stringent limit on a drifting proton-to-electron mass ratio from alcohol in the early universe.*
Julija Bagdonaite, Paul Jansen, Christian Henkel, Hendrick L. Bethlem, Karl M. Menten, and Wim Ubachs.
Science **339**, 46 (2013).
- *Static trapping of polar molecules in a traveling wave decelerator.*
Marina Quintero-Pérez[†], Paul Jansen[†], Thomas E. Wall, Joost E. van den Berg, Steven Hoekstra, and Hendrick L. Bethlem.
Phys. Rev. Lett. **110**, 133003 (2013).
- *Methyl mercaptan (CH_3SH) as a probe for μ variation*
Paul Jansen, Li-Hong Xu, Isabelle Kleiner, Hendrick L. Bethlem, and Wim Ubachs
accepted by Phys. Rev. A (2013).
- *Prospects for high-resolution microwave spectroscopy of methanol in a Stark-deflected molecular beam*
Paul Jansen, Isabelle Kleiner, Congsen Meng, Ronald M. Lees, Maurice H.M. Janssen, Wim Ubachs, and Hendrick L. Bethlem
accepted by Mol. Phys. (2013).

[†]These authors contributed equally to this work.

